华南师范大学图书馆

*Library of South China Normal University*

广州石牌 TEL：020—85214537—860

# 检索证明

**编号：202210284158**

**委托检索单位：**汕头职业技术学院

**委托人：**陈明忠

**检索课题：**文献被《科学引文索引扩展版》（SCIE）的收录情况

**检索数据库：《科学引文索引扩展版》（SCIE）**

**检出记录数：1**

**检索结果：**

对《科学引文索引扩展版》的检索结果表明，委托人提供的 1 篇文章（发表于 2022 年）被《科学引文索引扩展版》收录（详见附录）。

**华南师范大学图书馆信息咨询部**

**2022 年 10 月 28 日**

华南师范大学图书馆 信息咨询部

附录：

第 1 篇

**标题**：Network Flow Anomaly Detection Based on Improved Echo State Network

**作者**：Chen, MZ (Chen, Mingzhong) [1];Qiu, B (Qiu, Bin) [2];Ji, J (Ji, Jie) [3]

**来源出版物**：WIRELESS COMMUNICATIONS & MOBILE COMPUTING 卷:2022 文献号:4252766 出版年:JUL 8 2022

**在 WOS 核心合集中的被引频次**：0

DOI：10.1155/2022/4252766

**入藏号**：WOS:000852894000003

**文献类型**：Article

**地址**：[ 1 ]Shantou Polytech, Dept Mech & Elect Engn, Shantou 515078, Peoples R China[ 2 ]Shantou Polytech, Dept Comp, Shantou 515078, Peoples R China[ 3 ]Shantou Univ, Network & Informat Ctr, Shantou 515063, Peoples R China

**通讯作者地址**：Chen, Mingzhong(通讯作者)Shantou Polytech, Dept Mech & Elect Engn, Shantou 515078, Peoples R China

**电子邮件地址**：cmzgjjx@163.com;

ISSN：1530-8669

eISSN：1530-8677

**2021 年影响因子**：2.146　　**五年影响因子**：2.052

**以上结果均由委托人提交确认！**

华南师范大学图书馆

*Library of South China Normal University*

广州石牌 TEL：020—85214537—860

# 检索证明

**编号：202210284162**

**委托检索单位：**汕头职业技术学院

**委托人：**陈明忠

**检索课题：**文献被《工程索引》（Engineering Village Compendex）的收录情况

**检索数据库：《工程索引》（Engineering Village Compendex）**

**检出记录数：1**

**检索结果：**

对《工程索引》的检索结果表明，委托人提供的 1 篇文章（发表于 2022 年）被《工程索引》收录（详见附录）。

**华南师范大学图书馆信息咨询部**

华南师范大学图书馆 信息咨询部

2022 年 10 月 28 日

附录：

第 1 篇

**标题**：Network Flow Anomaly Detection Based on Improved Echo State Network

**作者**：Chen, Mingzhong[1];Qiu, Bin[2];Ji, Jie[3];

**来源出版物**：Wireless Communications and Mobile Computing 卷:2022 出版年:2022

**DOI**：10.1155/2022/4252766

**入藏号**：20223012399715

**文献类型**：Journal article (JA)

**地址**：Department of Mechanical and Electrical Engineering, Shantou Polytechnic, Shantou; 515078, China[1];Departments of Computer, Shantou Polytechnic, Shantou; 515078, China[2];Network and Information Center, Shantou University, Shantou; 515063, China[3];

**通讯作者**：Chen, Mingzhong;

**ISSN**：1530-8669

**基金详情**：

**以上结果均由委托人提交确认！**

报告编号：HDJS0320223081

湖南大學圖書館
HUNAN UNIVERSITY LIBRARY

# 文献检索报告

**委托人：**刘毅嘉

**检索数据库：**

1. SCI-E 美国《科学引文索引》
2. JCR 期刊引证数据库

**检索结果：**

1. SCI-E 美国《科学引文索引》收录论文 1 篇；
2. 其他详细信息请见附件。

**检索日期：**2022 年 11 月 09 日

**声明：**1.本报告检索的文献信息均由委托人提供并确认，如果由于委托人提供信息不实而造成任何后果，本中心概不负责。

检索人（签名）：

湖南大学图书馆科技查新与文献检索中心

附件:

**SCI-E 美国《科学引文索引》**

**第 1 条，共 1 条**

**标题:** Asymmetric diffraction grating via optical vortex light in a tunneling quantum dot molecule

**作者:** Liu, YJ (Liu, Yijia);Xiang, Y (Xiang, Yuan);Mohammed, AA (Abdulsalam Mohammed, Abdulrazak)

**来源出版物:** LASER PHYSICS LETTERS **卷:** 19 **期:** 9 **文献号:** 095205 **DOI:** 10.1088/1612-202X/ac81bb **出版年:** SEP 1 2022

**Web of Science 核心合集中的 "被引频次":**0

**入藏号:** WOS:000835786300001

**文献类型:** Article

**地址:** [Liu, Yijia] Shantou Polytechn, Dept Econ Management, Shantou 515078, Guangdong, Peoples R China

[Xiang, Yuan] Shanghai Maritime Univ Econ & management, Dept Logist Econ, Shanghai 201306, Peoples R China

[Abdulsalam Mohammed, Abdulrazak] Cihan Univ, Commun & Comp Engn Dept, Erbil, Iraq

**通讯作者地址:**[Liu, Yijia] (corresponding author), Shantou Polytechn, Dept Econ Management, Shantou 515078, Guangdong, Peoples R China

**电子邮件地址:** zzhangkb@hotmail.com

**Web of Science 类别:** Optics;Physics, Applied

**ISSN:** 1612-2011

**impact factor**

**2021 年影响因子:1.704**

**JCR 期刊分区（2021）:**

| JCR® 类别 | 类别中的排序 | JCR 分区 |
|---|---|---|
| **PHYSICS, APPLIED** | **119/161** | **Q3** |
| **OPTICS** | **74/101** | **Q3** |

**输出日期:** 2022 年 11 月 09 日

LETTER

# Asymmetric diffraction grating via optical vortex light in a tunneling quantum dot molecule



IOP Publishing | Astro Ltd Laser Physics Letters
Laser Phys. Lett. **19** (2022) 095205 (6pp) https://doi.org/10.1088/1612-202X/ac81bb

## Letter

# Asymmetric diffraction grating via optical vortex light in a tunneling quantum dot molecule

**Yijia Liu[1,*], Yuan Xiang[2] and Abdulrazak Abdulsalam Mohammed[3]**

[1] Department of Economic Management, Shantou Polytechnic, Shantou, Guangdong 515078, People's Republic of China
[2] Department of Logistics Economics, Shanghai Maritime University of Economics and management, Shanghai 201306, People's Republic of China
[3] Communication and Computer Eng. Dep, Cihan University, Erbil, Iraq

E-mail: zzhangkb@hotmail.com

Received 5 July 2022
Accepted for publication 17 July 2022
Published 3 August 2022

**Abstract**

In this letter, we have put out a fresh idea for managing the diffraction sample of optical vortex light that was transmitted from a four-level quantum dot molecule. We describe the creation of a new weak laser field via inter-dot tunneling, which causes the diffraction grating to be dependent on the orbital angular momentum (OAM) of the optical vortex light. We found that the relative phase between the implemented lights and the OAM number of the vortex light affect the intensity distribution of the asymmetric grating. Additionally, we discovered that the maximum amount of probe energy could be dispersed in higher orders of diffracted angles that were negative and positive by modifying the inter-dot tunneling and OAM number.

Keywords: electromagnetically induced grating, optical vortex light, tunneling effect

(Some figures may appear in colour only in the online journal)

## 1. Introduction

It is known that quantum coherence and interference effects can be used to control the optical response of coherent systems [1–3]. In multi-level quantum structures, quantum coherence and interference lead to a number of phenomena, such as electromagnetically induced transparency (EIT) [3], optical solitons [1], four-wave mixing [4], optical bistability [5, 6], and other phenomena [7–12]. In a typical three-level atomic system where the absorption of weak probe light is controlled, the EIT phenomena can be manipulated by using a strong coupling light. In fact, many other phenomena in quantum nonlinear optics are caused by the EIT effect [13–15]. For instance, a distinct phenomenon known as an electromagnetically induced grating (EIG) is produced when the control field is switched out for a standing wave (SW) [8, 16–22]. The amplitude and dispersion of the probe field become spatially periodic as a result of SW patterning of the coupling light. As a result, high order directions are formed from the transmitted probe light. Due to the EIG's broad use in nonlinear optics, numerous quantum systems have theoretically examined it. For instance, Wan *et al* [23] investigated the EIG in a four-level atomic system using enhanced nonlinear modulation by spontaneously generated coherence (SGC). They discovered that the third order of nonlinearity is boosted and the linear absorption is simultaneously decreased due to the presence of quantum interference caused by SGC. As a result, the probe energy may move from diffractions of zero order to those of high order. The EIG pattern of the transmitted probe

* Author to whom any correspondence should be addressed.

 

light from a double V-type quantum system that is close to a plasmonic nanostructure was examined by Vafafard *et al* [24]. They discovered that the presence of plasmonic nanostructure can change the quantum system's dispersion characteristics, which in turn affects how the Fraunhofer diffraction pattern behaves. The transmitted probe light's asymmetric diffraction pattern has recently undergone extensive research [25–27]. In another study by Asadpour *et al*, the diffraction grating from three and four levels quantum system via optical vortex and composite vortex light have been investigated [21, 22]. They have shown that by adjusting the orbital angular momentum (OAM) number of the vortex light, the intensity distribution of the diffraction grating can be manipulated in different regions. In this letter, we discussed the diffraction grating of the optical vortex light from four-level quantum dot molecule (QDM) via electron tunneling effect. We show that in the presence of the electron tunneling, the weak signal light can be generated that cause to phase dependent of the diffraction grating, respectively.

## 2. Model and equations

A QDM consists of two QDs coupled by electron tunneling is presented in figure 1. A weak probe light with Rabi-frequency $\Omega_p$ and detuning $\Delta_p$ interacts with transition $|1\rangle \leftrightarrow |2\rangle$. The coupling and signal driving fields with Rabi-frequencies $\Omega_c, \Omega_s$ and detuning $\Delta_c, \Delta_s$ interacts with transitions $|3\rangle \leftrightarrow |4\rangle$ and $|1\rangle \leftrightarrow |4\rangle$, respectively. The levels $|2\rangle$ and $|3\rangle$ are coupled by the electron tunneling process $T_e$. The optical susceptibility of the QDM related to the coherence term $\rho_{21}$. The steady state analytical expression for the coherence term $\rho_{21}$ can be obtained as follow:

$$\rho_{21} = \frac{\Omega_p\left[i\left(\gamma\delta_p - \delta_p^2\right) - |\Omega_c|^2\right] + \Omega_c^*\Omega_s T_e e^{i\phi}}{(\gamma - i\delta_p)\left(iT_e^2 + \gamma\delta_p - i\delta_p^2 + i|\Omega_c|^2\right)} \tag{1}$$

where $\gamma$ corresponds to the decay rate of QDM and $\phi$ denotes the relative phase between applied lights. Here, we assume $\Delta_c = 0$ and $\Delta_p = \Delta_d = \delta_p$. When the coupling field is in the form of a SW along $x$–$y$ directions, we can write the coupling Rabi-frequency as $\Omega_c(x,y) = \Omega_{c0}[\sin(\pi x/\Lambda_{cx}) + \sin(\pi y/\Lambda_{cy})]$, to realize the periodic spatial modulation, where $\Lambda_x(\Lambda_y)$ is the space period.

Under the slowly varying envelope approximation, the diffraction pattern of the probe light is given in the steady-state regime as follows:

$$\frac{\partial E_p}{\partial z} = i\frac{\pi}{\varepsilon_0\lambda_p}P_p,\ P_p = \varepsilon_0(\chi_p)E_p. \tag{2}$$

Parameter $\lambda_p$ corresponds to the wavelength of the probe light. The transmission function for the probe field is given as:

$$T(x,y) = \exp(-Im(\chi_p)L)\exp(i\mathrm{Re}(\chi_p)L). \tag{3}$$

The first and second terms in the exponential correspond to the amplitude and the phase modulations, respectively.

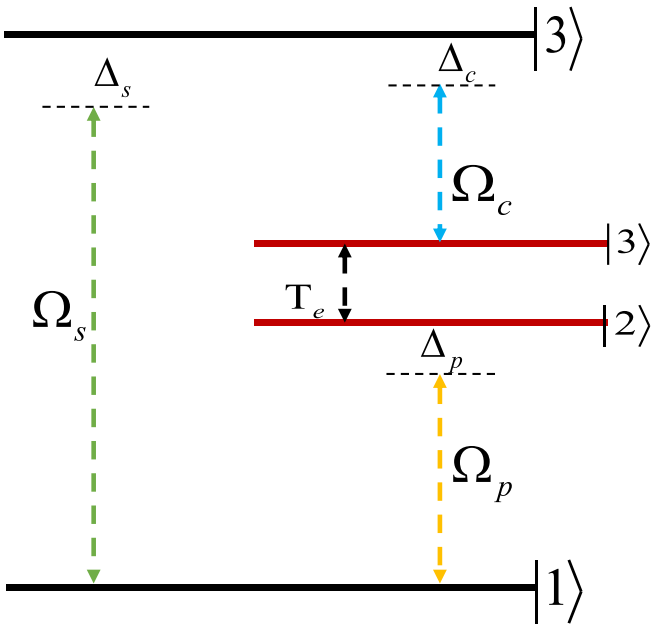


**Figure 1.** Four-level QDM with tunneling effect.

By using of Fourier transformation of the transmission function $T(x,y)$, we obtain Fraunhofer diffraction equation as follows:

$$H_p(\theta_x,\theta_y) = |E(\theta_x,\theta_y)|^2\frac{\sin^2(M\pi R\sin\theta_x)}{M^2(\pi R\sin\theta_x)}\frac{\sin^2(N\pi R\sin\theta_y)}{N^2(\pi R\sin\theta_y)} \tag{4}$$

where

$$E(\theta_x,\theta_y) = \int_0^1 dx\int_0^1 T(x,y)\exp(-i2\pi xR\sin\theta_x) \times \exp(-i2\pi yR\sin\theta_y)dy. \tag{5}$$

$\theta_x$, and $\theta_y$ show the diffraction angle concerning the $z$-direction. Parameters $M$ and $N$ correspond to the number of spatial periods along $x$ and $y$ direction.

In the follow, we consider that the weak signal probe is a vortex beam. Therefore, we have:

$$E_s = \int \varepsilon_s(r/w_s)^{l_p}e^{il_s\varphi_s}e^{r^2/w^2}dr \tag{6}$$

where, $r = \sqrt{x^2+y^2}$, $\varphi_p = \arctan(y/x)$, $l_s$ is the OAM number and $w_s$ is the beam waist, respectively.

In figure 2, we display the Fraunhofer diffraction pattern versus $\sin\theta_x$ and $\sin\theta_y$ in the absence of electron tunneling effect for different value of OAM number. We find that in the absence of tunneling parameter, the quantum system is not depend to the OAM number of the vortex light and we have similar results for different of OAM number, respectively. In this case, most of probe energy gathers in the zero order and we have not any intensity distribution in high orders of grating. In the next step and in figure 3, we show the effect of electron tunneling on Fraunhofer diffraction pattern when the

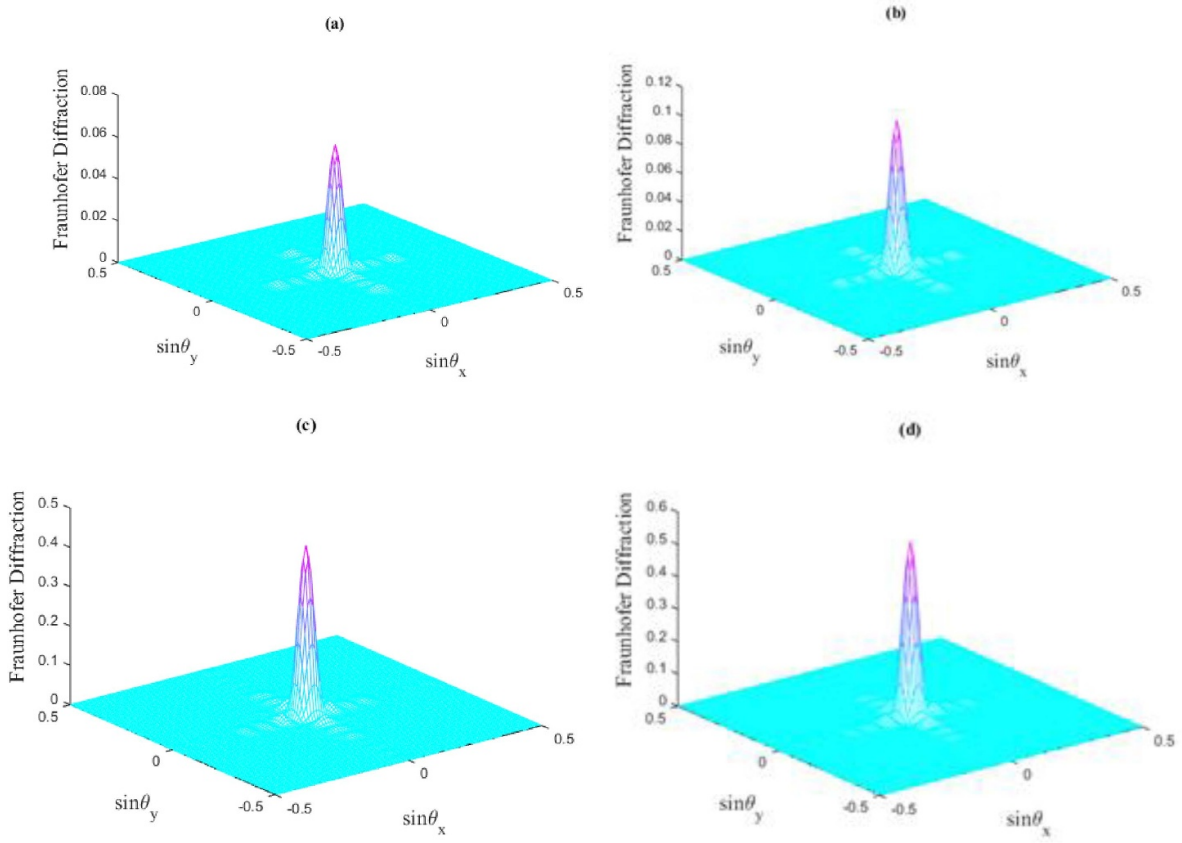


**Figure 2.** Fraunhofer diffraction pattern versus $\sin\theta_x$ and $\sin\theta_y$ in the absence of tunneling effect for (a) $l_s = 1$, (b) $l_s = 2$, (c) $l_s = 3$ and (d) $l_s = 4$. The other selected parameters are $\gamma = 1$, $\delta_p = 0.5\gamma$, $\Omega_c = 3\gamma$, $\Omega_s = 0.1\gamma$, $\phi = 0$ and $M = N = 4$.

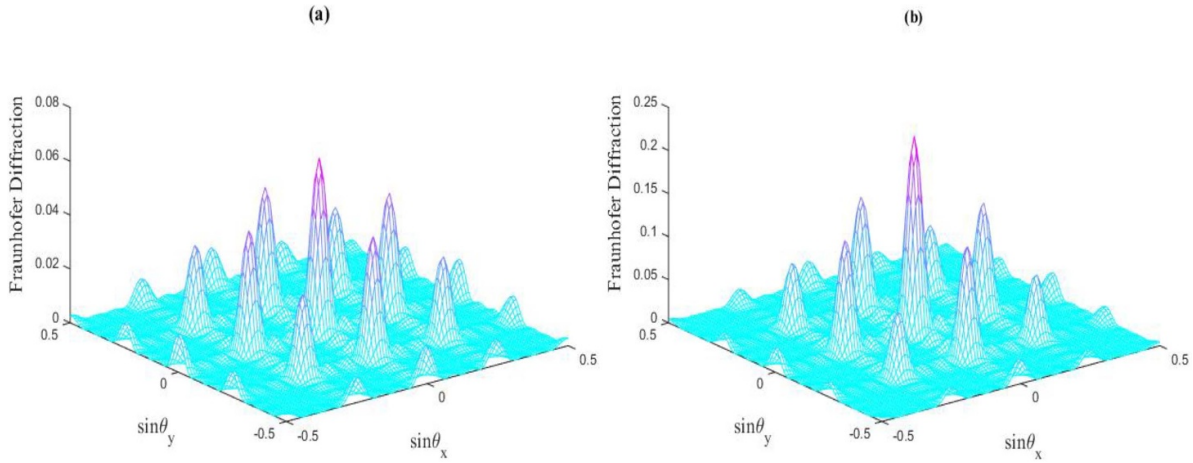


**Figure 3.** Fraunhofer diffraction pattern versus $\sin\theta_x$ and $\sin\theta_y$ for $l_s = 0$ and (a) $T_e = 5\gamma$, and (b) $T_e = 10\gamma$. The other selected parameters are same as figure 2.

optical vortex light becomes Gaussian light i.e. $l_s = 0$. Here, we realized that for $T_e = 5\gamma$ some of probe energy transfer to the high orders, but most of probe energy remains in the zero order, respectively. Here, we find that due to phase modulation of transmission function, the probe energy may transfer to the high orders. By enhancing the electron tunneling effect to $T_e = 10\gamma$ (b), we find that the intensity distribution of the diffraction grating in different orders are enhanced, but most of probe energy is also gathers in the zero-order, respectively. In the other words, the diffracted orders of grating increases when we enhance the electron tunneling effect. In figure 4, we display the Fraunhofer diffraction pattern via different values of OAM number in the presence of the electron tunneling effect, respectively. It is found that the asymmetric diffraction pattern can be realized when we introduce the OAM number of the vortex light as a new controllable parameter for

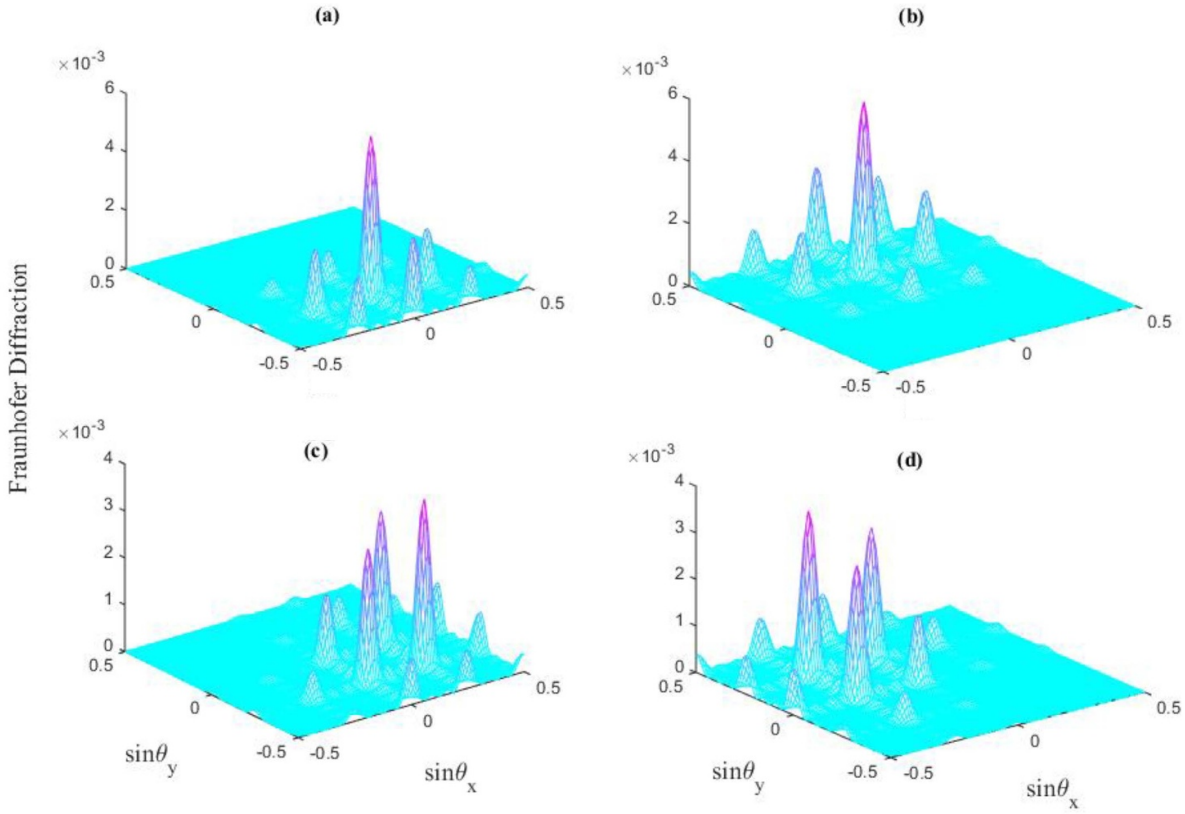


**Figure 4.** Fraunhofer diffraction pattern versus $\sin\theta_x$ and $\sin\theta_y$ in the presence of tunneling effect ($T_e = 5\gamma$) for (a) $l_s = 1$, (b) $l_s = 2$, (c) $l_s = 3$ and $l_s = 4$. The selected parameters are same as figure 2.

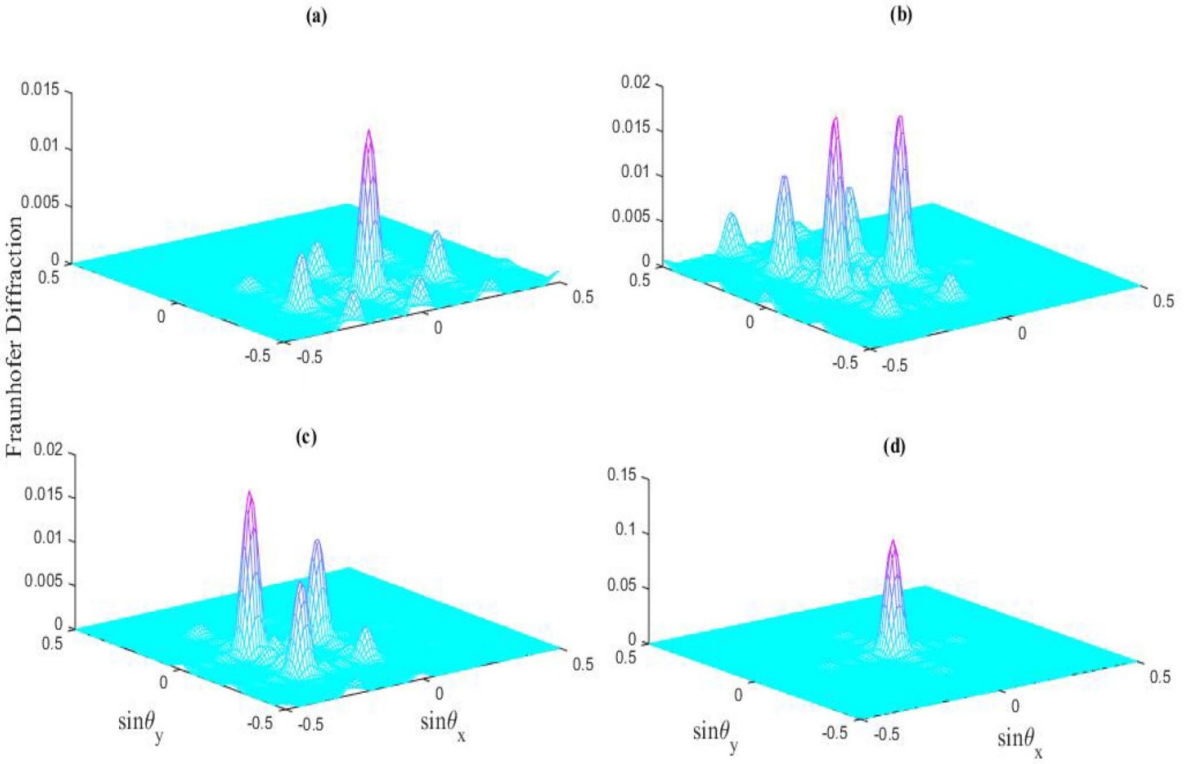


**Figure 5.** Fraunhofer diffraction pattern versus $\sin\theta_x$ and $\sin\theta_y$ for different values of relative phase (a) $\phi = \pi/6$, (b) $\phi = \pi/4$, (c) $\phi = \pi/3$ and (d) $\phi = \pi/2$. The selected parameters are $T_e = 5\gamma$, $l_s = 4$ and others are same as figure 2.

adjusting the Fraunhofer diffraction pattern. We find that by changing the OAM number from $l_s = 1$ (a) to $l_s = 4$ (d), the probe energy may transfer from zero order to the high order of directions. Moreover, the regions of the diffracted photons are changed when we alter the OAM number of the vortex light, respectively. From equation (1), one can find that the coherence term $\rho_{21}$ depends on the relative phase between applied lights $\phi$. Therefore, in figure 5, we fix the OAM number $l_s$ to 4 and plot the Fraunhofer diffraction pattern for different values of relative phase $\phi$, respectively. Here, we find that the diffraction pattern of the probe light can be shifted from one region to other regions by transferring the probe energy from zero order to the high orders. However, for $\phi = \frac{\pi}{2}$ (d), most of probe energy remains in the zero order and the symmetric diffraction pattern can be realized.

## 3. Conclusion

In conclusion, we have explored the electron tunneling effect-based Fraunhofer diffraction pattern in a four-level QDM. An optical vortex light that carries OAM and a two-dimensional SW pattern, respectively, both interact with the QDM. We discover that when we alter the OAM number of the vortex light, Fraunhofer diffraction pattern becomes symmetric even in the absence of electron tunneling and the majority of probe energy remains in the zero order. However, some of the probe energy may pass to the high orders in the symmetric pattern of the diffracted photons by taking into account the electron tunneling and for the Gaussian optical field. We discovered that the majority of probe energy transfers to the high orders and asymmetric diffracted light becomes feasible when we take into account the OAM number of vortex light on Fraunhofer diffraction pattern of the probe light. Additionally, the regions of the diffracted photons can be varied by varying the OAM number and relative phase between applied light.

## Acknowledgments

Philosophy and social science planning project for young innovative talents in colleges and universities in Guangdong Province; Guangdong Provincial Department of Education (2020wqncx193).

## References

[1] Wu Y and Deng L 2004 Ultraslow optical solitons in a cold four-state medium *Phys. Rev. Lett.* **93** 143904
[2] Wu Y 2005 Two-color ultraslow optical solitons via four-wave mixing in cold-atom media *Phys. Rev.* A **71** 053820
[3] Wu Y and Yang X 2005 Electromagnetically induced transparency in V-, Λ-, and cascade-type schemes beyond steady-state analysis *Phys. Rev.* A **71** 053806
[4] Wu Y, Saldana J and Zhu Y 2003 Large enhancement of four-wave mixing by suppression of photon absorption from electromagnetically induced transparency *Phys. Rev.* A **67** 013811
[5] Asadpour S H and Rahimpour Soleimani H 2016 Phase dependence of optical bistability and multistability in graphene nanostructure under external magnetic field *Laser Phys. Lett.* **13** 015204
[6] Asadpour S H and Rahimpour Soleimani H 2016 Phase dependence of optical bistability and multistability in a four-level quantum system near a plasmonic nanostructure *J. Appl. Phys.* **119** 023102
[7] Asadpour S H, Hamedi H R and Jafari M 2018 Enhancement of Goos–Hänchen shift due to a Rydberg state *Appl. Opt.* **57** 4013–9
[8] Asadpour S H, Panahpour A and Jafari M 2018 Phase-dependent electromagnetically induced grating in a four-level quantum system near a plasmonic nanostructure *Eur. Phys. J. Plus* **133** 411
[9] Wu Y 2008 Matched soliton pairs of four-wave mixing in molecular magnets *J. Appl. Phys.* **103** 104903
[10] Zeinali B and Ghazanfarian J 2020 Turbulent flow over partially superhydrophobic underwater structures:The case of flow over sphere and step *Ocean Engineering* **195** 106688
[11] Si L-G, Guo L-X, Xiong H and Wu Y 2018 Tunable high-order-sideband generation and carrier-envelope-phase–dependent effects via microwave fields in hybrid electro-optomechanical systems *Phys. Rev.* A **97** 023805
[12] Zhu G-L, Lü X-Y, Wan L-L, Yin T-S, Bin Q and Wu Y 2018 Controllable nonlinearity in a dual-coupling optomechanical system under a weak-coupling regime *Phys. Rev.* A **97** 033830
[13] Asadpour S H, Faizabadi E, Kudriašov V, Paspalakis E and Hamedi H 2021 Swapping of orbital angular momentum states of light in a quantum well waveguide *Eur. Phys. J. Plus* **136** 457
[14] Asadpour S H, Paspalakis E and Hamedi H R 2021 Exchange of optical vortices in symmetry-broken quantum systems *Phys. Rev.* A **103** 063705
[15] Asadpour S H, Abbas M and Hamedi H R 2022 Exchange of orbital angular momentum of light via noise-induced coherence *Phys. Rev.* A **105** 033709
[16] Ling H Y, Li Y-Q and Xiao M 1998 Electromagnetically induced grating: homogeneously broadened medium *Phys. Rev.* A **57** 1338
[17] Asghar S, Qamar S and Qamar S 2016 Electromagnetically induced grating with Rydberg atoms *Phys. Rev.* A **94** 033823
[18] Sahrai M, Bozorgzadeh F and Khoshsima H 2016 Phase control of electromagnetically induced grating in a four-level atomic system *Opt. Quantum Electron.* **48** 438
[19] Yu-Yuan C, Zhuan-Zhuan L and Ren-Gang W 2017 Electromagnetically induced 2D grating via refractive index enhancement in a far-off resonant system *Laser Phys. Lett.* **14** 075202
[20] Vafafard A, Sahrai M, Hamedi H R and Asadpour S H 2020 Tunneling induced two-dimensional phase grating in a quantum well nanostructure via third and fifth orders of susceptibility *Sci. Rep.* **10** 7389
[21] Asadpour S H, Kirova T, Qian J, Hamedi H R, Juzeliūnas G and Paspalakis E 2021 Azimuthal modulation of electromagnetically induced grating using structured light *Sci. Rep.* **11** 20721
[22] Asadpour S H, Hamedi H R, Kirova T and Paspalakis E 2022 Two-dimensional electromagnetically induced phase grating via composite vortex light *Phys. Rev.* A **105** 043709
[23] Wan R-G, Kou J, Jiang L, Jiang Y and Gao J-Y 2011 Electromagnetically induced grating via enhanced nonlinear modulation by spontaneously generated coherence *Phys. Rev.* A **83** 033824
[24] Vafafard A, Sahrai M, Siahpoush V, Hamedi H R and Asadpour S H 2020 Optically induced diffraction gratings

based on periodic modulation of linear and nonlinear effects for atom-light coupling quantum systems near plasmonic nanostructures *Sci. Rep.* **10** 16684

[25] Liu Y-M, Gao F, Fan C-H and Wu J-H 2017 Asymmetric light diffraction of an atomic grating with PT symmetry *Opt. Lett.* **42** 4283–6

[26] Shui T, Yang W-X, Liu S, Li L and Zhu Z 2018 Asymmetric diffraction by atomic gratings with optical PT symmetry in the Raman-Nath regime *Phys. Rev.* A **97** 033819

[27] Tian S C, Wan R G, Wang L J, Shu S L, Lu H Y, Zhang X, Tong C Z, Feng J L, Xiao M and Wang L J 2018 Asymmetric light diffraction of two-dimensional electromagnetically induced grating with PT symmetry in asymmetric double quantum wells *Opt. Express* **26** 32918–30

Talanta 246 (2022) 123523

Contents lists available at ScienceDirect

Talanta

journal homepage: www.elsevier.com/locate/talanta

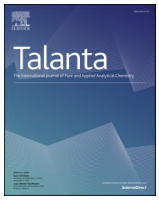

# A highly sensitive photoelectrochemical biosensor for CEA analysis based on hollow NiS@NiO/$TiO_2$ composite with typal p-n heterostructure

Delun Zheng [a,b,1], Jianying Yang [c,1], Zengyao Zheng [c], Mingxuan Peng [a], Jiayang Chen [a], Yaowen Chen [d], Wenhua Gao [a,d,*]

[a] Department of Chemistry and Laboratory for Preparation and Application of Ordered Structural Materials of Guangdong Province, Shantou University, Shantou, Guangdong, 515063, PR China
[b] Department of Natural Sciences, Shantou Polytechnic, Shantou, Guangdong, 515078, PR China
[c] Guangdong Shantou Supervision Testing Institute of Quality & Measuring, Shantou, Guangdong, 515041, PR China
[d] Analysis & Testing Center, Shantou University, Shantou, Guangdong, 515063, PR China

ARTICLE INFO

*Keywords:*
Photoelectrochemical
p-n type heterostructure
Hollow NiS@NiO
Carcinoembryonic antigen detection

ABSTRACT

Heterostructured construction is regarded as a valuable approach to improve photoelectrochemical (PEC) performances. Herein, porous hollow NiS@NiO spheres were prepared derived from the Ni(TCY) MOFs precursor. Photoactive $TiO_2$ was coupled with as-prepared NiS@NiO to form a close heterojunction interface of NiS@NiO/$TiO_2$. NiS@NiO/$TiO_2$ modified ITO electrode (NiS@NiO/$TiO_2$/ITO) displayed fiercely enhanced photocurrent response, which was 4687-fold than that of NiS@NiO/ITO (0.008 μA) and 8.5-fold than that of $TiO_2$/ITO (4.41 μA), respectively. Remarkable PEC property could be ascribed to the hollow NiS@NiO spheres with thin-shell structure provided there is a larger active surface area for harvesting the visible light. Most importantly, the p-n type NiS@NiO/$TiO_2$ heterojunction could lead to generating more photo-excited charge carriers ($e^-/h^+$) and efficiently hinder the recombination of carriers, resulting in significantly augmented photocurrent output. Based on this outstanding PEC property, NiS@NiO/$TiO_2$/ITO electrode fabricated sensing platform (BSA/*anti*-CEA/NiS@NiO/$TiO_2$/ITO, BSA=Bovine serum albumin) exhibited high sensitivity for monitoring CEA (Carcinoembryonic antigen). Wide linear detection range was from 0.001 to 45 ng $mL^{-1}$ and with a low detection limit of $1.67 \times 10^{-4}$ ng $mL^{-1}$ (S/N = 3). Prepared biosensors also showed good reproducibility, stability and had satisfying specificity. Thus, the proposed NiS@NiO/$TiO_2$ heterostructured composite afforded well-design and synthesis strategy for constructing high-performance photoactive materials from MOFs-derivate.

## 1. Introduction

Carcinoembryonic antigen (CEA), as the tumor marker generated by the tumor cells from the human body, most possibly exists in the serum of patients with colorectal [1], breast [2], cystadenocarcinoma [3], and other carcinomas. CEA is widely used for the clinical diagnosis and treatment of cancer. The initial cancer diagnosis and effective treatment have very important significance in reducing the mortality of patients. Thus, the sensitive and precise detection of CEA in the early stage is indispensable and still urgently needed. Different analysis techniques have been developed to detect the CEA, such as fluorescence [4], enzyme-linked immunosorbent assays [5], electrochemiluminescence [6], and photoelectrochemical (PEC) [7,8], etc. Among them, the PEC method has attracted wide interest due to several advantages of simple operation, high selectivity, Low-background signal, and low-cost detection [9,10]. Apparently, for the structure of PEC biosensors, the photoelectric active materials are the pivotal component, because it makes the changed biology or chemistry information to convert into a noticeable PEC output which affects the sensitivity improvement of analyte. Up to now, a variety of photoactive materials have been employed for improving the PEC property, including the metal oxides [11,12], metal chalcogenides [13,14], organic polymers [15,16], metal-organic frameworks (MOFs) [17,18], etc.

As a typical transitional-metal oxide, $TiO_2$ has many merits such as

* Corresponding author. Department of Chemistry and Laboratory for Preparation and Application of Ordered Structural Materials of Guangdong Province, Shantou University, Shantou, Guangdong, 515063, PR China.
*E-mail address:* whgao@stu.edu.cn (W. Gao).
[1] Both the authors contributed to the paper equally.

https://doi.org/10.1016/j.talanta.2022.123523
Received 1 March 2022; Received in revised form 26 April 2022; Accepted 1 May 2022
Available online 6 May 2022

large surface area, high stability as well as photoelectric activity, which is potentially promising for developing PEC sensors. However, due to the wide bandgap, $TiO_2$ only absorbs the ultraviolet (UV)-light with a wavelength range of $\lambda < 400$ nm [19,20], and most biomolecules can be harmed by UV-light. So, $TiO_2$ does not very beneficial to be applied in PEC biosensors. Many efforts have been employed to enable the visible-light utilization of $TiO_2$, for intense, coupling $TiO_2$ with other photoactive materials to form the heterojunction is regarded as an effective strategy. In a heterojunction, the internal electric field is spontaneously built among different components which can boost the spatial separation of photo-excited $e^-/h^+$ pairs [21,22]. Zhang etc. [23] prepared a heterostructured $Fe_2O_3/TiO_2$ photocatalyst that could enhance the solar-energy conversion efficiency and showed excellent property for photoelectrochemical water oxidation. Singh etc. [24] used a heterostructure of $BiVO_4/TiO_2$ to achieve the improved photo-absorption capacity and $BiVO_4/TiO_2$ as the photoelectrode material with high photocatalytic activity for water splitting. Gao etc. [25] reported a heterojunction formation between $TiO_2$ and CdS, which displayed the increased photoactivity in UV regions and based on $CdS/TiO_2$ nanocomposite structured PEC sensor exhibited high sensitivity for nitrite assay.

Another strategy to improve the photo-electric performance is to tailor the particular morphologies or construct, such as hollow structures [26], thin-wall [27], hierarchical architectures [28], and high porosities [29]. The photoactive material with a hollow structure can strengthen the light-harvesting ability due to its multiple reflection effects, resulting in the generation of more charge carriers within the interior void. Meanwhile, hollow structures provide plentiful active sites for the related interface reactions, which can lead to promoting photocatalytic efficiency. Moreover, the thinner-shelled configuration of hollow materials can shorten the transportation distance of charge carriers, thus reducing the recombination opportunity of photo-induced electron-hole pairs. Guo etc. [30] designed a hollow octahedral $Cu_2$-xS with abundant reaction sites and further fabricated the sandwich-layered composite of $Cu_2$-xS/CdS/$Bi_2S_3$ that could aid in photocatalytic $H_2$ evolution performance, as well as displayed the photocatalytic degradation efficiency for 2,4-dichlorophenol. Dinh etc. [31] proposed the thin-shell $Au/TiO_2$ hollow photocatalysts exhibited notable photonic behavior which originated from the macroscopic voids of hollow spheres and thus led to an enhancement in the photocatalytic activity. Pei etc. [32] developed hollow graphene growing on the TaON particles surface in situ, obtained graphene@TaON materials with the spatially separated active sites could achieve the improvement of the visible-light-driven $CO_2$ reduction. Our groups [33] anteriorly had synthesized a hollow $ZnIn_2S_4$ nanocage material based on ZIF-8 MOF--derivants, which exhibited the promoted visible-light captures capability. These above facts have proved that hollow structure with compelling virtues improves PEC properties. Nevertheless, to tailor the rational hollow geometry and well-remaining its intrinsic microstructure-activity of photoactive material still has a few challenges.

In this paper, we successfully constructed MOF-derived porous hollow NiS@NiO spheres by a simple solvothermal method and calcination strategy. Based on the well-matched band gap between NiS@NiO (2.02 eV) and $TiO_2$ (3.40 eV), the formed NiS@NiO/$TiO_2$ heterojunction modified ITO electrode (NiS@NiO/$TiO_2$/ITO) displayed a notable photocurrent response compared with the NiS@NiO material or monophasic $TiO_2$. The sharply enhanced photocurrent signal was owed to the interior hollow cavity of NiS@NiO with multiple reflection effects that could improve the light-absorption response. What is more, the p-n type NiS@NiO/$TiO_2$ heterostructured formation led to producing more photo-induced charge carriers ($e^-/h^+$), as well as efficiently achieving the separation and migration of $e^-/h^+$ pairs. Benefiting from the outstanding photoelectric conversion efficiency, NiS@NiO/$TiO_2$/ITO modified electrode surface was successively introduced with *anti*-CEA and BSA (Bovine serum albumin) biomolecule to fabricate a PEC biosensor. The sensing platform (BSA/*anti*-CEA/NiS@NiO/$TiO_2$/ITO) had been successfully applied for the CEA assay and obtained the wide linear detection range from 0.001 to 45 ng $mL^{-1}$ with a low LOD (limit of detection) value of $1.67 \times 10^{-4}$ ng $mL^{-1}$. Furthermore, the prepared sensor also showed good stability and satisfying specificity in the monitoring process of CEA. This excellent analysis property of the developed biosensor demonstrated the great potential application of the hollow heterostructured photoactive materials in PEC sensors.

## 2. Experimental section

Chemicals, reagents, and apparatus had been reported on supporting information.

### 2.1. Synthesis of Ni(TCY), NiS@NiO, and NiS@NiO/$TiO_2$

The Ni(TCY) was prepared by a simple hydrothermal method. First, 0.145 g $Ni(NO_3)_2 \cdot 6H_2O$ (0.5 mmol) and 0.177 g trithiocyanuric acid (TCY) (1 mmol) were dissolved in 60 mL methyl alcohol under stirring for 1.5 h, then the mixture was transferred into 100 mL steel reactor and kept at 120 °C for 24 h. After cooling to room temperature, the brown products were carefully collected with centrifugation at a velocity of 10,000 rpm, and then washed three times by the DDW and ethanol. The obtained precipitates were vacuum dried at 60 °C for 10 h and finally got the pure Ni(TCY).

The Ni(TCY) precursor was mixed with $TiO_2$ (1:1, m/m), then the mixture of Ni(TCY)/$TiO_2$ was transferred into the furnace and calcining at 450 °C for 1.5 h under isolated air. After naturally cooling to room temperature, the dark gray NiS@NiO/$TiO_2$ was obtained. The black NiS@NiO was achieved at the same experimental conditions without adding $TiO_2$ particles. The preparation process of NiS@NiO/$TiO_2$ composite is shown in Scheme 1A.

### 2.2. Fabrication of the PEC biosensor

In brief, the indium tin oxide (ITO) electrodes were ultrasonically washed with acetone, 1.0 M NaOH/ethanol (1:1, V/V), and DDW for 15 min every time. Before modification, the NiS@NiO/$TiO_2$ compound (1.35 mg $mL^{-1}$, dissolved in DDW) was ultrasonic treatment for 15 min, then 9 μL of well-dispersive NiS@NiO/$TiO_2$ solutions were dropped onto the ITO electrode surface. After drying spontaneously, obtained the NiS@NiO/$TiO_2$ modified ITO electrode (NiS@NiO/$TiO_2$/ITO). For comparison, the Ni(TCY)/ITO, NiS@NiO/ITO, and $TiO_2$/ITO electrodes were prepared in the same manner.

Afterward, 9 μL 25 mg $mL^{-1}$ *anti*-CEA was dropped on the NiS@NiO/$TiO_2$/ITO electrode surface and stored for 3 h at 4 °C, then rinsing with 0.1 M PBS to obtain the modified electrode of *anti*-CEA/NiS@NiO/$TiO_2$/ITO. 7 μL of 1 wt% BSA included 0.1 M PBS (pH 7.4) was covered onto the *anti*-CEA/NiS@NiO/$TiO_2$/ITO electrode surface for 1 h to block nonspecific adsorption. Followed by washing with PBS, the obtained electrode was denoted as BSA/*anti*-CEA/NiS@NiO/$TiO_2$/ITO.

Finally, 9 μL of different concentrations solutions of CEA were respectively dropped to the above-modified electrode (BSA/*anti*-CEA/NiS@NiO/$TiO_2$/ITO) and then incubated for 60 min at 4 °C. After rinsing with PBS, the PEC biosensor was successfully fabricated (shown in Scheme 1B).

### 2.3. PEC and electrochemical measurements

The PEC measurement was performed in 0.1 M PBS (pH 7.4) containing 0.15 M AA (ascorbic acid). A self-made photoelectric chemical system was constituted by the CHI 650E electrochemical station with a xenon lamp light source. The excitation source of the xenon lamp was 420 nm with a light intensity of 20 mW $cm^{-2}$ and switched on every 10 s under 0.0 V bias voltages. EIS was executed at a potential of +0.172 V with the frequency range from 0.01 Hz to $1 \times 10^4$ Hz. Cyclic

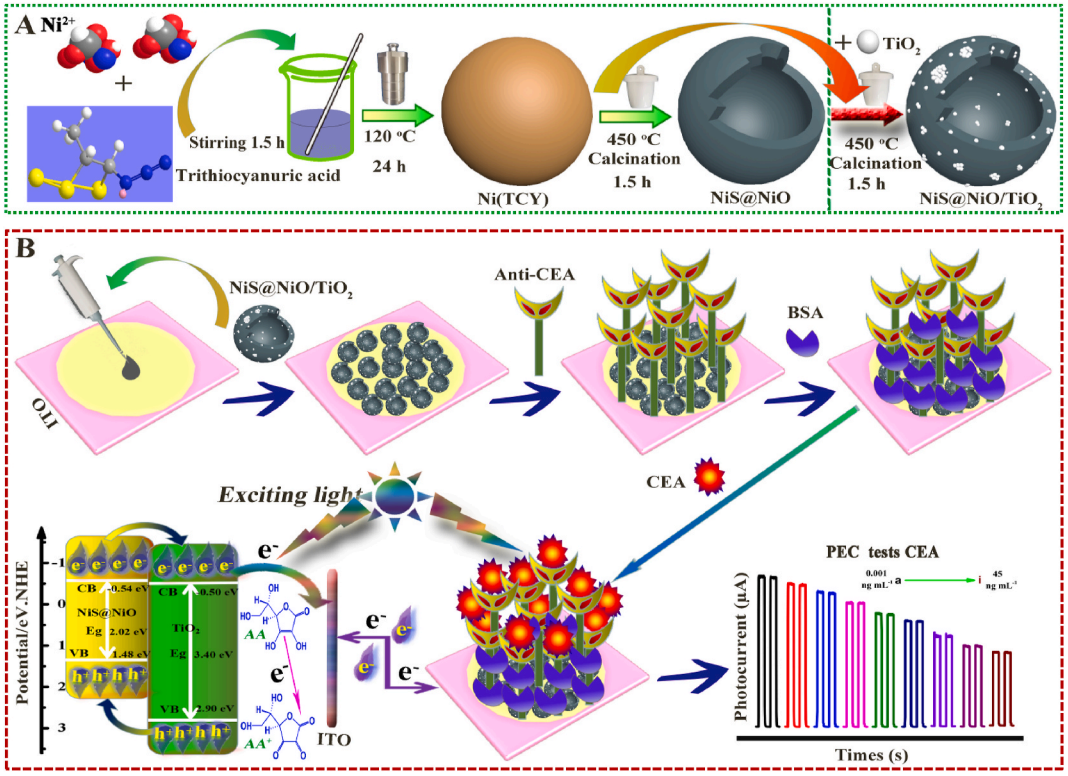


**Scheme 1.** Schematic illustration of the synthesis process of (A) NiS@NiO/$TiO_2$ and the fabrication processes of (B) PEC biosensors for CEA detection.

voltammetry (CV) was carried out in 5.0 mM $[Fe(CN)_6]^{3-/4-}$ containing 0.1 M KCl. The scanned potential range of CV was from +0.6 V to −0.2 V with a scan rate of 0.1 V $s^{-1}$.

## 3. Results and discussion

### 3.1. Characterization of prepared materials

The morphological features of the prepared samples were examined by field emission scanning electron microscope (FESEM). As shown in Fig. S1A, a large number of dispersed Ni(TCY) exhibited the similar

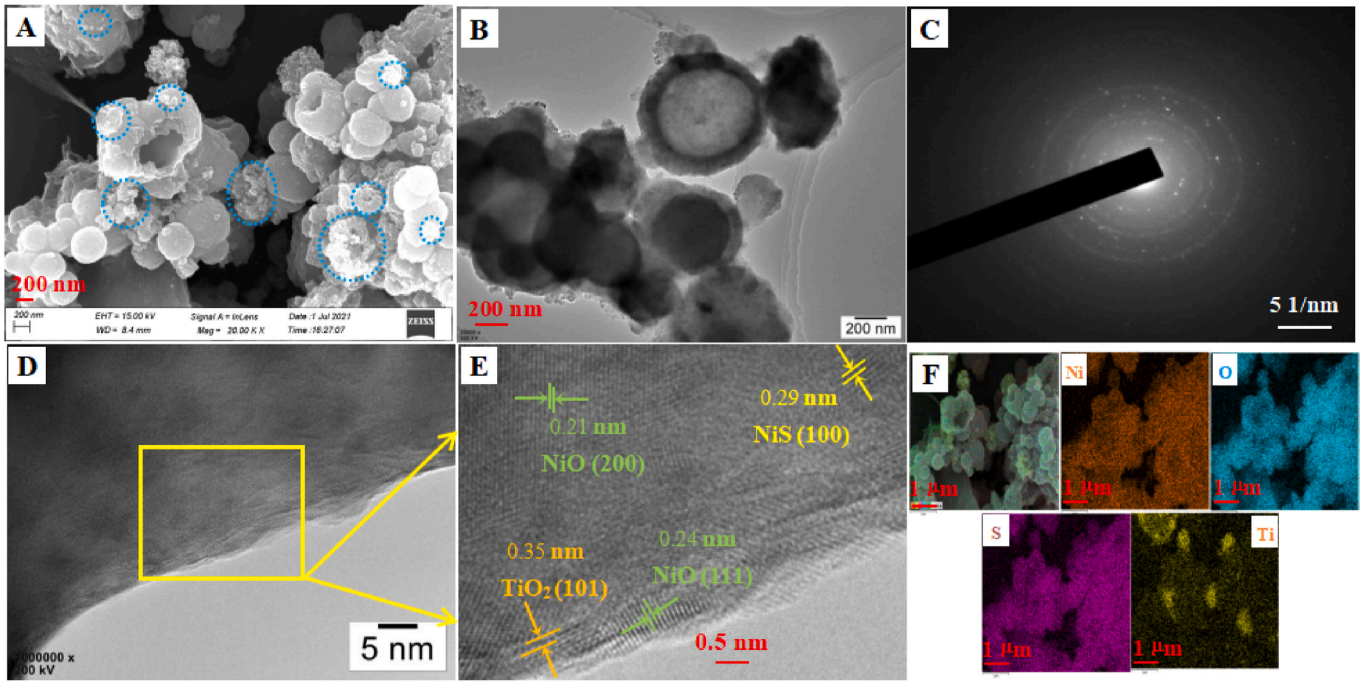


**Fig. 1.** FESEM images of (A) NiS@NiO/$TiO_2$; TEM images of (B) NiS@NiO; SAED pattern of (C) NiS@NiO/$TiO_2$; High-resolution TEM (HRTEM) images of (D and E) NiS@NiO/$TiO_2$; Elemental mapping images of (F) Ni, O, S, and Ti elementals of NiS@NiO/$TiO_2$.

shape of a sphere, and with the particle size range was from 0.5 μm to 1.9 μm. From the amplified SEM view (Fig. S1B), the spherical Ni(TCY) displayed high porosity with small sizes. After calcining the Ni(TCY) precursor, the converted NiS@NiO showed an obvious cracked position (Fig. S1C), which was also observed in the NiS@NiO/$TiO_2$ composite (Fig. 1A), as well as in which lots of $TiO_2$ particles (blue wireframes marking) were compactly connecting with the NiS@NiO. Fig. 1B showed the TEM images of NiS@NiO, and the hollow and thin-shelled microstructures could be seen compared with its solid precursors (inset of Fig. S1B). Fig. 1C illustrated the selected area electron diffraction (SAED) pattern of NiS@NiO/$TiO_2$ with the various diffraction rings, demonstrating that NiS@NiO/$TiO_2$ had the polycrystalline structure. From the HRTEM image of NiS@NiO/$TiO_2$ (Fig. 1D and E), the typical interplanar spacing of 0.21 nm, 0.24 nm, and 0.29 nm corresponded to that of (200) plane, (111) plane, and (100) plane of NiO and NiS [34,35], respectively, the interplanar spacing of 0.35 nm corresponds to the (101) plane of $TiO_2$ [36]. Fig. 1F showed the elemental mapping images with the uniform distribution of Ni, Ti, S, and O elements in NiS@NiO/$TiO_2$. The SEM/TEM images and elemental mapping images of Ni (TCY) and NiS@NiO were also surveyed in Fig. S2(Ā F).

The phase structure of prepared materials was analyzed by PXRD (powder X-ray diffraction) pattern. As illustrated in Fig. S3A, there were no obvious diffraction peaks on Ni(TCY), indicating that the obtained Ni (TCY) was amorphous. The diffraction peaks that arose at 25.31°, 37.93°, 48.16°, 54.14°, and 55.23° corresponded to the (101), (004), (200), (105), and (211) lattice planes of $TiO_2$ (JCPDS, No: 73-1764). In Fig. S3B, the characteristic peaks at around 30.05°, 35.07°, 45.93°, and 53.85° were assigned to the (100), (111), (101), and (110) crystallographic planes of NiS (JCPDS, No: 75-0613) [37], the characteristic peaks at about 37.33°, 43.41°, 62.95°, and 75.96° were assigned to the (111), (200), (220), and (311) crystallographic planes of NiO (JCPDS, No: 47-1049) [38]. These characteristic diffraction peaks were also presented on the NiS@NiO/$TiO_2$ (Fig. 2A), confirming the formation of NiS@NiO/$TiO_2$ composite.

Fig. 2B showed the FT-IR spectroscopy of Ni(TCY), NiS@NiO, and NiS@NiO/$TiO_2$. The absorption peak at 1642 $cm^{-1}$ was attributed to the stretching vibration of C═N in the trithiocyanuric acid ligand, which also existed in NiS@NiO and NiS@NiO/$TiO_2$. The absorption band peaks of Ni(TCY) at 1426 $cm^{-1}$, 1243 $cm^{-1}$, and 873 $cm^{-1}$ demonstrated the interaction between thiocyanate and $Ni^{2+}$[39].

Fig. 2C showed the optical properties of UV–vis DRS (diffuse reflectance spectra) of obtained materials. It could be seen that pure Ni (TCY) and $TiO_2$ particles only had the harvesting capacity in the UV-light region, while NiS@NiO displayed the obvious visible-light response compared with its precursor of Ni(TCY). Furthermore, the visible-light absorption intensity ($\lambda \geq 380$ nm) of NiS@NiO/$TiO_2$ was dramatically increased than all other prepared materials, confirming that the heterostructural NiS@NiO/$TiO_2$ composite could further enhance the photo-capturing capability.

The surface compositions and chemical bonding state of synthesized materials were also explored by X-ray photoelectronic spectroscopy (XPS). Fig. 2D showed the XPS results of NiS@NiO and NiS@NiO/$TiO_2$ with their corresponding elements. Fig. 3A described the high-resolution Ni 2p core-level spectrums of NiS@NiO/$TiO_2$. The spectra of Ni 2p could be fitted by the spin-orbit doublets of $2p_{3/2}$ and $2p_{1/2}$ as well with two shake-up satellites (Sat.). The binding energies at 856.7 and 874.3 eV corresponds to the Ni $2p_{3/2}$ and $2p_{1/2}$ of $Ni^{2+}$, respectively, and two shake-up satellites of Ni 2p were at about 861.3 and 880.0 eV [40-42].

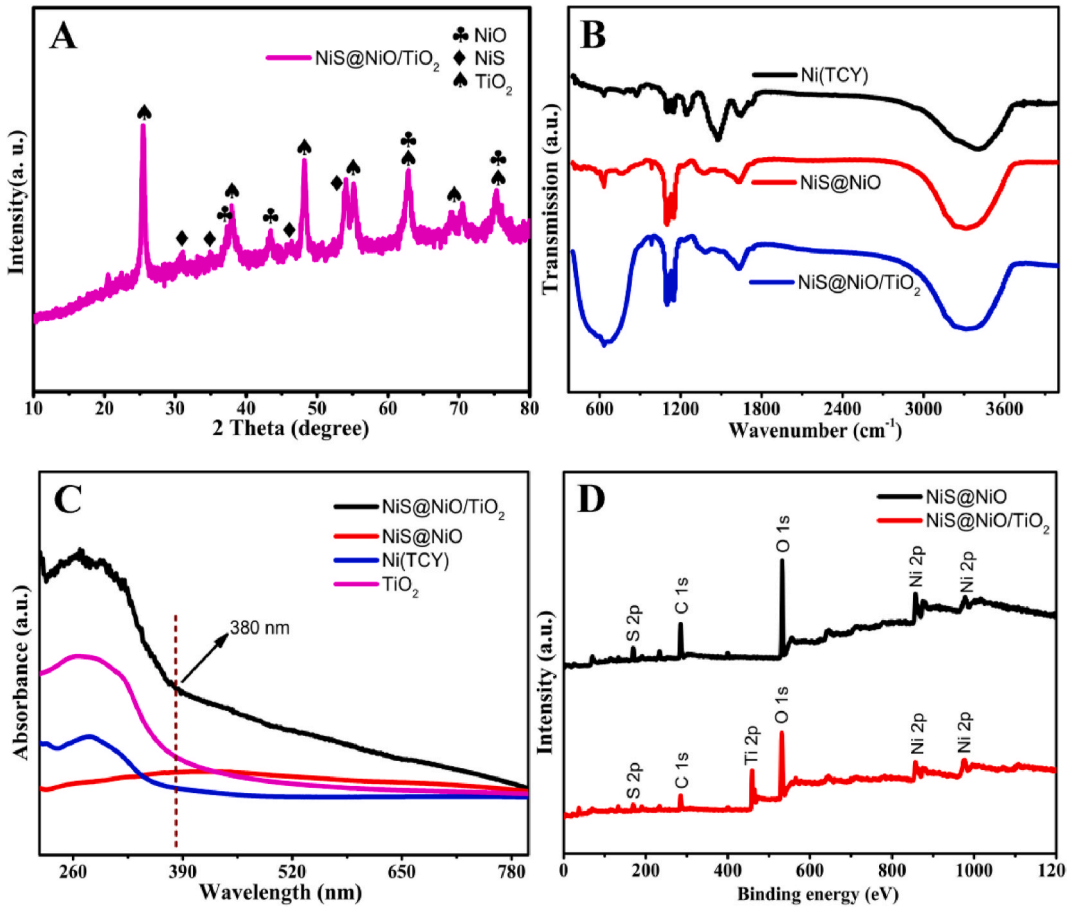


**Fig. 2.** XRD patterns of (A) NiS@NiO/$TiO_2$; FT-IR spectra of (B) Ni(TCY), NiS@NiO and NiS@NiO/$TiO_2$; UV–vis spectra of (C) $TiO_2$, Ni(TCY), NiS@NiO and NiS@NiO/$TiO_2$; XPS spectra of (D) NiS@NiO and NiS@NiO/$TiO_2$.

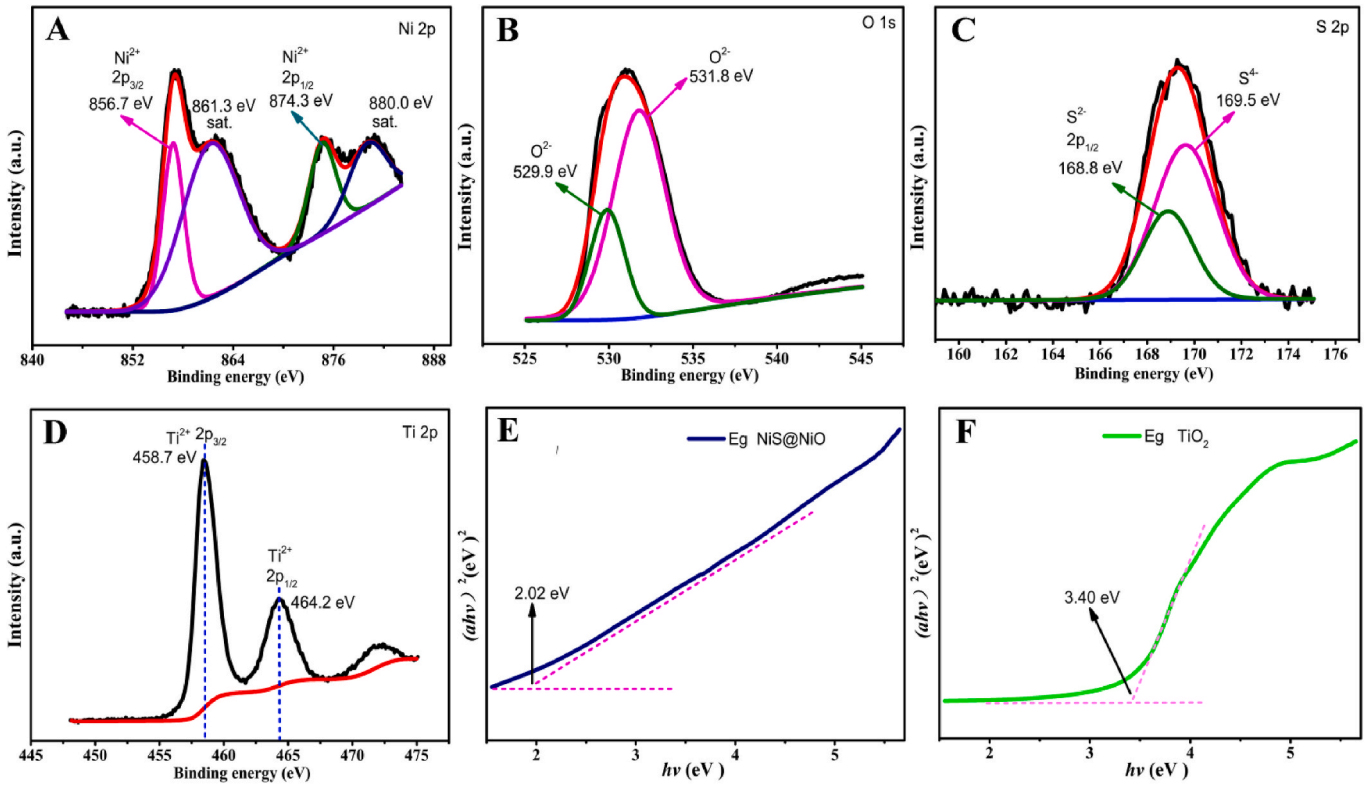


**Fig. 3.** High-resolution XPS spectra of (A) Ni 2p, (B) O 1s, (C) S 2p of NiS@NiO/$TiO_2$, (D) Ti 2p of $TiO_2$ in NiS@NiO/$TiO_2$; Plots of $(ahv)^2$ vs. photon energy ($hv$) of (E) NiS@NiO and (F) $TiO_2$.

The characteristic peaks at 531.8 and 529.9 eV were attributed to the $O^{2-}$ [43] (Fig. 3B). In Fig. 3C, the binding energies of S 2p at 168.8 eV (S $2p_{1/2}$) and 169.5 eV were ascribed to $S^{2-}$ and $S^{4-}$ in NiS@NiO/$TiO_2$ [44-46], respectively. Fig. 3D showed the Ti 2p core-level spectrum of NiS@NiO/$TiO_2$, and the binding energies at 458.7 and 464.2 eV corresponds to $Ti^{4+}$ [47,48], respectively. All above XPS results suggested that the NiS@NiO/$TiO_2$ composite was achieved. In addition, the high-resolution XPS spectra of NiS@NiO with their corresponding elements were also investigated in Fig. S4(C ~ E).

### 3.2. PEC mechanism

From the UV–vis DRS characterization (Fig. 2C) and based on the empirical equation of $ahv = A\ (hv\text{-}Eg)^{1/2}$, the Eg values of NiS@NiO, $TiO_2$, and NiS@NiO/$TiO_2$ were calculated to be 2.02, 3.40, and 2.93 eV (Fig. 3E, F, and Fig. S4F), respectively. Moreover, with the VB-XPS exploration, the VB potentials of NiS@NiO and NiS@NiO/$TiO_2$ were measured at 1.48 and 1.45 eV (Fig. S5A and B), respectively. The $E_{CB}$ positions of $TiO_2$ were −0.50 eV (vs NHE) according to reported literature [49]. As well as, with the empirical formulae:

$$E_{CB} = E_{VB} - Eg,$$

The corresponding $E_{CB}$ potentials of NiS@NiO and $E_{VB}$ positions of $TiO_2$ could be gained at −0.54 eV and 2.90 eV, respectively. These results indicated that the CB and VB potentials of $TiO_2$ were lower than that of NiS@NiO, and hence NiS@NiO/$TiO_2$ composite could form a well-matched heterostructure. Under illumination, the photo-excited electron in the CB of NiS@NiO was transferred to the CB of $TiO_2$, and the hole in the VB of $TiO_2$ was transferred to the VB of NiS@NiO and then scavenged by the electron donor of AA, which resulted in enhanced photocurrent output. The markedly enhanced photocurrent response of NiS@NiO/$TiO_2$ could be further explained by the following points: (I) hollow and thin-shell NiS@NiO with the increased surface area could improve the light-responsive property; (II) the heterogeneous NiS@NiO/$TiO_2$ with typical p-n formation endowed abundant active-sites to lead to more photo-induced charge carriers and concurrently promote their separation/migration; (III) a close connected interface between NiS@NiO and $TiO_2$ could reduce the charges transfer distance. The PEC property of NiS@NiO/$TiO_2$/ITO electrode and the detection mechanism of fabricated PEC biosensor (BSA/*anti*-CEA/NiS@NiO/$TiO_2$/ITO) as shown in Scheme 1B.

In the Nyquist plots of the EIS (electrochemical impedance spectra) method, the electron transfer resistance ($R_{et}$) can be determined by the impedance semicircle diameter. The EIS measurement of BSA/*anti*-CEA/NiS@NiO/$TiO_2$/ITO electrode was surveyed using $[Fe(CN)_6]^{3-/4-}$ as a redox probe (Fig. 4A). It could be seen that the small semicircle on the bare ITO electrode (curves a) corresponded to 76 Ω. Compared to the Ni (TCY)/ITO modified electrode (curve b) with the greatest $R_{et}$ value of 540 Ω, the $R_{et}$ value of NiS@NiO/ITO electrode reduced (87 Ω, curve c), indicating the hollow NiS@NiO spheres could accelerate the electronic transfer of electrode interface. When the $TiO_2$, *anti*-CEA, and BSA were respectively introduced to the NiS@NiO/ITO electrode surface, the $R_{et}$ value orderly increased to 163 Ω, 300 Ω, and 410 Ω (curve d, e and f), indicating the above-modified materials or substances that hindered the electron transfer due to poor conductivity. The stepwise assembly process of BSA/*anti*-CEA/NiS@NiO/$TiO_2$/ITO electrode was also surveyed by CV (cyclic voltammetry, Fig. S6A) techniques with the redox probe of $[Fe(CN)_6]^{3-/4-}$, and the obtained result was in good agreement with the EIS analyses, revealing the PEC biosensor was successfully fabricated.

The preparation process of the modified electrode was deeply explored by the PEC measures, and the results were recorded in 0.1 M PBS (pH 7.4) (Fig. 4B). On the bare ITO electrodes (curve a), it could not find only photocurrent response signal, while the NiS@NiO/ITO electrode had a slight photocurrent value of 0.008 μA (Fig. S6B, curve b), which were attributed to the hollow NiS@NiO with the larger surface area could improve the visible-light absorption. Nevertheless, on the NiS@NiO/$TiO_2$/ITO modified electrode, the photocurrent value fiercely

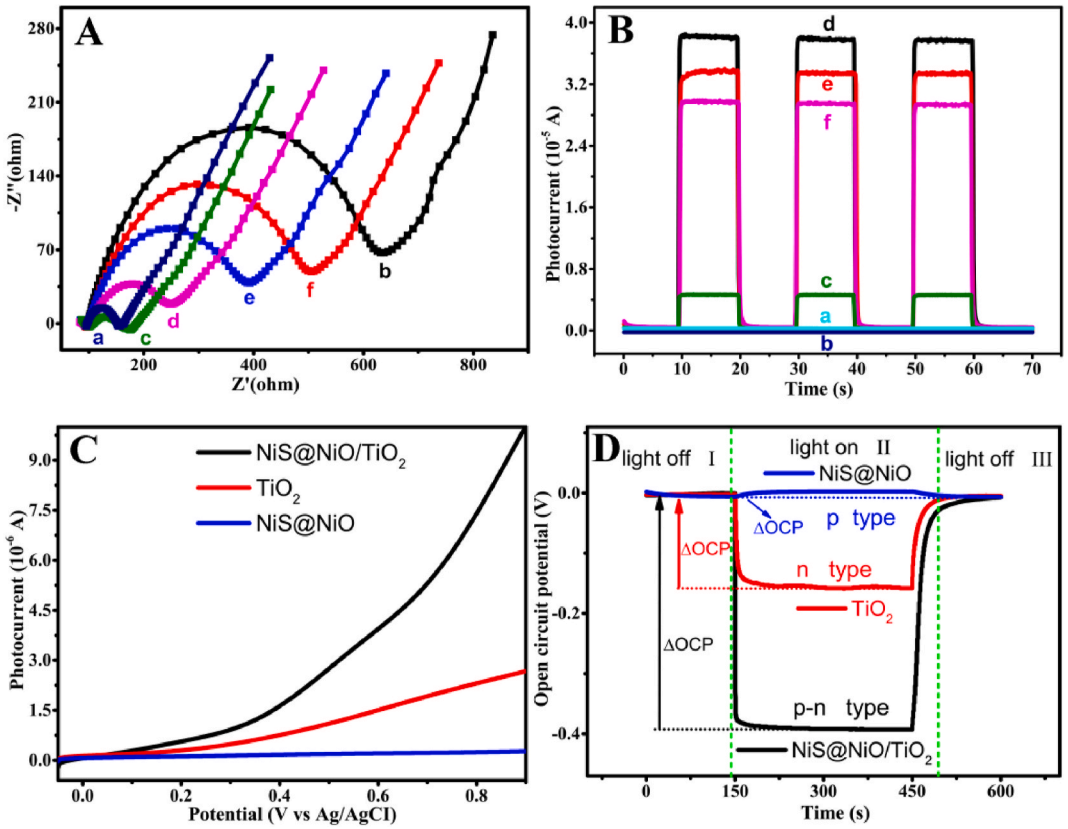


**Fig. 4.** EIS (A) of bare ITO (a), Ni(TCY)/ITO (b), NiS@NiO/ITO (c), NiS@NiO/$TiO_2$/ITO (d), *anti*-CEA/NiS@NiO/$TiO_2$/ITO (e), BSA/*anti*-CEA/NiS@NiO/$TiO_2$/ITO (f) in 5 mM $[Fe(CN)_6]^{3-/4-}$ containing 0.1 M KCl; PEC of (B) bare ITO (a), NiS@NiO/ITO (b), $TiO_2$/ITO (c), NiS@NiO/$TiO_2$/ITO (d), *anti*-CEA/NiS@NiO/$TiO_2$/ITO (e), BSA/*anti*-CEA/NiS@NiO/$TiO_2$/ITO (f) in 0.1 M PBS (pH 7.4); (D) LSV patterns in 0.1 M $Na_2SO_4$ with a scan rate of 80 mV $s^{-1}$ and (E) OCP curves in 0.1 M PBS (pH 7.4) of the $TiO_2$, NiS@NiO, NiS@NiO/$TiO_2$ modified ITO electrodes.

increased to 37.5 μA (Fig. 4B, curve d), which was 4687-fold than that of NiS@NiO/ITO (0.008 μA) and 8.5-fold than that of $TiO_2$/ITO (4.41 μA, Fig. 4B, curve c), respectively. It was an authentic explanation that NiS@NiO/$TiO_2$ heterojunction with the p-n type formation could significantly enhance the transformation efficiency of photon-to-electricity. After the *anti*-CEA and BSA were successively immobilized on the NiS@NiO/$TiO_2$/ITO electrode interface, the photocurrent signal decreased to 33.8 μA and 29.1 μA (curves e and f) owing to their insulating performance and hindrance effect. These PEC results also confirmed the successful manufacture of the PEC biosensor.

Fig. 4C illustrated the linear sweep voltammetry (LSV) patterns of obtained materials modified ITO electrodes under visible-light irradiation in 0.1 M $Na_2SO_4$. It was seen that NiS@NiO material had barely LSV response, while monocomponent $TiO_2$ particle displayed obvious enhanced LSV signal than NiS@NiO. It was worth noting that NiS@NiO/$TiO_2$ had the greatest LSV intensity compared to NiS@NiO or $TiO_2$, which could be ascribed to p-n type NiS@NiO/$TiO_2$ heterojunction with the improved photoelectric property. Fig. 4D showed the open circuit potential (OCP) patterns of the above materials in 0.1 M PBS (pH 7.4) including 0.15 M AA. In the $TiO_2$ particle and NiS@NiO/$TiO_2$ composite, observed that the upward surface band bends (region I) depending on their potential of redox equilibration in the dark, which also confirmed that the n-type $TiO_2$ component existed in NiS@NiO/$TiO_2$. Under continuous illumination, the OCP response of $TiO_2$ and NiS@NiO/$TiO_2$ materials towards the negative rapidly reached a steady-state (region II) due to the accumulation of photo-generated electrons. After the light stimulation was switched off, the OCP signal gradually increased again (region III) due to the recombination of photo-induced charge carriers. While the OCP behaviors of NiS@NiO were opposite compared to the above-proposed materials, proving the p-type NiS@NiO obtained. For these results, the p-n type NiS@NiO/$TiO_2$ composite was successfully achieved. Besides, the charge separation efficiency can be identified by the ΔOCP (change values of OCP). The ΔOCP value of NiS@NiO/$TiO_2$ showed an enhancement than the NiS@NiO and $TiO_2$, demonstrating that the p-n type heterogeneous NiS@NiO/$TiO_2$ could generate more $e^-/h^+$ and then accelerate their transition/migration.

### 3.3. PEC response of the optimization experiments shown on supporting information

#### 3.3.1. PEC analysis properties of the prepared biosensor

Under optimized conditions, the prepared BSA/*anti*-CEA/NiS@NiO/$TiO_2$/ITO biosensor was further applied to monitor different concentrations of CEA. As described in Fig. 5A, under the visible-light illumination, the photocurrent response was gradually decreased with the increased concentrations of CEA, suggesting the intensive effect between CEA and BSA/*anti*-CEA/NiS@NiO/$TiO_2$/ITO. The changed photocurrent values ($\Delta I_{PEC}$) were consistent with the logarithm of the CEA concentration (log $C_{CEA}$) from 0.001 to 45 ng $mL^{-1}$, the linear equation was $\Delta I_{PCE}$ (μA) = −0.278 log $C_{CEA}$ (ng $mL^{-1}$) + 1.812 ($R^2$ = 0.9967) (Fig. 5B). Based on the 3 signal-to-noise ratio (S/N = 3), a low LOD value was 1.67 × $10^{-4}$ ng $mL^{-1}$. Moreover, compared to previously reported literature (shown in Table S1), the developed PEC biosensor displayed a wider linear range and lower LOD for CEA detection, suggesting the p-n type NiS@NiO/$TiO_2$ heterojunction had amplified the PEC effect for which to improve the CEA detection sensitivity.

### 3.4. Stability, selectivity, and reproducibility of the PEC biosensors

Fig. 5C showed the stability of the proposed PEC biosensor, it was

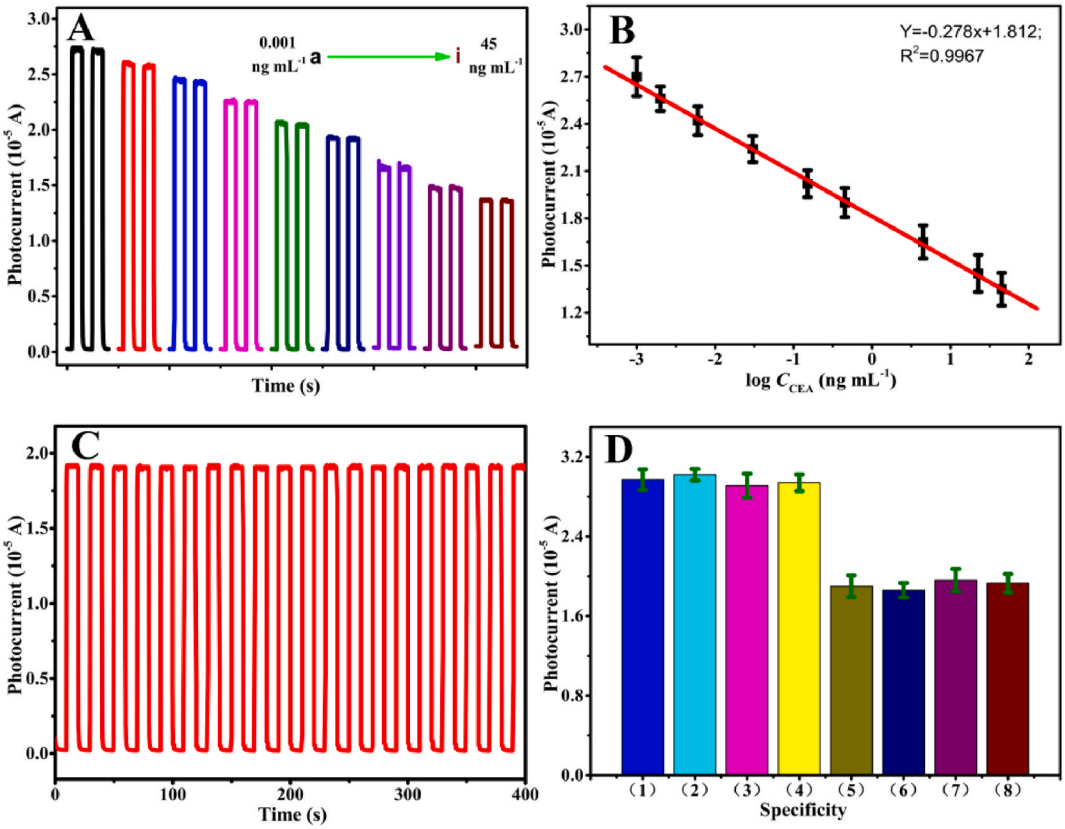


**Fig. 5.** PEC responses of (A) BSA/*anti*-CEA/NiS@NiO/$TiO_2$/ITO biosensor in the presence of (a-i): 0.001, 0.002, 0.006, 0.03, 0.15, 0.45, 4.5, 22.5, 45 ng $mL^{-1}$; The plot of (B) $\Delta I_{PCE}$ versus the logarithm values of $C_{CEA}$ (log $C_{CEA}$); Time–based photocurrent response of (C) BSA/*anti*-CEA/NiS@NiO/$TiO_2$/ITO biosensor in the presence of 0.5 ng $mL^{-1}$ CEA in 0.1 M PBS (pH 7.4) with light on and off cycles; Selectivity of (D) the PEC biosensors to CEA, (1) blank, (2) blank + 150 ng $mL^{-1}$ BSA, (3) blank + 150 ng $mL^{-1}$ AFP, (4) blank + 150 ng $mL^{-1}$ PSA, (5) 0.5 ng $mL^{-1}$ CEA, (6) 0.5 ng $mL^{-1}$ CEA + 150 ng $mL^{-1}$ BSA, (7) 0.5 ng $mL^{-1}$ CEA + 150 ng $mL^{-1}$ AFP, (8) 0.5 ng $mL^{-1}$ CEA + 150 ng $mL^{-1}$ PSA.

found that no significant photocurrent signals change on BSA/*anti*-CEA/NiS@NiO/$TiO_2$/ITO electrodes after interaction with 0.5 ng $mL^{-1}$ CEA under irradiation cycles for 400 s and ten on/off, confirming that the PEC biosensor had long-term stability for the target substance analysis. Besides, compared to the original photocurrent intensity (100%), the fabricated PEC biosensor was stored for a week at 4 °C, and photocurrent was reduced to 94.3%. When the storage time exceeded two weeks, the photocurrent declined to 87.1% (Fig. S6D), indicating that the catalytic activity of *anti*-CEA on the modified electrode was still well-retained.

The selectivity of this PEC sensor was examined by adding the representative interfering substances of AFP (Alpha-fetoprotein), BSA (Bovine serum albumin), and PSA (Prostate-specific antigen), respectively. The comparison was carried out in the blank +150 ng $mL^{-1}$ interferences and the mixture of 0.5 ng $mL^{-1}$ CEA with above interferences. The results showed that no distinct photocurrent changes in the presence of mentioned interfering substances (Fig. 5D), confirming the PEC biosensor had good selectivity.

The reproducibility of the biosensor was studied by comparing the PEC response current of three equilibrium results of BSA/*anti*-CEA/NiS@NiO/$TiO_2$/ITO electrode after incubation with 8.5 × $10^{-2}$ ng $mL^{-1}$ CEA. Gained relative standard deviation (RSD) corresponds to 7.2%, indicating that the PEC biosensors had satisfying reproducibility.

### 3.5. Analysis of the biosensor in blood samples

To assess the practicability of the PEC sensor, the recovery experiment was investigated using a standard addition method. Under illumination, the different concentrations of CEA (0, 1.0, 10 ng $mL^{-1}$) in human serum samples were detected. The results showed that the changed recoveries were from 95.3% to 105.1% with the RSD value of 1.89%–3.83% (Table S2), indicating the designed PEC biosensor had great potential applicability for CEA detection in clinical analyses.

## 4. Conclusion

In summary, hollow NiS@NiO with a thin-shell structure was prepared via the Ni(TCY) MOFs derived calcination method. The obtained NiS@NiO combined with $TiO_2$ to form a NiS@NiO/$TiO_2$ heterojunction exhibiting an intense photocurrent response than the monophasic $TiO_2$ or NiS@NiO compound. It could be explained by the multiple light-capture effects from the hollow and thin-shell structure of NiS@NiO. Of note, heterostructured NiS@NiO/$TiO_2$ with p-n type formation had internal electric fields to produce more electron-hole carriers, and accelerated their separation and transfer effectively. The excellent photoelectric conversion efficiency of the NiS@NiO/$TiO_2$ modified ITO electrode was a benefit to improve the accuracy and anti-interference property during the test process. Hence, the further fabricated PEC biosensor (BSA/*anti*-CEA/NiS@NiO/$TiO_2$/ITO) displayed high sensitivity for CEA detection within a wide linear range and with a low LOD value. The proposed sensor also showed good stability, reproducibility, and selectivity in CEA analysis. This work demonstrated the marvelous potential of hollow NiS@NiO/$TiO_2$ heterostructured spheres in the PEC sensing field, which could develop its applications in clinical diagnosis, environmental monitoring or food analysis.

## Credit author statement

Submission of this manuscript does not contain research published or

written by others or other institutions. All the authors listed have approved the manuscript that is enclosed.

## Declaration of competing interest

The authors declare that they have no known competing financial interests or personal relationships that could have appeared to influence the work reported in this paper.

## Acknowledgements

We are grateful for the financial support from Guangdong Basic and Applied Basic Research Foundation (No. 2019A1515010618), the Guangdong Special Funds for the Science & Technology Project (No. 2019ST029 & No. 2019ST089), 2020 Li Ka Shing Foundation Cross-Disciplinary Research Grant (Project Number 2020LKSFG06C) and Shantou Polytechnic Supported Project (No. 2019SZK2019Y01).

## Appendix A. Supplementary data

Supplementary data to this article can be found online at https://doi.org/10.1016/j.talanta.2022.123523.

## References

[1] J. Miao, X. Wang, L. Lu, P. Zhu, C. Mao, H. Zhao, Y. Song, J. Shen, Electrochemical immunosensor based on hyperbranched structure for carcinoembryonic antigen detection, Biosens. Bioelectron. 58 (2014) 9–16.
[2] K.J. Huang, D.J. Niu, W.Z. Xie, W. Wang, A disposable electrochemical immunosensor for carcinoembryonic antigen based on nano-Au/multi-walled carbon nanotubes-chitosans nanocomposite film modified glassy carbon electrode, Anal. Chim. Acta 659 (2010) 102–108.
[3] J. Li, L. Liu, Y. Ai, Y. Liu, H. Sun, Q. Liang, Self-polymerized dopamine-decorated Au NPs and coordinated with Fe-MOF as a dual binding sites and dual signal-amplifying electrochemical aptasensor for the detection of CEA, ACS Appl. Mater. Interfaces 12 (2020) 5500–5510.
[4] H. Miao, L. Wang, Y. Zhuo, Z. Zhou, X. Yang, Label-free fluorimetric detection of CEA using carbon dots derived from tomato juice, Biosens. Bioelectron. 86 (2016) 83–89.
[5] R. de la Rica, M.M. Stevens, Plasmonic ELISA for the ultrasensitive detection of disease biomarkers with the naked eye, Nat. Nanotechnol. 7 (2012) 821–824.
[6] D. Wang, Y. Li, Z. Lin, B. Qiu, L. Guo, Surface-enhanced electrochemiluminescence of Ru@$SiO_2$ for ultrasensitive detection of carcinoembryonic antigen, Anal. Chem. 87 (2015) 5966–5972.
[7] X. Zhang, J. Peng, Y. Song, Y. Chen, F. Lu, W. Gao, Porous hollow carbon nanobubbles@ZnCdS multi-shelled dodecahedral cages with enhanced visible-light harvesting for ultrasensitive photoelectrochemical biosensors, Biosens. Bioelectron. 133 (2019) 125–132.
[8] Y. Chen, W. Deng, Y. Tan, Q. Xie, CdS quantum-dots-decorated $V_2O_5$ nanosheets as chemically etchable active materials for sensitive photoelectrochemical immunoassay of carcinoembryonic antigen, ACS Appl. Mater. Interfaces 12 (2020) 29066–29073.
[9] L. Cui, J. Hu, M. Wang, X.K. Diao, C.C. Li, C.Y. Zhang, Mimic peroxidase- and $Bi_2S_3$ nanorod-based photoelectrochemical biosensor for signal-on detection of polynucleotide Kinase, Anal. Chem. 90 (2018) 11478–11485.
[10] L. Fan, G. Liang, W. Yan, Y. Guo, Y. Bi, C. Dong, A highly sensitive photoelectrochemical aptasensor based on $BiVO_4$ nanoparticles-$TiO_2$ nanotubes for detection of PCB72, Talanta 233 (2021) 122551.
[11] J. Huang, Y. Zhang, Y. Ding, Rationally designed/constructed CoOx/$WO_3$ anode for efficient photoelectrochemical water oxidation, ACS Catal. 7 (2017) 1841–1845.
[12] S. Bera, S.A. Lee, C.-M. Kim, H. Khan, H.W. Jang, S.-H. Kwon, Controlled synthesis of vertically aligned $SnO_2$ nanograss-structured thin films for $SnO_2$/$BiVO_4$ core–shell heterostructures with highly enhanced photoelectrochemical properties, Chem. Mater. 30 (2018) 8501–8509.
[13] Y. Hou, Z. Wen, S. Cui, X. Guo, J. Chen, Constructing 2D porous graphitic $C_3N_4$ nanosheets/nitrogen-doped graphene/layered $MoS_2$ ternary nanojunction with enhanced photoelectrochemical activity, Adv. Mater. 25 (2013) 6291–6297.
[14] Y. Xiong, L. Yang, D.K. Nandakumar, Y. Yang, H. Dong, X. Ji, P. Xiao, S.C. Tan, Highly efficient photoelectrochemical water oxidation enabled by enhanced interfacial interaction in 2D/1D $In_2S_3$@$Bi_2S_3$ heterostructures, J. Mater. Chem. 8 (2020) 5612–5621.
[15] J.T. Kirner, R.G. Finke, Water-oxidation photoanodes using organic light-harvesting materials: a review, J. Mater. Chem. 5 (2017) 19560–19592.
[16] D. Shao, Y. Cheng, J. He, D. Feng, L. Zheng, L. Zheng, X. Zhang, J. Xu, W. Wang, W. Wang, F. Lu, H. Dong, L. Li, H. Liu, R. Zheng, H. Liu, A spatially separated organic-inorganic hybrid photoelectrochemical cell for unassisted overall water splitting, ACS Catal. 7 (2017) 5308–5315.
[17] J.B. Pan, B.H. Wang, J.B. Wang, H.Z. Ding, W. Zhou, X. Liu, J.R. Zhang, S. Shen, J. K. Guo, L. Chen, C.T. Au, L.L. Jiang, S.F. Yin, Activity and stability boosting of an oxygen-vacancy-rich $BiVO_4$ photoanode by NiFe-MOFs thin layer for water oxidation, Angew. Chem. 60 (2021) 1433–1440.
[18] X. Deng, R. Li, S. Wu, L. Wang, J. Hu, J. Ma, W. Jiang, N. Zhang, X. Zheng, C. Gao, L. Wang, Q. Zhang, J. Zhu, Y. Xiong, Metal-organic framework coating enhances the performance of $Cu_2O$ in photoelectrochemical $CO_2$ reduction, J. Am. Chem. Soc. 141 (2019) 10924–10929.
[19] S. Han, S.-H. Choi, S.-S. Kim, M. Cho, B. Jang, D.-Y. Kim, J. Yoon, T. Hyeon, Low-temperature synthesis of highly crystalline $TiO_2$ nanocrystals and their application to photocatalysis, Small 1 (2005) 812–816.
[20] S. Kment, F. Riboni, S. Pausova, L. Wang, L. Wang, H. Han, Z. Hubicka, J. Krysa, P. Schmuki, R. Zboril, Photoanodes based on $TiO_2$ and $\alpha$-$Fe_2O_3$ for solar water splitting-superior role of 1D nanoarchitectures and of combined heterostructures, Chem. Soc. Rev. 46 (2017) 3716–3769.
[21] C. Jiang, S.J.A. Moniz, A. Wang, T. Zhang, J. Tang, Photoelectrochemical devices for solar water splitting-materials and challenges, Chem. Soc. Rev. 46 (2017) 4645–4660.
[22] S. Wang, B.Y. Guan, Y. Lu, X.W.D. Lou, Formation of hierarchical $In_2S_3$-$CdIn_2S_4$ heterostructured nanotubes for efficient and stable visible light $CO_2$ reduction, J. Am. Chem. Soc. 139 (2017) 17305–17308.
[23] Peng Zhang, Yu Le, X.W.D. Lou, Construction of heterostructured $Fe_2O_3$-$TiO_2$ microdumbbells for photoelectrochemical water oxidation, Angew. Chem. Int. Ed. 57 (2018) 15076–15080.
[24] A.P. Singh, N. Kodan, B.R. Mehta, A. Held, L. Mayrhofer, M. Moseler, Band edge engineering in $BiVO_4$/$TiO_2$ heterostructure: enhanced photoelectrochemical performance through improved charge transfer, ACS Catal. 6 (2016) 5311–5318.
[25] B. Gao, X. Zhao, Z. Liang, Z. Wu, W. Wang, D. Han, L. Niu, CdS/$TiO_2$ nanocomposite-based photoelectrochemical sensor for a sensitive determination of nitrite in principle of etching reaction, Anal. Chem. 93 (2021) 820–827.
[26] Y. Yu, X. Yin, A. Kvit, X. Wang, Evolution of hollow $TiO_2$ nanostructures via the Kirkendall effect driven by cation exchange with enhanced photoelectrochemical performance, Nano Lett. 14 (2014) 2528–2535.
[27] D. Zheng, M. Chen, J. Peng, J. Chen, T. Chen, Y. Chen, L. Huang, W. Gao, An enhanced photoelectrochemical biosensor for colitoxin DNA based on HKUST-1/$TiO_2$ and derived HKUST-CuO/$TiO_2$ heterogeneous composites, Mikrochim. Acta 188 (2021) 328.
[28] W. Wang, C. Jin, L. Qi, Hierarchical CdS nanorod@SnO2 nanobowl arrays for efficient and stable photoelectrochemical hydrogen generation, Small (2018), e1801352.
[29] H. Wang, X. Liu, S. Wang, L. Li, Dual templating fabrication of hierarchical porous three-dimensional ZnO/carbon nanocomposites for enhanced photocatalytic and photoelectrochemical activity, Appl. Catal. B Environ. 222 (2018) 209–218.
[30] M. Guo, T. Zhao, Z. Xing, Y. Qiu, K. Pan, Z. Li, S. Yang, W. Zhou, Hollow octahedral $Cu_2$-xS/CdS/$Bi_2S_3$ p-n-p type tandem heterojunctions for efficient photothermal effect and robust visible-light-driven photocatalytic performance, ACS Appl. Mater. Interfaces 12 (2020) 40328–40338.
[31] C.T. Dinh, H. Yen, F. Kleitz, T.O. Do, Three-dimensional ordered assembly of thin-shell Au/$TiO_2$ hollow nanospheres for enhanced visible-light-driven photocatalysis, Angew. Chem. 53 (2014) 6618–6623.
[32] L. Pei, Y. Yuan, W. Bai, T. Li, H. Zhu, Z. Ma, J. Zhong, S. Yan, Z. Zou, In situ-grown island-shaped hollow graphene on TaON with spatially separated active sites achieving enhanced visible-light $CO_2$ reduction, ACS Catal. 10 (2020) 15083–15091.
[33] J. Peng, J. Yang, B. Chen, S. Zeng, D. Zheng, Y. Chen, W. Gao, Design of ultrathin nanosheet subunits $ZnIn_2S_4$ hollow nanocages with enhanced photoelectric conversion for ultrasensitive photoelectrochemical sensing, Biosens. Bioelectron. 175 (2021) 112873.
[34] M. Wang, J. Han, Y. Hu, R. Guo, Y. Yin, Carbon-incorporated NiO/$TiO_2$ mesoporous shells with p-n heterojunctions for efficient visible light photocatalysis, ACS Appl. Mater. Interfaces 8 (2016) 29511–29521.
[35] C. Li, H. Wang, S.B. Naghadeh, J.Z. Zhang, P. Fang, Visible light driven hydrogen evolution by photocatalytic reforming of lignin and lactic acid using one-dimensional NiS/CdS nanostructures, Appl. Catal. B Environ. 227 (2018) 229–239.
[36] Y. Wang, C. Zhu, G. Zuo, Y. Guo, W. Xiao, Y. Dai, J. Kong, X. Xu, Y. Zhou, A. Xie, C. Sun, Q. Xian, 0D/2D $Co_3O_4$/$TiO_2$ Z-scheme heterojunction for boosted photocatalytic degradation and mechanism investigation, Appl. Catal. B Environ. 278 (2020) 119298.
[37] D. Zhang, H. Mou, F. Lu, C. Song, D. Wang, A novel strategy for 2D/2D NiS/graphene heterostructures as efficient bifunctional electrocatalysts for overall water splitting, Appl. Catal. B Environ. 254 (2019) 471–478.
[38] Z. Liu, M. Zhou, Co-modification with cost-effective nickel oxides and nickel sulfides on $CuInS_2$ nanosheets photocathode for enhanced photoelectrochemical performance, ACS Sustain. Chem. Eng. 8 (2019) 512–519.
[39] J. Chen, J.M. Xie, C.K. Xia, Y. Zhu, J. Chen, Synthesis, characterization and photoluminescent property of a hexanuclear Nickel(+2) complex with trithiocyanuric acid, Chin. J. Inorg. Chem. 29 (2013) 2433–2437.
[40] L. Yang, M. Gao, B. Dai, X. Guo, Z. Liu, B. Peng, An efficient NiS@N/S-C hybrid oxygen evolution electrocatalyst derived from metal-organic framework, Electrochim. Acta 191 (2016) 813–820.
[41] J.T. Ming Sun, Cheng Gao, Ting Lin, Shaomin Peng, Fangze Deng, Fei Ye, Yu Lin, In situ growth of burl-like nickel cobalt sulfide on carbon fiber as high-performance supercapacitors, J. Mater. Chem. 3 (2015) 1730–1736.
[42] R. Bhosale, S. Kelkar, G. Parte, R. Fernandes, D. Kothari, S. Ogale, NiS1.97: a new efficient water oxidation catalyst for photoelectrochemical hydrogen generation, ACS Appl. Mater. Interfaces 7 (2015) 20053–20060.

[43] B. Huang, W. Yang, Y. Wen, B. Shan, R. Chen, $Co_3O_4$-modified $TiO_2$ nanotube arrays via atomic layer deposition for improved visible-light photoelectrochemical performance, ACS Appl. Mater. Interfaces 7 (2015) 422–431.
[44] J. Wen, J. Xie, Z. Yang, R. Shen, H. Li, X. Luo, X. Chen, X. Li, Fabricating the robust g-$C_3N_4$ nanosheets/Carbons/NiS multiple heterojunctions for enhanced photocatalytic $H_2$ generation: an insight into the trifunctional roles of nanocarbons, ACS Sustain. Chem. Eng. 5 (2017) 2224–2236.
[45] D.-T. Nguyen, C.-C. Nguyen, M. St-Jean, S. Chabot, S. Kaliaguine, T.-O. Do, All in one: contributions of Ni dopants and Ni/NiS dual cocatalysts to the enhanced efficiency of $TiO_2$ photocatalyst for the degradation of organic pollutants, ACS Appl. Nano Mater. 1 (2018) 6864–6873.
[46] F. Mu, Q. Cai, H. Hu, J. Wang, Y. Wang, S. Zhou, Y. Kong, Construction of 3D hierarchical microarchitectures of Z-scheme UiO-66-$(COOH)_2$/$ZnIn_2S_4$ hybrid decorated with non-noble $MoS_2$ cocatalyst: a highly efficient photocatalyst for hydrogen evolution and Cr(VI) reduction, Chem. Eng. J. 384 (2020).
[47] L. Li, J. Yan, T. Wang, Z.J. Zhao, J. Zhang, J. Gong, N. Guan, Sub-10 nm rutile titanium dioxide nanoparticles for efficient visible-light-driven photocatalytic hydrogen production, Nat. Commun. 6 (2015) 5881.
[48] X. Shi, M. Fujitsuka, Z. Lou, P. Zhang, T. Majima, In situ nitrogen-doped hollow-$TiO_2$/g-$C_3N_4$ composite photocatalysts with efficient charge separation boosting water reduction under visible light, J. Mater. Chem. 5 (2017) 9671–9681.
[49] W. Li, D. Li, S. Meng, W. Chen, X. Fu, Y. Shao, Novel approach to enhance photosensitized degradation of rhodamine B under visible light irradiation by the ZnxCd1-xS/$TiO_2$ nanocomposites, Environ. Sci. Technol. 45 (2011) 2987–2993.

Microchimica Acta (2022) 189:166
https://doi.org/10.1007/s00604-022-05280-y

ORIGINAL PAPER

# Sensitive photoelectrochemical detection of colitoxin DNA based on NCDs@CuO/ZnO heterostructured nanocomposites with efficient separation capacity of photo-induced carriers

**Delun Zheng[1,2] · Jianying Yang[3] · Zengyao Zheng[3] · Mingxuan Peng[1] · Kwan-Ming Ng[1] · Yaowen Chen[1] · Linjia Huang[4] · Wenhua Gao[1]**

Received: 8 December 2021 / Accepted: 11 March 2022


## Abstract

A metal–organic framework (MOF) of Cu-TPA (terephthalic acid) microsphere was prepared, followed by calcinating the MOF precursor of Cu-TPA/ZIF-8 mixture to obtain the CuO/ZnO. N-doped carbon dots (NCDs) were employed to combine the CuO/ZnO composite to form a tripartite heterostructured architecture of NCDs@CuO/ZnO, which led to a fierce enlargement of the photocurrent response. This was ascribed to the thinner-shell structure of the CuO microsphere and the fact that hollow ZnO particles could sharply promote the incidence intensity of visible light. The more porous defectiveness exposed on CuO/ZnO surface was in favor of rapidly infiltrating electrolyte ions. The p-n type CuO/ZnO composite with more contact interface could abridge the transfer distance of photo-induced electron ($e^{-1}$)/hole ($h^{+}$) pairs and repress their recombination availably. NCDs not only could boost electron transfer rate on the electrode interface but also successfully sensitized the CuO/ZnO composite, which resulted in high conversion efficiency of photon-to-electron. The probe DNA (S1) was firmly assembled on the modified ITO electrode surface (S1/NCDs@CuO/ZnO) through an amidation reaction. Under optimal conditions, the prepared DNA biosensor displayed a wide linear range of $1.0\times10^{-6}\sim7.5\times10^{-1}$ nM and a low limit of detection (LOD) of $1.81\times10^{-7}$ nM for colitoxin DNA (S2) measure, which exhibited a better photoelectrochemistry (PEC) analysis performance than that obtained by differential pulse voltammetry techniques. The relative standard deviation (RSD) of the sensing platform for target DNA detection of $5.0\times10^{-2}$ nM was 6.3%. This proposed DNA biosensor also showed good selectivity, stability, and reproducibility, demonstrating that the well-designed and synthesized photoactive materials of NCDs@CuO/ZnO are promising candidates for PEC analysis.

**Keywords** Photoelectrochemical · NCDs@CuO/ZnO composite · Tripartite-heterostructure · DNA biosensor

## Introduction

The photoelectrochemical (PEC) technique not only inherits the advantages of electrochemical methods such as simplicity, portability, and easiness to miniaturize but also possesses lower bias potentials and higher sensitivity than its electrochemical counterparts [1]. Recently, PEC fabricated biosensors have widely gained attention such as the simultaneous detection of multiple micro-RNAs biomarkers [2], the biomolecules of cells [3], DNA [4], antibiotics [5], and so forth [6]. To obtain high-performance PEC biosensors for DNA detection, the photoactive and electrocatalytic materials play an important role that can significantly influence the improvement of the analytical sensitivity [7 ~ 9]. Moreover, an effective immobilization of the single-stranded probe DNA (S1) on the modified interface is indispensability,

✉ Wenhua Gao
whgao@stu.edu.cn

1 Department of Chemistry and Laboratory for Preparation and Application of Ordered Structural Materials of Guangdong Province, Shantou University, Shantou, Guangdong 515063, People's Republic of China

2 Department of Natural Sciences, Shantou Polytechnic, Shantou, Guangdong 515078, People's Republic of China

3 Guangdong Shantou Supervision Testing Institute of Quality & Measuring, Shantou, Guangdong 515041, People's Republic of China

4 Institute of Chemical Engineering, Guangdong Academy of Sciences, Guangzhou, Guangdong 510665, People's Republic of China

Published online: 30 March 2022

which relates to various properties of the biosensor such as accuracy, stability, and lifetime. Therefore, the design and synthesis of the excellent photoactive material are still urgently needed, as well as a well-defined matrix interface for functional immobilization should be carefully thought.

So far, various photoactive materials such as $TiO_2$ [10], CuO [11, 12], ZnO [13], $Bi_2S_3$ [14], and CdS [15] have been employed for the construction of PEC sensor. Among them, CuO has received extensive concern owing to its narrow band gap (1.4 ~ 1.7 eV) [16] and good electron conductivity. ZnO has a wide band energy gap (*Eg*) and shows the photo-activity performance only in the UV light region [17]. Moreover, due to the fast recombination of photo-induced carriers, the photocatalytic efficiency of ZnO is restricted [18]. And the pure photoactive material's inherent defects such as rapid recombination of electron–hole pairs and poor capability for visible light absorption, limit their further application in PEC analysis [19]. Considerable efforts have been transformed for coupling varieties of photoactive materials with better-matched energy levels to form the heterostructure composite which can extend the visible spectral range and accelerate charge carrier separation, resulting in promoted photocurrent output [20, 21].

Being a porous material, metal–organic frameworks (MOFs) are constructed by transition metal ions and organic ligands. Due to the specific surface area, exposed active sites, and versatile structures, MOFs have been extensively applied in the area of supercapacitors [22], catalysis [23], sensing [24], etc. Recently, the MOF precursors are employed to fabricate functional materials because of their controllable properties. By treating the precursor template under specific conditions, MOFs can be adjusted to the tailored morphologies such as hollow cages, hierarchical structures, and heterojunction composite [25, 26]. MOF-derived products can be the main structure of the MOF precursor morphologies, as well as owe the merit of combing various components such as metal oxides and metal sulfide [27, 28]. Further, through controlling the pore size and crystalline structure, MOF-ramification can provide more photocatalytic and electrochemical active sites, which greatly promote the ion diffusion and the electron transport rate [29]. Hu et al. [30] prepared a hierarchically structured octahedral CuO by treating a Cu-MOF precursor (HKUST-1) at alkaline conditions, exhibiting an ultra-high capacity for the Li + storage. Zhang et al. [31] constructed a core/shell nanocomposites of $Fe_3O_4$@C/Cu(CuO) through calcining the mixture of $Fe_3O_4$ and HKUST-1, which showed an obvious photocatalytic activity for the degradation of methylene blue (MB). Our work [32] had reported a hierarchical hollow ZnCdS@$MoS_2$ heterostructure cage which derived from ZIF-8 polyhedral cages and obtained greatly amplifying photocurrents response because of the close contact heterojunction interface. Thus, MOF-derivatives can be used as the great potential of photoactive materials to fabricate PEC biosensors.

Carbon dots (CDs) are assembled by carbon atom aggregates or small graphene nanoplatelets [33]. The typical size of CDs is in the range of about ~ 10 nm and with a relatively narrow band gap. Compared to the semiconductor materials or other metal complexes, CDs are more environmentally friendly and can be used as an ideal optical material [34]. Based on its excellent properties of photo-stability, biocompatibility, and easily functionalized as interface matrix, CDs have been widely applied in photocatalysis [35], optical imaging [36], sensors [37], etc. But a disadvantage of the poor electron transfer capability of CDs still limits its practical applications in electrochemical analysis. To overcome this problem, heteroatoms doping with N or S were proposed, and the obtained doped-CD composite not only shows an improvement in electro-catalysis property but also can improve significantly the optical capability [38]. For instance, Shi et al. [35] prepared the N-doped CDs (NCDs) with different atom ratios of N/C and the maximum level of N atom doping showed an enhanced electron transfer rate. Our work [40] previously synthesized NCDs could successfully sensitize the photoactive material of $TiO_2$ and further improve the photo-to-electron conversion efficiency of NCDs/$TiO_2$ composite.

Inspired by this, a novel Cu-TPA microsphere and its composite of Cu-TPA/ZIF-8 were successively synthesized. Through calcination, the Cu-TPA/ZIF-8 precursor template had a compact connective hetero-constructed composite of CuO/ZnO. Afterward, NCDs were assembled onto CuO/ZnO surface and the formed NCDs@CuO/ZnO showed the greatest photocurrent response signal than the CuO or CuO/ZnO composite, which could be explained as following reasons: (i) the well-matched energy band gaps of CuO, ZnO, and NCDs (*Eg* = 1.78, 3.20, and 2.98 eV, respectively) made the tri-heterojunction interfaces to accelerate the separation/migration of $e^{-1}/h^+$ carriers; (ii) the thin-shell structure of CuO and hollow polyhedron of ZnO could improve the light-absorption capability; (iii) the close contact CuO/ZnO interface with p-n type heterostructured system could shorten the carrier transfer distance and facilitate photo-to-electron conversion; (iv) the heterogeneous CuO/ZnO composite could be sensitized effectively by the NCDs which led to an enhanced photocurrent output. It was notable that NCDs were also employed as a functional matrix material for immobilization of the single-stranded probe DNA (S1) through a gentle amidation reaction between carboxyl groups (-COOH) and amino groups (-$NH_2$). The obtained probe modified electrode of S1/NCDs@CuO/ZnO/ITO was finally applied to detect the colitoxin DNA (S2). The photoactive material of NCDs@CuO/ZnO could further expand its tremendous application such as the photocatalytic production of hydrogen or the pollutant degradation.

## Experimental section

### The reagents and apparatus (the other reagents and apparatus are shown in the Electronic Supporting Material (ESM))

#### Reagents

Copper nitrate trihydrate ($Cu(NO_3)_2{\cdot}3H_2O$, 99%), benzene-1,3,5-tricarboxylic acid (BTC, 99%), terephthalic acid (TPA), and phosphate buffer (PB, $Na_2HPO_4{\cdot}12H_2O$/$KH_2PO_4$) were purchased from Aladdin Chemical Reagent Co., Ltd. (Shanghai, China). Ethylenediaminetetraacetic acid (EDTA), ethyl-3-(3-dimethylaminopropyl) carbodiimide (EDC, 99%), N-hydrosulfosuccinimide (NHS, 99.8%), and Tris (hydroxymethyl) aminomethane (Tris) were obtained from Sinopharm Chemical Reagent Co., Ltd. (China). Ammonium citrate and ethylenediamine were obtained from Xilong Chemical Co. Ltd. (Shantou, China). The other reagents were of analytical grade and gained commercially. All aqueous solutions were prepared with the deionized water.

#### Apparatus

The electrochemical experiments were carried out on a CHI 650E electrochemical analyzer (Shanghai CH Instrument Company). The conventional three-electrode system was consisted of bare or modified indium tin oxide (ITO) as working electrode, Ag/AgCl/(3 M) as reference electrode, and Pt wire as auxiliary electrode. The irradiation light source was from a 300-W Xe lamp, and the light intensity was measured using a touch screen thorlabs (PM200, USA).

*Synthesis of Cu-TPA, Cu-TPA/ZIF-8, and NCD*s.

The Cu-TPA (TPA: terephthalic acid) was synthesized by a solvothermal method according to reported literature [41] with a modification. Firstly, 0.6 g $Cu(NO_3)_2{\bullet}3H_2O$ (2.48 mmol) with 0.3 g TPA (1.8 mmol) was dissolved in 10 mL deionized water; then, 10 mL N, N-dimethylformamide (DMF) and and 10 mL ethanol were added into the above solution. Subsequently, the mixture was stirred for 30 min and transferred into a Teflon-lined stainless steel reactor (50 mL) with a treatment of heating at 95 °C for 24 h. After cooling to room temperature, the products were carefully gathered through centrifugation (8000 rpm, 10 min), washed with water and ethanol, and dried at 60 °C for 6 h under vacuum. Finally, the blue Cu-TPA particles were obtained.

The Cu-TPA/ZIF-8 composite was prepared as follows: 0.11 g of as-prepared Cu-TPA and 0.09 g of $Zn(NO_3)_2{\bullet}6H_2O$ (0.3 mmol) were dissolved in 50 mL methanol and treated with sonication to form a well-dispersed solution. Then, 0.22 g of 2-methylimidazole (0.26 mmol) was added into the mixture under stirring and reacted for 6 h. After that, the gained products of Cu-TPA/ZIF-8 were washed by centrifugation (8000 rpm, 10 min) with water and ethanol, respectively. ZIF-8 was synthesized in the above experiment process without adding the Cu-TPA.

NCDs were prepared by the hydrothermal method [40]. Under stirring, 1.0 g of ammonium citrate and 5 mL of ethylenediamine were dispersed in 10 mL deionized water. The mixture was subsequently transferred to a 50 mL Teflon-lined stainless steel reactor and heated for 5 h at 200 °C. The obtained orange-red solution was centrifuged (10,000 rpm, 10 min) and concentrated supernatant was further dialyzed for 24 h with the membranes of 1000 cutoffs. After freeze-drying at the vacuum condition, the brown N-doped CD powder was gained.

### Preparation of CuO/ZnO and CuO/ZIF-8 composite

The as-fabricated Cu-TPA/ZIF-8 MOF precursors were transferred into a muffle furnace and calcined at 400 °C for 1.5 h. When cooling down to room temperature naturally, the dark gray product of CuO/ZnO was obtained. The CuO and ZnO particles were prepared in the same experimental condition without adding ZIF-8 or Cu-TPA. CuO was mixed with ZIF-8 (1:1, m/m) to obtain the CuO/ZIF-8 composite.

### Fabrication of the DNA biosensor

Before modification, the ITO electrode was severally washed with acetone, 1.0 M NaOH, and deionized water three times. Subsequently, 8 µL suspension solutions (1.3 mg $mL^{-1}$) of CuO/ZnO were drop-cast on the cleaned ITO electrode surface and dried naturally. Then, the CuO/ZnO modified ITO electrode (CuO/ZnO/ITO) was immersed into 1 mg $mL^{-1}$ NCD solution for 6 h. After thorough coupling, the desired electrode was marked as NCDs@CuO/ZnO/ITO.

The NCDs@CuO/ZnO/ITO electrode was immersed into 0.5 mL PBS solution (50 mM) with 20 mM NHS (N-hydrosulfosuccinimide) and 8 mM EDC (ethyl-3-(3-dimethylaminopropyl) carbodiimide) for 15 min in order to reactivate the carboxylic groups. After rinsing the modified electrode with the TE buffer solution (10 µM Tris–HCl, 1.0 mM EDTA, pH 8.0), 10 µL 0.1 µM S1 was dropped onto as-prepared NCDs@CuO/ZnO/ITO electrode for incubating 3 h. Dried at room temperature, the probe DNA modified electrode (S1/NCDs@CuO/ZnO/ITO) based on the covalent-linking reaction between S1 and NCDs was successfully fabricated.

### Hybridization reaction of the modified electrode

The S1/NCDs@CuO/ZnO/ITO was put into a 200-μL different concentration of S2 and incubated at 42 °C for 40 min. Then, it was washed with TE buffer solution to remove the un-hybridized S2. The hybridized electrode was termed S2-S1/NCDs@CuO/ZnO/ITO. The hybridization of S1/NCDs@CuO/ZnO/ITO with S3, S4, and S5 DNA sequences was performed with same experimental steps.

## Results and discussion

### Characterization of prepared materials

The morphology and microstructure of the synthesized products were investigated by FESEM and TEM. As well seen in Fig. 1A and insert of Fig. 1A, the shape of Cu-TPA was similarly microsphere structured with the diameter range of 0.5 ~ 11 μm, which also indicated that the good crystallinity of the Cu-TPA was obtained. From the enlarged SEM image (Fig. 1B), a large number of micro-pores could be observed on Cu-TPA. Compared to the Cu-TPA precursor, CuO/ZnO composites had a much coarser surface with a distinct macropore in size of about 0.3 ~ 1.7 μm (Fig. 1C). In Fig. 1D, the ZnO particles were welded with the CuO microsphere to form the composite of CuO/ZnO. Figure 1E shows that the ZIF-8 had a typical rhombic dodecahedron structure with a smooth surface, and the average particle size was about 250 ~ 350 nm. In addition, the SEM image of Cu-TPA/ZIF-8 is shown in Fig. S2. The SEM results demonstrated that the CuO/ZnO composite still maintained the basic morphologies of their precursor templates of Cu-TPA or ZIF-8.

The microstructure characteristics of Cu-TPA and CuO/ZnO composite were further investigated in the TEM analysis. As seen in the insert of Fig. 1E, ZnO particles had a well-retained rhombus shape with a hollow structure. Compared to the pure Cu-TPA (insert of Fig. 1B), CuO microsphere displayed a thinner crystalline structure with a greater roughness of the microsphere edge (Fig. 1F and insert), which may be caused by the hyperthermia pyrolysis process. Meanwhile, distributed ZnO particles with a similar rhombic shape were also found in CuO/ZnO composite. The TEM result was in agreement with the SEM investigation of CuO/ZnO. Elemental mapping images (Fig. S3C) manifested the homogeneous distribution of Cu, Zn, O, and C elements in the hetero-structured composite of CuO/ZnO.

Figure S3A shows the TEM measurements of NCD nanoparticles. It was found that the spherical-like shapes of NCDs were continuously distributed, and an average diameter of NCDs was determined to be 18 ~ 23 nm. From the HRTEM image (Fig. S3B and insert), the typical lattice spacing of 0.34 nm corresponded to a graphitic structure of the NCDs [42], which also proved that the NCDs had been successfully synthesized.

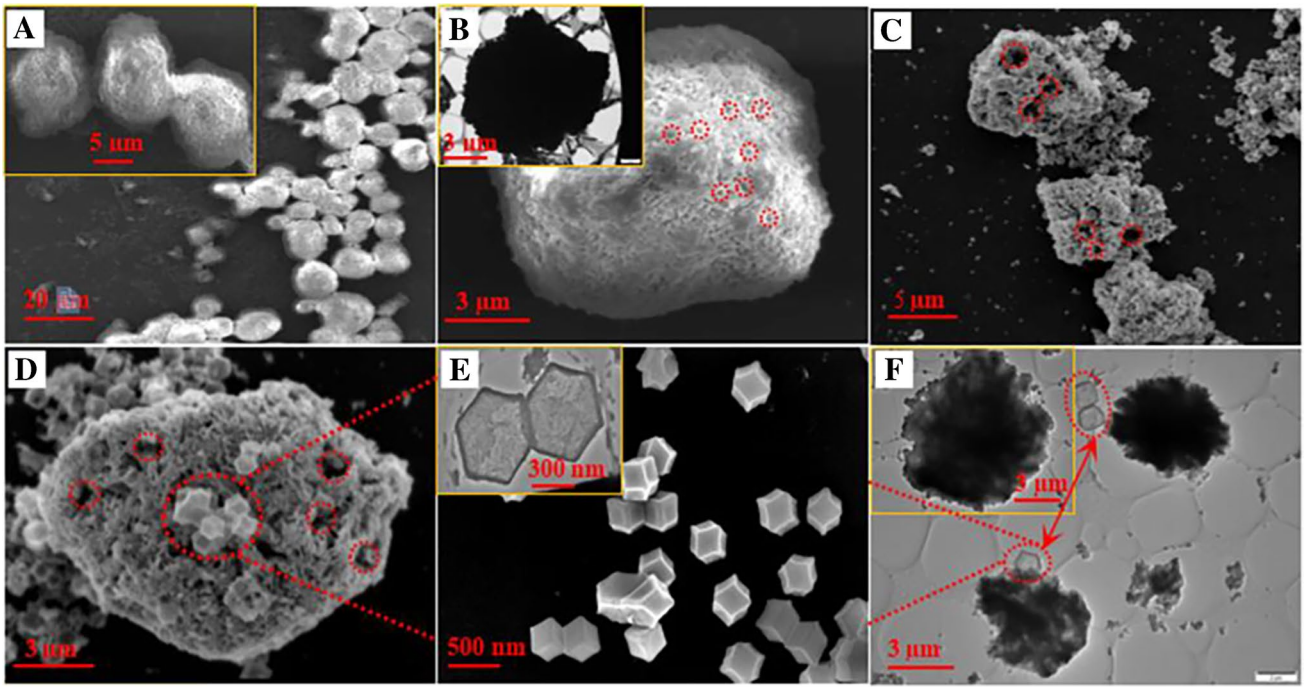


**Fig. 1** Low magnification and high magnification SEM images of (**A** and inset of **A**, **B**) Cu-TPA, (**C**, **D**) CuO/ZnO, and (**E**) ZIF-8; TEM images of (inset of **B**) Cu-TPA, (inset of E) ZIF-8, and (**F**) CuO/ZnO

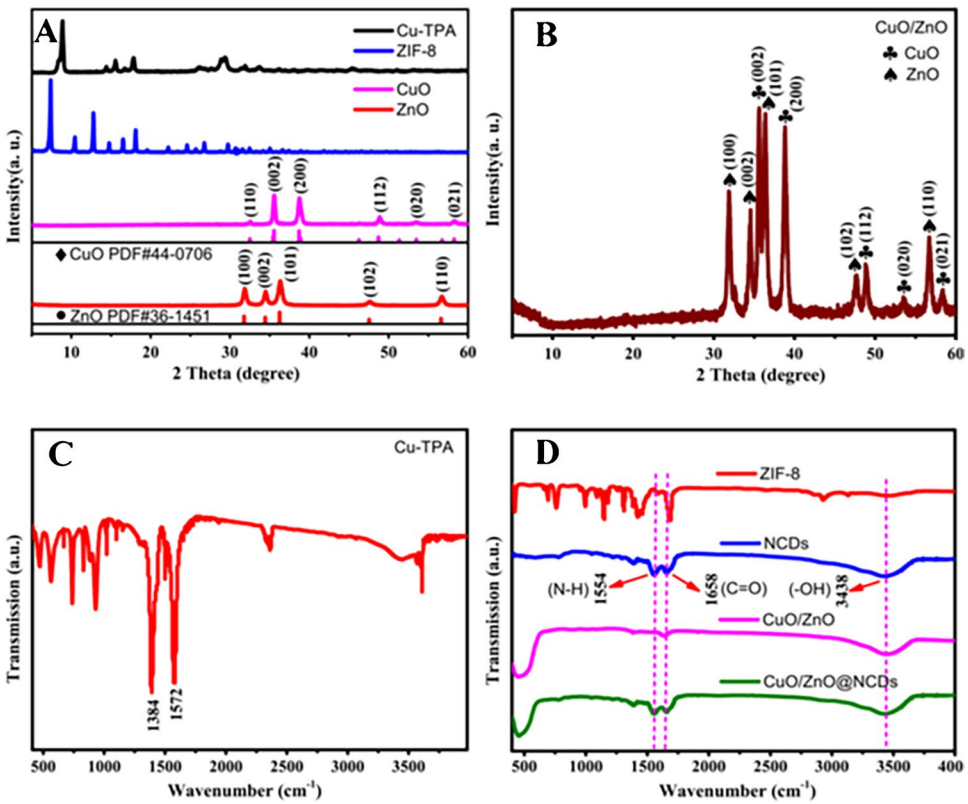


**Fig. 2** XRD patterns of (**A**) Cu-TPA, ZIF-8, CuO, ZnO and (**B**) CuO/ZnO, FT-IR spectra of (**C**) Cu-TPA and (**D**) ZIF-8, NCDs, CuO/ZnO, NCDs@CuO/ZnO

The phase composite and crystal structure of the synthesized products were examined by XRD pattern. As seen in Fig. 2A, the characteristic diffraction peaks of Cu-TPA and ZIF-8 were in good agreement with the literature reported [43, 44], respectively, indicating that the Cu-TPA and ZIF-8 had been prepared successfully with high purity. The diffraction peaks at 32.5°, 35.5°, 38.8°, 48.8°, 53.5°, and 58.33° observed in XRD pattern were indexed to the characteristic (110), (002), (200), (112), (020), and (021) planes of CuO (PDF#04–0706). The peaks at 31.8°, 34.7°, 36.7°, 47.7°, and 56.3° could be indexed to (100), (002), (101), (102), and (110) planes of ZnO (PDF#36–1451). Figure 2B shows the strong and sharp diffraction peaks of CuO and ZnO, testifying that the CuO/ZnO composite was successfully synthesized. The typical XRD pattern of NCDs with the $2\theta = 24.8°$ is also shown in Fig. S4A. Figure S4B shows the thermogravimetric (TG) patterns of Cu-TPA and Cu-TPA/ZIF-8, in which both products could be stable up to approximately 320 °C. It was noteworthy that Cu-TPA/ZIF-8 had been decomposed at the temperature of 400 °C.

The FT-IR pattern of the synthesized products was determined by FT-IR spectroscopy. As seen in Fig. 2C, the characteristic peak values of 1384 $cm^{-1}$ and 1572 $cm^{-1}$ of Cu-TPA coincided with the reported literature [41]. Figure 2D shows the FT-IR pattern of ZIF-8, NCDs, CuO/ZnO, and NCDs@CuO/ZnO. The characteristic peaks at 1554 $cm^{-1}$, 1658 $cm^{-1}$, and 3834 $cm^{-1}$ were assigned to the N–H, C = O, and O–H bonds of NCDs [45], respectively, which are also preserved in NCDs@CuO/ZnO. In addition, the characteristic peak at about 500 $cm^{-1}$ was ascribed to the specific vibration of the Cu–O bond in CuO/ZnO and NCDs@CuO/ZnO. The Raman spectrum of CuO/ZnO is shown in Fig. S4C, in which two typical peaks at 1365 $cm^{-1}$ and 1568 $cm^{-1}$ were ascribed to the D-band and G-band, respectively.

The surface composition and chemical bonding state of the synthesized products were also investigated using XPS measurement. Figure 3A shows the XPS survey spectra of CuO, NCDs, and CuO/ZnO with their composing elements of Cu, Zn, N, O, and C, respectively. Figure 3B shows the high-resolution Cu 2p core-level spectrum of CuO/ZnO at about 933.6 and 953.6 eV which correspond to the Cu $2p_{3/2}$ and Cu $2p_{1/2}$ peaks, respectively, indicating that the oxidation state of Cu in CuO/ZnO was + 2 [46]. Meanwhile, two shakeup satellite peaks at approximately 941.3 and 962.1 eV also revealed the copper oxidation state of + 2. The high-resolution Cu 2p, O1s, and C 1 s spectra of CuO are shown in Fig. S5A ~ C. Figure 3C displays that the peaks at 1022.0 eV and 1045.1 eV were attributed to Zn $3d_{3/2}$ and Zn $3d_{1/2}$ of $Zn^{2+}$ in CuO/ZnO [47]. Figure 3D shows the O1s spectra with two peaks at about 529.7 eV and 530.6 eV, which was attributed to the existence of $O^{2-}$ in Cu–O and Zn–O bonding linker [48]. Meanwhile, the high-resolution N1s spectrum of NCDs was observed at about 962.1 eV, and the peaks that appeared at 284.7 eV and 287.7 eV (Fig. S5D ~ F) may

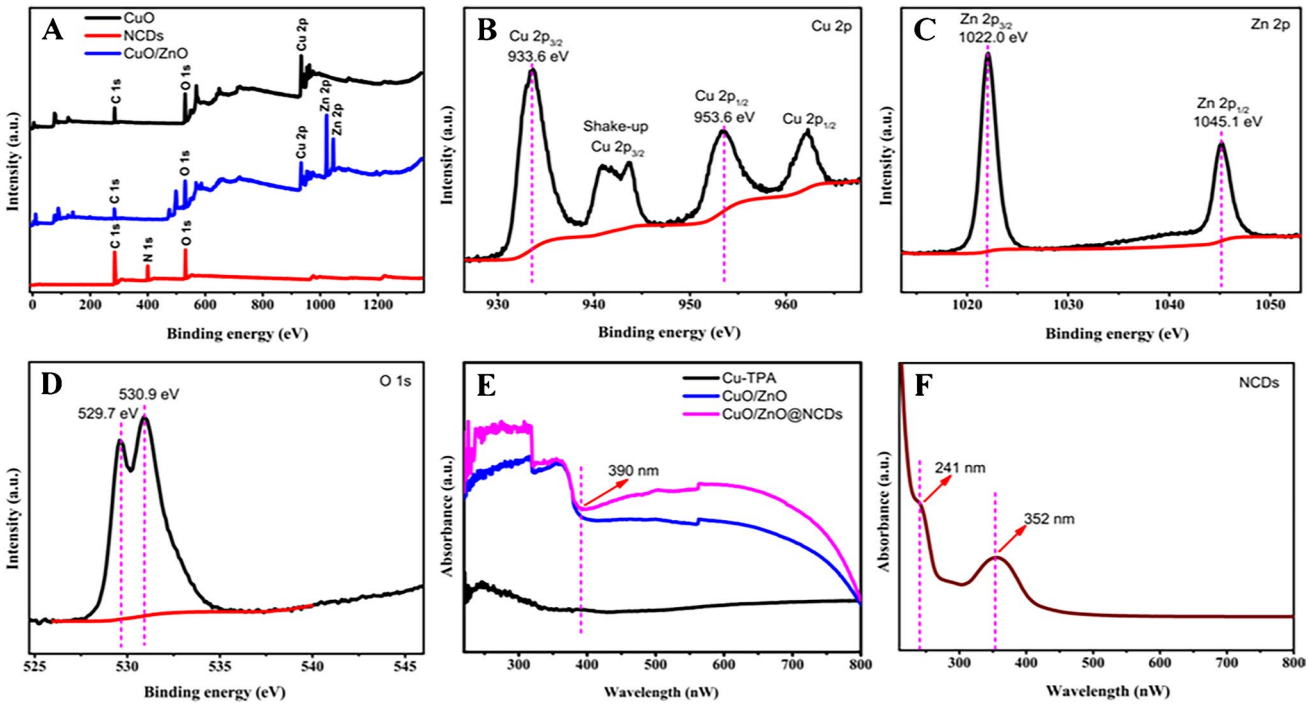


**Fig. 3** XPS spectra of (**A**) CuO, NCDs, CuO/ZnO, High-resolution XPS spectra of (**B**) Cu 2p, (**C**) Zn 2p, (**D**) O 1 s of CuO/ZnO; UV–vis spectra of (**E**) Cu-TPA, CuO/ZnO, NCDs@CuO/ZnO, and (**F**) NCDs

be attributed to the C–C/C = C and C–OH/C–O–C bonds in NCDs [49], respectively. All above XPS results verified that the desired materials were successfully synthesized.

The UV–vis absorbance performance of prepared materials was investigated by diffuse reflectance spectroscopy (DRS). As observed in Fig. 3E, the pure Cu-TPA only had the photo-absorption property in the UV-light region, while the NCDs showed two absorption peaks of UV-light at about 241 and 352 nm (Fig. 3F), which was ascribed to the π–π* transition of C = C bond and the n–π* transition of C = O bond [42], respectively. Compared with pure Cu-TPA and NCDs, CuO/ZnO and NCDs@CuO/ZnO not only had remarkable absorption in the UV-light region but also showed obvious absorption properties in the visible-light region of $\lambda > 390$ nm. The result could be attributed to the heterogeneous interface composites formed among the CuO, ZnO, and NCDs. Furthermore, NCDs@CuO/ZnO displayed a better harvesting ability for visible-light than CuO/ZnO, demonstrating that the NCD nanoparticles could effectively sensitize the composite of CuO/ZnO.

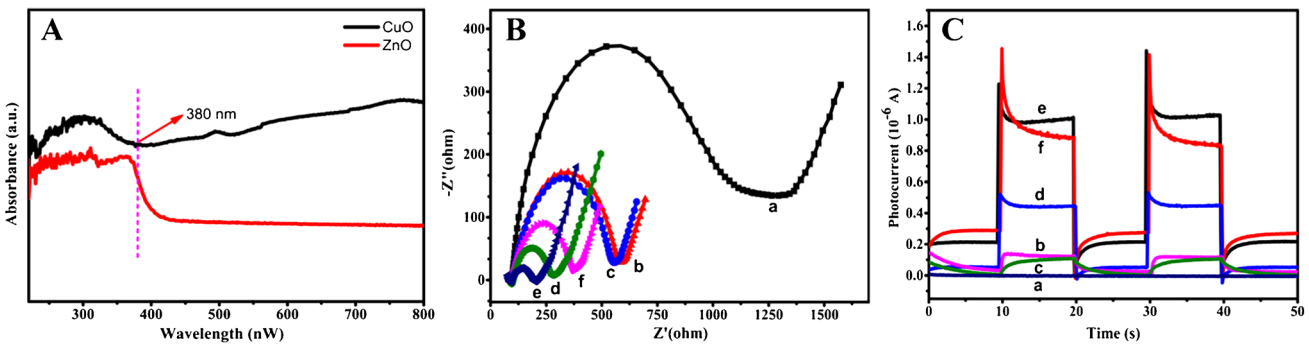


**Fig. 4** (**A**) UV–vis spectrum of CuO and ZnO; (**B**) EIS and (**C**) PEC response of Cu-TPA/ZIF-8/ITO (**a**), CuO/ZIF-8/ITO (**b**), CuO/ITO (**c**), CuO/ZnO/ITO (**d**), NCDs@CuO/ZnO/ITO (**e**), S1/NCDs@CuO/ZnO/ITO (**f**); EIS and PEC experiments were conducted in 5 mM $[Fe(CN)_6]^{3-/4-}$ containing 0.1 M KCl and in 0.1 M PBS (pH 7.4), respectively

## PEC mechanism

The UV–vis DRS of CuO and ZnO were also surveyed (Fig. 4A). It was found that the light absorption ability of ZnO declined at the wavelength of 380 nm, while the absorption intensity of CuO gradually enhanced in a range from 380 to 800 nm. This phenomenon could be explained by the thin-wall structure of the CuO microsphere which led to generating multiple scattering/reflection effects. In addition, based on the $(ahv)^2$ versus $(hv)$ plots with the following empirical equation [9]: $ahv = A\ (hv - Eg)^{1/2}$, where $hv$, $a$, and A belong to the photon energy, a constant, and absorption coefficient, respectively. The $Eg$ values of CuO, ZnO, and NCDs were estimated to be about 1.78, 3.20, and 2.98 eV (Fig. S6A ~ C), respectively. Meanwhile, using the valence band (VB)–XPS spectra, the VB potentials of CuO and NCDs were calculated at about 0.68 and 2.16 eV (Fig. S6D and E). The CB potentials could be obtained according to the empirical formula of $E_{CB} = E_{VB} - Eg$ ($E_{CB}$ and $E_{VB}$ were the CB and VB edge potentials, respectively). Hence, the corresponding CB potentials of CuO and NCDs were − 1.10 and − 0.82 eV. Additionally, the $E_{VB}$ value of ZnO was 2.16 eV based on its CB positions value of − 0.5 eV [50, 51]. These results revealed that the narrower $Eg$ value of CuO was compared with the ZnO and NCDs, and the CB and VB potentials of CuO were higher than that of NCDs and ZnO. Therefore, the composite of CuO, ZnO, and NCDs was assembled onto the ITO electrode to form tri-heterostructures. Under visible-light excitation, the photo-excited electrons in the CB of CuO were transferred to the CB of NCDs and ZnO orderly, while the holes in the VB of ZnO were transferred to the VB of NCDs and CuO subsequently, resulting in an enhanced photocurrent response. The significantly increased property of photo-to-electron was mostly attributed to the thin-shell structure of CuO microsphere with hollow ZnO particles which could extend the visible-light capture. Besides, the interlaced band structures of NCDs@CuO/ZnO formed tri-heterojunction could effectively separate the photo-generated $e^{-1}/h^{+}$. The last but not least, the high electro-catalysis of NCDs further facilitated the electron transfer. When the special DNA sequences (S1, S2) were introduced, the photocurrent values had decreased visibly due to their inferior conductivity. The detection mechanism of the DNA biosensor is shown in Scheme 1B.

## Electrochemical and PEC behavior of the modified electrodes

Electrochemical impedance spectroscopy (EIS) was an effective tool that reflected the interface properties of modified electrodes [52]. In EIS, the electron-transfer resistance ($R_{et}$) value can be estimated by measuring a semicircle diameter at higher frequencies equals. As shown in Fig. 4B, the Cu-TPA/ZIF-8/ITO electrode (curve a) obtains the greatest $R_{et}$ value of 1180 Ω, which indicated a very poor electron transferring ability on the electrode surface. The modified electrodes of CuO/ZIF-8/ITO (curve b) and CuO/ITO (curve c) possessed the approximate $R_{et}$ values of 473 Ω and 486 Ω, respectively, while the $R_{et}$ value on CuO/ZnO/ITO (curve d) decreased substantially (190 Ω) that was ascribed to the synergistic effect of CuO/ZnO composite that could improve the electrochemical property on the electrode surface. NCDs@CuO/ZnO/ITO electrode (curve e) exhibited a smaller arc radius with the $R_{et}$ value of 103 Ω, indicating that NCDs promoted the electron transfer rate of the redox probe of $[Fe(CN)_6]^{3-/4-}$ owing to the excellent electric conductivity. When the probe DNA (S1) was immobilized on NCDs@CuO/ZnO/ITO electrode, the $R_{et}$ value significantly boosted (curve f, 292 Ω) due to negatively charged phosphate backbone with the steric hindrance effect of S1 which inhibited the electron transfer of $[Fe(CN)_6]^{3-/4-}$. The preparation process of the modified electrode was also investigated by CVs (Fig. S6F and Fig. S7A). All the EIS and CV results prove that the S1/NCDs@CuO/ZnO/ITO electrode was fabricated successfully.

To deeply study the photoelectric property of various modified electrodes, all photoelectric tests were recorded in 0.1 M PBS (pH 7.4) and the results are shown in Fig. 4C. It was obvious that the photocurrent response on Cu-TPA/ZIF-8/ITO (curve a) was almost zero. Compared with Cu-TPA/ZIF-8/ITO, the photocurrent values of CuO/ZIF-8/ITO and CuO/ITO (0.12 μA and 0.1 μA, curves b and c) were increasing obviously. This result was due to the porous thin structure of the CuO microsphere that had good charge penetration property. On the CuO/ZnO/ITO electrode (curve d), the photocurrent intensity increased to 0.45 μA, which was ascribed to the p-n type heterogeneous construction of CuO/ZnO composite that could accelerate the photo-generated electron/hole pair separation. Nevertheless, the photocurrent responses of NCDs@CuO/ZnO/ITO (curve e) had the biggest value (1.03 μA), which was 2.28-fold than that of CuO/ZnO/ITO and 10.3-fold than that of CuO/ITO, respectively, indicating that the more efficient sensitization effect with higher conductivity of NCDs could enlarge remarkably the photocurrent strength. Afterward, the photocurrent intensity of S1/NCDs@CuO/ZnO/ITO decreased slightly (curve f) due to the hindrance effect and low conductivity of S1. The PEC results confirmed that this sensing interface for DNA detection was proposed successfully.

The linear sweep voltammetry (LSV) tests of NCDs@CuO/ZnO, CuO/ZnO, CuO, and Cu-TPA/ZIF-8 were carried out in 0.1 M $Na_2SO_4$ at a potential range of 0.0 ~ 0.75 V vs. Ag/AgCl. As shown in Fig. 5A, the LSV curve of Cu-TPA/ZIF-8 exhibited no photocurrent effect under continuous visible-light irradiation because of the much great

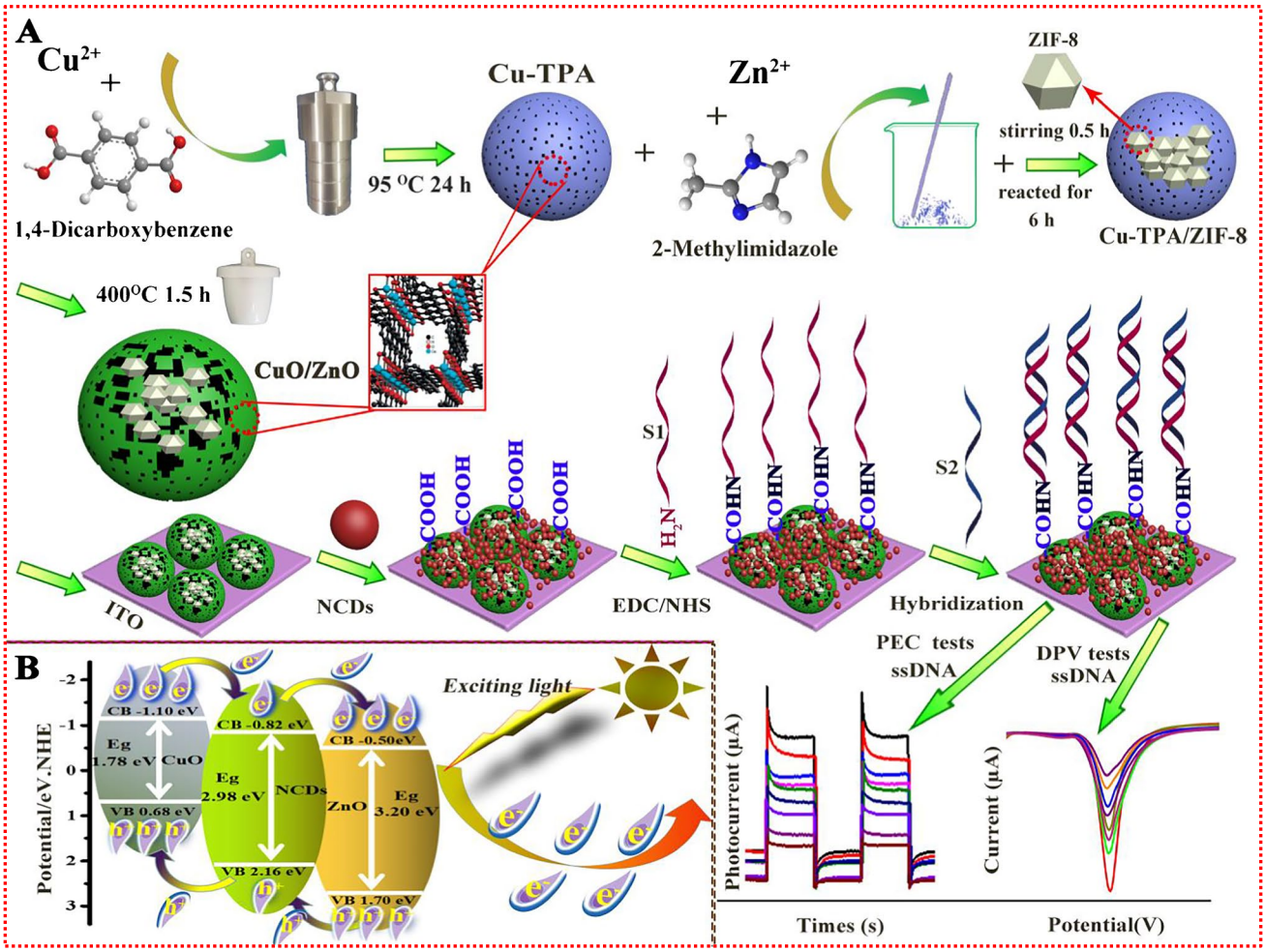


**Scheme 1** (**A**) Schematic illustration of the synthesis process of CuO/ZnO and the construction processes of PEC and DPV biosensors for colitoxin DNA detection. (**B**) Photogenerated electron–hole transfer mechanism based on NCDs@CuO/ZnO

recombination rate of photo-generated $e^{-1}/h^{+}$ pairs. However, the photocurrent response of LSV on CuO and CuO/ZnO showed an escalating trend, which demonstrated that the heterojunction composite of CuO/ZnO could facilitate photo-generated $e^{-1}/h^{+}$ pair transfer and separate speedily. It was noted that the highest LSV response was obtained on NCDs@CuO/ZnO; this reason could be attributed to the excellent conductivity of NCDs which could further enhance the PEC property.

The open-circuit potential (OCP) patterns of NCDs@CuO/ZnO, CuO/ZnO, and CuO under dark and visible-light irradiation were recorded in 0.1 M PBS (pH 7.4) solution. As depicted in Fig. 5B, the feature peak of OCP on CuO verified that the presence of n-type CuO. In the dark, the proposed materials of CuO, CuO/ZnO, and NCDs@CuO/ZnO all displayed a downward surface band bending (region I) due to the potential of redox equilibration [53]. Under continuous illumination owing to the photo-generated electrons accumulating, the OCP response of the above materials increases quickly towards a positive Fermi level and reaches a steady state (region II). After the irradiation was switched off, the OCP intensity gradually decreased (region III), which may be ascribed to the recombination of photo-generated charge carriers [36]. In addition, the change values of OCP (ΔOCP) could manifest the charge separation efficiency of different modified materials; it was easily found that the ΔOCP values of CuO/ZnO and NCDs@CuO/ZnO both exhibited greater than the single-component material of CuO, demonstrating that p-n type heterogeneous composites got more photo-generated electrons and both accelerated charge carriers change efficiently. These OCP results also revealed that the NCD nanoparticles could achieve the photo-sensitive effect for CuO/ZnO.

## PEC analysis properties of the prepared biosensor

Under optimized conditions, the developed DNA biosensor was applied to detect different concentrations of colitoxin

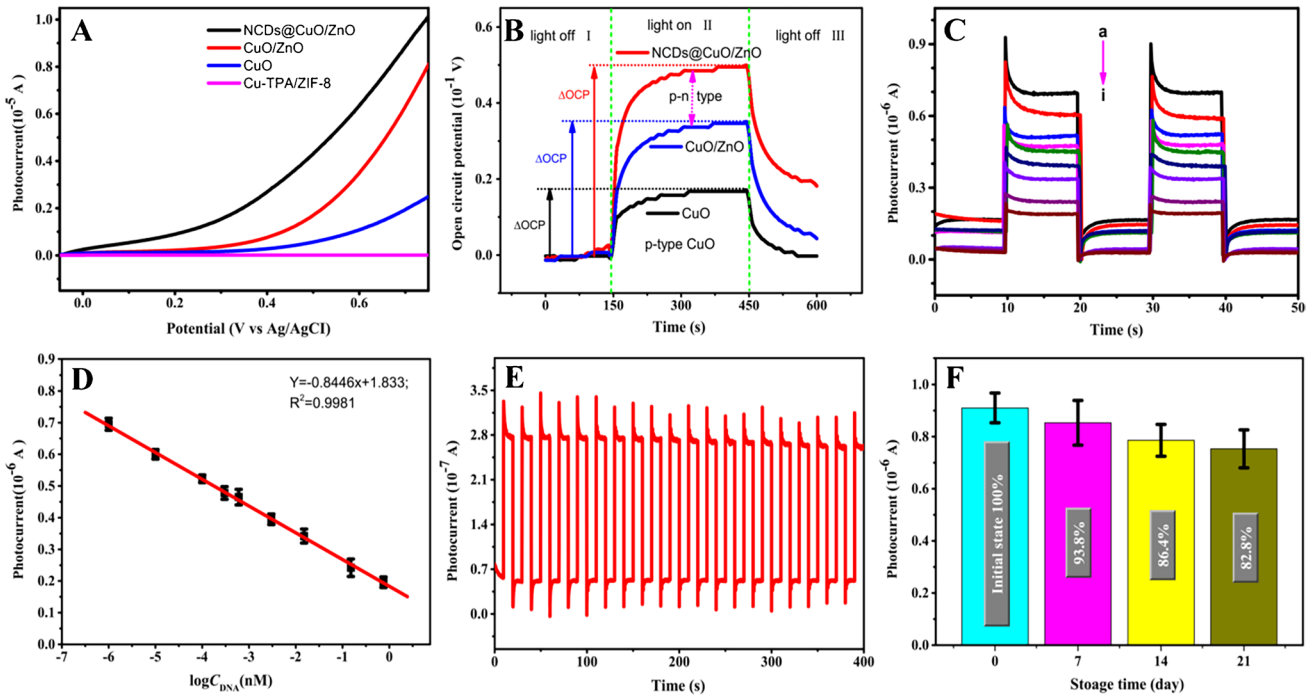


**Fig. 5** (**A**) LSV patterns of NCDs@CuO/ZnO, CuO/ZnO, CuO, and Cu-TPA/ZIF-8 in 0.1 M $Na_2SO_4$ with a scan rate of 80 mV $s^{-1}$, (**B**) OCP curves of NCDs@CuO/ZnO, CuO/ZnO, CuO in 0.1 M PBS (pH 7.4); (**C**) PEC response and (**D**) the corresponding logarithmic curve of S1/NCDs@CuO/ZnO/ITO sensor for the detection of different concentrations of target DNA (S2). (a–i) $1.0\times10^{-6}$, $1.0\times10^{-5}$, $1.0\times10^{-4}$, $3.0\times10^{-4}$, $6.0\times10^{-4}$, $3.0\times10^{-3}$, $1.5\times10^{-2}$, $1.5\times10^{-1}$, $7.5\times10^{-1}$ nM; (**E**) time-based photocurrent response of S2-S1/NCDs@CuO/ZnO/ITO electrodes with light on and off cycles; (**F**) the photocurrent responses of as-prepared biosensor after different storage time (day) in PBS (0.1 M, pH 7.4)

DNA (S2). Figure 5C shows the photocurrent response gradually decreases with increasing concentrations of S2, suggesting that more and more double-helix structure of DNA had been formed on the modified electrode surface, and the photocurrent change values ($\Delta I$) were commendably proportional to the logarithm of the target DNA concentration (log $C_{S2}$) from $1.0\times10^{-6}$ to $7.5\times10^{-1}$ nM (Fig. 5D). The linear equation was $\Delta I$ (μA) = −0.8446 log $C_{DNA}$ (nM) + 1.833 ($R^2$ = 0.9981) and with a low LOD value of $1.81\times10^{-7}$ nM based on 3 signal-to-noise ratio (S/N = 3). To further probe whether this PEC biosensor had the best analytical performance for target DNA, S1/NCDs@CuO/ZnO/ITO hybridization response with different concentrations of S2 was also investigated by the electrochemical method of DPV. Figure S9B and C show the change values of DPV increased accordingly with the increase of S2 concentration ($C_{S2}$) in the range from $1.0\times10^{-5}$ to $2.5\times10^{-2}$ nM with a LOD value of $2.43\times10^{-6}$ nM (S/N = 3). Through comparison of this result and others reported in the literature (shown in Table S1), it could be found that the prepared PEC biosensor exhibited a wider linear range. This superior analytic ability may be attributed to that NCDs@CuO/ZnO composites had the mainly photoelectric activity compared with its electrochemical property, and as well the synergetic amplifying effect of multiple heterogeneous architectures with a contact interface.

## Stability, selectivity, and reproducibility of PEC biosensor

Figure 5E shows the stability of the prepared PEC biosensor; it was found that no significant photocurrent signals change on S1/NCDs@CuO/ZnO/ITO modified electrodes after the biosensors hybridization with $8.0\times10^{-2}$ nM colitoxin DNA under irradiation cycles for 400 s and when on/off, which demonstrated that the developed PEC biosensor had superior long-term stability for target DNA analysis. When the fabricated PEC biosensor was stored for a week at 4 °C, the photocurrent was reduced to 93.8% compared with the original photocurrent intensity (100%). When the storage time exceeded 2 weeks, the photocurrent declined to 86.4% (Fig. 5F), suggesting that the modified electrode had the receivable stability.

Figure S7C shows the selectivity investigation of fabricated colitoxin DNA sensor hybridization with the complementary DNA sequence (S2), non-complementary DNA sequence (S5), and the mismatch DNA sequences: single-base mismatched DNA (S3) and three-base mismatched

DNA (S4). At the depiction of PEC results, S1/NCDs@CuO/ZnO/ITO electrode had the highest PEC responses. After the biosensor was hybridized with S2 (curve e), the PEC signals significantly decreased, indicating the efficient hybridization reaction occurrence on the electrode surface. When the biosensor was hybridized with S5 (curve b), the photocurrent change was negligible, suggesting that the non-specific absorption did not occur. When this biosensor was hybridized with S3 (curve d) and S4 (curve c), the decreased photocurrent signals were still higher than that obtained on the hybridized electrode with S2, displaying that the S3 and S4 DNA sequences only occurred as partial hybridization with the S1. The corresponding histogram of photocurrent values is shown in Fig. S9A, demonstrating that the developed photochemical biosensors possessed excellent selectivity.

The reproducibility of the biosensor was studied by comparing the PEC response current of three equilibrium results of S1/NCDs@CuO/ZnO/ITO electrode after hybridization with $5.0 \times 10^{-2}$ nM target DNA. The obtained relative standard deviation (RSD) was corresponding to 6.3%, indicating that the fabricated biosensors had satisfactory reproducibility.

## Conclusion

In this work, the MOF-derived hetero-structured composite of CuO/ZnO was synthesized, and the MOF-derived morphologies of CuO/ZnO particles possessed the advantage for harvesting UV–visible light. The porous flaw structure of CuO/ZnO was profitable for the electrolytic ion accessing. The obtained compact contact interface of CuO/ZnO could reduce the transport distance of the charge carriers. CuO/ZnO was coupled with NCDs to form the hierarchical band gap energies architecture that could further accelerate charge carrier separation and migration. This tri-heterogeneous composite of NCDs@CuO/ZnO modified ITO electrode resulted in a remarkable PEC signal response. The PEC analysis results of proposed biosensor displayed a better sensing performance than the DPV characterization method. In general, this work broadened the practical application of the MOF-derivative, and the proposed method provided a promising strategy for the inexpensive, accurate, and convenient detection of DNA in the bio-molecular diagnostic areas.

In this paper, the tri-heterostructured NCDs@CuO/ZnO system and its PEC mechanism were initially explored. Further work will be focused on the construction of novel heterojunctions and to improve the practical application ability in other fields.

**Supplementary Information** The online version contains supplementary material available at https://doi.org/10.1007/s00604-022-05280-y.

**Funding** This work was financially supported by the Guangdong Basic and Applied Basic Research Foundation (No. 2019A1515010618), the Guangdong Special Funds for the Science & Technology Project (No. 2019ST029 & No. 2019ST089), 2020 Li Ka Shing Foundation Cross-Disciplinary Research Grant (Project Number 2020LKSFG06C), and Shantou Polytechnic Supported Project (No. 2019SZK2019Y01).

## Declarations

**Conflict of interest** The authors declare no competing interests.

## References

1. Chang J, Lv W, Li Q, Li H, Li F (2020) One-step synthesis of methylene blue-encapsulated ZIF for dual-signal fluorescent and homogeneous electrochemical biosensing. Anal Chem 92:8959–8964. https://doi.org/10.1021/acs.analchem.0c00952
2. Chang J, Lv W, Wu J, Li H, Li F (2021) Simultaneous photoelectrochemical detection of dual microRNAs by capturing CdS quantum dots and methylene blue based on target-initiated strand displaced amplification. Chin Chem Lett 32:775–778. https://doi.org/10.1016/j.cclet.2020.05.041
3. Qian Z, Bai H, Wang G, Xu J, Chen H (2010) A photoelectrochemical sensor based on CdS-polyamidoamine nano-composite film for cell capture and detection. Biosens Bioelectron 25:2045–2050. https://doi.org/10.1016/j.bios.2010.01.036
4. Long D, Li M, Wang H, Chai Y, Li Z, Yuan R (2020) Ultrasensitive photoelectrochemical assay for DNA detection based on a novel $SnS_2/Co_3O_4$ sensitized structure. Anal Chem 92:14769–14774. https://doi.org/10.1021/acs.analchem.0c03497
5. Chen F, Han D, Chen H (2020) Liposome-assisted enzymatic modulation of plasmonic photoelectrochemistry for immunoassay. Anal Chem 92:8450–8458. https://doi.org/10.1021/acs.analchem.0c01162
6. Guo J, Liu D, Yang Z, Weng W, Chan E, Zeng Z, Wong K, Lin P, Chen S (2020) A photoelectrochemical biosensor for rapid and ultrasensitive norovirus detection. Bioelectrochemistry 136:107591. https://doi.org/10.1016/j.bioelechem.2020.107591
7. Yu X, Wang Y, Chen X, Wu K, Chen D, Ma M, Huang Z, Wu W, Li C (2015) White-light-exciting, layer-by-layer-assembled ZnCdHgSe quantum dots/polymerized ionic liquid hybrid film for highly sensitive photoelectrochemical immunosensing of neuron specific enolase. Anal Chem 87:4237–4244. https://doi.org/10.1021/ac504456w
8. Li F, Zhou Y, Wang S, Yin H, Chen Y, Luo H, Ai S (2020) One step preparation of CN-$WS_2$ nanocomposite with enhanced photoactivity and its application for photoelectrochemical detection of 5-formylcytosine in the genomic DNA of maize seedling. Biosens Bioelectron 151:111973. https://doi.org/10.1016/j.bios.2019.111973
9. Zheng D, Chen M, Peng J, Jiayang Chen J, Chen T, Chen Y, Huang L, Gao W (2021) An enhanced photoelectrochemical biosensor for colitoxin DNA based on HKUST-1/$TiO_2$ and derived HKUST-CuO/$TiO_2$ heterogeneous composites. Microchim Acta 188(10):328–338. https://doi.org/10.1007/s00604-021-04999-4
10. Wu F, Yu Y, Yang H, German L, Li Z, Chen J, Yang W, Huang L, Shi W, Wang L, Wang X (2017) Simultaneous enhancement of charge separation and hole transportation in a $TiO_2$–$SrTiO_3$ core–shell nanowire photoelectrochemical system. Adv Mater 29:1701432. https://doi.org/10.1002/adma.201701432
11. Li C, He J, Xiao Y, Li Y, Delaunay J-J (2020) Earth-abundant Cu-based metal oxide photocathodes for photoelectrochemical water

splitting, Energy Environ. Sci 13:3269–3306. https://doi.org/10.1039/D0EE02397C
12. Yang C, Wu Q, Jiang Z, Wang X, Huang C, Li Y (2021) Cu vacancies enhanced photoelectrochemical activity of metal-organic gel-derived CuO for the detection of L-cysteine. Talanta 228:122261–122268. https://doi.org/10.1016/j.talanta.2021.122261
13. Shao M, Ning F, Wei M, Evans D, Duan X (2014) Hierarchical nanowire arrays based on ZnO core-layered double hydroxide shell for largely enhanced photoelectrochemical water splitting. Adv Funct Mater 24:580–586. https://doi.org/10.1002/adfm.201301889
14. Bondarenko E, Streltsov E, Malashchonak M, Mazanik A, Kulak A, Skorb E (2017) Giant incident photon-to-current conversion with photoconductivity gain on nanostructured bismuth oxysulfide photoelectrodes under visible-light illumination. Adv Mater 29:1702387. https://doi.org/10.1002/adma.201770287
15. Qiu B, Zhu Q, Du M, Fan L, Xing M, Zhang J (2017) Efficient solar light harvesting CdS/$Co_9S_8$ hollow cubes for Z-Scheme photocatalytic water splitting. Angew Chem Int Ed 56:2684–2688. https://doi.org/10.1002/anie.201612551
16. Septina W, Prabhakar R, Wick R, Moehl T, Tilley SD (2017) Stabilized solar hydrogen production with CuO/CdS heterojunction thin film photocathodes. Chem Mater 29:1735–1743. https://doi.org/10.1021/acs.chemmater.6b05248
17. Trang T, Phan T, Nam N, Thu V (2020) In situ charge transfer at the Ag@ZnO photoelectrochemical interface toward the high photocatalytic performance of $H_2$ evolution and RhB degradation. ACS Appl Mater Interfaces 12:12195–12206. https://doi.org/10.1021/acsami.9b15578
18. Petrella A, Cozzoli PD, Curri ML, Striccoli M, Cosma P, Agostiano A (2004) Photoelectrochemical study on photosynthetic pigments-sensitized nanocrystalline ZnO films. Bioelectrochem 63:99–102. https://doi.org/10.1016/j.bioelechem.2003.09.016
19. Low JX, Yu JG, Jaroniec M, Wageh S, Al-Ghamdi AA (2017) Heterojunction photocatalysts. Adv Mater 29:1601694. https://doi.org/10.1002/adma.201601694
20. Bhat S, Pawar S, Potphode D, Moon C, Suh J, Kim C, Choi S, Patil D, Kim J, Shin J, Jang H (2019) Substantially enhanced photoelectrochemical performance of $TiO_2$ nanorods/CdS nanocrystals heterojunction photoanode decorated with $MoS_2$ nanosheets. Appl Catal B Environ 259:118102. https://doi.org/10.1016/j.apcatb.2019.118102
21. Kment S, Riboni F, Pausova S, Wang L, Wang L, Han H, Hubicka Z, Krysa J, Schmuki P, Zboril R (2017) Photoanodes based on $TiO_2$ and a-$Fe_2O_3$ for solar water splitting-superior role of 1D nanoarchitectures and of combined heterostructures. Chem Soc Rev 46:3716–3769. https://doi.org/10.1039/C6CS00015K
22. Peng H, Raya J, Richard F, Baaziz W, Ersen O, Ciesielski A, Samori P (2020) Synthesis of robust MOFs@COFs porous hybrid materials via an aza-diels-alder reaction: towards high-performance supercapacitor materials. Angew Chem Int Ed 59:19602–19609. https://doi.org/10.1002/ange.202008408
23. Dhakshinamoorthy A, Li Z, Garcia H (2018) Catalysis and photocatalysis by metal organic frameworks. Chem Soc Rev 47:8134–8172. https://doi.org/10.1039/C8CS00256H
24. Ding Y, Zhang X, Peng J, Zheng D, Zhang X, Song Y, Chen Y, Gao W (2020) Ultra-sensitive electrochemiluminescence platform based on magnetic metal-organic framework for the highly efficient enrichment. Sens Actuators B Chem 324:128700. https://doi.org/10.1016/j.snb.2020.128700
25. Huang G, Li Q, Yin D, Wang L (2017) Hierarchical porous Te@$ZnCo_2O_4$ nanofibers derived from Te@metal-organic frameworks for superior lithium storage capability. Adv Funct Mater 27:1604941. https://doi.org/10.1002/adfm.201604941
26. Guo Y, Tang J, Qian H, Wang Z, Yamauchi Y (2017) One-pot synthesis of zeolitic imidazolate framework 67-derived hollow $Co_3S_4$@$MoS_2$ heterostructures as efficient bifunctional catalysts. Chem Mater 29:5566–5573. https://doi.org/10.1021/acs.chemmater.7b00867
27. Tang R, Zhou S, Li H, Chen R, Zhang L, Yin L (2020) Halogen bonding induced aqueously stable CsPbBr 3@MOFs-derived $C_o3_O4$/N-doped-C heterostructure for high-performance photoelectrochemical water oxidation. Appl Catal B Environ 265:118583. https://doi.org/10.1016/j.apcatb.2019.118583
28. Zhao X, Feng J, Liu J, Lu J, Shi W, Yang G, Wang G, Feng P, Cheng P (2018) Metal-organic framework-derived ZnO/ZnS heteronanostructures for efficient visible-light-driven photocatalytic hydrogen production. Adv Sci 5:1700590. https://doi.org/10.1002/advs.201700590
29. Wang Q, Gao F, Xu B, Cai F, Zhan F, Gao F, Wang Q (2017) ZIF-67 derived amorphous $CoNi_2S_4$ nanocages with nanosheet arrays on the shell for a high-performance asymmetric supercapacitor. Chem Eng J 327:387–396. https://doi.org/10.1016/j.cej.2017.06.124
30. Hu X, Li C, Lou X, Yang Q, Hu B (2017) Hierarchical CuO octahedra inherited from copper metal-organic frameworks: high-rate and high-capacity lithium-ion storage materials stimulated by pseudocapacitance. J Mater Chem A 5:12828–12837. https://doi.org/10.1039/C7TA02953E
31. Zhang Y, Qiu L, Yuan Y, Zhu Y, Jiang X, Xiao J (2014) Magnetic $Fe_3O_4$@C/Cu and $Fe_3O_4$@CuO core-shell composites constructed from MOF-based materials and their photocatalytic properties under visible light. Appl Catal B Environ 144:863–869. https://doi.org/10.1016/j.apcatb.2013.08.019
32. Zhang X, Peng J, Ding Y, Zheng D, Lin Y, Chen Y, Gao W (2020) Rationally designed hierarchical hollow ZnCdS@$MoS_2$ heterostructured cages with efficient separation of photogenerated carriers for photoelectrochemical aptasensing of lincomycin. Sens Actuators B Chem 306:127552. https://doi.org/10.1016/j.snb.2019.127552
33. Xu R, Gu Y, Ploehn H, Gearheart L, Raker K, Scrivens W (2004) Electrophoretic analysis and purification of fluorescent single-walled carbon nanotube fragments. J Am Chem Soc 126:12736–12737. https://doi.org/10.1021/ja040082h
34. Lv W, Wang X, Wu J, Li H, Li F (2019) pH and $H_2O_2$ dual-responsive carbon dots for biocatalytic transformation monitoring. Chin Chem Lett 30:1635–1638. https://doi.org/10.1016/j.cclet.2019.06.029
35. Vazquez-Gonzalez M, Liao W, Cazelles R, Wang S, Yu X, Gutkin V, Willner I (2017) Mimicking horseradish peroxidase functions using $Cu^{2+}$-modified carbon nitride nanoparticles or $Cu^{2+}$-modified carbon dots as heterogeneous Catalysts. ACS Nano 11:3247–3253. https://doi.org/10.1021/acsnano.7b00352
36. Liu C, Lu D, You X, Shi G, Deng J, Zhou T (2020) Carbon dots sensitized lanthanide infinite coordination polymer nanoparticles: towards ratiometric fluorescent sensing of cerebrospinal Abeta monomer as a biomarker for Alzheimer's disease. Anal Chim Acta 1105:147–154. https://doi.org/10.1016/j.aca.2020.01.021
37. Nekoueian K, Amiri M, Sillanpää M, Marken F, Boukherroub R, Szunerits S (2019) Carbon-based quantum particles: an electroanalytical and biomedical perspective. Chem Soc Rev 48:4281–4316. https://doi.org/10.1039/C8CS00445E
38. Zhang G, Ji Q, Wu Z, Wang G, Liu H, Qu J, Li J (2018) Facile "spot-heating" synthesis of carbon dots/carbon nitride for solar hydrogen evolution synchronously with contaminant decomposition. Adv Funct Mater 28:1706462. https://doi.org/10.1002/adfm.201706462
39. Shi R, Li Z, Yu H, Shang L, Zhou C, Waterhouse G, Wu L, Zhang T (2017) Effect of nitrogen doping level on the performance of N-doped carbon quantum dot/$TiO_2$ composites for photocatalytic hydrogen evolution. Chemsuschem 10:4650–4656. https://doi.org/10.1002/cssc.201700943

40. Cheng W, Zheng Z, Yang J, Chen M, Yao Q, Chen Y, Gao W (2019) The visible light-driven and self-powered photoelectrochemical biosensor for organophosphate pesticides detection based on nitrogen doped carbon quantum dots for the signal amplification. Electrochim Acta 296:627–636. https://doi.org/10.1016/j.electacta.2018.11.086
41. Wang X, Wang Q, Wang Q, Gao F, Gao F, Yang Y, Guo H (2014) Highly dispersible and stable copper terephthalate metal-organic framework-graphene oxide nanocomposite for an electrochemical sensing application. ACS Appl Mater Interfaces 6:11573–11580. https://doi.org/10.1021/am5019918
42. Li Z, Yu H, Bian T, Zhao Y, Zhou C, Shang L, Liu Y, Wu LZ, Tung CH, Zhang T (2015) Highly luminescent nitrogen-doped carbon quantum dots as effective fluorescent probes for mercuric and iodide ions. J Mater Chem C 3:1922–1928. https://doi.org/10.1039/C4TC02756F
43. Carson CG, Hardcastle K, Schwartz J, Liu X, Hoffmann C, Gerhardt RA, Tannenbaum R (2009) Synthesis and structure characterization of copper terephthalate metal-organic frameworks. Eur J Inorg Chem 2009:2338–2343. https://doi.org/10.1002/ejic.200801224
44. Dong S, Li C, Ge X, Li Z, Miao X, Yin L (2017) ZnS-$Sb_2S_3$@C core-double shell polyhedron structure derived from metal-organic framework as anodes for high performance sodium ion batteries. ACS Nano 11:6474–6482. https://doi.org/10.1021/acsnano.7b03321
45. Huang Q, Lin X, Zhu J, Tong Q (2017) Pd-Au@carbon dots nanocomposite: Facile synthesis and application as an ultrasensitive electrochemical biosensor for determination of colitoxin DNA in human serum. Biosens Bioelectron 94:507–512. https://doi.org/10.1016/j.bios.2017.03.048
46. Cots A, Bonete P, Gomez R (2018) Improving the stability and efficiency of CuO photocathodes for solar hydrogen production through modification with Iron. ACS Appl Mater Interfaces 10:26348–26356. https://doi.org/10.1021/acsami.8b09892
47. Jeong K, Deshmukh PR, Park J, Sohn Y, Shin WG (2018) ZnO-$TiO_2$ core–shell nanowires: a sustainable photoanode for enhanced photoelectrochemical water splitting, ACS Sustainable Chem. Eng 6:6518–6526. https://doi.org/10.1021/acssuschemeng.8b00324
48. Kwiatkowski M, Bezverkhyy I, Skompska M (2015) ZnO nanorods covered with $TiO_2$ layer: simple sol-gel preparation, optical, photocatalytic and photoelectrochemical properties. J Mater Chem A 3:12748–12760. https://doi.org/10.1039/C5TA01087J
49. Han H, Karlicky F, Pitchaimuthu S, Shin S, Chen A (2019) Highly ordered N-doped carbon dots photosensitizer on Metal-Organic Framework-decorated ZnO nanotubes for improved photoelectrochemical water splitting. Small 15:1902771. https://doi.org/10.1002/smll.201902771
50. Jiang C, Moniz S, Wang A, Zhang T, Tang J (2017) Photoelectrochemical devices for solar water splitting-materials and challenges. Chem Soc Rev 46:4645–4660. https://doi.org/10.1039/c6cs00306k
51. Zhang X, Zhang R, Yang A, Qin Wang Q, Kong R, Qu F (2017) Aptamer based photoelectrochemical determination of tetracycline using a spindle-like ZnO-CdS@Au nanocomposite. Mikrochim Acta 184(11):4367–4374. https://doi.org/10.1007/s00604-017-2477-8
52. Zhuge W, Li X, Feng S, S, (2020) Visible-light photoelectrochemical sensor for glutathione based on $CoFe_2O_4$-nanosphere-sensitized copper tetraaminophthalocyanine–graphene oxide. Microchem J 155:104726–104732. https://doi.org/10.1016/j.microc.2020.104726
53. Kamimura J, Bogdanoff P, Ramsteiner M, Corfdir P, Feix F, Geelhaar L, Riechert H (2017) P-type doping of GaN nanowires characterized by photoelectrochemical measurements. Nano Lett 17:1529–1537. https://doi.org/10.1021/acs.nanolett.6b04560

Analytica Chimica Acta 1212 (2022) 339913

Contents lists available at ScienceDirect

Analytica Chimica Acta

journal homepage: www.elsevier.com/locate/aca

# *In-situ* preparation of hollow $CdCoS_2$ heterojunction with enhanced photocurrent response for highly photoelectrochemical sensing of organophosphorus pesticides

Delun Zheng [a,b,1], Min Chen [c,1], Yaowen Chen [d], Wenhua Gao [a,d,*]

[a] Department of Chemistry and Laboratory for Preparation and Application of Ordered Structural Materials of Guangdong Province, Shantou University, Shantou, Guangdong, 515063, PR China
[b] Department of Natural Sciences, Shantou Polytechnic, Shantou, Guangdong, 515078, PR China
[c] Shantou Inspection and Testing Center, Shantou, Guangdong, 515041, PR China
[d] Analysis & Testing Center, Shantou University, Shantou, Guangdong, 515063, PR China

## HIGHLIGHTS

- The porous and hollow $CdCoS_2(2)$ microsphere could improve the visible-light absorption ability, which led to vastly promoting the PEC response.
- The thin-wall $CdCoS_2(2)$ particles had a large surface area and could provide abundant photoactive sites for the surface-related redox reactions.
- $CdCoS_2(2)$ formed the type heterojunction architecture that could generate more charge carriers, increasing the photoelectric conversion efficiency.
- The conductivity of Ag nanoparticles was combined with $CdCoS_2(2)$, and obtained $CdCoS_2(2)$@Ag composite displayed the marked photocurrent output due to the synergistic photoelectric effect.
- This MOF-based biosensor was successfully applied for the OPs (chlorpyrifos) detection and also had potential application in actual sample analysis.

## GRAPHICAL ABSTRACT

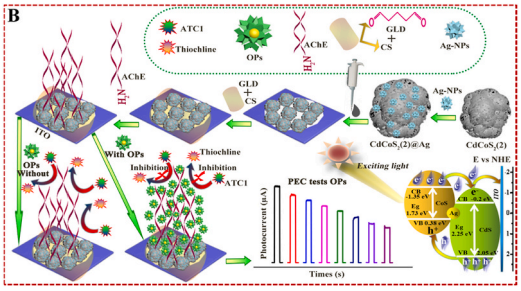


## ARTICLE INFO

*Keywords:*
Photoelectrochemical biosensor
Heterostructure
PEC response

## ABSTRACT

In this study, a porous hollow $CdCoS_2(2)$ microsphere was synthesized based on the ZIF-67-S MOFs derived method of sulfurization reaction and calcination process. Under visible light irradiation, the resulting $CdCoS_2(2)$ composite showed a markedly enhanced photoelectrochemical (PEC) response. The photocurrent value of the

* Corresponding author. Department of Chemistry and Laboratory for Preparation and Application of Ordered Structural Materials of Guangdong Province, Shantou University, Shantou, Guangdong, 515063, PR China.
*E-mail address:* whgao@stu.edu.cn (W. Gao).
[1] Both the authors contributed to the paper equally.

https://doi.org/10.1016/j.aca.2022.339913
Received 14 February 2022; Received in revised form 30 April 2022; Accepted 4 May 2022
Available online 10 May 2022

$CdCoS_2$(2) composite
Organophosphate pesticides detection

$CdCoS_2$(2) modified ITO electrode was 93-fold and 41-fold than that of CoS and CdS materials, respectively. Promoting the photo-absorption ability by internal multilight scattering/reflection was due to the porous and hollow nature of $CdCoS_2$(2). Furthermore, obtained $CdCoS_2$(2) heterostructure *in-situ* with a close contact interface could facilitate the separation/migration of photo-induced carriers. The $CdCoS_2$(2) was also mixed with Ag nanoparticles (NPs) to further improve the PEC response. Acetylcholinesterase (AChE) as a bio-recognition molecule was immobilized on the glutaraldehyde-chitosan (GLD-CS) modified $CdCoS_2$(2)@Ag electrode surface by cross-linking effect. AChE could hydrolyze the acetylcholine chloride (ATCl) to produce an electron donor of thiocholine which led to the elevated photocurrent output. When the bioactivity of AChE was inhibited by the organophosphate pesticides (chlorpyrifos as substrate), the reduced production of thiocholine resulted in a decline in photocurrent. Under optimal conditions, the structured AChE/GLD-CS/$CdCoS_2$(2)@Ag/ITO sensing platform was successfully achieved for chlorpyrifos detection. The wide linear response range was from 0.001 to 270 μg $mL^{-1}$ and with a low detection limit of 0.57 ng $mL^{-1}$. The proposed PEC biosensor also exhibited excellent selectivity and good stability, demonstrating the designed porous hollow $CdCoS_2$(2)@Ag heterostructured composite promised to be a great application in the PEC sensors.

## 1. Introduction

Organophosphate pesticides (OPs), as control and effective insecticides, have been widely utilized to improve crop production all over the world [1]. However, using OPs in excessive doses is risky since it can pollute drinking water and cause a variety of food safety issues [2]. Furthermore, OPs can inhibit the activity of acetylcholinesterase (AChE), which results in a disturbance of the normal nervous system. Thus, the OPs residues in agricultural products are harmful to humans or other mammals, and it is of great importance to measure OPs with sensitive, accurate, and rapid techniques.

Various analytical methods such as gas/liquid chromatography mass-spectrometry [3], fluorescence [4], electrochemiluminescences (ECL) [5], and photoelectrochemistry (PEC) [6] have been applied to monitor the OPs residues. Among these techniques, the PEC method has gained greater scientific attention due to its low background, ultra-sensitivity, and easy operation [7,8]. The photoactive materials play a very important role in improving the sensitivity of PEC biosensors.

Hitherto, numerous photoactive materials including the metal oxides (ZnO [9] and $TiO_2$ [10]), metal chalcogenides (CdS [11] and CoS [12]), organics [13], Metal-organic frameworks (MOFs) [14], etc have been developed for PEC sensors. Among them, the semiconductor material type of CdS has an excellent light-harvesting ability with a narrow band gap in the range of about 1.4–1.7 eV [15]. Nevertheless, the serious photo-corrosion effect of CdS results in fast recombination of photo-induced carrier charges, thus the CdS stability remains unsatisfactory [16]. Thus, these inherent defects on CdS are not conducive to the fabrication of a PEC biosensor with visible-light driving.

Coupling CdS with other photoactive materials to form a heterogeneous composite can be an effective way to improve the photoelectric property of CdS. Because heterostructured materials can combine the advantages of different components, they can generate a band gap that is more appropriate for suppressing electron/hole pair recombination. Vamvasakis et al. [17] successfully prepared a β-$Ni(OH)_2$ modified CdS nano-heterojunction and compared it with the single component of CdS, β-$Ni(OH)_2$/CdS heterojunction that showed highly photocatalysis activity and stability for $H_2$ evolution. Wang et al. [18] structured a hierarchical photoanode of CdS/CdSe heterojunction displaying an enhanced photocurrent density under visible light irradiation, which was 3.83 times higher than that of CdS nanorods (NRs).

As newly emerged functional materials, MOFs have unique merits such as the specific surface area, high porosity, and controllable morphology. But the design and preparation of innovative MOFs with enhanced photo-activity is still necessary. Under specific conditions, MOFs precursor can be revised as tailored structures such as the hierarchical morphology, hollow, thin-wall, and multi-shelled cages [19–21], and the gained MOF-derivatives also well retain the corresponding structural features of their precursors. MOF-derivants with hollow structures in photoelectrochemistry possess several kinds of compelling properties. Firstly, hollow scaffolds can facilitate the light-harvesting by multiple reflection/scattering effects inside the cavity, resulting in more photo-generated charge carriers [22,23]. Secondly, thin-shelled configuration on hollow architectures reduces the diffusion length of charges and thus weakens the recombination of $e^-/h^+$ pairs [24,25]. Finally, the large surface area of hollow particles can provide plentiful reactive sites to accelerate surface-related reactions [26,27].

Previously [28] we have synthesized the hollow nanocage of $ZnIn_2S_4$ (ZIS-HNCs) based on MOFs derivatization. Compared with the irregular morphologies of $ZnIn_2S_4$ nano-flower, ZIS-HNCs exhibited reinforced visible-light capturing and PEC properties. We [29] previously prepared MOF-derived hollow C@ZnCdS polyhedral material for fabricating a PEC sensing platform which showed a high sensitivity for CEA detection due to the excellent hollow structure of C@ZnCdS. Lou et al. [23] constructed hierarchical hollow Co/$ZnIn_2S_4$ composites (Co/ZIS) which started with ZIF-8 as a precursor, and the Co/ZIS photo-catalyst had high efficiency for $H_2$ evolution.

Inspired by the above pioneering works, herein, a porous hollow $CdCoS_2$(2) microsphere with a heterojunction was controllably designed and prepared. The ZIF-67-S material was first synthesized via a simple solution reaction, then acting as a precursor template, which was performed by the *in-situ* sulfidation reaction with cadmium source to obtain the $CdCoS_2$(1) derivants. After a thermal treatment for $CdCoS_2$(1), the photoactive $CdCoS_2$(2) was achieved. As expected, under illumination, the $CdCoS_2$(2) modified ITO electrode exhibited a greatly enhanced photocurrent response (3.72 μA), which was 13.7-fold, 93-fold, and 41-fold than that of $CdCoS_2$(1), CoS, and CdS modified electrodes, respectively. This outstanding PEC property could be ascribed to porous hollow $CdCoS_2$(2) which promoted the visible-light harvesting capacity. Meanwhile, the CdS and CoS components with well-matched energy band-formed heterojunction architecture could make more efficient separation of charges, resulting in improved photon-to-electron conversion efficiency. Afterward, compositing $CdCoS_2$(2) with the conductivity Ag-NPs could further increase the photocurrent response signal.

The $CdCoS_2$(2)@Ag/ITO electrode was modified with glutaraldehyde-chitosan (GLD-CS), and AChE was covalently immobilized on the modified electrode surface by the cross-linking reaction. When the acetylcholine chloride (ATCl) was introduced, the fabricated AChE/GLD-CS/$CdCoS_2$(2)@Ag/ITO sensing platform displayed enhanced photocurrent due to the AChE could catalyze ATCl to generate photoactive thiocholine which could serve as an electron donor to strengthen the separation efficiency of photo-induced $e^-/h^+$ pairs. When the chlorpyrifos was present, the photocurrent intensity decreased obviously because the chlorpyrifos could suppress the activity of AChE. Based on the relationship of the inhibition effect between chlorpyrifos and photocurrent responses, this visible-light-driven PEC biosensor was successfully applied for the chlorpyrifos detection and had a wider linear range (0.001–270 μg $mL^{-1}$) with a low LOD value (0.57 ng $mL^{-1}$).

## 2. Experimental section

### 2.1. Material, reagents, and apparatus have been reported on supporting information

#### 2.1.1. Preparation of ZIF-67-S, $CdCoS_2$(1), $CdCoS_2$(2), and Ag-NPs

The ZIF-67-S microspheres were synthesized following the previously reported method with a minor modification [30]. Typically, a 0.291 g (1 mmol) $Co(NO_3)_2$ $6H_2O$ and 0.328 g (4 mmol) 2-methylimidazole were separately dissolved in 40 mL methanol, and the solutions were mixed quickly under stirring. The obtained mixture was added to 4 mmol CTAB (Hexadecyl trimethyl ammonium bromide) (1.45 g CTAB dissolved in 180 mL DDW) and subsequently stirred for 3 h to obtain a homogeneous solution. Finally, the suspension was washed with ethanol and DDW via centrifugation. The violet product of ZIF-67-S was successfully prepared after further drying at 60 °C under a vacuum for 10 h.

$CdCoS_2$(2) was synthesized via a simple reflux reaction using the ZIF-67-S as a sacrificial template. Briefly, 40 mg of as-prepared ZIF-67-S and 200 mg of $CdC1_2$ were dissolved in 35 mL methanol with ultrasonication dispersion for 15 min. Afterward, 180 mg of thioacetamide (TAA) was added to the above dispersion solution. The obtained mixture was transferred into a three-flask and refluxed at 90 °C for 1 h under stirring. After cooling down to ambient temperature, the precipitate was collected and washed with ethanol three times followed by overnight drying at 60 °C overnight, thus giving a green-yellow sample of $CdCoS_2$(1). The obtained $CdCoS_2$(1) was further subjected to a calcination strategy at 550 °C for 3 h to get the dark-gray product of $CdCoS_2$(2). For comparison, the CoS and CdS were synthesized through the above same method except removing the procedure of adding $CdC1_2$ and ZIF-67-S, respectively.

Ag-NPs were prepared by a simple process as follows: 0.073 g (0.25 mmol) of sodium citrate was dissolved in 25 mL and followed by adding 0.33 g (2 mmol) of $AgNO_3$ and stirring for 15 min at room temperature. Then, the mixture was heated at 90 °C for 3 h to gain the purple-black product of Ag-NPs. After that, 15 μL of $CdCoS_2$(2) (1.5 mg $mL^{-1}$) was mixed with 15 μL above Ag-NPs (1.5 mg $mL^{-1}$) to form the $CdCoS_2$(2) @Ag composite.

### 2.2. Fabrication of the modified electrodes

Before the modification, ITO electrodes were sequentially washed with acetone, 1 M NaOH/ethanol mixture (1:1, v/v), and DDW under successive ultrasonication (each time for 15 min). Then, the cleaned ITO electrodes were dried at 60 °C.

Initially, 12 μL uniformly dispersed $CdCoS_2$(2)@Ag solution was dropped onto the bare ITO substrate. The obtained $CdCoS_2$(2)@Ag)/ITO electrode was covered with 9 μL of 5% GLD/0.07% CS (1:1, v/v), after drying at room temperature, the modified electrode (GLD-CS/$CdCoS_2$(2) @Ag)/ITO) was carefully rinsed with DDW several times. Afterward, 9 μL AChE solutions (125 U $mL^{-1}$) were added onto GLD-CS/$CdCoS_2$(2) @Ag/ITO electrode surface and kept at 4 °C for 12 h to gain the AChE/GLD-CS/$CdCoS_2$(2)@Ag composite modified ITO electrode through a coupling reaction between the AChE and GLD. After rinsing with 0.1 M PBS (pH 7.4) to remove the physical adsorption of AChE, the sensor electrode of AChE/GLD-CS/$CdCoS_2$(2)@Ag/ITO was successfully prepared. For comparison, the other modified electrodes were fabricated in the same manner.

### 2.3. Detection of real samples

A total of 10 mL of the river water sample was centrifuged for 8 min (10,000 r/min), then the obtained supernatant was diluted with 0.1 M PBS (pH 7.4) to 45 mL.

Similarly, for the preparation of the cabbage sample, 5 mL of the acetonitrile was added to 5 g cabbage and shocked for 30 min. After centrifuging for 8 min (10,000 r/min), the supernatant was diluted into 45 mL with 0.1 M PBS (pH 7.4). Subsequently, the known chlorpyrifos concentrations were respectively added to prepared samples for recovery monitor.

### 2.4. PEC and electrochemical measurements

The sensor electrode was immersed several times in different concentrations of chlorpyrifos for 8 min. Then, the PEC and DPV measurements were carried out in 0.1 M PBS (pH 7.4) containing 0.8 mM ATCl. The excitation source of the xenon lamp was 420 nm with the intensity of 20 mW $cm^{-2}$ and switched on every 10 s under 0.0 V bias voltages. EIS was conducted at a potential of +0.172 V with its frequency range from $1.0 \times 10^4$ Hz–0.01 Hz. The DPVs were conducted at a pulse period of 0.2 s with an amplitude of 0.05 V.

## 3. Results and discussion

### 3.1. Morphological and structural features of synthesized materials

The surface morphologies of prepared samples were investigated by scanning electron microscopy (SEM). It was observed in Fig. 1A, that the synthesized ZIF-67-S particles were microsphere structure and uniformly distributed. Fig. 1B shows that the $CdCoS_2$(1) also well-remained the spherical shape of ZIF-67-S, and the particles diameter range was from 450 to 800 nm. But the roughness of $CdCoS_2$(1) displayed a slight reduction as-compared with its precursor through a sulfurization effect (Figs. S1A and B). Fig. 1C illustrated the SEM morphologies of the $CdCoS_2$(2) particle. It was found that the particle size of $CdCoS_2$(2) had increased to about 1000 nm, and there were some mesoporous/macropores on the $CdCoS_2$(2) surface with a width from 40 to 180 nm.

The microstructures of $CdCoS_2$(2) were also characterized by the high-resolution transmission electron microscope (HRTEM) images. As seen, the relatively bright regions of $CdCoS_2$(2) (Fig. 1D) proved that the hollow structure had a thin shell compared to the solid $CdCoS_2$(1) microsphere (Fig. 1G). The magnified TEM image of single-$CdCoS_2$(2) (Fig. 1E ~ F) revealed that the interplanar spacings of 0.34, 0.21, and 0.18 nm corresponding to the (111), (220), and (311) planes of CdS NPs respectively (Fig. S1G ~ H), indicated that the CdS had the polycrystalline structure [31]. While no obvious lattice fringe of the amorphous CoS could be found. This result was agreed with the SAED pattern (Fig. 1H and Fig. S1I). Besides, the component elements of Co, Cd, and S of $CdCoS_2$(2) could be identified in Fig. 1I, which were well consistent with the component elements of $CdCoS_2$(1) (Fig. S1C). This EDS mapping manifested the successful formation of the $CdCoS_2$(2) composite.

The nitrogen adsorption-desorption technique was also applied to determine the BET surface area and pore-structure of as-prepared samples. As seen in Fig. S2A, the shape of the nitrogen adsorption-desorption isotherms displayed that $CdCoS_2$(2) had some type of hysteresis loops, indicating the presence of mesoporous structure in this composite [32], and the calculated BET surface area of $CdCoS_2$(2) was 1022.4 $m^2$ g. The pore size distribution of $CdCoS_2$(2) was further explored by the Barret-Joyner-Halenda (BJH) model based on the desorption branch. As shown in Figs. S2B and a sharp peak centered at 50.6 nm appeared in the pore size distribution plot, which agreed with the mesopore characteristic as revealed in the SEM image (Fig. 1C).

### 3.2. Characterization of the prepared materials

The phase structures of the prepared samples were investigated by an X-ray diffractometer (XRD). As shown in Fig. 2A, all the characteristic peaks of ZIF-67-S were consistent with pure ZIF-67, and the amorphous feature of the CoS crystal was well-matched as previously reported [12]. In Fig. 2B, the typical peaks located at 24.8°, 26.5°, 28.2°, 43.7°,47.9°, and 52.0° were indexed to the (100), (002), (101), (110), (103) and (112) planes of CdS (JCPDS: 77–2306), respectively. And all of those characteristic diffraction peaks were also clearly presented in

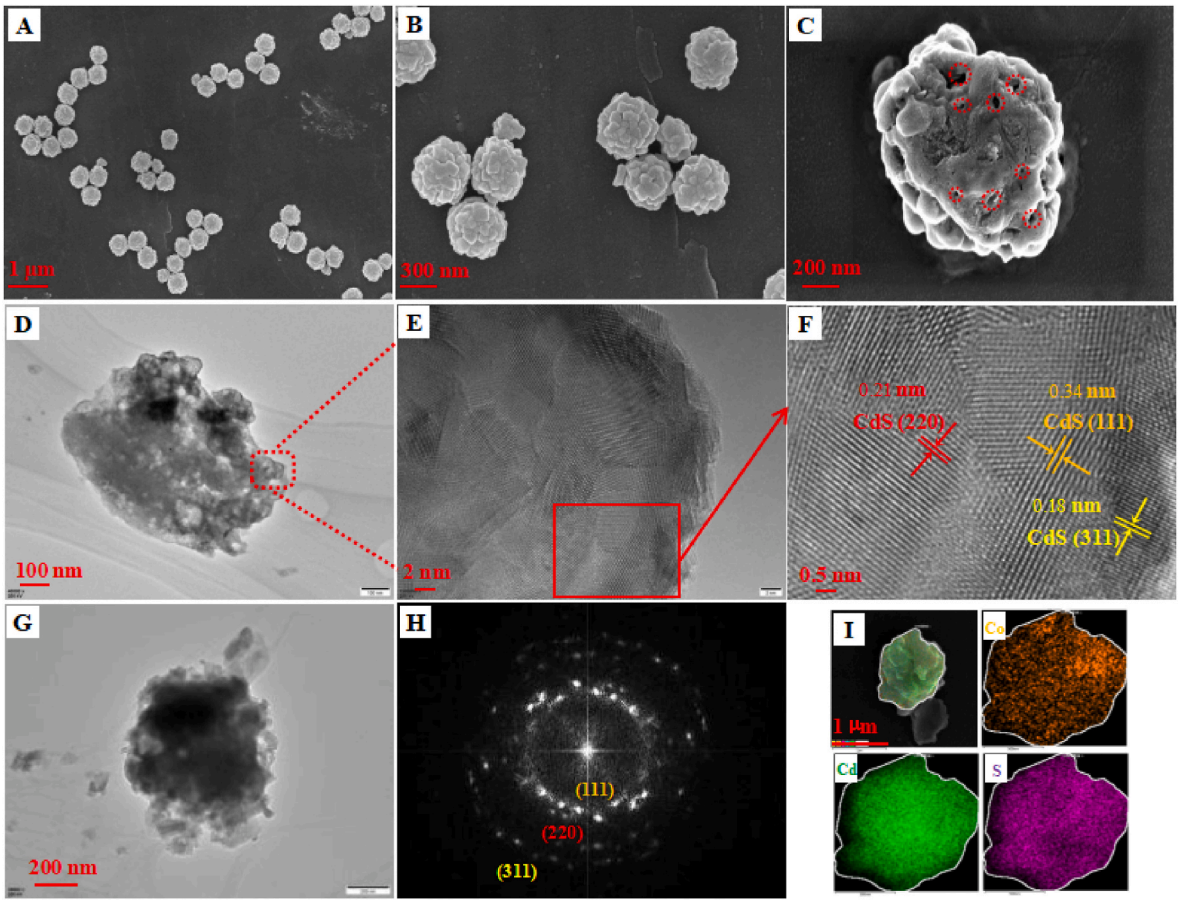


**Fig. 1.** SEM images of (A) ZIF-67-S, (B) $CdCoS_2$(1) and (C) $CdCoS_2$(2); TEM images of (D) $CdCoS_2$(2) and (G) $CdCoS_2$(1), High-resolution TEM (HRTEM) images of (E ~ F) $CdCoS_2$(2); SAED pattern of (H) $CdCoS_2$(2); Elemental mapping images of (I) Co, Cd, and S elementals of $CdCoS_2$(2).

$CdCoS_2$(1), $CdCoS_2$(2), and $CdCoS_2$(2)@Ag. This result also demonstrated the co-existence of CoS and CdS in the above composites. Furthermore, the characteristic peaks at 38.7° and 44.1° were ascribed to the (111) and (200) lattice diffractions of Ag-NPs [33], which revealed the formation of $CdCoS_2$(2)@Ag composite.

The optical properties of prepared materials were investigated by UV–vis diffuse reflectance spectroscopy (DRS). As illustrated in Fig. 2C, ZIF-67-S only had the photo-absorption property in the UV-light region. Compared with the ZIF-67-S, $CdCoS_2$(1) and $CdCoS_2$(2) displayed enhanced visible-light absorption, but the presented photo-absorption intensity of $CdCoS_2$(2) improved than that of $CdCoS_2$(1), which could be explained by the porous hollow $CdCoS_2$(2) particles with multiple scattering/reflection effect. On the $CdCoS_2$(2)@Ag composite, the light-absorption ranged from ≥360 nm and showed increased photo-capturing capability clearly than all the other as-prepared materials. In the insert of Fig. 2C, the whole light-absorption intensity of CdS showed an obvious enhancement compared with the CoS. In Fig. 2D, the UV-light absorption wavelength at about 291 nm was corresponding to the specific spectra of OPs (chlorpyrifos) [34,35].

The surface composition and chemical state of as-synthesized materials were investigated by X-ray photoelectronic spectroscopy (XPS). Fig. 3A showed the XPS results of CdS, CoS, and $CdCoS_2$(2) with their corresponding component elements, respectively. The high-resolution Co 2p core-level spectra of $CdCoS_2$(2) and CoS were shown in Fig. 3B and **C**, respectively. In Fig. 3B**,** both doublet peaks at 794.5 and 779.3 eV were attributable to the Co $2p_{1/2}$ and Co $2p_{3/2}$ of $Co^{3+}$ of $CdCoS_2$(2), while the peaks at 782.1 and 798.2 eV corresponded to the Co $2p_{1/2}$ and Co $2p_{3/2}$ of $Co^{2+}$, respectively. Further, two shakeup-satellite peaks were presented at 802.1 and 785.9 eV, respectively [36]. Fig. 3D displayed the Cd 3d spectra of $CdCoS_2$(2) and CdS, in which two distinct peaks at 412.4 and 405.6 eV of $CdCoS_2$(2) were ascribed to the Cd $3d_{3/2}$ and Cd $3d_{5/2}$ of $Cd^{2+}$ [37], respectively. Fig. 3E showed the S 2p spectra of CoS, CdS, and $CdCoS_2$(2). The peaks at around 161.9 and 163.1 eV were assigned to S $2p_{1/2}$ and S $2p_{3/2}$ of $S^{2-}$ of $CdCoS_2$(2), and a type shakeup-satellite peak of $CdCoS_2$(2) was located around 168.8 eV [38, 39]. Thus, it could be confirmed that cobalt-cadmium sulfide ($CdCoS_2$(2)) includes the $Co^{2+}$, $Co^{3+}$, $Cd^{2+}$, and $S^2$ ions.

To explore the stepwise modification process of the PEC sensor, electrochemical impedance spectroscopy (EIS) measurements were carried out by the redox probe of $[Fe(CN)_6]^{3-/4-}$. As seen in Fig. 3F, the bare ITO electrode had the smallest electron transfer resistance ($R_{et}$) value of 135 Ω (curve a). After the CoS and $CdCoS_2$(1) were assembled onto the bare ITO electrode, the $R_{et}$ values increased to 760 Ω and 450 Ω (curves f and d), respectively. But the $R_{et}$ value of $CdCoS_2$(2) (curve e, 350 Ω) showed an obvious decrease than the CoS/ITO or $CdCoS_2$(1)/ITO electrode, demonstrating that $CdCoS_2$(2) had higher charge transfer kinetics. After Ag-NPs were combined with $CdCoS_2$(2), the $R_{et}$ value of $CdCoS_2$(2)@Ag (curve b) decreased to 215 Ω due to the excellent electronic conductivity of Ag-NPs. When the GLD-CS and AChE were continuously modified on the $CdCoS_2$(2)@Ag/ITO electrode surface, the $R_{et}$ values increased progressively, which could be ascribed to the insulation effect of those assembled materials. The cyclic voltammetry (CV) technique was also used to characterize different modified electrodes (shown in Fig. S4A) and the consequences were consistent with the EIS assay. All the results demonstrated that the sensing platform was manufactured successfully.

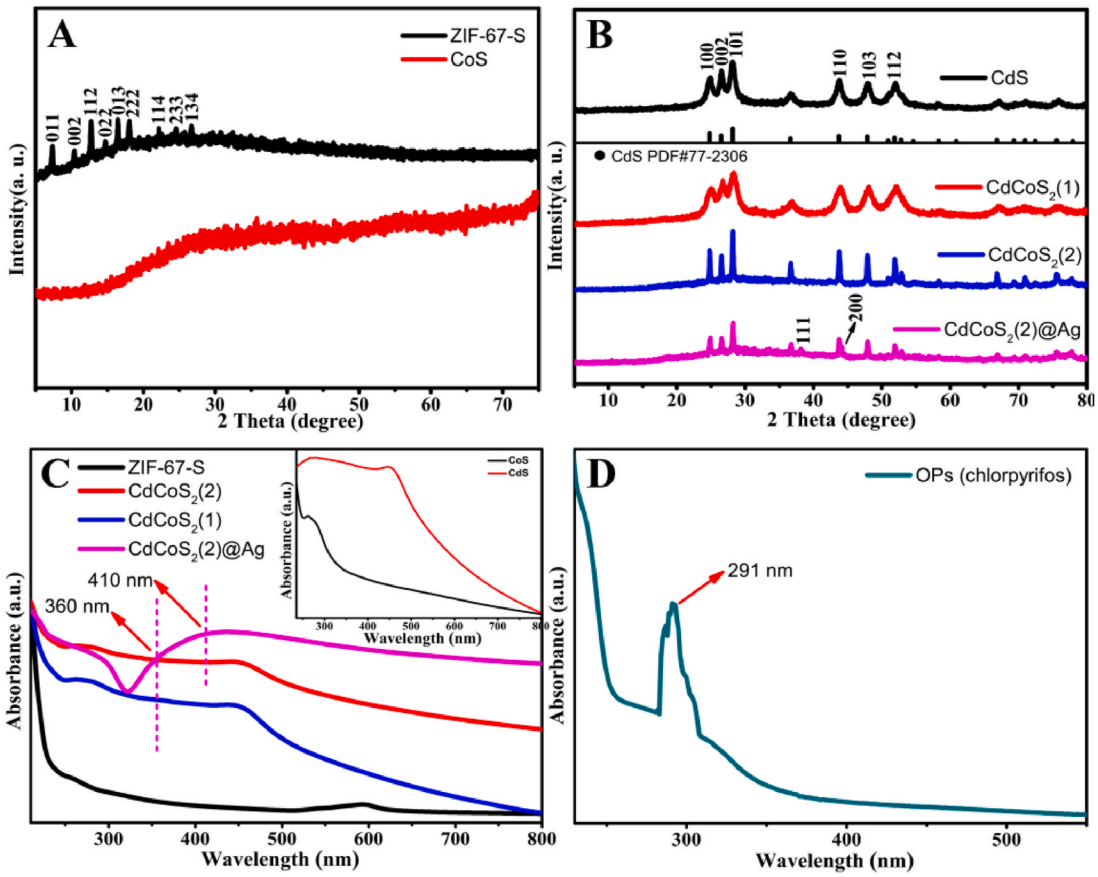


**Fig. 2.** XRD patterns of (A) ZIF-67-S and CoS, (B) CdS, $CdCoS_2$(1), $CdCoS_2$(2) and $CdCoS_2$(1)@Ag; UV–vis spectra of (C) ZIF-67-S, $CdCoS_2$(1), $CdCoS_2$(2) and $CdCoS_2$(1)@Ag, (inset of C) CoS and CdS, and (D) OPs (chlorpyrifos).

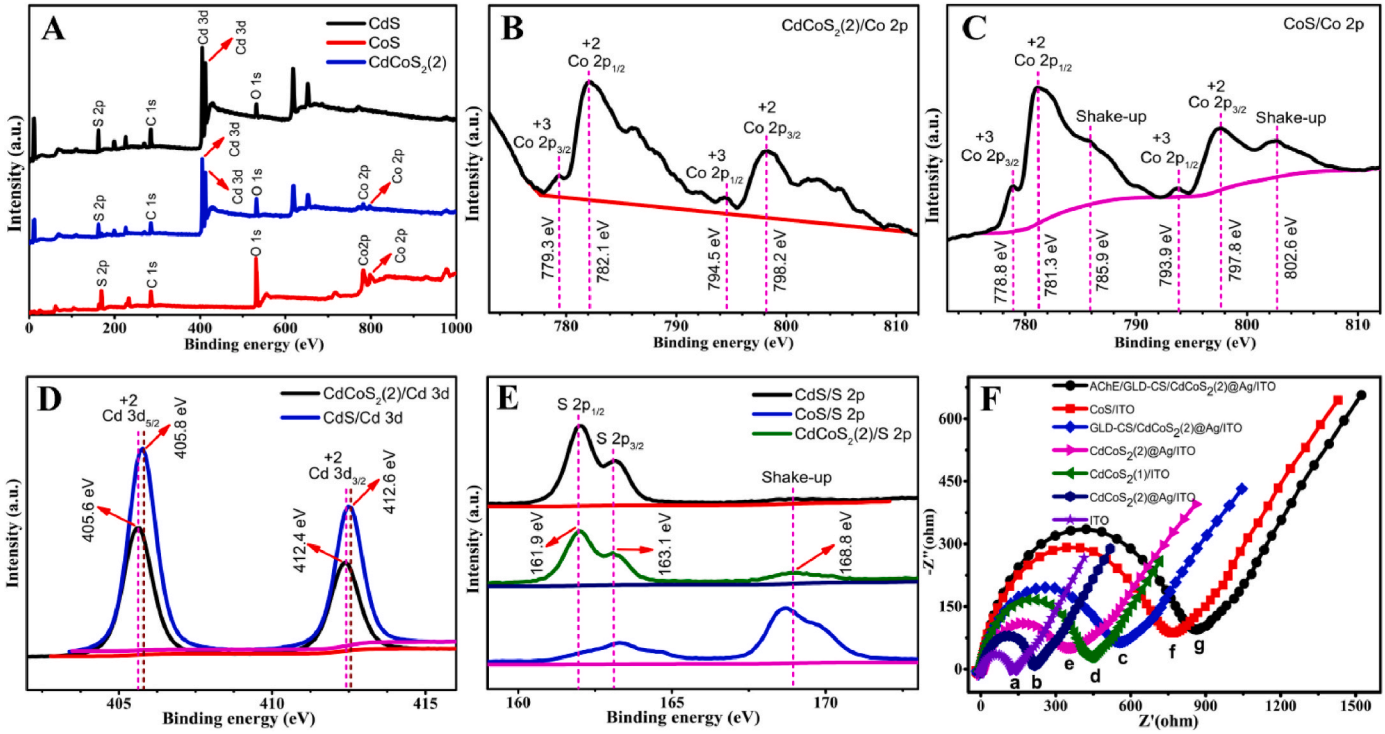


**Fig. 3.** XPS spectra of (A) CdS, CoS, and $CdCoS_2$(2); High-resolution XPS spectra of Co 2p of (B) $CdCoS_2$(2), and (C) CoS, Cd 3d of (D) $CdCoS_2$(2), and CdS, S 2p of (E) CdS, CoS, and $CdCoS_2$(2); EIS of (F) bare ITO (a), $CdCoS_2$(2)@Ag/ITO (b), GLD-CS/$CdCoS_2$(2)@Ag/ITO (c), $CdCoS_2$(1)@Ag/ITO (d), $CdCoS_2$(2)@Ag/ITO (e), CoS/ITO (f), AChE/GLD-CS/$CdCoS_2$(2)@Ag/ITO/ITO (g) in 5 mM $[Fe(CN)_6]^{3-/4-}$ containing 0.1 M KCl.

### 3.3. PEC properties of different electrodes and PEC mechanism

To deeply monitor the stepwise construction process of the PEC sensor, all PEC examination was carried out in the PBS (0.1 M, pH 7.4) solution. As shown in Fig. 4A, no photocurrent was found on the bare ITO electrode (curve a). After the ITO was modified with CoS, CdS, and $CdCoS_2$(1) (curve b, c, and d), obtained photocurrent intensities were corresponding to 0.04, 0.09, and 0.27 μA, respectively, indicating that the $CdCoS_2$(1) could improve the PEC property. However, the photocurrent intensity on the $CdCoS_2$(1)/ITO electrode dramatically increased to 3.72 μA (curve e), which was 93 times and 41 times higher than that of the single-component CoS and CdS modified electrode. The superior photoelectric conversion efficiency of the $CdCoS_2$(2) composite was ascribed to the porous hollow $CdCoS_2$(2) which could promote the light absorption ability. When the Ag-NPs were combined with $CdCoS_2$(2), the photocurrent response of $CdCoS_2$(2)@Ag/ITO electrode (curve f) was increased slightly due to the synergistic effect in this composite. When the GLD-CS and AChE were successively assembled onto $CdCoS_2$(2)@Ag/ITO electrode, owing to the steric hindrance effect of those materials, which led to the gradually decreased photocurrents (curve g and h). Nevertheless, when the ATC1 was introduced into the characterization solution, the photocurrent signal of the $CdCoS_2$(2)@Ag/ITO electrode had increased distinctly (curve i). This could be explained by the catalytic hydrolysis of AChE making ATCl generate thiocholine which also served as the electron donor to strengthen the separation of charge carriers ($e^-/h^+$). The PEC result demonstrated the successful construction of the PEC biosensor.

The linear sweep voltammetry (LSV) assay of as-prepared materials modified electrode was performed in 0.1 M $Na_2SO_4$ with a potential range from 0.0 V to 0.9 V vs. Ag/AgCl. As shown in Fig. 4B, under visible-light irradiation, the LSV response indicated that the bare ITO electrode had no photo-generated current. $CdCoS_2$(1) composite exhibited enhanced LSV intensity compared to mono-component CoS or CdS material with a slightly LSV response. While $CdCoS_2$(2) material displayed a greater LSV response than that of $CdCoS_2$(1), which was attributed to the superior microstructure of the hollow $CdCoS_2$(2). The $CdCoS_2$(2)@Ag composite gained the highest LSV response, suggesting that the synergistic effect could further heighten the photocurrent signal. All the above-gained results of electrochemical and PEC assay verified that the $CdCoS_2$(2)@Ag composite could significantly improve the photoelectric activity.

Fig. 4C showed the open circuit potential (OCP) patterns of bare ITO and prepared materials modified ITO electrodes under dark and visible-light irradiation. There was scarcely an OCP response current on the bare ITO electrode. In the dark, the CoS, CdS, $CdCoS_2$(1), $CdCoS_2$(2), and $CdCoS_2$(2)@Ag materials displayed an upward surface band bending (region I) due to the potential of redox equilibration [40]. Under light irradiation, the OCP on those materials was negatively rapid and reached a steady-state due to the accumulating photo-generated electrons (region II). After the irradiation was removed, the OCP gradually increased again (region III), this could be ascribed to the recombination of photo-induced charge carriers.

The resulting OCP curves also revealed the type n feature of all proposed materials. Simultaneously, the OCP response change (ΔOCP) value of $CdCoS_2$(2) increased more than that of the CoS and CdS. It was attributed to n-n type heterojunctions formed between CoS and CdS which could elevate the property of photon-to-electron transition. Besides, $CdCoS_2$(2)@Ag displayed the greatest ΔOCP than other materials

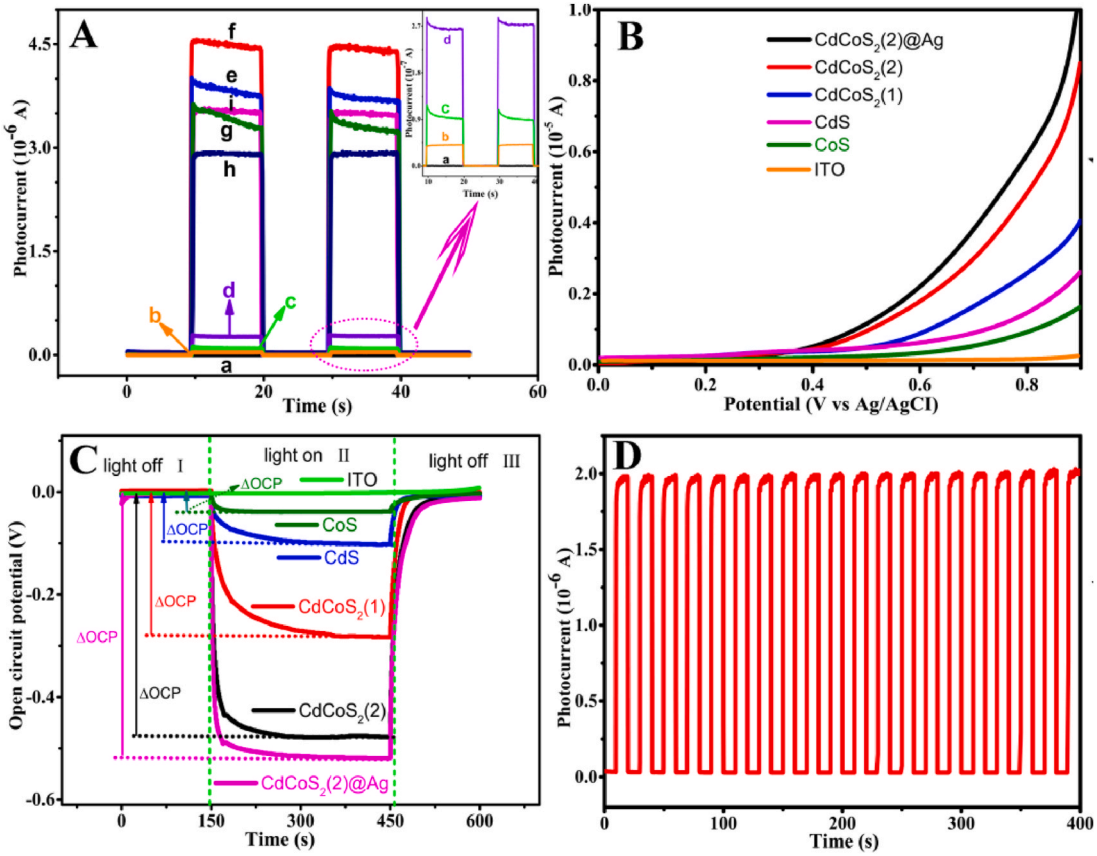


**Fig. 4.** (A) PEC response of bare ITO (a), CoS/ITO (b), CdS/ITO (c), $CdCoS_2$(1)/ITO (d), $CdCoS_2$(2)/ITO (e), $CdCoS_2$(2)@Ag/ITO (f), GLD-CS/$CdCoS_2$(2)@Ag/ITO (g), AChE/GLD-CS/$CdCoS_2$(2)@Ag/ITO (h) in 0.1 M PBS (pH 7.4) and (i) in the presence of 0.8 mM ATCl; (B) LSV patterns in 0.1 M $Na_2SO_4$ with a scan rate of 80 mV $s^{-1}$; (C) OCP curves in 0.1 M PBS (pH 7.4) of bare ITO and modified ITO electrodes; (D) Time–based photocurrent response of AChE/GLD-CS/$CdCoS_2$(2)@Ag/ITO biosensor in the presence of 2.5 μg $mL^{-1}$ chlorpyrifos in 0.1 M PBS (pH 7.4) containing 0.8 mM ATCl with light on and off cycles.

because of the synergistic effect from every component in this composite.

Moreover, according to the empirical equation of $ahv = A\ (hv - Eg)^{1/2}$, the Eg values of CoS and CdS were calculated to be 1.73 and 2.25 eV (Fig. S3C ~ **D**), respectively. And with the VB-XPS pattern, the VB potentials of CoS and CdS were evaluated at about 0.38 and 2.05 eV (Fig. S3E ~ **F**). Besides, based on the formulae of $E_{CB} = E_{VB} - Eg$, the corresponding CB potentials ($E_{CB}$) of CoS and CdS were calculated to be 1.35 and −0.20 eV, respectively.

The above results revealed that the CB and VB potentials of CoS were higher than that of CdS, and a type heterojunction of $CdCoS_2$(2) could be speculated. Under visible light, the photo-generated electron in the CB of CoS was transferred to the CB of CdS, while the hole in the VB of CdS was transferred to the VB of CoS, which resulted in a significantly enhanced photocurrent response. Also, the composited Ag-NPs could be acted as a valid electron acceptor for $CdCoS_2$(2) to further reinforce the photocurrent output. The porous, hollow, and thin-wall microstructure of $CdCoS_2$(2) could provide a specific surface area from its interior cavity, which increased the active site and led to improving the efficiency of light-harvesting. Second, the *in-situ* synthesized heterojunction on $CdCoS_2$(2) with a compact contact interface was beneficial to shorten the transfer distance of the photo-generated charges. Third, the formed staggered band structure among the CoS and CdS could effectively facilitate the $e^-/h^+$ separation and migration. Finally, the synergistic amplifying effect of every component in $CdCoS_2$(2)@Ag composite was indispensability, such as the Ag-NPs could assist to achieve the overall PEC capability. Besides, the acetylcholine chloride (ATCl) could generate thiocholine via a catalytic hydrolysis reaction by AChE. The thiocholine served as an electron donor not only could reinforce the separation of charge carriers but also improves the electrocatalytic activity toward the electrode surface, which led to the enhanced photocurrent and electrochemical response (as shown in Fig. S3). The PEC mechanism of the prepared composite was shown in Scheme 1B.

### 3.4. PEC response of the optimization experiments shown on supporting information

#### 3.4.1. PEC analysis properties of the prepared biosensor

The analytic performance of the proposed PEC biosensor was surveyed in 0.1 M PBS (pH 7.4) containing 0.8 mM ATCl. As illustrated in Fig. 5A, under the optimal experimental conditions, the photocurrent response of the PEC sensor decreased continuously with the concentration of chlorpyrifos from 0.001 to 270 μg mL, and the changed photocurrent related to the logarithmic values of OPs (chlorpyrifos) concentration showed the good linear relationship. The regression equation was $\Delta I_{PEC}$ (μA) = −0.296 + 2.1626 log $C_{OPs}$ (μg $mL^{-1}$) ($R^2$ = 0.9976) with a low LOD of 0.57 ng $mL^{-1}$ (S/N = 3) (Fig. 5B). Compared to the DPV analysis results (the regression equation was $\Delta I_{pc}$ ($1.0 \times 10^{-4}$

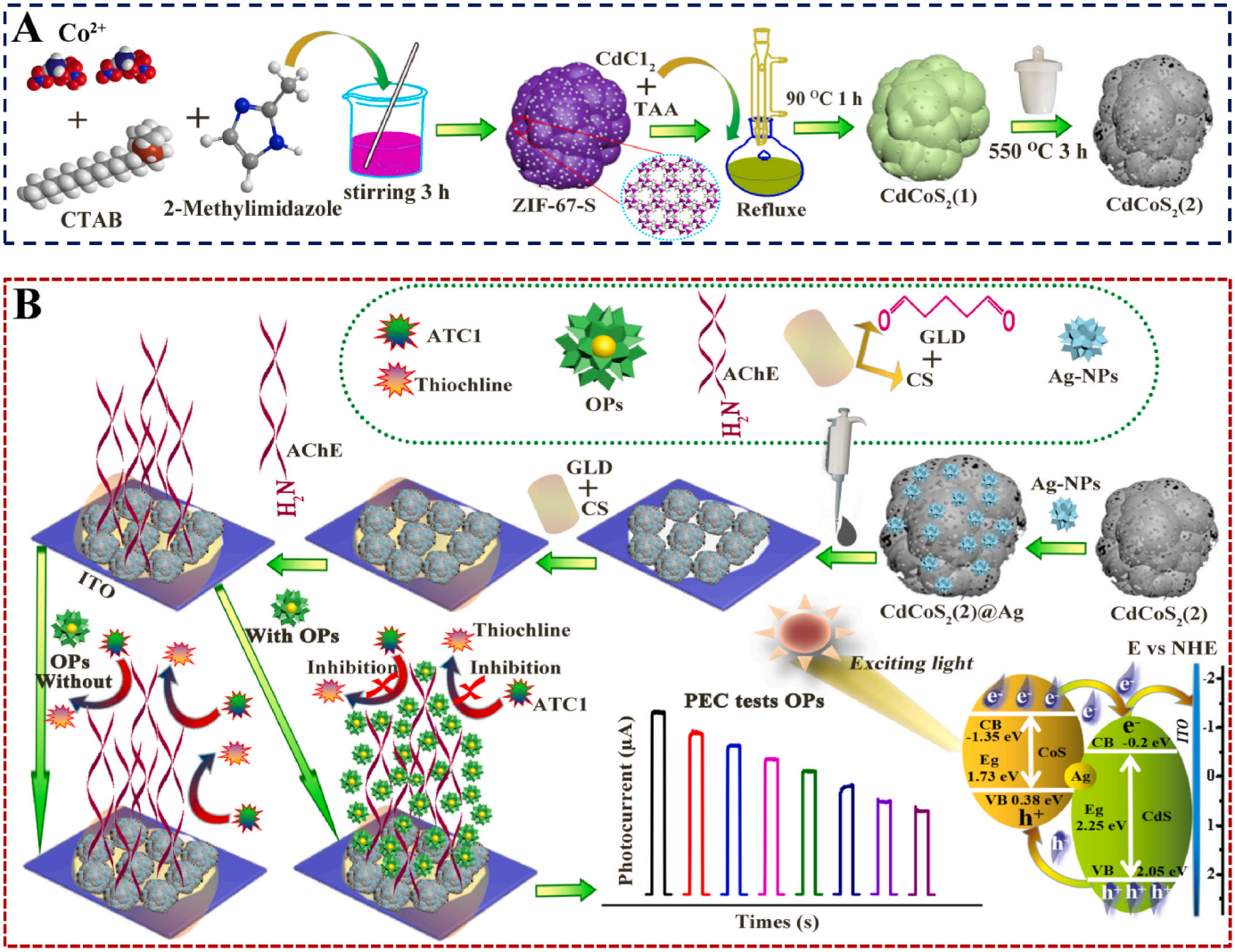


**Scheme 1.** (A) The preparation processes of $CdCoS_2$(2) and (B) schematic illustration of the proposed PEC biosensors for OPs detection.

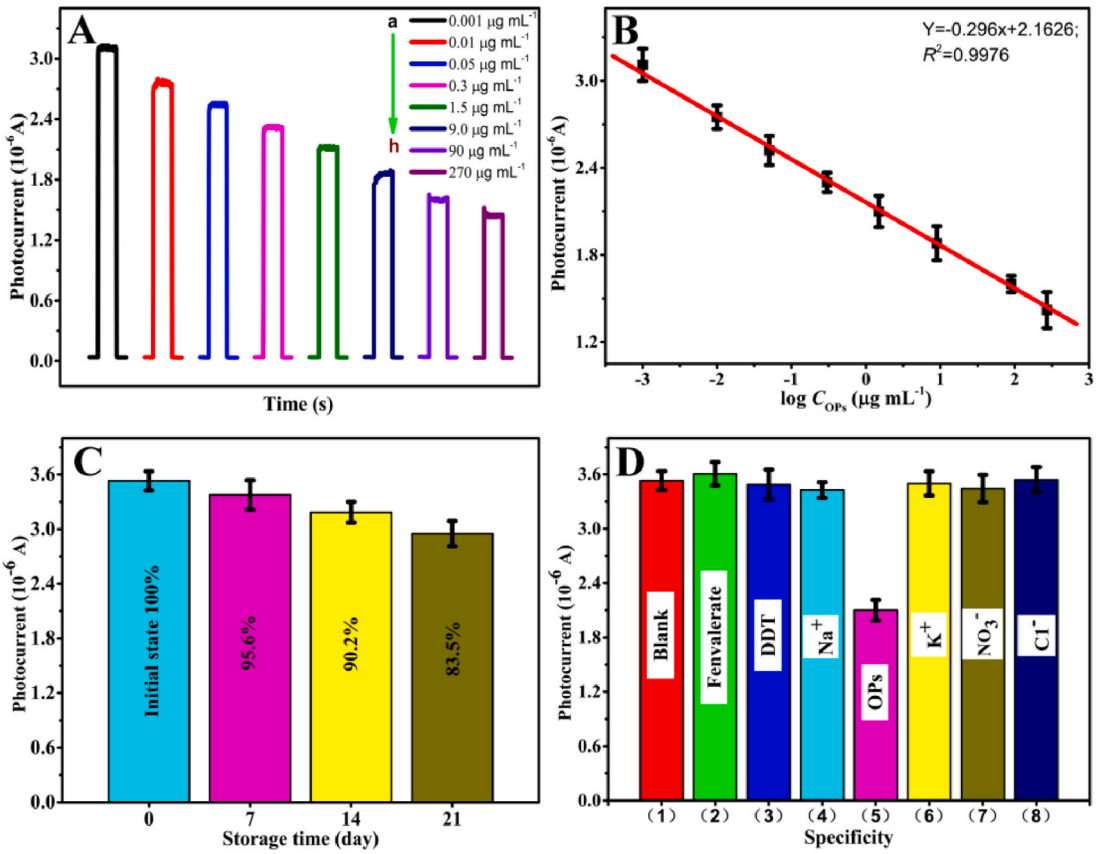


**Fig. 5.** PCE responses of (A) AChE/GLD-CS/$CdCoS_2$(2)@Ag/ITO biosensor in 0.1 M PBS (pH 7.4) containing 0.8 mM ATCl at different concentrations of chlorpyrifos: (a–h) 0.001, 0.01, 0.05, 0.3, 1.5, 9.0, 90, 270 μg $mL^{-1}$; The plot of (B) $\Delta I_{PCE}$ versus the logarithm values of $C_{OPs}$ (log $C_{OPs}$); The photocurrent responses of (C) as-prepared biosensor after different storage time (day) in PBS (0.1 M, pH 7.4) containing 0.8 mM ATCl; (D) Selectivity of the PEC biosensor in PBS (0.1 M, pH 7.4) containing 0.8 mM ATCl in the presence of 1.5 μg $mL^{-1}$ OPs (chlorpyrifos), Fenvalerate, 2,4-Dichlorodiphenyltrichloroethane (DDT) and 150 μg $mL^{-1}$ inorganic ions of $K^+$, $Na^+$, $Cl^-$ and $NO_3^-$.

A) = 1.3451 log $C_{OPs}$ (μg $mL^{-1}$) + 4.038 with a linear range from 0.001 to 7.5 μg $mL^{-1}$ and LOD of 0.84 ng $mL^{-1}$) (Figs. S6A and B) and other reported methods (**Table S**1), this PEC sensing platform exhibited a relatively wider linear range and a lower LOD for chlorpyrifos assay.

### 3.5. Stability, selectivity, and reproducibility of PEC biosensor

Fig. 4D showed the stability of the PEC biosensor. It could be found that no significant photocurrent change on AChE/GLD-CS/$CdCoS_2$(2) @Ag/ITO electrode after the biosensors reaction with 2.5 μg $mL^{-1}$ chlorpyrifos under irradiation cycles for 400 s and ten on/off, demonstrating that the PEC biosensor had excellent long-term stability for chlorpyrifos monitor. Besides, the fabricated PEC biosensor was stored at 4 °C for a week, the photocurrent reduced to 95.6%, and when the storage time was two weeks, the photocurrent declined to 90.2% (Fig. 5C), suggesting that the catalytic activity of AChE on the modified electrode was still well retained.

The selectivity of the PEC biosensor was also investigated (Fig. 5D). The photocurrent intensities on modified electrodes were gained in 0.1 M PBS (pH 7.4) containing 0.8 mM ATCl in the presence of 1.5 μg $mL^{-1}$ chlorpyrifos, fenvalerate, 2,4-dichlorodiphenyltrichloroethane (DDT) and 150 μg $mL^{-1}$ inorganic ion of $K^+$, $Na^+$, $Cl^-$ and $NO_3^-$. No distinct photocurrent changes were observed except in the presence of chlorpyrifos, testifying that the developed PEC biosensor had satisfactory selectivity.

For the reproducibility investigation of the PEC biosensor, three AChE/GLD-CS/$CdCoS_2$(2)@Ag/ITO electrodes were applied to monitor 0.1 μg $mL^{-1}$ chlorpyrifos and obtained relative standard deviation (RSD) of 2.7%. This result indicated the reproducibility of the PEC sensor was also acceptable.

### 3.6. Real samples analysis

The practical application of the PEC sensor was evaluated with a standard additional method according to the procedure mentioned in Section 2.4. The experimental results as summarized in **Table S**2, and the recovery values of the sample solution were from 94.2% to 105.0% with the changed RSD values of 1.74%–3.27%, respectively. Furthermore, the results obtained by the PEC sensor were consistent with the results obtained by GC-MS, which revealed that the proposed PEC biosensor can be utilized for chlorpyrifos detection in real samples.

## 4. Conclusions

In summary, the heterostructured $CdCoS_2$(2) photoactive material was controllably structured via the MOFs derived method. The ZIF-67-S as the sacrificial template was performed by the *in-situ* sulfidation with cadmium source precursors, then calcining the MOF-derivants to gain a porous hollow $CdCoS_2$(2) composite. The PEC assays showed that the $CdCoS_2$(2) modified ITO electrode had greater photocurrent output than the individual component CoS or CdS, revealing the tailored morphologies of $CdCoS_2$(2) could strengthen visible-light harvesting. And the well-matched band structures between CoS and CdS played an important role in elevating the separation efficiency of charges. The high conductivity of Ag-NPs also could further improve the photocurrent intensity of $CdCoS_2$(2)@Ag. Benefiting from the outstanding PEC performance of $CdCoS_2$(2)@Ag, a developed PEC biosensor had been successfully applied for the chlorpyrifos analysis. Compared to the DPV

results, the AChE/GLD-CS/$CdCoS_2$(2)@Ag/ITO modified electrode displayed superior sensitivity (the LOD reached 0.57 ng mL). Thus, this work could provide a novel strategy for developing different photoactive materials from MOF-derived products. In the meanwhile, this PEC biosensor appeared to be a promising tool for detecting organophosphate pesticides (OPs) in the environment or food.

## Compliance with ethical standards

The author(s) declare that they have no competing interests.

## CRediT authorship contribution statement

**Delun Zheng:** Conceptualization, Visualization, Investigation, Methodology, Data curation, Writing – original draft. **Min Chen:** Conceptualization, Investigation, Methodology. **Yaowen Chen:** Writing – review & editing, Supervision. **Wenhua Gao:** Conceptualization, Supervision, Resources, Funding acquisition, Project administration.

## Declaration of competing interest

The authors declare that they have no known competing financial interests or personal relationships that could have appeared to influence the work reported in this paper.

## Acknowledgements

We are grateful for the financial support from Guangdong Basic and Applied Basic Research Foundation (No. 2019A1515010618), the Guangdong Special Funds for the Science & Technology Project (No. 2019ST029 & No. 2019ST089), 2020 Li Ka Shing Foundation Cross-Disciplinary Research Grant (Project Number 2020LKSFG06C) and Shantou Polytechnic Supported Project (No. 2019SZK2019Y01).

## Appendix A. Supplementary data

Supplementary data to this article can be found online at https://doi.org/10.1016/j.aca.2022.339913.

## References

[1] A. Kumaravel, M. Chandrasekaran, Electrochemical determination of chlorpyrifos on a nano-$TiO_2$ cellulose acetate composite modified glassy carbon electrode, J. Agric. Food Chem. 63 (2015) 6150–6156.
[2] Y. Qin, Y. Wu, G. Chen, L. Jiao, L. Hu, W. Gu, C. Zhu, Dissociable photoelectrode materials boost ultrasensitive photoelectrochemical detection of organophosphorus pesticides, Anal. Chim. Acta 1130 (2020) 100–106.
[3] H. Li, J. Li, Q. Xu, X. Hu, Poly(3-hexylthiophene)/$TiO_2$ nanoparticle-functionalized electrodes for visible light and low potential photoelectrochemical sensing of organophosphorus pesticide chlopyrifos, Anal. Chem. 83 (2011) 9681–9686.
[4] X. Yan, Y. Song, C. Zhu, H. Li, D. Du, X. Su, Y. Lin, $MnO_2$ nanosheet-carbon dots sensing platform for sensitive detection of organophosphorus pesticides, Anal. Chem. 90 (2018) 2618–2624.
[5] H. Chen, H. Zhang, R. Yuan, S. Chen, Novel double-potential electrochemiluminescence ratiometric strategy in enzyme-based inhibition biosensing for sensitive detection of organophosphorus pesticides, Anal. Chem. 89 (2017) 2823–2829.
[6] J. Tan, B. Peng, L. Tang, C. Feng, J. Wang, J. Yu, X. Ouyang, X. Zhu, Enhanced photoelectric conversion efficiency: a novel h-BN based self-powered photoelectrochemical aptasensor for ultrasensitive detection of diazinon, Biosens. Bioelectron. 142 (2019), 111546.
[7] W. Cheng, Z. Zheng, J. Yang, M. Chen, Q. Yao, Y. Chen, W. Gao, The visible light-driven and self-powered photoelectrochemical biosensor for organophosphate pesticides detection based on nitrogen doped carbon quantum dots for the signal amplification, Electrochim. Acta 296 (2019) 627–636.
[8] L. Ge, Q. Hong, H. Li, C. Liu, F. Li, Direct laser writing of metal sulfide graphene nanocomposite photoelectrode toward sensitive photoelectrochemical sensing, Adv. Funct. Mater. 29 (2019), 1904000.
[9] R. Yang, X. Yan, Y. Li, X. Zhang, J. Chen, Nitrogen-doped porous carbon-ZnO nanopolyhedra derived from ZIF-8: new materials for photoelectrochemical biosensors, ACS Appl. Mater. Interfaces 9 (2017) 42482–42491.
[10] Y. Chen, H. Yin, F. Li, J. Zhou, L. Wang, J. Wang, S. Ai, Polydopamine-sensitized $WS_2$/black-$TiO_2$ heterojunction for histone acetyltransferase detection with enhanced visible-light-driven photoelectrochemical activity, Chem. Eng. J. 393 (2020), 124707.
[11] J. Chang, W. Lv, J. Wu, H. Li, F. Li, Simultaneous photoelectrochemical detection of dual microRNAs by capturing CdS quantum dots and methylene blue based on target-initiated strand displaced amplification, Chin. Chem. Lett. 32 (2021) 775–778.
[12] L. Zhang, P. Li, L. Feng, X. Chen, J. Jiang, S. Zhang, A. Zhang, G. Chen, H. Wang, Controllable fabrication of visible-light-driven CoSx/CdS photocatalysts with direct Z-scheme heterojunctions for photocatalytic Cr(VI) reduction with high efficiency, Chem. Eng. J. 397 (2020), 125464.
[13] Q. Hong, L. Ge, W. Wang, X. Liu, F. Li, Oligonucleotide-modulated photocurrent enhancement of a tetracationic porphyrin for label-free homogeneous photoelectrochemical biosensing, Biosens. Bioelectron. 121 (2018) 90–95.
[14] W.W. Zhan, Q. Kuang, J.Z. Zhou, X.J. Kong, Z.X. Xie, L.S. Zheng, Semiconductor@metal–organic framework core–shell heterostructures: a case of ZnO@ZIF-8 nanorods with selective photoelectrochemical response, J. Am. Chem. Soc. 135 (2013) 1926–1933.
[15] W. Septina, R.R. Prabhakar, R. Wick, T. Moehl, S.D. Tilley, Stabilized solar hydrogen production with CuO/CdS heterojunction thin film photocathodes, Chem. Mater. 29 (2017) 1735–1743.
[16] H. Wang, H. Ye, B. Zhang, F. Zhao, B. Zeng, Electrostatic interaction mechanism based synthesis of a Z-scheme BiOI-CdS photocatalyst for selective and sensitive detection of $Cu^{2+}$, J. Mater. Chem. 5 (2017) 10599–10608.
[17] I. Vamvasakis, O. Papadas, T. Tzanoudakis, C. Drivas, S.A. Choulis, S. Kennou, G. S. Armatas, Visible-light photocatalytic $H_2$ production activity of β-$Ni(OH)_2$ modified CdS mesoporous nano-heterojunction networks, ACS Catal. 8 (2018) 8726–8738.
[18] Z. Wang, T.D. Nguyen, L.P. Yeo, C.K. Tan, L. Gan, A.I.Y. Tok, Periodic FTO IOs/CdS NRs/CdSe clusters with superior light scattering ability for improved photoelectrochemical performance, Small 16 (2020), 1905826.
[19] G. Huang, Q. Li, D. Yin, L. Wang, Hierarchical porous Te@$ZnCo_2O_4$ nanofibers derived from Te@metal-organic frameworks for superior lithium storage capability, Adv. Funct. Mater. 27 (2017), 1604941.
[20] M. Hu, Y. Ju, K. Liang, T. Suma, J. Cui, F. Caruso, Void engineering in metal-organic frameworks via synergistic etching and surface functionalization, Adv. Funct. Mater. 26 (2016) 5827–5834.
[21] K. Shen, X. Chen, J. Chen, Y. Li, Development of MOF-derived carbon-based nanomaterials for efficient catalysis, ACS Catal. 6 (2016) 5887–5903.
[22] B.C. Qiu, Q.H. Zhu, M.M. Du, L.G. Fan, M.Y. Xing, J.L. Zhang, Efficient solar light harvesting CdS/$Co_9S_8$ hollow cubes for z-scheme photocatalytic water splitting, Angew. Chem. Int. Ed. 56 (2017) 2684–2688.
[23] S. Wang, Y. Wang, S.L. Zhang, S.Q. Zang, X.W.D. Lou, Supporting ultrathin $ZnIn_2S_4$ nanosheets on Co/N-doped graphitic carbon nanocages for efficient photocatalytic $H_2$ generation, Adv. Mater. 31 (2019), 1903404.
[24] L. Zhang, L. Feng, P. Li, X. Chen, J. Jiang, S. Zhang, C. Zhang, A. Zhang, G. Chen, H. Wang, Direct Z-scheme photocatalyst of hollow CoSx@CdS polyhedron constructed by ZIF-67-templated one-pot solvothermal route: a signal-on photoelectrochemical sensor for mercury (II), Chem. Eng. J. 395 (2020), 125072.
[25] X. Zhang, J. Peng, Y. Ding, D. Zheng, Y. Lin, Y. Chen, W. Gao, Rationally designed hierarchical hollow ZnCdS@$MoS_2$ heterostructured cages with efficient separation of photogenerated carriers for photoelectrochemical aptasensing of lincomycin, Sensor. Actuator. B Chem. 306 (2020), 127552.
[26] M. Xiao, Z. Wang, M. Lyu, B. Luo, S. Wang, G. Liu, H.M. Cheng, L. Wang, Hollow nanostructures for photocatalysis: advantages and challenges, Adv. Mater. 31 (2019), 1801369.
[27] P. Zhang, S. Wang, B.Y. Guan, X.W. Lou, Fabrication of CdS hierarchical multi-cavity hollow particles for efficient visible light $CO_2$ reduction, Energy Environ. Sci. 12 (2019) 164–168.
[28] J. Peng, J. Yang, B. Chen, S. Zeng, D. Zheng, Y. Chen, W. Gao, Design of ultrathin nanosheet subunits $ZnIn_2S_4$ hollow nanocages with enhanced photoelectric conversion for ultrasensitive photoelectrochemical sensing, Biosens. Bioelectron. 175 (2021), 112873.
[29] X. Zhang, J. Peng, Y. Song, Y. Chen, F. Lu, W. Gao, Porous hollow carbon nanobubbles@ZnCdS multi-shelled dodecahedral cages with enhanced visible-light harvesting for ultrasensitive photoelectrochemical biosensors, Biosens. Bioelectron. 133 (2019) 125–132.
[30] Q. Wang, F. Gao, B. Xu, F. Cai, F. Zhan, F. Gao, Q. Wang, ZIF-67 derived amorphous $CoNi_2S_4$ nanocages with nanosheet arrays on the shell for a high-performance asymmetric supercapacitor, Chem. Eng. J. 327 (2017) 387–396.
[31] C.V. Reddy, I.N. Reddy, B. Akkinepally, V.V.N. Harish, K.R. Reddy, S. Jaesool, Mn-doped $ZrO_2$ nanoparticles prepared by a template-free method for electrochemical energy storage and abatement of dye degradation, Ceram. Int. 45 (2019) 15298–15306.
[32] Q. Wang, Q. Wang, B. Xu, F. Gao, F. Gao, C. Zhao, Flower-shaped multiwalled carbon nanotubes@nickel-trimesic acid MOF composite as a high-performance cathode material for energy storage, Electrochim. Acta 281 (2018) 69–77.
[33] J. Tang, Y. Liu, J. Hu, S. Zheng, X. Wang, H. Zhou, B. Jin, Co-based metal-organic framework nanopinnas composite doped with Ag nanoparticles: a sensitive electrochemical sensing platform for simultaneous determination of dopamine and acetaminophen, Microchem. J. 155 (2020), 104759.
[34] Q. Liu, Y. Yin, N. Hao, J. Qian, L. Li, T. You, H. Mao, K. Wang, Nitrogen functionalized graphene quantum dots/3D bismuth oxyiodine hybrid hollow microspheres as remarkable photoelectrode for photoelectrochemical sensing of chlopyrifos, Sensor. Actuator. B Chem. 260 (2018) 1034–1042.
[35] X.L. Han, F.F. Tian, Y.S. Ge, F.L. Jiang, L. Lai, D.W. Li, Q.L. Yu, J. Wang, C. Lin, Y. Liu, Spectroscopic, structural and thermodynamic properties of chlorpyrifos

bound to serum albumin: a comparative study between BSA and HSA, J. Photochem. Photobiol. B Biol. 109 (2012) 1–11.
[36] Q. Shen, R. Bibi, L. Wei, D. Hao, N. Li, J. Zhou, Well-dispersed CoSx nanoparticles modified tubular sulfur doped carbon nitride for enhanced photocatalytic $H_2$ production activity, Int. J. Hydrogen Energy 44 (2019) 14550–14560.
[37] F.X. Xiao, J. Miao, B. Liu, Layer-by-Layer self-assembly of CdS quantumdots/graphene nanosheets hybrid films for photoelectrochemical and photocatalytic applications, J. Am. Chem. Soc. 136 (2014) 1559–1569.
[38] W. Wei, L. Mi, Y. Gao, Z. Zheng, W. Chen, X. Guan, Partial ion-exchange of nickel-sulfide-derived electrodes for high performance supercapacitors, Chem. Mater. 26 (2014) 3418–3426.
[39] J. Zhou, J. Qin, X. Zhang, C. Shi, E. Liu, J. Li, N. Zhao, C. He, 2D space-confined synthesis of few-Layer $MoS_2$ anchored on carbon nanosheet for lithium-ion battery anode, ACS Nano 9 (2015) 3837–3848.
[40] J. Kamimura, P. Bogdanoff, M. Ramsteiner, P. Corfdir, F. Feix, L. Geelhaar, H. Riechert, P-type doping of GaN nanowires characterized by photoelectrochemical measurements, Nano Lett. 17 (2017) 1529–1537.

Microchemical Journal 181 (2022) 107779

Contents lists available at ScienceDirect

Microchemical Journal

journal homepage: www.elsevier.com/locate/microc

# Ultrasensitive photoelectrochemical sensing platform based on heterostructural CuO/NCDs@Au nanocomposites with the efficient photo-induced carrier separation

Delun Zheng [a,b], Zengyao Zheng [c], Jianying Yang [c], Yanping Xu [a], Kwan-Ming Ng [a], Linjia Huang [d], Yaowen Chen [a], Wenhua Gao [a,*]

[a] Department of Chemistry and Laboratory for Preparation and Application of Ordered Structural Materials of Guangdong Province, Shantou University, Shantou, Guangdong 515063, PR China
[b] Department of Natural Sciences, Shantou Polytechnic, Shantou, Guangdong 515078, PR China
[c] Guangdong Shantou Supervision Testing Institute of Quality & Measuring, Shantou, Guangdong 515041, PR China
[d] Institute of Chemical Engineering, Guangdong Academy of Sciences, Guangzhou, Guangdong 510665, PR China

ARTICLE INFO

*Keywords:*
MOF-derivant of CuO
NCDs@Au nanoflows
Heterojunction
Photoelectrochemical
AFP detection

ABSTRACT

Heterogeneous composite is considered a valuable material to boost the photo-electrochemical (PEC) properties. Herein, the porous hollow and thin-shell CuO particles were prepared by calcining a Cu-BTC precursor. *N*-doped carbon dots (NCDs) as both reductor and stabilizer can reduce the $Au^{+}$ to gain regularly nanoflower NCDs@Au, which further to create type-II heterogeneous interface of CuO/NCDs@Au. PEC monitoring results showed that the CuO/NCDs@Au nanocomposite displayed markedly improved photocurrent response than the mono-component CuO or CuO/NCDs. This outstanding photoelectric property was ascribed to the multiple reflection/scattering effects from the porous hollow structure of CuO particles which led to more photo-induced $e^{-}/h^{+}$ pairs. The obtained heterostructured CuO/NCDs@Au could magnify synergistically the photocurrent output signal. Ab (antibodies) was accurately immobilized on the CuO/NCDs@Au modified ITO electrode via a facility amidation reaction. Fabricated Ab/CuO/NCDs@Au/ITO PEC sensing platform for AFP (alpha-fetoprotein) detection manifested an enhanced sensitivity ($3.32 \times 10^{-4}$ ng $mL^{-1}$) with wide linear range (0.001 ~ 300 ng $mL^{-1}$), which was superior compared to the electrochemical results. This works developed an excellent heterojunction nanocomposite of CuO/NCDs@Au, which provided well-synthesized strategies for structuring high-performance photocatalysts based on MOFs derivant.

## 1. Introduction

Alpha-fetoprotein (AFP) is used as an important biomarker of malignant tumors, and it mostly exists in patient's serums, colorectal and bladder carcinomas. The AFP concentration in serum of healthy person is usually less than 25 ng $mL^{-1}$, but this concentration significantly increases in the patients having liver cancer. So, the sensitive and rapid methods of AFP detection play an imperative part for diagnosing cancers previously. Several methods have been developed for AFP detection in human serum, including the fluorescence spectroscopy, enzyme-linked immunosorbent assay (ELISA), high-performance liquid chromatography (HPLC), chemiluminescence, mass spectrometric immunoassays, and radioimmunoassay [1–3]. Despite many efforts, these techniques still have some disadvantages, for example the complex operation process, high cost, limited selectivity or sensitivity, requirement of proficient operator and long detection time. Photoelectrochemical (PEC) biosensor is widely used in the detection of tumor markers because of its high sensitivity, rapidity, easy operation and minimal sample consumption [4,5].

In photoelectrochemical (PEC) analysis, the photoactive material is a critical factor in which it reliably influences the PEC performance [6,7]. To date, various kinds of photoactive materials have been proposed for the application of PEC studies, such as the $TiO_2$ [8], ZnO [9], $WO_3$ [10], CdS [11], $WS_2$ [12], Metal-organic frameworks (MOFs) [13], Au NPs [14] and carbon dots (CDs) materials [15]. Nevertheless, the application of pristine photoactive material was still limited because of its inherent

* Corresponding author.
*E-mail address:* whgao@stu.edu.cn (W. Gao).

https://doi.org/10.1016/j.microc.2022.107779
Received 11 January 2022; Received in revised form 18 June 2022; Accepted 9 July 2022
Available online 16 July 2022

defects such as poor visible light absorption, serious aggregation of photo-generated carriers, and tardigrade charge transfer [16]. Surmounting these limitations caused inferior PEC performance, establishing composited hetero-structure material with proper band-gap energy position was considered as a promising approach [17,18]. Moreover, hybrid nanocomposite materials with porous and hollow structures also could effectively promote carriers separation and transportation [19,20]. However, various photoelectric materials may be incompatible which resulted in weak structural stability and poor uniformity of the prepared heterojunction composites [21]. Hence, adopting reliable routes and controllable strategies to get anticipant heterostructured photocatalysts were still urgently required.

Carbon dots (CDs) materials are assembled by the $sp^2$ hybridized carbon atom or small graphene nanoplatelets [22]. Due to various advantages of CDs such as the good biocompatibility, low cytotoxicity, easy functionalization, excellent electro-catalysis, and photo-induced properties, CDs have been applied diffusely in the fields of catalysis, bioimaging, photovoltaics, sensors, etc [23–26]. Recently, doping of the CDs with heteroatoms has gained more attention because it not only enhances the conductivity capability but also benefits the optical property [27,28]. Among the heteroatoms, the atomic size of nitrogen (N) is most approachable to CDs, which leads to improving the CDs performance such as the interior electronic environment [29]. As well as the *N*-doped CDs (NCDs) can be used as an effective photosensitizer for magnifying the signal response. Cheng et al. [30] prepared the nitrogen-doped carbon dots (NCDs) that could improve the photocurrent response of the NCDs/$TiO_2$ composite. Shi et al. [31] explored the NCDs with different atom ratios of N/C and obtained the highest *N*-doping level that showed enhanced electron transfer capacity. Additionally, it is noteworthy that CDs can be employed as the reductant and stabilizer to reduce metal ions such as $Ag^+$, $Cu^{2+}$, $Au^+$, and obtained nanoparticles can further improve the electron transfer. For instance, Huang et al. [32] synthesized a nano-composite of Pd-Au@CDs by using the stabilizing and reducing agent of CDs, which exhibited higher electric conductivity properties than the monocomponent material of CDs.

Metal-organic frameworks are the type of porous coordination polymers fabricated by transition metal ions and organic ligands. Owing to the specific merits of large surface area, exposed active sites, and versatile structures, MOFs materials have been widely used in the field of gas adsorption or separation [33], catalysis [34], and sensing [35,36]. However, there are still some defects for MOFs such as weak electronic conductivity, poor photocatalytic activity, and inferior mechanical ability. Recently, MOFs as the precursor materials converted into new compositions with excess morphology and structure have gained an enthusiastic interest [37,38]. These MOF-derivatives not only inherit the main morphologies from their precursors but also can fabricate the functionalized features such as thin-shell structures, multi-shelled cages, hollow-shape morphologies, etc. Moreover, they possess the merit of the changed components including metal sulfide, metal oxides, or C elements which may further improve their electrochemical properties [39,40]. Our works [16] previously proposed MOF-derived porous carbon nano-bubbles of C@ZnCdS prepared by the sulfurization and calcination strategies, and the C@ZnCdS composite exhibited superior photoelectron-chemical performance because of the synergistic effect from their porous shells and carbon layers. Hu et al. [41] synthesize hierarchically structured CuO octahedral particles based on Cu-BTC MOFs, benefiting from this structural feature, it displayed a good capability for the $Li^+$ storage and transfer.

MOFs with hollow structures are also considered as an effective approach for promoting photo-electric behaviors. In the interior void of hollow materials, it can lead to the multiple reflection effect and further reinforce the light-harvesting, resulting in more photo-generated charge carriers [42]. On the other hand, hollow structures provide an efficient channel for immensely immerging the electrolyte solution which is conducive to transporting the electrical charges [43]. Otherwise, the thinner-shell feature of hollow structures can reduce the transferred distance of photo-excited $e^{-1}/h^+$ pairs, hence effectually restraining the recombination of the charge carriers [44,45]. Our works [46] had prepared hollow $ZnIn_2S_4$ polyhedral nanocages derived from the ZIF-8 MOFs precursor, in which the visible light absorption capacity distinctly enhanced and consequently improved the photoelectric conversion efficiency. Zhang et al. [47] using ZIF-67 MOFs as sacrificial templates fabricated another hollow polyhedral composite of CoSx@CdS and it not only reinforced the photo-absorption capacity but also supplied plenty of active sites to facilitate the redox reactions. Although the hollow geometry affords an effective route for improving the physicochemical properties, hollow materials with higher electrical conductivity and reasonable band gap still demand a well-design and feasible strategy.

Inspired by these above pioneering works, herein, we presented porous hollow and thin-shell CuO particles derived from the Cu-BTC MOFs acting as precursor templates. The NCDs were successfully synthesized via a solvothermal method and also used as a reducing agent to obtain a well-regular NCDs@Au nanoflower composite by a simple reduction strategy. Subsequently, NCDs@Au materials were coupled with the as-prepared CuO particles to create type-II heterojunction photocatalysts of CuO/NCDs@Au. The PEC properties of prepared materials were severally surveyed by photocurrent monitoring. The gained results revealed that CuO/NCDs@Au nanocomposite exhibiting the most superior photocurrent response compared with monocomponent CuO particles or CuO/NCDs, which was attributed to thin-shell and hollow CuO particles with large surface area as well formed heterostructured architecture of CuO/NCDs@Au. Moreover, the abundant carboxyl groups of NCDs could be further employed as a functional substance for effectively immobilizing Ab on ITO electrode surface to build a sensing platform of Ab/CuO/NCDs@Au/ITO. The fabricated PEC biosensor for AFP detection indicated a wider linear range with a relatively low limit of detection (LOD) value than the results of the electrochemical method obtained. This proposed biosensor also showed good stability, excellent selectivity, and acceptable reproducibility in AFP assay.

## 2. Experimental section

Chemicals, reagents, and apparatus had been reported on supporting information.

### 2.1. Synthesis of Cu-BTC, NCDs and NCDs@Au

The Cu-BTC was prepared by the solvothermal method according to previous literature with slight modification [48]. Firstly, 0.621 g Cu$(NO_3)_2{\cdot}3H_2O$ (2.57 mmol) and 0.303 g BTC (benzene-1,3,5-tricarboxylic acid, 1.44 mmol) were successively added into 15 mL deionized water (DDW) with 15 mL ethanol, stirring adequately for 15 min at room temperature, the mixture was further ultrasonicated for 10 min to gain a homogeneous solution. Following this, the compound was transferred to a 50 mL Teflon-lined autoclave and heated for 20 h at a temperature of 120 °C. When naturally cooled to room temperature, obtained Cu-BTC blue particles were carefully collected under centrifugation with a velocity of 8000 rpm and then washed several times with water and ethanol (volume ratio of 1:1). Finally, the precipitates were vacuum dried at 60 °C overnight to obtain the pure Cu-BTC products.

*N*-doped CDs were synthesized by a straightforward hydrothermal method [49]. 1.0 g ammonium citrate was dissolved in 10 mL DDW, and 5 mL ethylenediamine was added to the solution. After stirring vigorously for 15 min, the gained bright and yellow mixture was taken into 50 mL Teflon-lined autoclave and had been heated for 5 h at 200 °C. After cooling down to room temperature, the changed orange-red solution was centrifuged at 10000 rpm for 10 min. Then, the concentrated supernatant was dialyzed for 24 h with a dialysis membrane of 1000 cutoffs. Finally, the brown NCDs powder was obtained by vacuum freeze-drying. In addition, the CDs were prepared in the same processes

without using ethylenediamine as the nitrogen source.

The NCDs@Au nanoparticles were prepared by a simple reduction method [32]. First, 150 μL $HAuCl_4$ solution (1 mg $mL^{-1}$) was added into 150 μL NCDs solution (1 mg $mL^{-1}$). Then, this mixture was heated at 90 °C in a water bath for 60 min and obtained the regular nanoflower products of NCDs@Au.

### 2.2. Preparation of CuO particles and CuO/NCDs@Au nanocomposites

The MOF-derived product of CuO was achieved by calcining the Cu-BTC precursor for 1.5 h at 380 °C under isolated air, and the Cu-BTC materials had been translated into black CuO particles. The as-obtained CuO (1 mg $mL^{-1}$) and NCDs@Au were mixed in a volume ratio (1:1) and ultrasonicated for 15 min to get a well-dispersive nanocomposite of CuO/NCDs@Au. The CuO/NCDs composite was prepared in the same experiment condition. The preparation process of CuO/NCDs@Au was shown in Scheme 1A.

### 2.3. Fabrication of the PEC and electrochemical biosensor

In brief, the indium tin oxide (ITO) electrodes were ultrasonically cleaned with acetone, 1.0 M NaOH/ethanol (1:1), and DDW for 15 min, respectively. Then, 9 μL as-prepared CuO/NCDs@Au solutions were dropped onto the ITO electrode. After drying spontaneously, the modified electrode of CuO/NCDs@Au/ITO was obtained. For comparison, the other modified electrodes of CuO/ITO and CuO/NCDs/ITO were also prepared in the same way.

Afterward, the CuO/NCDs@Au/ITO electrode was immersed into 50 mM PBS buffer (pH 7.4) including 25 mM NHS and 12 mM EDC for 30 min to activate the carboxylic groups of NCDs. Immediately, 8 μL of Ab solution (25 μg $mL^{-1}$, Ab was attenuated with 0.1 M PBS) was dropped onto the CuO/NCDs@Au/ITO electrode surface and incubated for 6 h at 4 °C to form the Ab/CuO/NCDs@Au/ITO electrode via a gentle amidation reaction.

The electrode was rinsed with PBS (0.1 M, pH 7.4), 10 μL of 1 wt% BSA solution (0.1 g BSA dissolve into 10 mL DDW) was covered on Ab/CuO/NCDs@Au/ITO surface for 40 min to block non-specific adsorption binding, and the electrode was washed with PBS (0.1 M, pH 7.4) to clean physically adsorbed BSA. The final sensor electrode of BSA/Ab/CuO/NCDs@Au/ITO was successfully established and stored at 4C° for further analysis.

### 2.4. PEC analysis procedures

8 μL various concentrations of AFP solution were severally dropped on the BSA/Ab/CuO/NCDs@Au/ITO surface and incubated for 1 h at

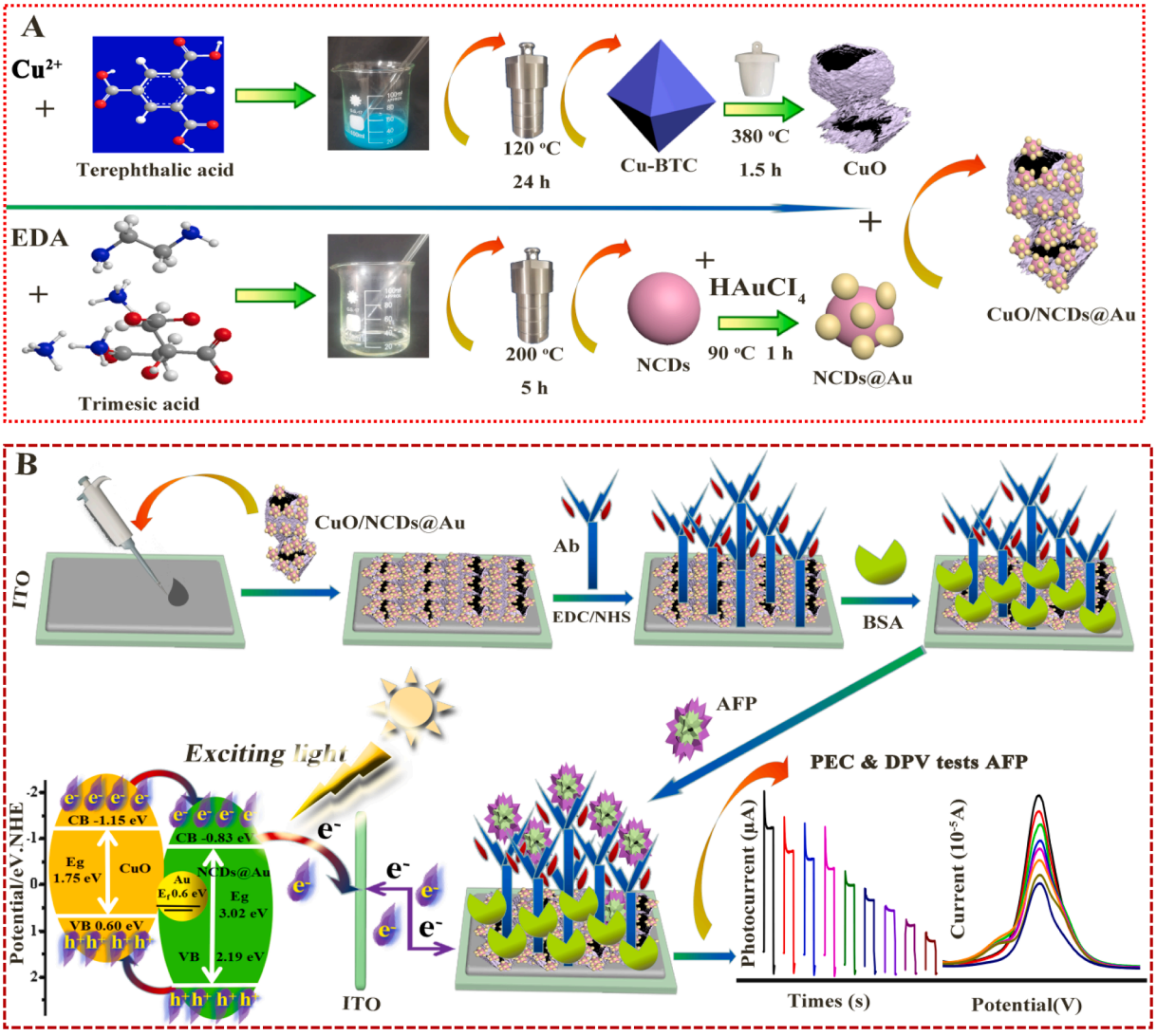


**Scheme 1.** Schematic illustration of the synthesis process of CuO/NCDs@Au (A) and the fabrication processes of PEC and electrochemical biosensors for AFP detection (B).

room temperature, and then rinsing carefully with PBS (0.1 M, pH 7.4). The properties of the sensor electrode (AFP/BSA/Ab/CuO/NCDs@Au/ITO) were carried out by the PEC and DPV (differential pulse voltammetry) measurements in 0.1 M PBS (pH 7.4), respectively. The wavelength of light excitation was 420 nm with an intensity of 25 mW $cm^{-2}$. The excited light source was switched on every 10 s with an applied potential of 0 V.

## 3. Results and discussion

### 3.1. Characterization of prepared materials

The morphologies and microstructure features of the prepared samples were surveyed by FESEM and TEM. From Fig. 1A, it could be observed that the Cu-BTC particle showed a smooth surface with sharp edges, suggesting the synthesized products had high purity and good crystallinity. Additionally, the opposite-vertical-apex length and edges length of Cu-BTC was estimated to be about 10 μm and 13 μm, respectively (inset of Fig. 1A), which was in accordant with the reported literature [50]. Fig. S1 showed that the CuO particles displayed an obvious roughness with porous morphological features compared with its solid Cu-BTC precursor. From the high-magnification image (Fig. 1B), the tearing holes in CuO particles with the diameter range was from about 2 μm ~ 5 μm, but still, the particle sizes could be well-maintained. From the TEM images of Cu-TPA (Fig. 1C), a single Cu-BTC particle exhibited the regular hexagon shape. But for the CuO particle (inset of Fig. 1D), it had been changed into a similar square with enhanced roughness of its edges. Furthermore, compared with the pristine Cu-BTC, CuO crystal had some distinct features such as thin-shell and hollow structure. The insets (a) and (b) of Fig. 1C displayed the selected area electron diffraction (SAED) pattern of crystalline natures of Cu-BTC and CuO, respectively. From the concentric diffraction rings on both of them, it could be concluded that these two samples had the same polycrystalline structure. While CuO particles had clearer diffraction rings than Cu-BTC, which may be attributed to the thinness hollow structure of CuO but a higher thickness crystal of pure Cu-BTC. From the HRTEM image of CuO (Fig. 1D), typical interplanar spacing was estimated to be about 0.23 nm, 0.25 nm, and 0.27 nm, which corresponded to that of (1 1 1) plane, (0 0 2) plane, and (1 1 0) plane of CuO [51], respectively. Meanwhile, the elemental mapping images (Fig. S2) showed that the uniform distribution of Cu, O, and C elements in as-obtained CuO particles. The above results testified that the Cu-BTC precursor had been adequately converted into CuO component material.

From the TEM image (Fig. 2A), it could be found that NCDs nanoparticles were continuously distributed with similar spheres, and the size distribution was in an average range of about 17 nm ~ 25 nm (inset of Fig. 2A). Interestingly, NCDs as a reductant could reduce the $Au^{+}$ into metallic $Au^{0}$, which formed a regular and well-distributed nanoflower composite of NCDs@Au (Fig. 2B and insert) with the diameter size of about 50 nm (Fig. 2C). These nano-size NCDs@Au particles could be well-dispersed on the surface of CuO as well as readily drilled into the interior cavity because of the porous CuO particles. The HRTEM image of NCDs@Au showed the lattice spacing of 0.23 nm (Fig. 2D and insert a) which agreed well with the Au (1 1 1) plane [52], and the lattice space of 0.34 nm revealing a graphitic structure of NCDs [49]. The SAED pattern of NCDs@Au displayed the good crystallinity with the diffraction rings (inset b of Fig. 2D) corresponding to the polycrystalline structures of NCDs@Au nanoparticles. The EDS analysis further confirmed that the NCDs@Au was consisted of C, N and Au elements (shown as Fig. S3). All these results indicate that the NCDs@Au nanocrystals were successfully prepared.

The surface compositions with a chemical bonding state of prepared materials were also surveyed by X-ray photoelectronic spectroscopy (XPS). Fig. 3A showed the obtained XPS results of CuO, NCDs, and NCDs@Au with their corresponding component elements, respectively. In Fig. 3B, the high-resolution Cu 2p core-level spectrums of CuO at about 933.7 and 953.8 eV corresponds to the Cu $2p_{3/2}$ and Cu $2p_{1/2}$ peaks, respectively, indicating that the oxidation state of copper (Cu) was +2. Together with two shakeup satellite peaks at about 941.2 and 962.3 eV, respectively, which also revealed the Cu oxidation state of +2 [53]. Fig. 3C showed the O 1s spectrum with peaks at about 529.8 eV which was attributed to the existence of $O^{2-}$ in Cu–O bonding linker, and

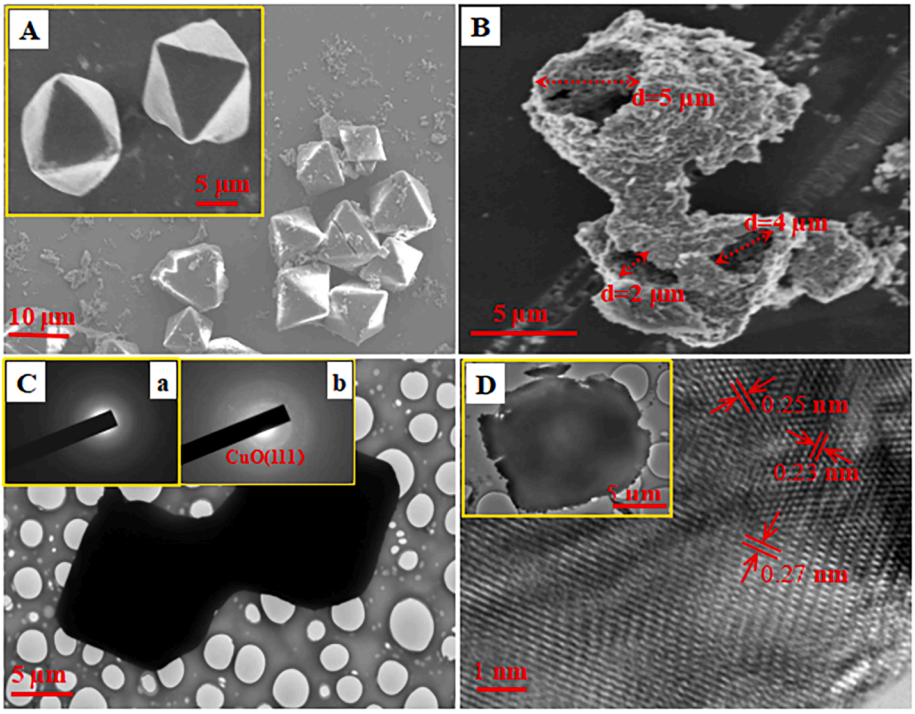


**Fig. 1.** SEM images of (A and inset) Cu-BTC, (B) CuO; TEM images of (C) Cu-BTC, (inset of D) CuO; HRTEM image of (D) CuO; SAED patterns of (inset a and b of C) Cu-BTC and CuO, respectively.

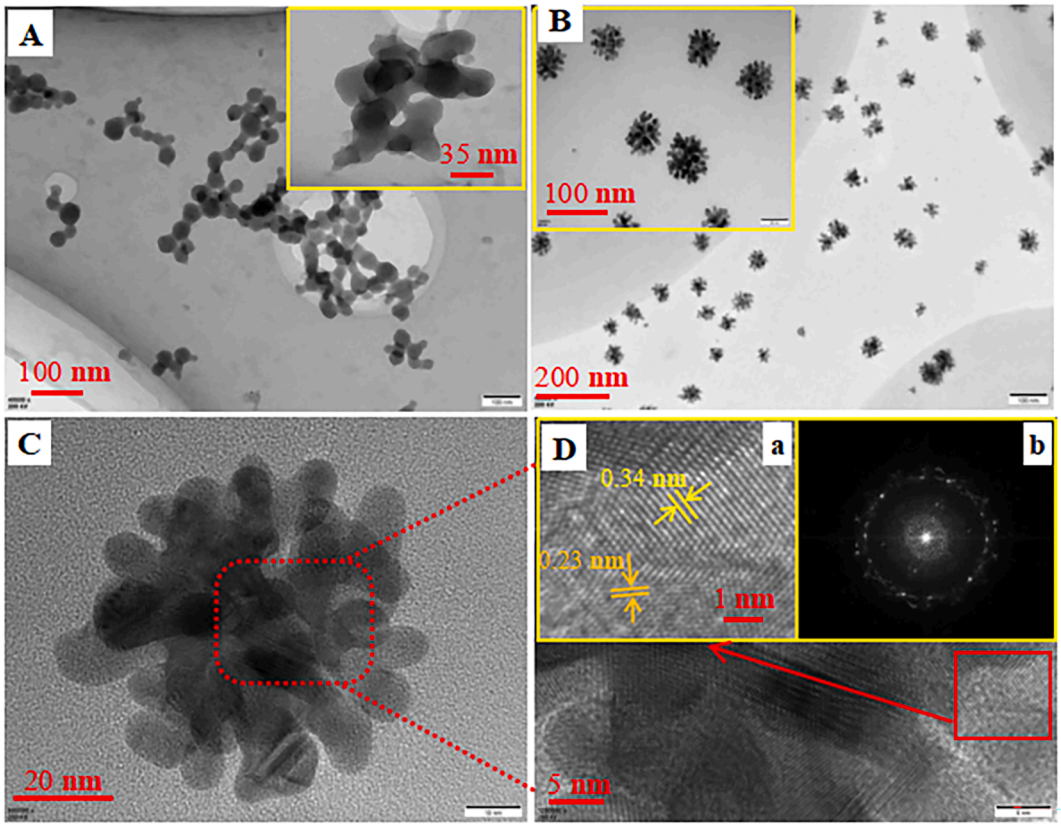


**Fig. 2.** TEM images of (A) NCDs with (inset) amplified views, (B and inset) NCDs@Au with (C) amplified views; HRTEM image of (D and insert a) NCDs@Au; SAED patterns of (inset b of D) NCDs@Au.

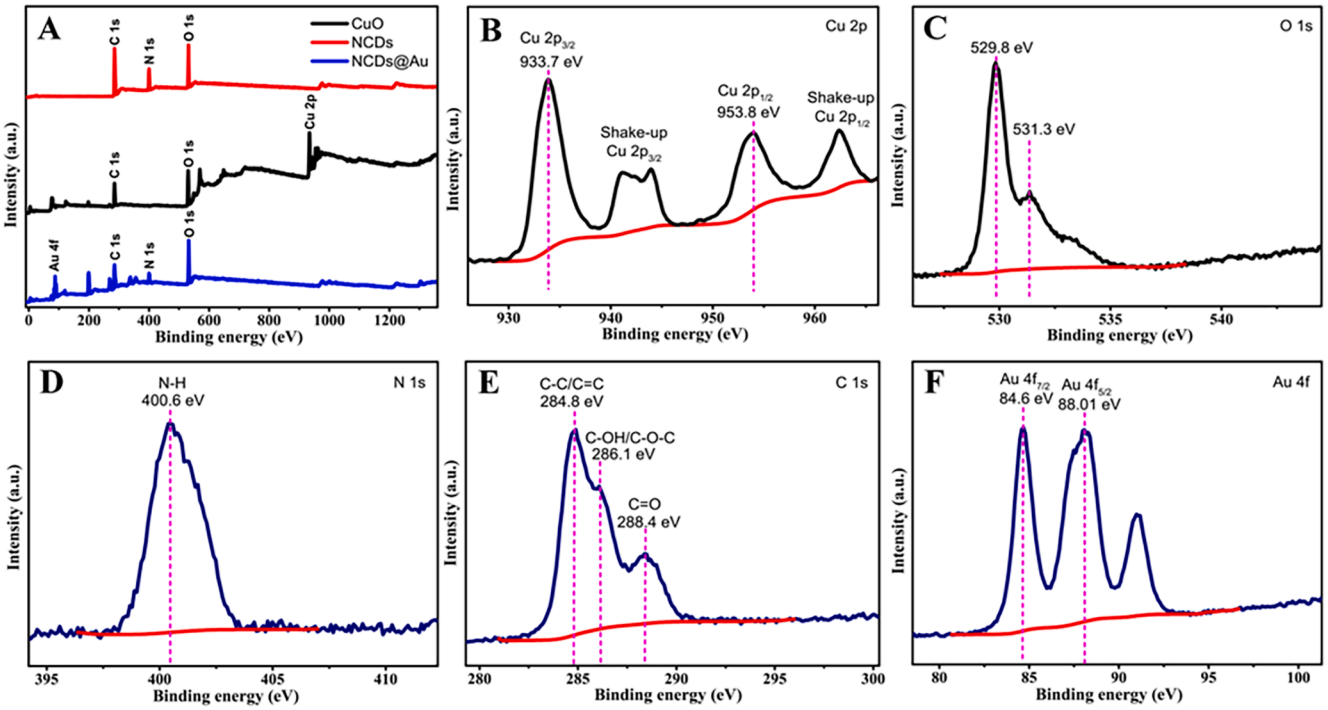


**Fig. 3.** XPS spectra of (A) CuO, NCDs and NCDs@Au; High-resolution XPS spectra of (B) Cu 2p and (C) O 1s of CuO; (D) N 1s, (E) C 1s and (F) Au 4f of NCDs@Au.

another peak at about 531.3 eV may come from the absorbed oxygen. Fig. 3D displayed the high-resolution N 1s spectrum of NCDs@Au with a strong peak at about 400.6 eV, which was attributed to the N—H bonds of NCDs [30]. The characteristic peaks at about 284.8 eV, 286.1 eV, and 288.4 eV (Fig. 3E) could be attributed to the C—C/C═C, C–OH/C—O—C, and C═O bonds in NCDs of NCDs@Au [27], respectively. In

Fig. 3F, the peaks observed at 84.6 eV and 88.01 eV belonged to the Au $4f_{7/2}$ and Au $4f_{5/2}$ peaks, respectively, indicating that the $AuCl_4^{2-}$ could be reduced to $Au^0$ by NCDs and the formation of NCDs@Au nanocomposite. In addition, the high-resolution XPS spectra of C 1s of CuO; N 1s, C 1s and O 1s of NCDs and O 1s of NCDs@Au were also displayed in Fig. S5. All XPS results suggested that the desired materials were successfully prepared.

The crystallographic structure of as-obtained materials was analyzed by the powder X-ray diffraction (XRD) pattern. As shown in Fig. 4A, all the diffraction peaks of Cu-BTC were in good agreement with the face-centered cubic phase in reported literature [54], testifying the pure Cu-BTC materials had been successfully synthesized. The typical diffraction peaks of CuO at 32.53°, 35.56°, 38.87°, 48.82°, 53.55°, and 58.34° corresponds to the (110), (002), (200), (112), (020), and (021) crystallographic planes (PDF#04–0784) [53], respectively, which evidenced the transformation of Cu-BTC MOFs into CuO particles. In the XRD pattern of NCDs@Au, the diffraction peaks at 38.12° and 44.27° were assigned to the face-centered-cubic planes of (111) and (200) of Au [55], respectively. In addition, a peak position at about 24.8° corresponds to the crystal plane of NCDs, which was further displayed in Fig. S4A. These results indicated the successful preparation of photoactive NCDs@Au material. The Raman pattern of CuO with detailed description was shown in Fig. S4B.

The FT-IR pattern of Cu-BTC, CuO, and NCDs was also investigated by FT-IR spectroscopy in Fig. 4B. The adsorption bands at 1450 $cm^{-1}$ and 1375 $cm^{-1}$ were assigned to the symmetric stretching of carboxylate groups (–COOH) of Cu-BTC, and the asymmetric stretching of –COOH groups of Cu-BTC presenting at $1450^{-1}$ and 1375 $cm^{-1}$ [54]. The adsorption bands of NCDs at 1554 $cm^{-1}$ and 1658 $cm^{-1}$ were assigned to the curving vibration of –C═O-NH-, while the adsorption bands at 1396 $cm^{-1}$ correspond to the curving vibration of C—O [30]. Besides, the absorbing feature peaks at approximately 498 $cm^{-1}$ and 512 $cm^{-1}$ were assigned to the Cu–O bond, the characteristic peak of all prepared materials at 3438 $cm^{-1}$ was indexed to the hydroxyl groups (–OH). Fig. 4C showed the thermogravimetric (TG) analysis of Cu-BTC, in which the thermodynamic stability could be maintained up to approximately 300 °C and presenting a dramatic thermal decomposition reaction. It was noted that at the temperature of 380 °C, Cu-BTC had been mostly thermal decomposed.

### 3.2. PEC mechanism

The optical properties of UV–vis DRS of the prepared materials were further evaluated. In Fig. 4D, it was found that CDs only had the collection capacity in the UV-light region, while the visible-light absorption wavelength of ≥ 380 nm was observed on CuO/NCDs and CuO/NCDs@Au. Compared to the CuO/NCDs materials, CuO/NCDs@Au heterostructural nanocomposites showed an enhanced photo-capturing capability. In the inset of Fig. 5A, CuO particles displayed the typical feature absorption of optical light due to their reversely narrow bandgap energy. It was also seen that both NCDs and NCDs@Au exhibited two feature absorption peaks of about 240 nm and 352 nm (Fig. 5A), respectively, which were attributed to the p–p* transition and n–p* transition caused by C═C bond and C═O bond [49]. An absorption peak position at 528 nm was ascribed to the surface plasmon resonance (SPR) of Au [56]. This result also confirmed that NCDs could smoothly reduce the $AuCl^{4-}$ to Au nanoparticles. Additionally, based on the empirical equation of $ahv = A\ (hv\text{-}Eg)^{1/2}$, the Eg values of CuO, NCDs@Au and NCDs were calculated to be 1.75, 3.02, and 2.98 eV (Fig. 5B ~ C and Fig. S5A), respectively. With the VB-XPS characterization, the VB potentials of CuO, NCDs@Au, and NCDs were measured at 0.60, 2.19, and 2.16 eV (Fig. S6A ~ B), respectively. Concurrently, with the empirical

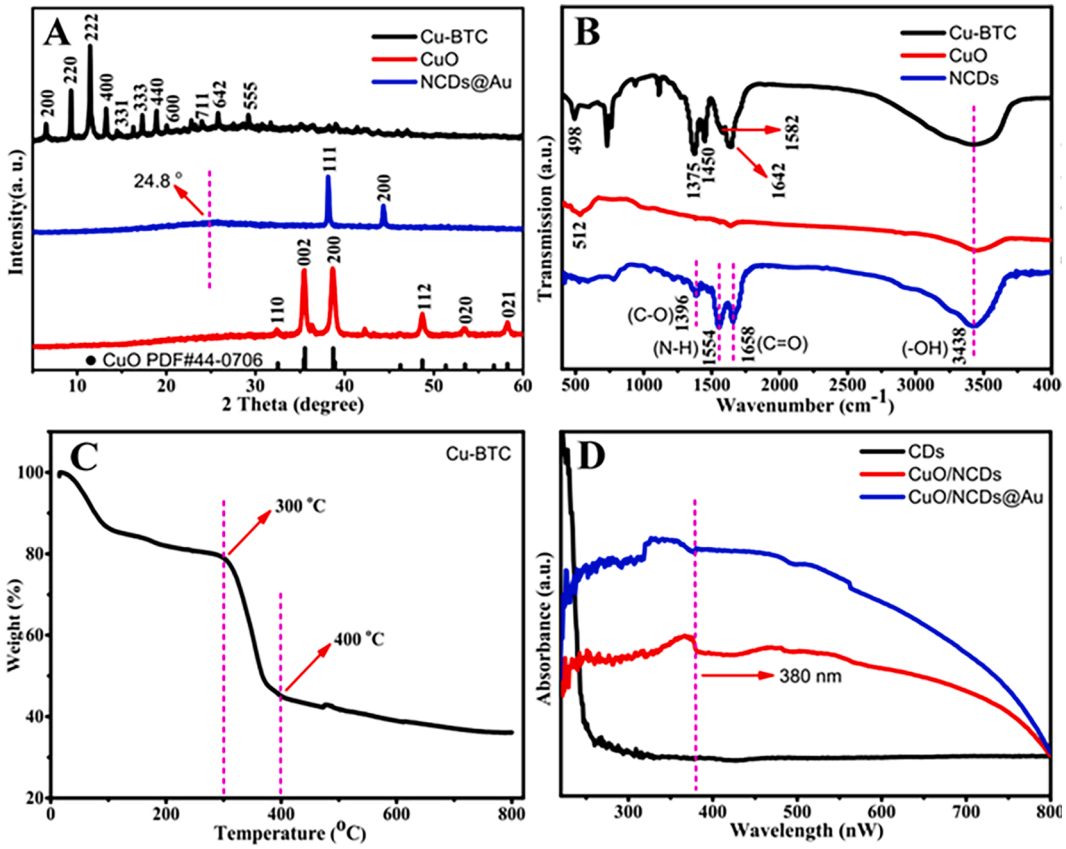


**Fig. 4.** XRD patterns of (A) Cu-BTC, CuO and CuO/NCDs@Au; FT-IR spectra of (B) Cu-BTC, CuO and NCDs; TG analysis of (C) Cu-BTC; UV–vis spectra of (D) CDs, CuO/NCDs and CuO/NCDs@Au.

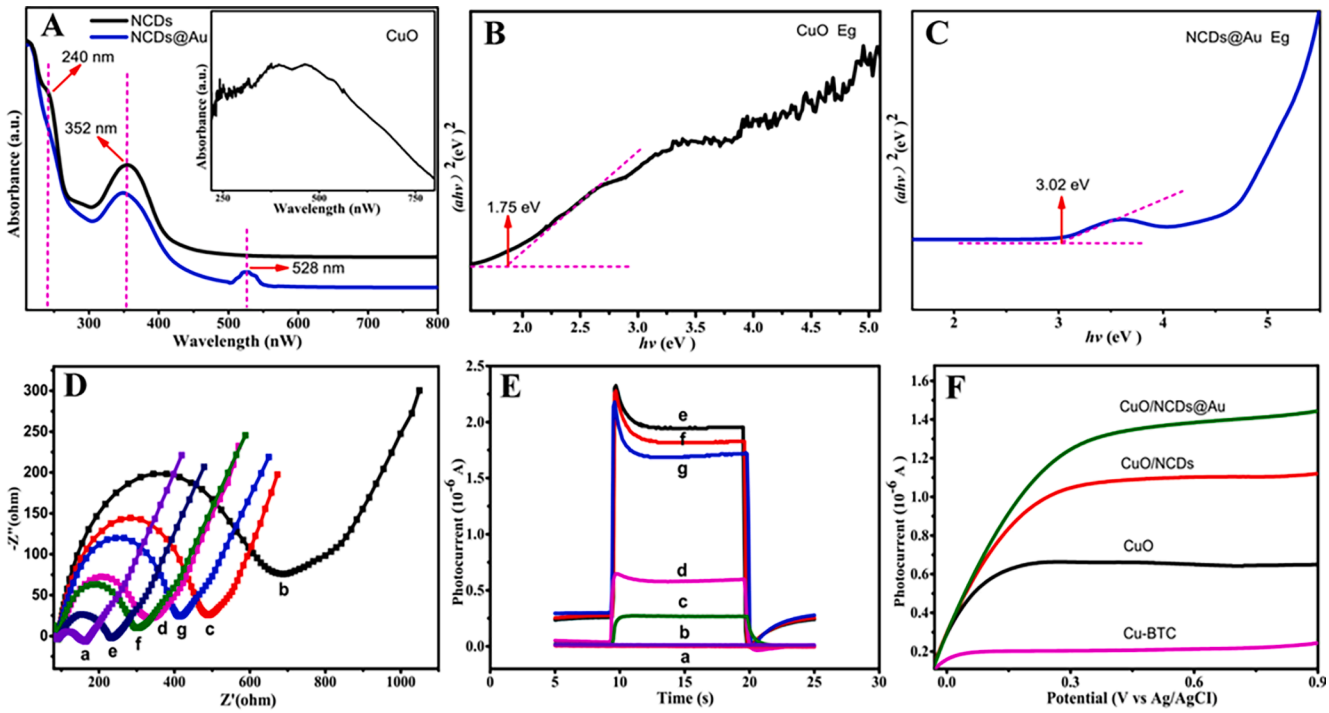


**Fig. 5.** UV–vis spectra of (A) NCDs, NCDs@Au and CuO (insert of A); Plots of $(ahv)^2$ vs photon energy ($hv$) of (B) CuO and (C) NCDs@Au; EIS of (D) bare ITO (a), Cu-BTC/ITO (b), CuO/ITO (c), CuO/NCDs/ITO (d), CuO/NCDs@Au/ITO (e), Ab/CuO/NCDs@Au/ITO (f), BSA/Ab/CuO/NCDs@Au/ITO (g) in 5 mM $K_3[Fe(CN)_6]/K_4[Fe(CN)_6]$ containing 0.1 M KCl; PEC of (E) bare ITO (a), Cu-BTC/ITO (b), CuO/ITO (c), CuO/NCDs/ITO (d) CuO/NCDs@Au/ITO (e), Ab/CuO/NCDs@Au/ITO (f), BSA/Ab/CuO/NCDs@Au/ITO (g) in 0.1 M PBS (pH 7.4); (F) LSV patterns of modified ITO electrodes in 0.1 M $Na_2SO_4$ with a scan rate of 80 mV $s^{-1}$.

formulae:

$$E_{CB} = E_{VB} - Eg,$$

the corresponding CB potentials ($E_{CB}$) of CuO and NCDs@Au could be obtained (-1.15 eV and −0.83 eV, respectively). These results reveal that the CB and VB potentials of NCDs@Au were lower than that of CuO, thus the hybrid materials of CuO/NCDs@Au could form a well-composited heterostructure. Under illumination, the photo-induced electron in the CB of CuO was transferred to the CB of NCDs@Au, while the hole in the VB of NCDs@Au was transferred to the VB of CuO. The gained greatest photocurrent response of CuO/NCDs@Au was ascribed to porous hollow CuO with special surface area. In which, it not only extended the photo-responsive range and intensity but also could combine the available NCDs@Au photoactive materials to form a tight contacted hetero-structure interface, resulting in increased $e^-/h^+$ pairs separation efficiency. Besides, a high electron conductivity of Au nanoparticles could also serve as an effective electron acceptor in CuO particles which further facilitated the charges transfer. Finally, a type II of hetero-junction system with the synergistic effect in CuO/NCDs@Au markedly reduced the recombination chance of electron-hole pairs. The PEC property and detection mechanism of the prepared AFP biosensor were shown in Scheme 1B.

### 3.3. Electrochemical and PEC behaviors

EIS is a valuable method to reflect the impedance change of the electrode surface, and the electron transfer resistance ($R_{et}$) can be directly determined by a semicircle diameter in the Nyquist plots. The stepwise modification process of the BSA/Ab/CuO/NCDs@Au/ITO electrode was investigated by EIS measurements using $[Fe(CN)_6]^{3-/4-}$ as the redox probe. As seen in Fig. 5D the small semicircle of bare ITO electrode (curves a) corresponds to the $R_{et}$ value of 70 Ω. Compared with the modified electrodes of CuO/ITO (407 Ω, curve c) and CuO/NCDs/ITO (288 Ω, curve d), Cu-BTC/ITO electrode (curve b) exhibited the greatest $R_{et}$ value of 605 Ω, indicating the solid Cu-BTC could not promote the electron transfer of $[Fe(CN)_6]^{3-/4-}$ towards the electrode surface. On the CuO/NCDs@Au/ITO electrode, the reduced $R_{et}$ value (157 Ω, curve e) displayed an excellent electrocatalysis property than the CuO/ITO or CuO/NCDs/ITO electrode, which was ascribed to the hollow structure of CuO particles, the high electrical conductivity of NCDs and Au nanoparticles formed resultful synergistic effect. When the Ab and BSA were immobilized onto the CuO/NCDs@Au/ITO, the $R_{et}$ values increased to 212 Ω and 330 Ω (curves f and g), respectively, indicating the poor conductivity of protein obstructed the charge transport. The modified process was also explored by CV (cyclic voltammetry) techniques in Fig. S6C, and obtained result was mainly corresponding to the EIS characterization. All EIS and CV results demonstrated that the AFP biosensor was successfully fabricated.

The stepwise construction process of the sensor platform was further studied by the PEC tests, and all the PEC analysis results were recorded in 0.1 M PBS (pH 7.4). As seen in Fig. 5E, there was no photocurrent response on both bare ITO and Cu-BTC/ITO electrodes (curve a, b). While the CuO/ITO electrode (curve c) had an obvious PEC response (0.25 μA), manifesting that the MOF-derived CuO particle could be employed as an efficient photoactive material. However, the photocurrent response value of CuO/NCDs@Au/ITO (curve e) was measured to be 1.96 μA, which was 7.8-fold than that of CuO/ITO and 3.2-fold than that of CuO/NCDs/ITO (0.61 μA, curve d). It was ascribed to the fact that the hollow structure of CuO particles could provide large surface area and more active sites for connecting another photoactive NCDs@Au to form a compact heterogeneous nanocomposite, resulting in greatly enhanced photon-to-electricity conversion efficiency. As well as, Au NPS as an effective electron acceptor in composite could promote the migration and separation of carriers. Afterward, Ab and BSA were introduced on CuO/NCDs@Au/ITO electrode interface successively, and obtained photocurrent values decreased to 1.81 μA and 1.72 μA (curve f and g), respectively, which could be due to their insulating property and hindrance effect. The PEC results also demonstrated the successful structure of the AFP biosensor.

Fig. 5F showed the linear sweep voltammetry (LSV) patterns of Cu-BTC, CuO, CuO/NCDs, and CuO/NCDs@Au modified ITO electrodes under visible light irradiation in 0.1 M $Na_2SO_4$. Compared to the Cu-BTC materials the LSV response intensity of CuO particles increased, indicating the hollow CuO particles could effectively promote the utilization efficiency of visible-light spectra. However, the hybrid CuO/NCDs@Au material displayed the highest photocurrent response than the mono-component CuO particles and CuO/NCDs composite. This phenomenon could be explained by the photoactive CuO, sensitizing effect of NCDs, and the high conductivity of Au synergistic effect formed with a heter-ojunction which could improve significantly the PEC property.

### 3.4. PEC response of the optimization experiments shown on supporting information

There were some vital factors that influencing the sensitivity on the sensing platform. In order to obtain the maximum PEC intensity, those experimental factors were further optimized. As displayed in Fig. S7A, the solution volume of the CuO/NCDs@Au that dropped onto ITO electrode was explored. It was found that the photocurrent response gradually increased with the solution volume of CuO/NCDs@Au in a range from 3 ~ 9 μL, and the highest photocurrent assigned to 9 μL. Thence, 9 μL of CuO/NCDs@Au solution was chosen as the optimal volume in following experiment. Fig. S7B showed that different pH values could influence the photocurrent intensity of the PEC electrode. When the buffer solution with the varied pH range from 5.5 ~ 9.0, the maximum photocurrent was corresponding to pH value of 7.4. Thus, the reasonable neutral environment of pH 7.4 was selected for next study. Fig. S7C showed that the electron inertness of the bio-protein antibody (Ab) could hinder the electron transferring of the redox probe, and the best concentration of Ab was 25 μg $mL^{-1}$.

Besides, the incubation time of Ab on CuO/NCDs@Au/ITO electrode was also investigated. As seen in Fig. S7D, when the time was transformed from 2 ~ 6 h, the photocurrent response of Ab/CuO/NCDs@Au/ITO decreased continuously, and reached a plateau at 6 h, indicating that a saturated incubation time of Ab was 6 h. So, 6 h was adopted for further analysis. In the final process of incubation for capturing antigens (AFP) on the BSA/Ab/CuO/NCDs@Au/ITO electrode, the incubation time was optimized to be 60 min (Fig. S7E).

### 3.5. PEC and DPV analysis properties of the prepared biosensors

The analytical performance of the developed PEC biosensor was investigated by incubating with various concentrations of AFP. As shown in Fig. 6A, under optimized conditions, the PEC response intensities gradually decreased with the increase of AFP concentration from 0.001 to 300 ng $mL^{-1}$, and showed a good linear relationship related to the logarithm concentration of AFP with a low LOD value of $3.32 \times 10^{-4}$ ng $mL^{-1}$ (LOD = 3S/$k$, where S is the standard deviation calculated from ten values of the photocurrent in the absence of AFP, $k$ represent the slope of the calibration curve) (Fig. 6B), the regression equation was $\Delta I_{PCE}$ (μA) = -0.187 log $C_{AFP}$ (ng $mL^{-1}$) + 0.8445 ($R^2$ = 0.9936) (all the standard deviation of photocurrent values was less than 5.0 %). To discriminate whether this PEC method had a superior analytical performance for AFP detection, the as-prepared biosensor was further examined by DPV techniques. Fig. S8B showed the DPV (differential pulse voltammetry) responses decreased accordingly with the increasing logarithm of AFP concentration from 0.001 ~ 60 ng $mL^{-1}$, and the linear equation was $\Delta I_{pa}$ (μA) = -0.111 log $C_{AFP}$ (ng $mL^{-1}$) + 0.8658 ($R^2$ = 0.9958) (all the standard deviation of DPV values was less

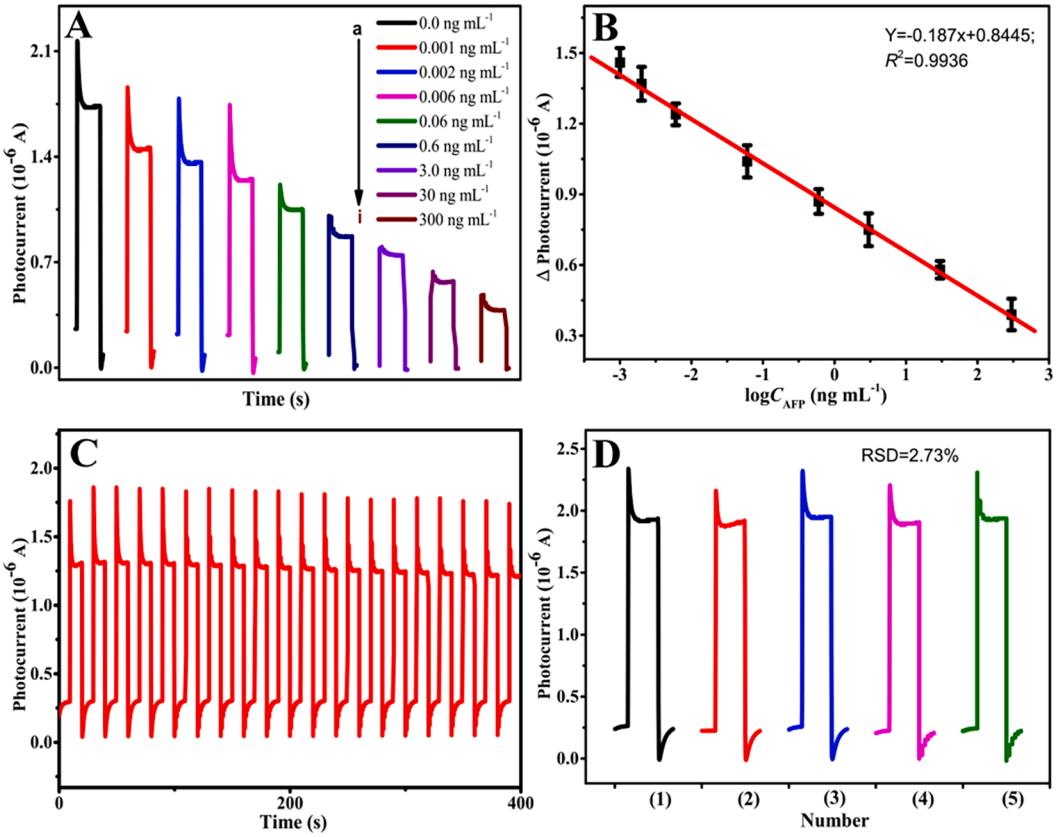


**Fig. 6.** (A) PEC responses of BSA/Ab/CuO/NCDs@Au/ITO biosensor in the presence of (a-i): 0, 0.001, 0.002, 0.006, 0.06, 0.6, 3.0, 30, 300 ng $mL^{-1}$; The plot of (B) $\Delta I_{PCE}$ versus the logarithm values of $C_{AFP}$ (log $C_{AFP}$); (C) Time–based photocurrent response of BSA/Ab/CuO/NCDs@Au/ITO biosensor in the presence of 0.005 ng $mL^{-1}$ AFP in 0.1 M PBS (pH 7.4) with light on and off cycles; (D) The photocurrent responses of five separate modified electrode of CuO/NCDs@Au/ITO in 0.1 M PBS (pH 7.4).

than 5.0 %) (Fig. S8C) with a LOD value of $8.1 \times 10^{-4}$ ng $mL^{-1}$ (S/N = 3). Through a comparison of these DPV results and other analysis methods (shown in Table S1), the proposed PEC biosensor displayed a better detection performance.

### 3.6. Stability, reproducibility, and selectivity of PEC biosensor

Fig. 6C showed the stability of the fabricated PEC biosensor. It was found that the photocurrent response had no significant variation after the biosensor incubation with 0.005 ng $mL^{-1}$ AFP under irradiation cycles for 400 s (ten on/off), demonstrating the PEC biosensor had long-term stability for AFP analysis. The photocurrent responses of five separate as-constructed electrodes of CuO/NCDs@Au/ITO were investigated and the obtained relative standard deviation (RSD) was 2.73 % (Fig. 6D), indicating that the CuO/NCDs@Au/ITO modified electrodes possessed excellent reproducibility.

In Fig. S8A, the selectivity of the as-prepared PEC sensor was also evaluated by measuring the photocurrent response with other interfering substances such as 0.06 ng $mL^{-1}$ CEA (carcinoembryonic antigen), PSA (prostate-specific antigen), BSA, and the mixture (0.06 ng $mL^{-1}$ AFP + 50 ng $mL^{-1}$ BSA), respectively. It could be seen that the almost same photocurrent responses are as the blank solution, suggesting that the proposed PEC biosensor had high specificity for the AFP detection.

### 3.7. Preliminary analysis for real samples

To further investigate the feasibility of the PEC sensor for AFP detection, the human serum samples were monitored by a standard addition method. First, the blood serum samples (provided by the Hospital of Shantou University) were diluted tenfold with 0.01 M PBS (pH 7.4). Then, different concentrations of AFP were respectively added into the human serum and measured by the prepared biosensor (Table S2). It could be found that after replacement of AFP with pure blood serum the photocurrent response had no significant effect on the detection result. When the sensing electrode was incubated with blood serum samples containing different AFP concentrations (1, 5, 10, 50 and 100 ng $mL^{-1}$), the recovery ranged between 112.6 % and 94.7 % were acceptable. And the obtained relative standard deviation (RSD) value of less than 3.77 %, which indicated that the proposed PEC platform had reliable applicability in clinical analyses for AFP detection.

## 4. Conclusions

In this paper, we proposed a novel type-II heterostructure nanocomposite of CuO/NCDs@Au to fabricate PEC platform (BSA/Ab/CuO/NCDs@Au/ITO) for A FP detection. Benefiting from the porous hollow and thin-shape structure of the CuO particles could reinforce a significant harvest of the visible light due to its multiple scattering and reflection mechanism. As well as, specific surface areas from the hollow structure of CuO were readily combined with nanoflower photoactive material of NCDs@Au to form a useful heterogeneous composite for enhancing the photocurrent output. Moreover, incorporated Au nanoparticles performed as an effective electron acceptor for CuO could accelerate the photo-generated carrier migration and separation effectively. This structured PEC biosensor displayed a better analytical property for AFP target detection than the electrochemical method obtained through comparing their detection linear range and LOD values. The designed PEC sensor also exhibited high stability, good selectivity, and satisfying reproducibility in AFP detection. Based on the outstanding photon-to-electricity conversion performance, CuO/NCDs@Au nanocomposite may enlighten more MOFs-derived products for building worthy heterojunction photoactive materials in other PEC fields.

## Declaration of Competing Interest

The authors declare that they have no known competing financial interests or personal relationships that could have appeared to influence the work reported in this paper.

## Data availability

No data was used for the research described in the article.

## Acknowledgements

We are grateful for the financial support from Guangdong Basic and Applied Basic Research Foundation (No. 2019A1515010618), the Guangdong Special Funds for the Science & Technology Project (No. 2019ST029 & No. 2019ST089), 2020 Li Ka Shing Foundation Cross-Disciplinary Research Grant (Project Number 2020LKSFG06C) and Shantou Polytechnic Supported Project (No. 2019SZK2019Y01).

## Appendix A. Supplementary data

Supplementary data to this article can be found online at https://doi.org/10.1016/j.microc.2022.107779.

## References

[1] J. Li, T. Gao, S. Gu, J. Zhi, J. Yang, G. Li, An electrochemical biosensor for the assay of alpha-fetoprotein-L3 with practical applications, Biosens. Bioelectron. 87 (2017) 352–357.
[2] Q. Li, D. Liu, L. Xu, R. Xing, W. Liu, K. Sheng, H. Song, Wire-in-tube IrOx architectures: alternative label-free immunosensor for amperometric immunoassay toward alpha-fetoprotein, ACS Appl. Mater. Interfaces 7 (2015) 22719–22726.
[3] Z.-J. Huang, W.-D. Han, Y.-H. Wu, X.-G. Hu, Y.-N. Yuan, W. Chen, H.-P. Peng, A.-L. Liu, X.-H. Lin, Magnetic electrochemiluminescent immunoassay with quantum dots label for highly efficient detection of the tumor marker α-fetoprotein, J. Electroanal. Chem. 785 (2017) 8–13.
[4] Y. Zhai, D. Liu, Y. Jiang, X. Chen, L. Shao, J. Li, K. Sheng, X. Zhang, H. Song, Near-infrared-light-triggered photoelectrochemical biosensor for detection of alpha-fetoprotein based on upconversion nanophosphors, Sens. Actuators B Chem. 286 (2019) 468–475.
[5] X. Mo, Y. Wang, Q. Xiao, X. Zhou, H. Li, Conjugated polymer sensitized hyperbranched titanium dioxide based photoelectrochemical biosensor for detecting AFP in serum, Surf. Interfaces 24 (2021), 101103.
[6] H. Ren, T. Dittrich, H. Ma, J.N. Hart, S. Fengler, S. Chen, Y. Li, Y. Wang, F. Cao, M. Schieda, Y.H. Ng, Z. Xie, X. Bo, P. Koshy, L.R. Sheppard, C. Zhao, C.C. Sorrell, Manipulation of charge transport by metallic $V_{13}O_{16}$ decorated on bismuth vanadate photoelectrochemical catalyst, Adv. Mater. 31 (2019) 1807204.
[7] X. Yu, Y. Wang, X. Chen, K. Wu, D. Chen, M. Ma, Z. Huang, W. Wu, C. Li, White-light-exciting, layer-by-layer-assembled ZnCdHgSe quantum dots/polymerized ionic liquid hybrid film for highly sensitive photoelectrochemical immunosensing of neuron specific enolase, Anal. Chem. 87 (8) (2015) 4237–4244.
[8] F. Wu, Y. Yu, H. Yang, L.N. German, Z. Li, J. Chen, W. Yang, L. Huang, W. Shi, L. Wang, X. Wang, Simultaneous enhancement of charge separation and hole transportation in a $TiO_2$–$SrTiO_3$ core–shell nanowire photoelectrochemical system, Adv. Mater. 29 (2017) 1701432.
[9] A. Kargar, K.e. Sun, Y.i. Jing, C. Choi, H. Jeong, Y. Zhou, K. Madsen, P. Naughton, S. Jin, G.Y. Jung, D. Wang, Tailoring n-ZnO/p-Si branched nanowire heterostructures for selective photoelectrochemical water oxidation or reduction, Nano Lett. 13 (7) (2013) 3017–3022.
[10] Z. Zhang, C. Zhao, S. Lin, H. Li, Y. Feng, X. Gao, Oxygen vacancy modified Bi2MoO6/WO3 electrode with enhanced photoelectrocatalytic degradation activity toward RhB, Fuel 285 (2021), 119171.
[11] J.A. Nasir, Z.u. Rehman, S.N.A. Shah, A. Khan, I.S. Butler, C.R.A. Catlow, Recent developments and perspectives in CdS-based photocatalysts for water splitting, J. Mater. Chem. A 8 (40) (2020) 20752–20780.
[12] F. Li, Y.L. Zhou, S.Y. Wang, H.S. Yin, Y. Chen, H.Y. Luo, S.Y. Ai, One step preparation of CN-$WS_2$ nanocomposite with enhanced photoactivity and its application for photoelectrochemical detection of 5-formylcytosine in the genomic DNA of maize seedling, Biosens. Bioelectron. 151 (2020), 111973.
[13] S. Lv, K. Zhang, L. Zhu, D. Tang, ZIF-8-assisted NaYF4:Yb, Tm@ZnO converter with exonuclease III-powered DNA walker for near-infrared light responsive biosensor, Anal. Chem. 92 (2020) 1470–1476.
[14] Y. Wang, X. Yu, X. Ye, K. Wu, T. Wu, C. Li, Resonance energy transfer between ZnCdHgSe quantum dots and gold nanorods enhancing photoelectrochemical immunosensing of prostate specific antigen, Anal. Chim. Acta 943 (2016) 106–113.
[15] Y.i. Lu, X.-L. Liu, L.i. He, Y.-X. Zhang, Z.-Y. Hu, G.e. Tian, X. Cheng, S.-M. Wu, Y.-Z. Li, X.-H. Yang, L.-Y. Wang, J.-W. Liu, C. Janiak, G.-G. Chang, W.-H. Li, G. Van

Tendeloo, X.-Y. Yang, B.-L. Su, Spatial heterojunction in nanostructured $TiO_2$ and its cascade effect for efficient photocatalysis, Nano Lett. 20 (5) (2020) 3122–3129.
[16] X. Zhang, J. Peng, Y. Song, Y. Chen, F. Lu, W. Gao, Porous hollow carbon nanobubbles@ZnCdS multi-shelled dodecahedral cages with enhanced visible-light harvesting for ultrasensitive photoelectrochemical biosensors, Biosens. Bioelectron. 133 (2019) 125–132.
[17] C. Xia, H. Wang, J.K. Kim, J. Wang, Rational design of metal oxide-based heterostructure for efficient photocatalytic and photoelectrochemical systems, Adv. Funct. Mater. 31 (12) (2021) 2008247.
[18] X. Gao, H.B. Wu, L. Zheng, Y. Zhong, Y. Hu, X.W.D. Lou, Formation of mesoporous heterostructured $BiVO_4/Bi_2S_3$ hollow discoids with enhanced photoactivity, Angew. Chem. Int. Ed. 126 (2014) 6027–6031.
[19] X. Zhang, J. Peng, Y. Ding, D. Zheng, Y. Lin, Y. Chen, W. Gao, Rationally designed hierarchical hollow ZnCdS@$MoS_2$ heterostructured cages with efficient separation of photogenerated carriers for photoelectrochemical aptasensing of lincomycin, Sens. Actuators B Chem. 306 (2020), 127552.
[20] F.M. Pesci, M.S. Sokolikova, C. Grotta, P.C. Sherrell, F. Reale, K. Sharda, N.a. Ni, P. Palczynski, C. Mattevi, $MoS_2/WS_2$ heterojunction for photoelectrochemical water oxidation, ACS Catal. 7 (8) (2017) 4990–4998.
[21] Y.J. Hwang, A. Boukai, P. Yang, High density n-Si/n-$TiO_2$ core/shell nanowire arrays with enhanced photoactivity, Nano Lett. 9 (1) (2009) 410–415.
[22] X. Xu, R. Ray, Y. Gu, H.J. Ploehn, L. Gearheart, K. Raker, W.A. Scrivens, Electrophoretic analysis and purification of fluorescent single-walled carbon nanotube fragments, J. Am. Chem. Soc. 126 (40) (2004) 12736–12737.
[23] P. Supchocksoonthorn, N. Thongsai, W. Wei, P. Gopalan, P. Paoprasert, Highly sensitive and stable sensor for the detection of capsaicin using electrocatalytic carbon dots grafted onto indium tin oxide, Sensors and Actuators B: Chemical 329 (2021), 129160.
[24] C. Liu, D. Lu, X. You, G. Shi, J. Deng, T. Zhou, Carbon dots sensitized lanthanide infinite coordination polymer nanoparticles: Towards ratiometric fluorescent sensing of cerebrospinal Abeta monomer as a biomarker for Alzheimer's disease, Anal. Chim. Acta 1105 (2020) 147–154.
[25] D.N. Nguyen, G.S. Gund, M.G. Jung, S.H. Roh, J. Park, J.K. Kim, H.S. Park, Core-Shell Structured MXene@Carbon Nanodots as Bifunctional Catalysts for Solar-Assisted Water Splitting, ACS Nano 14 (12) (2020) 17615–17625.
[26] M. Vázquez-González, W.-C. Liao, R. Cazelles, S. Wang, X.u. Yu, V. Gutkin, I. Willner, Mimicking horseradish peroxidase functions using $Cu^{2+}$-modified carbon nitride nanoparticles or $Cu^{2+}$-modified carbon dots as heterogeneous Catalysts, ACS Nano. 11 (3) (2017) 3247–3253.
[27] G. Zhang, Q. Ji, Z. Wu, G. Wang, H. Liu, J. Qu, J. Li, Facile "spot-heating" synthesis of carbon dots/carbon nitride for solar hydrogen evolution synchronously with contaminant decomposition, Adv. Funct. Mater. 28 (2018) 1706462.
[28] L. Hu, Y. Sun, Y. Zhou, L. Bai, Y. Zhang, M. Han, H. Huang, Y. Liu, Z. Kang, Nitrogen and sulfur co-doped chiral carbon quantum dots with independent photoluminescence and chirality, Inorg. Chem. Front. 4 (6) (2017) 946–953.
[29] H. Han, F. Karlicky, S. Pitchaimuthu, S.H.R. Shin, A. Chen, Highly ordered N-doped carbon dots photosensitizer on Metal-Organic Framework-decorated ZnO nanotubes for improved photoelectrochemical water splitting, Small 15 (2019) 1902771.
[30] W. Cheng, Z. Zheng, J. Yang, M. Chen, Q. Yao, Y. Chen, W. Gao, The visible light-driven and self-powered photoelectrochemical biosensor for organophosphate pesticides detection based on nitrogen doped carbon quantum dots for the signal amplification, Electrochim. Acta 296 (2019) 627–636.
[31] R. Shi, Z.i. Li, H. Yu, L.u. Shang, C. Zhou, G.I.N. Waterhouse, L.-Z. Wu, T. Zhang, Effect of nitrogen doping level on the performance of N-doped carbon quantum dot/$TiO_2$ composites for photocatalytic hydrogen evolution, ChemSusChem 10 (22) (2017) 4650–4656.
[32] Q. Huang, X. Lin, J.J. Zhu, Q.X. Tong, Pd-Au@carbon dots nanocomposite: Facile synthesis and application as an ultrasensitive electrochemical biosensor for determination of colitoxin DNA in human serum, Biosens. Bioelectron. 94 (2017) 507–512.
[33] M. Woellner, S. Hausdorf, N. Klein, P. Mueller, M.W. Smith, S. Kaskel, Adsorption and detection of hazardous trace gases by metal-organic frameworks, Adv. Mater. 30 (2018) 1704679.
[34] F. Leng, H. Liu, M. Ding, Q.-P. Lin, H.-L. Jiang, Boosting photocatalytic hydrogen production of porphyrinic MOFs: the metal location in metalloporphyrin matters, ACS Catal. 8 (2018) 4583–4590.
[35] Y. Ding, X. Zhang, J. Peng, D. Zheng, X. Zhang, Y. Song, Y. Chen, W. Gao, Ultra-sensitive electrochemiluminescence platform based on magnetic metal-organic framework for the highly efficient enrichment, Sens. Actuators B Chem. 324 (2020), 128700.
[36] W.P. Lustig, S. Mukherjee, N.D. Rudd, A.V. Desai, J. Li, S.K. Ghosh, Metal-organic frameworks: functional luminescent and photonic materials for sensing applications, Chem. Soc. Rev. 46 (2017) 3242–3285.
[37] R. Tang, S. Zhou, Z. Yuan, L. Yin, Metal-organic framework derived $Co_3O_4/TiO_2$/Si heterostructured nanorod array photoanodes for efficient photoelectrochemical water oxidation, Adv. Funct. Mater. 27 (2017) 1701102.
[38] X. Zhao, J. Feng, J. Liu, J. Lu, W. Shi, G. Yang, G. Wang, P. Feng, P. Cheng, Metal-organic framework-derived ZnO/ZnS heteronanostructures for efficient visible-light-driven photocatalytic hydrogen production, Adv. Sci. 5 (2018) 1700590.
[39] G. Huang, Q. Li, D. Yin, L. Wang, Hierarchical porous Te@$ZnCo_2O_4$ nanofibers derived from Te@metal-organic frameworks for superior lithium storage capability, Adv. Funct. Mater. 27 (2017) 1604941.
[40] R. Tang, S. Zhou, H. Li, R. Chen, L. Zhang, L. Yin, Halogen bonding induced aqueously stable CsPbBr 3@MOFs-derived $C_o3_O4$/N-doped-C heterostructure for high-performance photoelectrochemical water oxidation, Appl. Catal. B Environ. 265 (2020), 118583.
[41] X.S. Hu, C. Li, X.B. Lou, Q. Yang, B.W. Hu, Hierarchical CuO octahedra inherited from copper metal-organic frameworks: high-rate and high-capacity lithium-ion storage materials stimulated by pseudocapacitance, J. Mater. Chem. A 5 (2017) 12828–12837.
[42] B. Qiu, Q. Zhu, M. Du, L. Fan, M. Xing, J. Zhang, Efficient solar light harvesting CdS/$Co_9S_8$ hollow cubes for z-scheme photocatalytic water splitting, Angew. Chem. Int. Ed. 56 (10) (2017) 2684–2688.
[43] Q. Wang, F. Gao, B. Xu, F. Cai, F. Zhan, F. Gao, Q. Wang, ZIF-67 derived amorphous $CoNi_2S_4$ nanocages with nanosheet arrays on the shell for a high-performance asymmetric supercapacitor, Chem. Eng. J. 327 (2017) 387–396.
[44] H. Li, J. Li, Y. Zhu, W. Xie, R. Shao, X. Yao, A. Gao, Y. Yin, Cd(2+)-doped amorphous $TiO_2$ hollow spheres for robust and ultrasensitive photoelectrochemical sensing of hydrogen sulfide, Anal. Chem. 90 (8) (2018) 5496–5502.
[45] S. Wang, Y. Wang, S.L. Zhang, S.Q. Zang, X.W.D. Lou, Supporting ultrathin $ZnIn_2S_4$ nanosheets on Co/N-doped graphitic carbon nanocages for efficient photocatalytic $H_2$ generation, Adv. Mater. 31 (2019) 1903404.
[46] J. Peng, J. Yang, B. Chen, S. Zeng, D. Zheng, Y. Chen, W. Gao, Design of ultrathin nanosheet subunits $ZnIn_2S_4$ hollow nanocages with enhanced photoelectric conversion for ultrasensitive photoelectrochemical sensing, Biosens. Bioelectron. 175 (2021), 112873.
[47] L. Zhang, L. Feng, P. Li, X. Chen, J. Jiang, S. Zhang, C. Zhang, A. Zhang, G. Chen, H. Wang, Direct Z-scheme photocatalyst of hollow CoSx@CdS polyhedron constructed by ZIF-67-templated one-pot solvothermal route: a signal-on photoelectrochemical sensor for mercury (II), Chem. Eng. J. 395 (2020), 125072.
[48] Q. Wang, Y. Yang, F. Gao, J. Ni, Y. Zhang, Z. Lin, Graphene oxide directed one-step synthesis of flowerlike graphene@HKUST-1 for enzyme-free detection of hydrogen peroxide in biological samples, ACS Appl. Mater. Interfaces 8 (47) (2016) 32477–32487.
[49] Z.i. Li, H. Yu, T. Bian, Y. Zhao, C. Zhou, L.u. Shang, Y. Liu, L.-Z. Wu, C.-H. Tung, T. Zhang, Highly luminescent nitrogen-doped carbon quantum dots as effective fluorescent probes for mercuric and iodide ions, J. Mater. Chem. C 3 (9) (2015) 1922–1928.
[50] S.-Y. Chui, S.-F. Lo, J.P.H. Charmant, A.G. Orpen, I.D. Williams, A chemically functionalizable nanoporous material $[Cu_3(TMA)_2(H_2O)_3]n$, Science 283 (5405) (1999) 1148–1150.
[51] Y. Wang, Y. Lü, W. Zhan, Z. Xie, Q. Kuang, Z. Lansun, Synthesis of porous $Cu_2O$/CuO cages using Cu-based metal-organic-framework as templates and their gas-sensing properties, J. Mater. Chem. A 3 (2015) 12796–12803.
[52] G. Hu, C.-X. Hu, Z.-Y. Zhu, L. Zhang, Q. Wang, H.-L. Zhang, Construction of Au/CuO/$Co_3O_4$ tricomponent heterojunction nanotubes for enhanced photocatalytic oxygen evolution under visible light irradiation, ACS Sustainable Chem. Eng. 6 (7) (2018) 8801–8808.
[53] A. Cots, P. Bonete, R. Gómez, Improving the stability and efficiency of CuO photocathodes for solar hydrogen production through modification with Iron, ACS Appl. Mater. Interfaces 10 (31) (2018) 26348–26356.
[54] Y. Yang, Q. Wang, W. Qiu, H. Guo, F. Gao, Covalent immobilization of $Cu_3(btc)_2$ at chitosan-electroreduced graphene oxide hybrid film and its application for simultaneous detection of dihydroxybenzene isomers, J. Phys. Chem. C 120 (18) (2016) 9794–9803.
[55] Q. Hu, J. Yang, Z. Zheng, Y. Ding, Y. Chen, W. Gao, In situ $H_2O_2$ generation with gold nanoflowers as the coreactant accelerator for enzyme-free electrochemiluminescent immunosensing, Biosens. Bioelectron. 143 (2019), 111627.
[56] Ö. Metin, X. Sun, S. Sun, Monodisperse gold-palladium alloy nanoparticles and their composition-controlled catalysis in formic acid dehydrogenation under mild conditions, Nanoscale 5 (3) (2013) 910–912.

中国科学院武汉科技查新咨询检索中心

# 检 索 报 告

编号：2022-LD-00030421

委托单位：汕头职业技术学院

委 托 人：林惠标

检索要求：发表通讯作者论文“Use of Parallel ResNet for High-Performance Pavement Crack Detection and Measurement”被SCIE收录与2020年JCR数据库分区情况

检 索 结 果

| 数据库 | 论文收录（篇） | | | | |
|---|---|---|---|---|---|
| SCIENCE CITATION INDEX-EXPANDED | 1 | | | | |
| | 2020年JCR数据库分区情况 | | | | |
| Journal Citation Reports（JCR） | 分区 | 1 | 2 | 3 | 4 |
| | 篇数 | 0 | 1 | 0 | 0 |



说明：*JCR影响因子具体情况见附件；*每种期刊位于不同学科时其分区情况是变化的，当同一种期刊处于不同学科产生不同分区时，取分区高的进行统计。具体分区情况见附件。*通讯作者统计SCIE中Corresponding Address或Email地址中的作者论文。

| 声明 | 委托人接受本证明，视为已对本证明所列论文逐篇核对，确认无误，若有不实，由委托人承担全部责任。 | | | |
|---|---|---|---|---|
| 检索人 | 罗丹 | | 审核人 | |

中国科学院武汉科技查新咨询检索中心

（公章）

2022-03-04

联系人：罗 丹 联系电话：027-87197719

邮箱：chaxin@mail.whlib.ac.cn

主页：www.whlib.ac.cn

地址：武汉市武昌区小洪山西25号

# 检索附件：SCIE 收录论文情况

第 1 条，共 1 条
标题: Use of Parallel ResNet for High-Performance Pavement Crack Detection and Measurement
作者: Fan, Z (Fan, Zhun); Lin, HB (Lin, Huibiao); Li, C (Li, Chong); Su, J (Su, Jian); Bruno, S (Bruno, Salvatore); Loprencipe, G (Loprencipe, Giuseppe)
来源出版物: SUSTAINABILITY 卷: 14 期: 3 文献号: 1825 DOI: 10.3390/su14031825 出版年: FEB 2022
Web of Science 核心合集中的 "被引频次": 0
被引频次合计: 0
入藏号: WOS:000757214500001
语言: English
文献类型: Article
地址: [Fan, Zhun; Lin, Huibiao; Li, Chong] Key Lab Digital Signal & Image Proc Guangdong Pro, Shantou 515063, Peoples R China.
[Fan, Zhun; Lin, Huibiao; Li, Chong] Shantou Univ, Coll Engn, Shantou 515063, Peoples R China.
[Lin, Huibiao] Shantou Polytech, Dept Mech & Elect Engn, Shantou 515078, Peoples R China.
[Su, Jian] Guangzhou Environm Protect Investment Nansha Envi, Guangzhou 511470, Peoples R China.
[Bruno, Salvatore; Loprencipe, Giuseppe] Sapienza Univ, Dept Civil Construct & Environm Engn, Via Eudossiana 18, I-00184 Rome, Italy.
通讯作者地址: Lin, HB (通讯作者)，Key Lab Digital Signal & Image Proc Guangdong Pro, Shantou 515063, Peoples R China.
Lin, HB (通讯作者)，Shantou Univ, Coll Engn, Shantou 515063, Peoples R China.
Lin, HB (通讯作者)，Shantou Polytech, Dept Mech & Elect Engn, Shantou 515078, Peoples R China.
Loprencipe, G (通讯作者)，Sapienza Univ, Dept Civil Construct & Environm Engn, Via Eudossiana 18, I-00184 Rome, Italy.
电子邮件地址: zfan@stu.edu.cn; 13hblin@stu.edu.cn; 15cli@stu.edu.cn; sujian@grandtop.com.cn; salvatore.bruno@uniroma1.it; giuseppe.loprencipe@uniroma1.it
研究方向: Science & Technology - Other Topics; Environmental Sciences & Ecology
IDS 号: ZC0IL
eISSN: 2071-1050
期刊影响因子 ™
2020
3.251
五年
3.473

| JCR 学科类别 | 类别排序 | 类别分区 |
|---|---|---|
| ENVIRONMENTAL SCIENCES<br>其中 SCIE 版本 | 124/274 | Q2 |
| ENVIRONMENTAL SCIENCES<br>其中 SCIE 版本 | 124/274 | Q2 |
| GREEN & SUSTAINABLE SCIENCE & TECHNOLOGY<br>其中 SCIE 版本 | 30/44 | Q3 |
| GREEN & SUSTAINABLE SCIENCE & TECHNOLOGY<br>其中 SCIE 版本 | 30/44 | Q3 |

（END）

# 汕头大学图书馆

## 文献收录情况检索报告

委托人姓名：邓勇
委托人单位：工学院

**文献检索清单**（检索数据库详细记录附后）

| 文献 1 | | | |
|---|---|---|---|
| 标题 | Structural material with designed thermal twist for a simple actuation | | |
| 作者 | Nan Yang, Yong Deng, Jinlun Huang, Xiaodong Niu | | |
| 来源信息 | NANOTECHNOLOGY REVIEWS Volume: 11 Issue: 1 Pages: 414-422<br>Published: JAN 10 2022 ISSN: 2191-9089 | | |
| 检索数据库 | ☑SCI-E ☐SSCI ☐A&HCI | | |
| 入藏号 | WOS: 000740801800001 | 备注 | 中科院分区：工程技术 2 区，JCR: Q1<br>影响因子：7.848 |
| 委托人在作者中排名情况 | ☐第一作者 | ☑通讯作者 | ☐其他：第___作者 |

检索单位：汕头大学图书馆（盖 章）

检 索 人：（签字）

检索日期：**2022.3.4**

## Web of Science™

1 record(s) printed from Clarivate Web of Science

**Record 1 of 1**

**Title:** Structural material with designed thermal twist for a simple actuation

**Author(s):** Yang, N (Yang, Nan); Deng, Y (Deng, Yong); Huang, JL (Huang, Jinlun); Niu, XD (Niu, Xiaodong)

**Source:** NANOTECHNOLOGY REVIEWS **Volume:** 11 **Issue:** 1 **Pages:** 414-422 **DOI:** 10.1515/ntrev-2022-0026 **Published:** JAN 10 2022



**Cited Reference Count:** 45

**Abstract:** Materials with desired thermal deformation are very important for various engineering applications. Here, a material with the combination of chiral structure and TiNi shape memory alloy (SMA) sheets that performs a twist during heating is proposed. The thermo-mechanical properties of these materials are experimentally investigated. Inspired by this, a car-like material performing translational and rotational motion is designed, which illustrates the potential applications for the next-generation soft robotic devices. Based on this method, one can design remotely manipulated artificial muscles, nanorobots, revolute pairs, and thermal sensors or actuators in a noncontact fashion.

**Accession Number:** WOS:000740801800001

**Language:** English

**Document Type:** Article

**Author Keywords:** heat-driven actuators; kinematics properties; coupled thermo-mechanical properties; chiral structures; shape memory alloys

**KeyWords Plus:** MEMORY; DEFORMATION; FABRICATION; RESISTANCE

**Addresses:** [Yang, Nan; Deng, Yong; Huang, Jinlun; Niu, Xiaodong] Shantou Univ, Minist Educ, Intelligent Mfg Key Lab, Shantou 515063, Peoples R China.
[Deng, Yong] Shantou Polytech, Digital Technol Res & Applicat Ctr, Shantou 515078, Peoples R China.

**Corresponding Address:** Yang, N; Deng, Y; Niu, XD (corresponding author), Shantou Univ, Minist Educ, Intelligent Mfg Key Lab, Shantou 515063, Peoples R China.
Deng, Y (corresponding author), Shantou Polytech, Digital Technol Res & Applicat Ctr, Shantou 515078, Peoples R China.

**E-mail Addresses:** nyang@stu.edu.cn; dengyong@stu.edu.cn; xdniu@stu.edu.cn



**Publisher:** WALTER DE GRUYTER GMBH

**Publisher Address:** GENTHINER STRASSE 13, D-10785 BERLIN, GERMANY

**Web of Science Index:** Science Citation Index Expanded (SCI-EXPANDED)

**Web of Science Categories:** Chemistry, Multidisciplinary; Nanoscience & Nanotechnology; Materials Science, Multidisciplinary; Physics, Applied

**Research Areas:** Chemistry; Science & Technology - Other Topics; Materials Science; Physics

**IDS Number:** YE0DE

**ISSN:** 2191-9089

**eISSN:** 2191-9097

**29-char Source Abbrev.:** NANOTECHNOL REV

**ISO Source Abbrev.:** Nanotechnol. Rev.

**Source Item Page Count:** 9

**Funding:**

| Funding Agency | Grant Number |
|---|---|
| National Natural Science Foundation of China | 11872046 |
| Natural Science Foundation of Guangdong Province | 2021A1515010318 |
| Tianjin Natural Science Foundation | 18JCZDJC10030 |
| Natural Science Foundation in Shantou University | NTF19012 |
| Key Project of Guangdong Provincial Department of Education | 2021ZDZX2007 |
| Special Foundation of science and technology of Guangdong Province | 2019ST007 |
| CrossDisciplinary Research Funding | 2020LKSFG01D |

The authors thank the National Natural Science Foundation of China (11872046), Natural Science Foundation of Guangdong Province (2021A1515010318), Tianjin Natural Science Foundation (18JCZDJC10030), Natural Science Foundation in Shantou University (NTF19012), Key Project of Guangdong Provincial Department of Education (2021ZDZX2007), Special Foundation of science and technology of Guangdong Province (2019ST007), and CrossDisciplinary Research Funding (2020LKSFG01D).

**Open Access:** gold

**Output Date:** 2022-03-04

End of File

# Road Extraction using High Resolution Satellite Images based on Receptive Field and Improved Deeplabv3+

**Yun Wang, Suye Wang and XueBin Hong**

Department of Computer, Shantou Polytechnic, Shantou,515078, China

984145687@qq.com

**Abstract.** Road extraction from high resolution remote sensing images is an important and challenging computer vision task. This paper presents a road segmentation based on Receptive Field and Improved Deeplabv3+, which obtains the best training image set by calculating the edged energy function after simply clipping. To solve the problem of data homogeneity across as well as convergence, we innovatively use the initialization method Leaky-He to extract the layer backbone network in the network structure. Using the DeepGlobe Road Extraction dataset as the training dataset, the experimental results show that the best mIoU score of the test set is 0.7099, which can improve the results by 0.1919 and 0.1596 in this paper compared with U-Net and D-LinkNet classical networks.

## 1. Introduction

Road extraction from satellite images is a necessary step for many applications, such as vehicle navigation urban planning intelligent transportation, image registration, GIS updates, land use detection, etc. Due to the complexity of the environment around roads in high-resolution images, a variety of focusing algorithms have emerged. Most of these methods can be divided into three categories: generation of road pixel-level markers [1,2], detection of road skeletons [3,4], and a combination of both [5,6].

Road area segmentation is the preliminary task of road extraction, which can be used as guidance of the topology delineation. In recent years, Deep learning methods have been increasingly applied to information extraction from high-resolution satellite images due to their good performance and generalization ability [7,8]. Since Mihi et al. [9] applied deep learning methods to road extraction, other deep learning models have been applied to road extraction research[10,11]. Zhong et al.[12] introduced the fully convolutional network into the segmentation of the road area and achieved dense end-to-end reasoning. But the simple linear interpolation upsampling of FCN made the model performance poor. Evolved from FCN, U-Net has a symmetric encoder-decoder structure, and the decoder uses parameter-learnable deconvolution, which makes the semantic segmentation more accurate. Zhang et al. [13] and Alexander et al. [14] proposed a semantic segmentation road extraction neural network, which uses unit construction with a similar architecture to U-Net, allowing the model to use fewer parameters but obtain better performance. Although the U-Net segmentation algorithm subsamples the road remote sensing image several times, making a large number of image features less, the network does not take into account the perceptual domain of the image and therefore has shortcomings for small target extraction.

# 无檩空间网格结构装配式螺栓球柱节点高温受压性能研究

陈安阳[1],邹小舟[2],陈乐贤[3],何嘉年[3],裘　煜[2],李丽娟[3],罗运海[2],熊　哲[3]
(1.汕头职业技术学院 经济管理系,广东 汕头　515071; 2.广东翔顺建设集团有限公司,
广东 云浮　527400; 3.广东工业大学 土木与交通工程学院,广州　510006)

**摘　要:** 为了填补螺栓球柱节点在高温受压承载性能研究方面的空缺,借助有限元分析软件ABAQUS开展研究。首先,在校核模型可靠性的基础上,进一步提出了更符合实际情况的节点模型;其次,通过147个模型算例探究节点的破坏机理和各关键参数对节点受压承载性能的影响;最后,推导出节点的高温受压承载力公式。研究结果表明:提出的节点模型不仅更符合实际情况,而且对螺栓球柱节点受压性能的评估也更加保守和安全;当温度在300 ℃以内时,节点的初始刚度和承载力变化不明显,当温度大于300 ℃时,节点的初始刚度和承载力出现显著下降;高温下钢材屈服强度的折减系数可以较为准确地预测节点高温受压承载力的变化。

**关键词:** 螺栓球柱节点; 高温; 承载性能; 有限元分析
**中图分类号:** TU 352.1　　**文献标志码:** A　　**文章编号:** 1671－9379(2022)07－0084－13
DOI: 10.13969/j.cnki.cn31-1893.2022.07.010

# A Study on the Compressive Bearing Capacity of Prefabricated Bolted Ball-Cylinder Joints at Elevated Temperatures

*CHEN Anyang*[1], *ZOU Xiaozhou*[2], *CHEN Lexian*[3], *HE Jianian*[3], *QIU Yu*[2],
*LI Lijuan*[3], *LUO Yunhai*[2], *XIONG Zhe*[3]
(1. Department of economic management, Shantou Polytechnic, Shantou 515071, China; 2. Guangdong Xiangshun Construction Group Co., Ltd., Yunfu 527400, China; 3. School of Civil and Transportation Engineering, Guangdong University of Technology, Guangzhou 510006, China)
CHEN Anyang: 929976041@qq.com

**Abstract:** In order to study the compressive bearing capacity of bolted ball-cylinder joints at elevated temperatures, the finite element analysis software ABAQUS is used in this paper. Firstly, for checking the reliability of the model, a more practical joint model is proposed. Secondly, 147 model examples are used to evaluate the failure mechanism and the influence of key parameters on the bearing capacity of the joint. Finally, a formula of compressive bearing capacity at elevated temperatures is proposed. The results show that the proposed joint model is not only more consistent with the actual situation, but also more conservative and safe for evaluating the compressive performance of bolted ball-cylinder joint. When the temperature is less than 300 ℃, the initial stiffness and bearing capacity of the joint does not

收稿日期:2021-05-01;收到修改稿日期:2021-07-15
基金项目:广东省自然科学基金(2018A030310547),广东工业大学大学生创新创业训练计划项目(D202012012004437427)
作者简介:
陈安阳(1995—),男,硕士,主要从事钢结构方面的研究。E-mail:929976041@qq.com。
邹小舟(1978—),男,学士,高级工程师,主要从事土木建筑工程方面的工作。
通信作者:
何嘉年(1981—),男,博士,副教授,主要从事钢结构方面的研究。E-mail:jnhe@gdut.edu.cn。

change significantly. When the temperature is higher than 300 ℃, the initial stiffness and bearing capacity of the joint decreases significantly. The reduction factor of steel yield strength at elevated temperature can accurately predict the change of compressive bearing capacity of joints at elevated temperatures.

**Keywords:** bolted ball-cylinder joint; elevated temperature; bearing capacity; finite element analysis

为了推动空间结构的创新与发展，广大学者长期致力于空间节点的研发与性能研究工作[1-2]。近年来，由于无檩空间网格结构杰出的优越性，螺栓球柱节点作为一种适用于无檩空间网格结构的新型节点而备受关注，具有广阔的应用前景[3-4]。GUO 等[5-6]针对螺栓球柱节点的承载性能开展了大量研究：试验方面，通过 13 个节点试件的加载试验研究，总结了螺栓球柱节点在单向受压、单向受拉以及受弯作用下的破坏模式；数值分析方面，通过有限元分析软件 ABAQUS 进一步探究了节点的承载性能，推导了螺栓球柱节点的单向受压和单向受拉承载力公式。

然而，基于现阶段的研究成果，针对螺栓球柱节点的研究尚存在些许不足。其一，ZENG 等[6]的数值分析中，模型仍考虑了试验加载装置对杆件端部的强约束作用，导致节点在轴向荷载作用下未能发生偏转，表现出来的节点承载性能优于实际情况；其二，节点高温承载性能作为节点研究中的一个重要课题，目前还尚未见到相关报道[7-9]。空间节点的设计不仅要满足承受荷载的基本要求，其抵御火灾的能力也十分关键[10-11]。大量材性试验研究结果表明，钢材在温度超过 300 ℃时，其弹性模量和屈服强度均出现显著下降，当温度超过 600 ℃时则基本失去承载能力[12-13]。因此，开展螺栓球柱节点高温承载性能的研究对于保障结构安全具有重要意义。

为了弥补螺栓球柱节点在研究方面的不足，本文基于有限元分析软件 ABAQUS，建立合理可靠的螺栓球柱节点模型，采用稳态分析的方法，探究螺栓球柱节点在高温受压条件下的承载性能，进而提出其高温受压设计方法。

## 1　模型建立与校对

### 1.1　建模建立

#### 1.1.1　几何尺寸

螺栓球柱节点由空心圆柱体、实心半球体、矩形管、凹端板、凸垫片和高强螺栓等组件组成，如图 1 所示。此外，在模型中设有加载板以模拟试验加载装置。各组件几何尺寸均与文献[3]中试件尺寸一致，完整受压模型如图 2 所示。

#### 1.1.2　材料属性

在赋予各组件材料属性时，将所有组件分为 3 类。第 1 类，空心圆柱体（含加劲肋）、实心半球体、凸垫片和

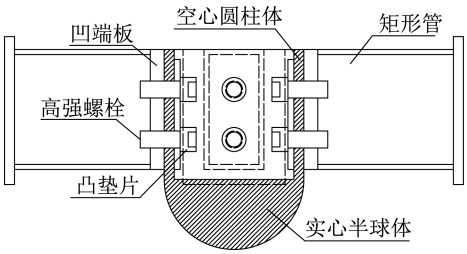


**图 1　螺栓球柱节点构造**

**Fig. 1　Details of bolted ball-cylinder joint**

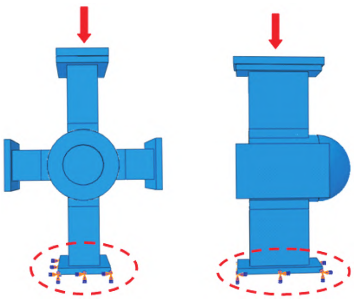

**图 2　螺栓球柱节点受压模型**

**Fig. 2　Compression model of bolted ball-cylinder joint**

矩形管（含凹端板），采用文献[3]中材性试验结果，通过将工程应力和工程应变转换为真实应力和塑性应变得到，采用三折线模型，如图 3a）所示。由材性试验结果可知，钢材的材性数值在一定范围内波动，本次建模取其弹性模量为 197 000 MPa，屈服强度为 195 MPa，抗拉强度为 560 MPa，对应的塑性应变分别为 0.001 和 0.170。第 2 类，10.9 级高强螺栓，根据规范《紧固件机械性能 螺栓、螺钉和螺柱》（GB/T 3098.1—2010）[14]可知，其屈服强度为 1 000×0.9=900 MPa，采用理想弹塑性模型，如图 3b）所示。第 3 类，加载板，将其设为刚度极大的弹性材料，弹性模量取为 $10^3$ 倍的钢材弹性模量。

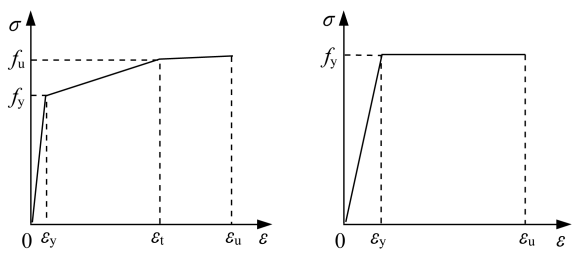


a）三折线模型　　b）理想弹塑性模型

**图 3　钢材本构模型**

**Fig. 3　Constitutive models of steel**

#### 1.1.3 分析步设置

本文通过如表1所示的6个分析步使模型各组件建立起平稳接触，从而模拟节点的受压试验。其中，“10 N”是为了用一个较小的螺栓荷载使各组件建立接触，“5 000 N”是为了模拟实际的螺栓荷载。

**表1 分析步设置**

**Tab. 1 Settings of analysis steps**

| 分析步 | 具体内容 |
|---|---|
| Step1 | 固定节点底部，建立各组件临时约束，施加10 N螺栓荷载 |
| Step2 | 解除临时约束 |
| Step3 | 沿加载方向施加微小的位移荷载 |
| Step4 | 修改螺栓荷载为5 000 N |
| Step5 | 固定螺栓长度 |
| Step6 | 施加实际的位移荷载 |

#### 1.1.4 接触关系

为了模拟各组件间的接触作用，模型中设置了多个接触对。其中，空心圆柱体和实心半球体为一个整体，凹端板与螺栓、加载板与矩形管在加载过程中紧密连接且基本无相对滑动，适用“Tie”约束。其余组件之间采用“表面与表面接触”，由于相对滑动量较小，故选用“小滑移”公式。“表面与表面接触”的接触属性中，切向行为设为“罚”，摩擦系数取为0.2；法向行为设为“硬”接触，并允许接触后分离。此外，还将加载板设为刚体，并设有参考点便于加载。

#### 1.1.5 单元类型与网格划分

8节点线性六面体减缩积分单元(C3D8R)和8节点线性六面体非协调单元(C3D8I)都适用于“小滑移”接触分析。其中，C3D8R对位移的求解结果比较精确，并且在大变形问题中容易收敛，而C3D8I能够克服剪切自锁问题，适用于受弯单元。结合模型加载情况，对空心圆柱体(含加劲肋)、实心半球体、凸垫片、螺栓、加载板采用C3D8R模拟；而凹端板在受压接触过程中，单元容易受弯发生“剪切自锁”，故对矩形管(含凹端板)采用C3D8I模拟。

为了得到较高的计算精度，有必要对各组件采用适当的网格划分技术和单元尺寸。参考文献[5-6]中节点模型的网格划分，本文对部分组件进行网格细化，具体方案如表2所示。

#### 1.1.6 边界条件与荷载

本模型的边界条件主要分为两部分：其一是对加载板的约束，由于试验时加载装置刚度很大且只沿加载方向移动，因此对加载板施加位移约束，限制其两个非加载方向的位移；其二是对模型本身的约束，对受压节点底部设置固定约束，荷载施加在加载板刚体参考点上。

**表2 网格划分方法**

**Tab. 2 Mesh dividing methods**

| 部件名称 | 网格划分技术 | 单元尺寸/mm |
|---|---|---|
| 空心圆柱体(含加劲肋) | 六面体扫略技术与中性轴算法 | 5 |
| 矩形管(含凹端板) | 六面体扫略技术与中性轴算法 | 5 |
| 实心半球体 | 六面体结构划分 | 5 |
| 凸垫片 | 六面体扫略技术与中性轴算法 | 4 |
| 螺栓 | 六面体扫略技术与中性轴算法 | 4 |
| 加载板 | 六面体结构划分 | 12 |

### 1.2 模型校核

本节选取文献[3]中节点JD5进行校核，以验证本次建模的可靠性。

#### 1.2.1 破坏模式

由图4a)、b)可知，有限元模型JD5在压力荷载作用下，空心圆柱体出现明显压扁变形。此外，空心圆柱体另一端由于实心半球体的约束，空心圆柱体壁出现明显弯曲，与试验节点变形一致。由图4c)可知，空心圆柱体在加劲肋处和矩形管压痕区域应力较大，符合节点的受力特征。

a) 节点JD5试验破坏模式

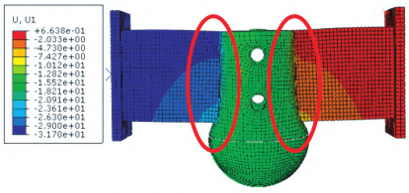


b) 模型JD5变形(单位：mm)

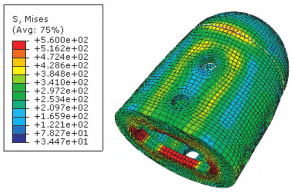


c) 模型JD5应力(单位：MPa)

**图4 节点JD5破坏模式对比[3]**

**Fig. 4 Comparison of failure modes of joint JD5[3]**

### 1.2.2　荷载-位移曲线

本小节从初始刚度和极限承载力两方面对荷载-位移曲线结果进行验证。由于加载前期曲线上升段接近于直线，故选取曲线拐点前一点与原点连线的斜率作为节点的初始刚度。

荷载-位移曲线的对比如图 5 所示。试验得到的极限承载力为 440.66 kN，有限元分析得到的极限承载力为 404.80 kN，相差 −8.14%。此外，试验曲线的初始刚度为 222.67 kN•mm$^{-1}$，有限元曲线的初始刚度为 233.53 kN•mm$^{-1}$，相差 4.88%。由此可见，螺栓球柱节点模型能较为可靠地模拟节点的受压性能。

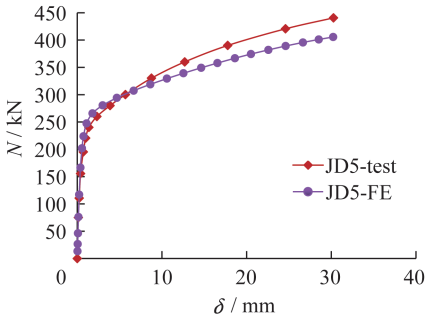


**图 5　节点 JD5 荷载-位移曲线对比**

**Fig. 5　Comparison of load-displacement curves of joint JD5**

## 1.3　实际节点模型

试验过程中，加载装置对杆件端部具有十分强的约束作用。然而，在实际工程中，节点的杆件端部并未受到该约束作用。另外，实际工程设计时，钢材本构往往考虑理想弹塑性模型。故本节基于加载板的约束作用和材料本构模型参数，对节点受压承载性能进行参数分析。

### 1.3.1　边界条件影响

图 6 中，“JD5-N”代表无加载板约束的节点模型。由此可见，对于受压节点 JD5，当解除加载板约束时，节点初始刚度和承载力有所下降，并且曲线伴有峰值出现，加载后期承载力大幅下降。有无加载板约束的节点的荷载-位移曲线具有十分明显的差异，这是破坏模式改变导致的。解除加载板约束后，由于空心圆柱体两端刚度不同（一端有实心半球体约束，另一端没有），在压力荷载作用下节点发生偏转，从而导致失稳，如图 7 所示。

### 1.3.2　材料本构模型影响

图 8 中，“JD5-I”代表采用钢材理想弹塑性模型的节点。如图所示，采用钢材理想弹塑性模型的节点的初始刚度没有发生变化，后期承载力趋于稳定。与采用“三折线模型”的节点相比，采用“理想弹塑性模型”的节点后期承载力较低，对节点受压承载性能的评估更为保守。

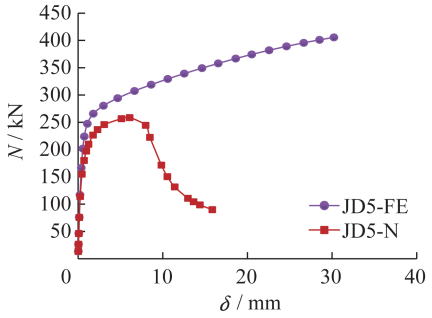


**图 6　加载板约束分析**

**Fig. 6　Constraint analysis of loading plate**

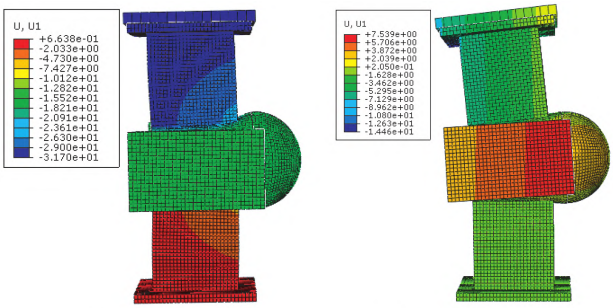

a) 有加载板约束　　b) 无加载板约束

**图 7　有无加载板约束下破坏模式对比（单位：mm）**

**Fig. 7　Comparison of failure modes with and without constraint of loading plate (Unit: mm)**

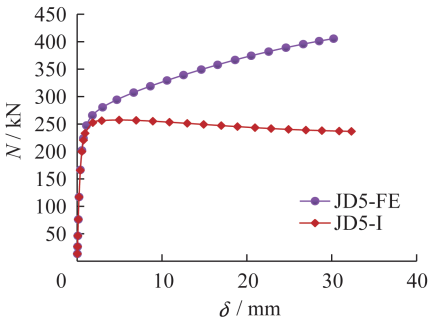


**图 8　钢材本构模型分析**

**Fig. 8　Analysis of constitutive model of steel**

基于上述分析，本文提出不考虑加载板约束且采用钢材理想弹塑性模型的螺栓球柱节点模型用于后续分析。该节点模型不仅符合工程实际，而且在承载性能评估方面具有更高的安全储备。

## 2　高温破坏机理与参数分析

本节基于螺栓球柱节点常温模型，假定高温下节点各组件的温度均匀分布，考虑不同温度下的材性变化，对节点的高温承载性能开展稳态研究。

## 2.1　材料本构

对于理想弹塑性本构模型，弹性模量和屈服强度是影响材料性能的两个关键指标。

#### 2.1.1 结构钢材料高温性能

本文选用Q235钢材进行分析，依据我国《建筑钢结构防火技术规范》(GB 51249—2017)[15]中对高温下结构钢材性的规定，计算钢材弹性模量和屈服强度随温度升高的折减系数，如式(1)和式(2)所示。

$$\chi_T=\begin{cases}\dfrac{7T-4\,780}{6T-4\,760} & 20\ ℃\leqslant T<600\ ℃\\ \dfrac{1\,000-T}{6T-2\,800} & 600\ ℃\leqslant T<1\,000\ ℃\end{cases} \tag{1}$$

$$\eta_T=\begin{cases}1.0 & 20\ ℃\leqslant T<300\ ℃\\ 1.24\times10^{-8}T^3-2.096\times10^{-5}T^2+9.228\times10^{-3}T-0.216\,8 & 300\ ℃\leqslant T<800\ ℃\end{cases} \tag{2}$$

式中：$\chi_T$为高温下钢材的弹性模量折减系数；$T$为钢材的温度；$\eta_T$为高温下钢材的屈服强度折减系数。

#### 2.1.2 高强螺栓材料高温性能

由于我国相关规范中尚未见对10.9级高强螺栓材料高温性能的规定，因此本节基于李国强等[16]的研究成果，得到10.9级高强螺栓材料在高温下弹性模量和屈服强度折减系数的计算公式，分别如式(3)和式(4)所示。

$$\omega_T=\frac{E_T}{E}=6\times10^{-9}T^3-8\times10^{-6}T^2+0.001\,6T+0.943\,3 \tag{3}$$

$$\lambda_T=\frac{f_{yT}}{f_y}=4\times10^{-9}T^3-6\times10^{-6}T^2+0.001\,1T+0.960\,3 \tag{4}$$

式中：$\omega_T$为高温下高强螺栓的弹性模量折减系数；$E_T$为高温下10.9级高强螺栓材料的弹性模量；$E$为常温下10.9级高强螺栓材料的弹性模量；$\lambda_T$为高温下高强螺栓的屈服强度折减系数；$f_{yT}$为高温下10.9级高强螺栓材料的屈服强度；$f_y$为常温下10.9级高强螺栓材料的屈服强度。

### 2.2 参数分析方案

本文通过建立147个节点模型探究螺栓球柱节点的高温受压承载性能，考虑了空心圆柱体外径$D$、空心圆柱体厚度$t$、空心圆柱体高度$H$、矩形管宽度$b_1$、矩形管高度$H_0$以及温度$T$等参数的影响，具体参数如表3所示。其中，温度$T$考虑了20 ℃、100 ℃、200 ℃、300 ℃、400 ℃、500 ℃和600 ℃这7个温度值的影响。

为了便于区分，本文规定下文模型编号中的“C”代表“受压”，“N”代表“节点”，“T”代表“温度”。以“CN1T100”为例，其代表“温度为100 ℃时的受压节点1”。

表3 参数分析方案

Tab. 3 Schemes of parameter analysis 单位：mm

| 模型编号 | $D$ | $t$ | $H$ | $b_1$ | $H_0$ |
|---|---|---|---|---|---|
| CN1T20～CN1T600 | 150 | 10 | 160 | 60 | 120 |
| CN2T20～CN2T600 | 110 | 10 | 160 | 60 | 120 |
| CN3T20～CN3T600 | 130 | 10 | 160 | 60 | 120 |
| CN4T20～CN4T600 | 170 | 10 | 160 | 60 | 120 |
| CN5T20～CN5T600 | 190 | 10 | 160 | 60 | 120 |
| CN6T20～CN6T600 | 150 | 8 | 160 | 60 | 120 |
| CN7T20～CN7T600 | 150 | 9 | 160 | 60 | 120 |
| CN8T20～CN8T600 | 150 | 11 | 160 | 60 | 120 |
| CN9T20～CN9T600 | 150 | 12 | 160 | 60 | 120 |
| CN10T20～CN10T600 | 150 | 10 | 120 | 60 | 120 |
| CN11T20～CN11T600 | 150 | 10 | 130 | 60 | 120 |
| CN12T20～CN12T600 | 150 | 10 | 140 | 60 | 120 |
| CN13T20～CN13T600 | 150 | 10 | 150 | 60 | 120 |
| CN14T20～CN14T600 | 150 | 10 | 160 | 50 | 120 |
| CN15T20～CN15T600 | 150 | 10 | 160 | 55 | 120 |
| CN16T20～CN16T600 | 150 | 10 | 160 | 65 | 120 |
| CN17T20～CN17T600 | 150 | 10 | 160 | 70 | 120 |
| CN18T20～CN18T600 | 150 | 10 | 160 | 60 | 130 |
| CN19T20～CN19T600 | 150 | 10 | 160 | 60 | 140 |
| CN20T20～CN20T600 | 150 | 10 | 160 | 60 | 150 |
| CN21T20～CN21T600 | 150 | 10 | 160 | 60 | 160 |

### 2.3 破坏机理

#### 2.3.1 破坏模式与荷载-位移曲线

通过对147个模型进行数值计算，得到了高温受压条件下各个节点的破坏模式与荷载-位移曲线。分析结果表明，螺栓球柱节点在高温受压条件下的破坏模式并未发生改变，与常温下的破坏模式一致。此外，在高温条件下，螺栓球柱节点的受压承载力出现了不同幅度的下降。以节点CN1为例，其在高温下的荷载-位移曲线如图9所示。由图可知，温度在300 ℃以内时，节点的承载力下降并不明显，各曲线基本重合；当温度大于300 ℃时，节点的承载力均出现显著下降。值得注意的是，21个节点在高温下均表现出上述相同的规律。

#### 2.3.2 失效演化过程

为了揭示螺栓球柱节点的高温受压失效演化过程，本节以CN1T600为例详述节点的破坏过程。如图10所示，图中Ⅰ点对应节点的初始状态，Ⅱ、Ⅲ、Ⅳ和Ⅴ点分别对应了节点加载过程中的4个关键时刻，其对应的节点状态如图11所示。

加载初期(Ⅱ点)，在矩形管的挤压下，空心圆柱体自由端部分材料最先进入屈服。此外，随着空心圆柱体自由端出现变形，矩形管开始发生倾斜。随着荷载的增加(Ⅲ点)，

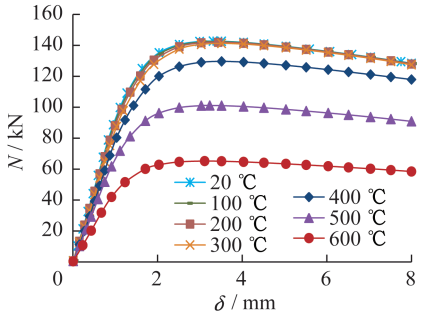


**图 9　节点 CN1 在高温下的荷载-移曲线**

**Fig. 9　Load-displacement curves of joint CN1 at elevated temperatures**

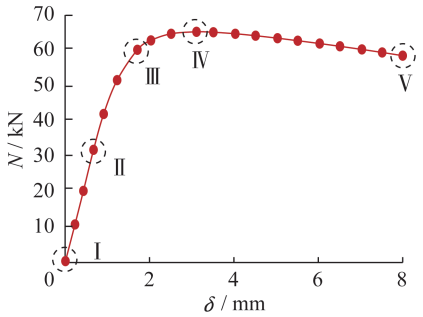


**图 10　模型 CN1T600 荷载-位移曲线**

**Fig. 10　Load-displacement curve of model CN1T600**

空心圆柱体材料在加载矩形管挤压区域内的屈服面积逐渐扩大，并在加载矩形管两端形成塑性铰。空心圆柱体自由端变形继续增加，矩形管倾斜幅度增大。加载中期（Ⅳ点），空心圆柱体自由端材料基本全部屈服，非加载矩形管两端也形成塑性铰，节点承载力达到峰值。此时，空心圆柱体自由端变形明显，矩形管出现明显倾斜。加载后期（Ⅴ点），节点出现过度变形，承载力持续下降。

## 2.4　参数影响

### 2.4.1　空心圆柱体外径的影响

节点 CN1～CN5 在不同温度下的初始刚度和极限承载力变化趋势如图 12 所示。以 600 ℃时的节点数据为例进行分析可知，随着空心圆柱体外径从 110 mm 逐级增长到 190 mm，节点的初始刚度分别逐级下降了 38.44%、25.48%、15.89% 和 11.44%，节点的极限承载力分别逐级下降了 12.08%、8.23%、1.24% 和 1.72%。由此可见，随着空心圆柱体外径的增大，螺栓球柱节点的高温受压初始刚度和极限承载力均降低，并且呈现出先迅速下降后趋于平缓的变化规律。

### 2.4.2　空心圆柱体厚度影响

节点 CN1 和 CN6～CN9 在不同温度下的初始刚度和极限承载力变化趋势如图 13 所示。以 600 ℃时的节点数据为例进行分析可知，当空心圆柱体厚度从 8 mm 增长到 12 mm 时，节点的初始刚度和极限承载力分别增大了 89.24% 和 79.89%。由此可见，空心圆柱体厚度是影响螺栓球柱节点高温受压性能的一个关键因素，节点的高温受压初始刚度和极限承载力随着空心圆柱体厚度的增大有明显提高。

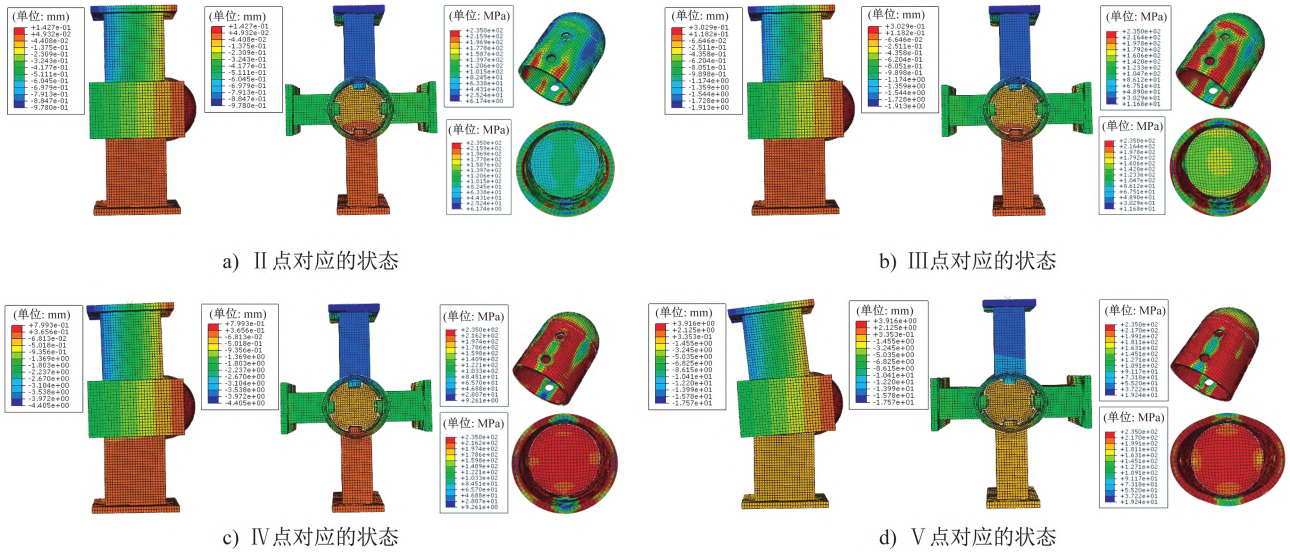


a）Ⅱ点对应的状态　　b）Ⅲ点对应的状态

c）Ⅳ点对应的状态　　d）Ⅴ点对应的状态

**图 11　受压节点破坏过程**

**Fig. 11　Failure processes of compressed joint**

### 2.4.3　空心圆柱体高度影响

节点 CN1 和 CN10～CN13 在不同温度下的初始刚度和极限承载力变化趋势如图 14 所示。以 600 ℃时的节点数据为例进行分析可知，随着空心圆柱体高度从 120 mm 逐级增长到 160 mm，节点的初始刚度分别逐级下降了 8.71%、12.41%、9.09% 和 8.08%，节点的极限承载力分

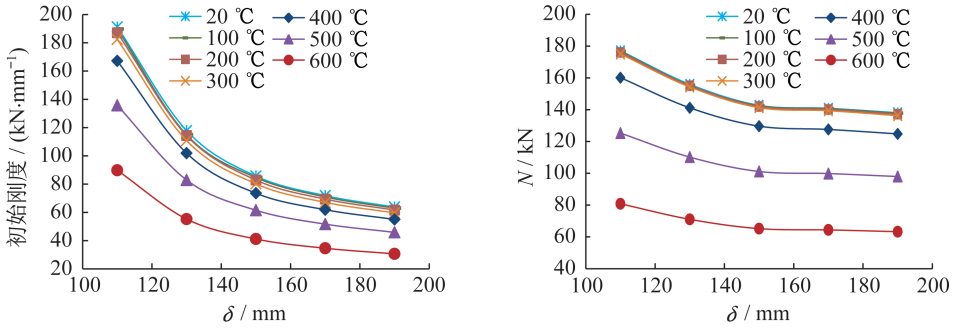


a) 对初始刚度影响　　b) 对承载力影响

**图12　空心圆柱体外径参数分析**

**Fig. 12　Parameter analysis of outer diameter of hollow cylinder**

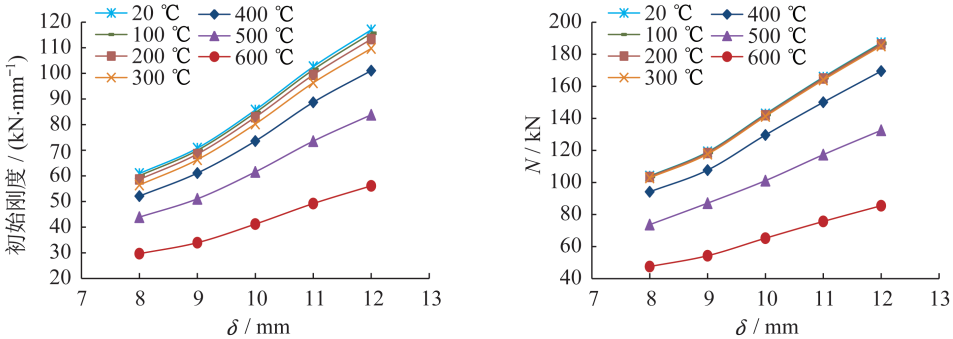


a) 对初始刚度影响　　b) 对承载力影响

**图13　空心圆柱体厚度参数分析**

**Fig. 13　Parameter analysis of thickness of hollow cylinder**

别逐级下降了4.50%、2.67%、1.83%和2.39%。由此可见，随着空心圆柱体高度的增大，螺栓球柱节点的高温受压初始刚度和极限承载力均出现下降，且变化幅度较为接近。

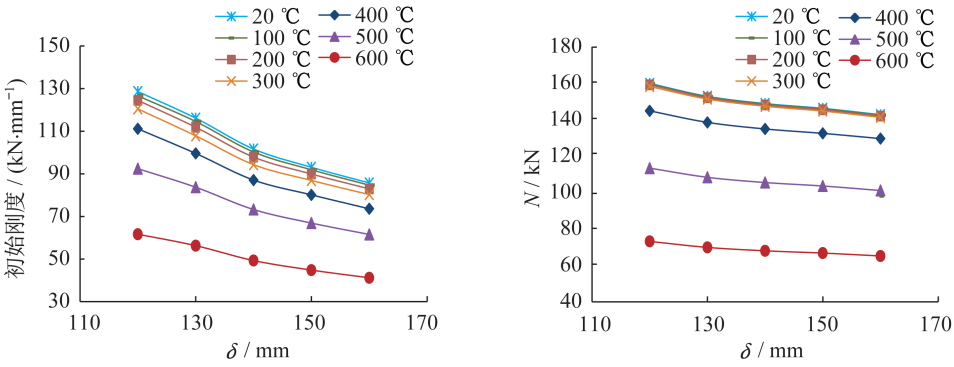


a) 对初始刚度影响　　b) 对承载力影响

**图14　空心圆柱体高度参数分析**

**Fig. 14　Parameter analysis of height of hollow cylinder**

### 2.4.4　矩形管宽度影响

节点CN1和CN14～CN17在不同温度下的初始刚度和极限承载力变化趋势如图15所示。以600 ℃时的节点数据为例分析进行可知，随着矩形管宽度从50 mm逐级增长到70 mm，节点的初始刚度分别逐级提高了5.46%、7.42%、4.24%和10.35%，节点的极限承载力分别逐级提高了7.29%、4.09%、4.34%和3.47%。由此可见，随着矩形管宽度的增大，节点的高温受压初始刚度和极限承载力均有所提高。

### 2.4.5　矩形管高度影响

节点CN1和CN18～CN21在不同温度下的初始刚度和极限承载力变化趋势如图16所示。以600 ℃时的节

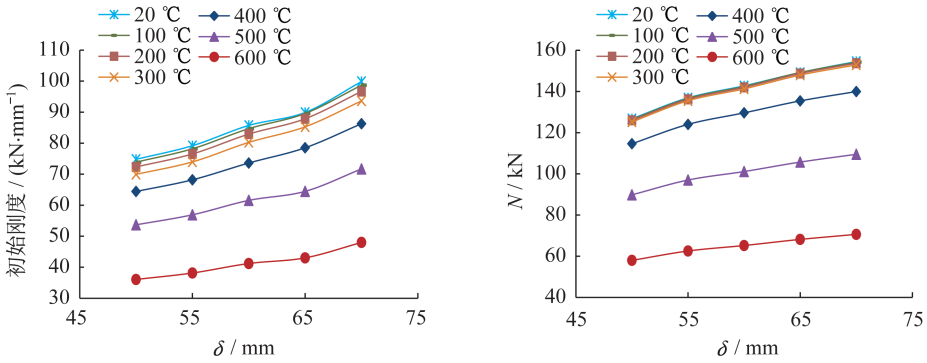


a) 对初始刚度影响　　b) 对承载力影响

**图 15　矩形管宽度参数分析**

**Fig. 15　Parameter analysis of width of rectangular tube**

点数据为例进行分析可知，随着矩形管高度从 120 mm 逐级增长到 160 mm，节点的初始刚度分别逐级提高了 16.45%、12.18%、4.56% 和 6.61%，节点的极限承载力分别逐级提高了 3.17%、7.87%、5.49% 和 5.44%。由此可见，随着矩形管高度的增大，节点的高温受压初始刚度和极限承载力也随之增大。

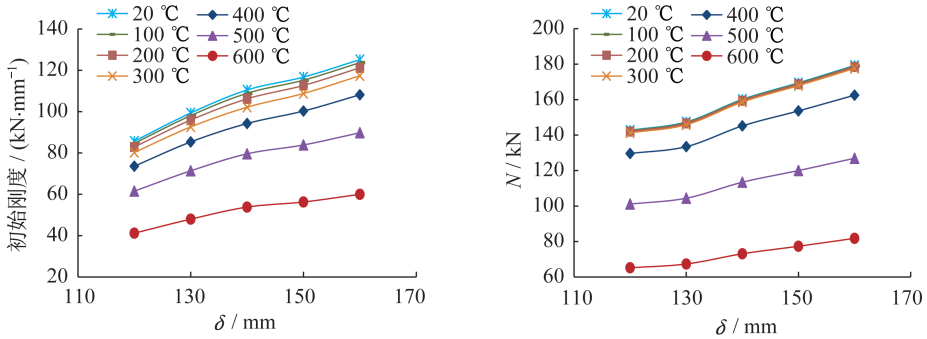


a) 对初始刚度影响　　b) 对承载力影响

**图 16　矩形管高度参数分析**

**Fig. 16　Parameter analysis of height of rectangular tube**

### 2.4.6　温度影响

由图 12～16 可知，在高温下螺栓球柱节点的受压初始刚度和极限承载力呈现出明显的变化规律。当温度在 300 ℃以内时，节点的受压初始刚度和极限承载力曲线十分接近，尤其是承载力曲线基本重合；当温度大于 300 ℃时，节点的受压初始刚度和极限承载力均出现大幅度下降。以节点 CN1 为例，随着温度从 20 ℃逐级增大到 600 ℃，节点的初始刚度分别逐级下降了 0.78%、1.38%、2.51%、8.33%、18.83% 和 33.83%，节点的极限承载力分别逐级下降了 0.20%、0.35%、0.59%、8.51%、21.77% 和 35.47%。

此外，为了探究温度对承载力的影响关系，本小节对比了高温下节点极限承载力的折减系数（高温下节点极限承载力与常温下节点极限承载力的比值）与高温下各材性指标的折减系数，如图 17 所示。图中，$\Psi_{FT}$ 为螺栓球柱节点的高温受压承载力折减系数。可以直观发现，高温受压承载力折减系数曲线与钢材屈服强度折减系数曲线基本重合。这说明在高温分析中，钢材的屈服强度折减系数可以预测温度对螺栓球柱节点极限承载力的影响规律。

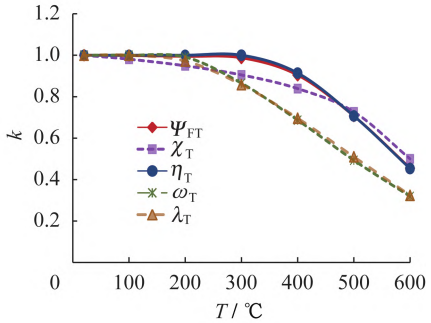


**图 17　折减系数对比**

**Fig. 17　Comparison of reduction coefficient**

## 3　承载力公式

### 3.1　破坏准则

结合 2.3.2 节所述，节点受压过程中会在空心圆柱体

上先后形成多处塑性铰，如图18所示。其中，空心圆柱体上2号塑性铰的形成晚于1号塑性铰的形成，并在2号塑性铰形成时达到承载力峰值。因此，定义节点在空心圆柱体上非加载管方向两端形成塑性铰（即形成2号塑性铰）时发生破坏，对应的承载力即为节点的受压极限承载力，即图10中的Ⅳ点。

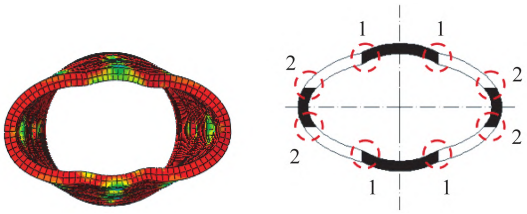


图18 塑性铰分布

Fig. 18 Distribution of plastic hinges

## 3.2 常温承载力公式

空心圆柱体是螺栓球柱节点受压的主要承力组件。在压力荷载作用下，空心圆柱体非加载端受到螺栓和凸垫片的约束作用形成一个刚性区域，且由于垫片宽度对节点受压承载力几乎没有影响，结合空心圆柱体的变形情况，该刚性区域宽度按螺头宽度取值；加载端受到矩形管、螺栓和凸垫片的共同作用形成另一个刚性区域，其宽度为矩形管宽度。受压过程中空心圆柱体先后在如图18所示的“1”和“2”位置处形成塑性铰导致节点失去承载力，此时空心圆柱体材料已经基本全部进入屈服状态。

根据对称性取节点的1/4结构用于分析，如图19a）所示，其中$t'$近似等于空心圆柱体厚度$t$，故按$t$计算。基于ZENG等[6]的研究，本文考虑两个刚性区域的影响，对螺栓球柱节点受压承载力公式进行优化。基于上述分析，可得空心圆柱体的受力简图如图19b）所示。

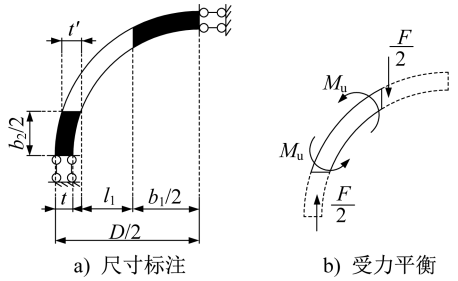


a）尺寸标注 b）受力平衡

图19 1/4节点受力简图

Fig. 19 Force diagram of 1/4 joint

由受力平衡可得式（5）和式（6），进而可推导出节点的受压承载力公式（式（7））。最后，再引入系数$\alpha$对公式进行修正，可得节点的最终承载力公式（式（8））。

$$\frac{F}{2}\left(l_1+\frac{t}{2}\right)=2M_u \tag{5}$$

$$M_u=\frac{H_0t^2f_y}{4} \tag{6}$$

$$F=\frac{2H_0t^2f_y}{2l_1+t} \tag{7}$$

$$F_1=\alpha\frac{2H_0t^2f_y}{2l_1+t} \tag{8}$$

$$l_1=\sqrt{\left(\frac{D}{2}-t\right)^2-\left(\frac{b_2}{2}\right)^2}-\frac{b_1}{2} \tag{9}$$

式中：$M_u$为极限弯矩；$f_y$为钢材的屈服强度；$F_1$为螺栓球柱节点的单向受压极限承载力；$b_2$为螺头宽度，根据螺栓规格取值。

## 3.3 高温承载力公式

基于2.4.6节的分析可知，高温下节点的受压极限承载力折减系数与钢材屈服强度折减系数十分接近。因此，基于螺栓球柱节点常温受压承载力公式，可以将钢材常温屈服强度$f_y$替换成高温下的钢材屈服强度$f_{y,T}$，进而得到节点的高温受压承载力公式，如式（10）所示，$f_{y,T}$的计算方法如式（11）所示。

$$F_{T1}=\alpha\frac{2H_0t^2f_{y,T}}{2\left[\sqrt{\left(\frac{D}{2}-t\right)^2-\left(\frac{b_2}{2}\right)^2}-\frac{b_1}{2}\right]+t} \tag{10}$$

$$f_{y,T}=\eta_T f_{y,20} \tag{11}$$

式中：$F_{T1}$为螺栓球柱节点的高温单向受压极限承载力；$f_{y,20}$为常温下（即温度为20 ℃时）钢材的屈服强度。

## 3.4 公式拟合与验证

通过数值计算得到147个节点模型的受压极限承载力数据，如表4所示。其中，$F_{T1,FE}$为高温下节点的受压极限承载力有限元计算值，$F_{T1,f}$为高温下节点的受压极限承载力公式计算值。

### 3.4.1 公式拟合

本文将通过Origin软件进行数据非线性拟合，确定公式中的影响系数$\alpha$。不难发现，系数$\alpha$是考虑公式中各几何参数影响的因子。因此，采用与节点各几何参数数值相关的无量纲函数关系式来表示系数$\alpha$，如式（12）所示。故只要确定式（12）中的$A$、$b$、$c$、$d$、$e$和$f$的数值，便可确定系数$\alpha$，进而对螺栓球柱节点的常温受压承载力公式进行修正。由拟合结果可得式（13）。

$$\alpha=AD^bt^cH^db_1^eH_0^f \tag{12}$$

$$\alpha=7.528\times10^{-2}D^{1.703}t^{-0.623}H^{-0.401}b_1^{-0.210}H_0^{-0.199} \tag{13}$$

**表4　数值分析结果**

**Tab. 4　Numerical analysis results**

| 模型编号 | 极限承载力 | | 误差/% | 模型编号 | 极限承载力 | | 误差/% |
|---|---|---|---|---|---|---|---|
| | $F_{T1,FE}$/kN | $F_{T1,f}$/kN | | | $F_{T1,FE}$/kN | $F_{T1,f}$/kN | |
| CN1T20 | 142.76 | 141.65 | −0.77 | CN11T400 | 138.52 | 140.71 | 1.58 |
| CN1T100 | 142.49 | 141.65 | −0.59 | CN11T500 | 108.37 | 108.85 | 0.44 |
| CN1T200 | 142.03 | 141.65 | −0.26 | CN11T600 | 69.92 | 69.74 | −0.25 |
| CN1T300 | 141.29 | 141.65 | 0.26 | CN12T20 | 148.84 | 149.45 | 0.41 |
| CN1T400 | 129.64 | 129.47 | −0.13 | CN12T100 | 148.61 | 149.45 | 0.57 |
| CN1T500 | 101.13 | 100.15 | −0.97 | CN12T200 | 148.13 | 149.45 | 0.89 |
| CN1T600 | 65.21 | 64.17 | −1.60 | CN12T300 | 147.38 | 149.45 | 1.40 |
| CN2T20 | 177.01 | 178.72 | 0.97 | CN12T400 | 134.91 | 136.59 | 1.25 |
| CN2T100 | 176.65 | 178.72 | 1.17 | CN12T500 | 105.52 | 105.66 | 0.13 |
| CN2T200 | 176.04 | 178.72 | 1.52 | CN12T600 | 68.05 | 67.70 | −0.52 |
| CN2T300 | 175.00 | 178.72 | 2.12 | CN13T20 | 146.21 | 145.37 | −0.58 |
| CN2T400 | 160.12 | 163.35 | 2.02 | CN13T100 | 145.97 | 145.37 | −0.41 |
| CN2T500 | 125.27 | 126.35 | 0.87 | CN13T200 | 145.50 | 145.37 | −0.09 |
| CN2T600 | 80.83 | 80.96 | 0.16 | CN13T300 | 144.74 | 145.37 | 0.43 |
| CN3T20 | 155.93 | 151.01 | −3.16 | CN13T400 | 132.48 | 132.87 | 0.30 |
| CN3T100 | 155.31 | 151.01 | −2.77 | CN13T500 | 103.60 | 102.78 | −0.80 |
| CN3T200 | 155.14 | 151.01 | −2.66 | CN13T600 | 66.81 | 65.85 | −1.44 |
| CN3T300 | 154.30 | 151.01 | −2.13 | CN14T20 | 126.78 | 130.34 | 2.80 |
| CN3T400 | 141.18 | 138.02 | −2.24 | CN14T100 | 126.51 | 130.34 | 3.03 |
| CN3T500 | 110.18 | 106.76 | −3.10 | CN14T200 | 126.02 | 130.34 | 3.42 |
| CN3T600 | 71.07 | 68.41 | −3.74 | CN14T300 | 125.24 | 130.34 | 4.07 |
| CN4T20 | 140.88 | 138.79 | −1.48 | CN14T400 | 114.64 | 119.13 | 3.92 |
| CN4T100 | 140.60 | 138.79 | −1.29 | CN14T500 | 89.82 | 92.15 | 2.59 |
| CN4T200 | 140.12 | 138.79 | −0.95 | CN14T600 | 57.99 | 59.04 | 1.82 |
| CN4T300 | 139.36 | 138.79 | −0.41 | CN15T20 | 136.92 | 135.51 | −1.03 |
| CN4T400 | 127.57 | 126.86 | −0.56 | CN15T100 | 136.66 | 135.51 | −0.84 |
| CN4T500 | 99.84 | 98.13 | −1.71 | CN15T200 | 136.22 | 135.51 | −0.52 |
| CN4T600 | 64.40 | 62.87 | −2.38 | CN15T300 | 135.51 | 135.51 | 0.00 |
| CN5T20 | 138.09 | 138.92 | 0.61 | CN15T400 | 124.03 | 123.86 | −0.14 |
| CN5T100 | 137.76 | 138.92 | 0.84 | CN15T500 | 97.00 | 95.81 | −1.23 |
| CN5T200 | 137.17 | 138.92 | 1.28 | CN15T600 | 62.55 | 61.39 | −1.86 |
| CN5T300 | 136.25 | 138.92 | 1.96 | CN16T20 | 149.23 | 148.92 | −0.21 |
| CN5T400 | 124.79 | 126.98 | 1.75 | CN16T100 | 149.23 | 148.92 | −0.21 |
| CN5T500 | 97.97 | 98.22 | 0.25 | CN16T200 | 148.75 | 148.92 | 0.11 |
| CN5T600 | 63.30 | 62.93 | −0.58 | CN16T300 | 147.97 | 148.92 | 0.64 |
| CN6T20 | 104.00 | 101.45 | −2.45 | CN16T400 | 135.43 | 136.11 | 0.50 |
| CN6T100 | 103.80 | 101.45 | −2.26 | CN16T500 | 105.72 | 105.28 | −0.42 |

续表

| 模型编号 | 极限承载力 | | 误差/% | 模型编号 | 极限承载力 | | 误差/% |
|---|---|---|---|---|---|---|---|
| | $F_{T1,FE}$/kN | $F_{T1,f}$/kN | | | $F_{T1,FE}$/kN | $F_{T1,f}$/kN | |
| CN6T200 | 103.46 | 101.45 | −1.94 | CN16T600 | 68.17 | 67.46 | −1.05 |
| CN6T300 | 102.90 | 101.45 | −1.40 | CN17T20 | 154.55 | 157.50 | 1.91 |
| CN6T400 | 94.18 | 92.73 | −1.54 | CN17T100 | 154.25 | 157.50 | 2.10 |
| CN6T500 | 73.68 | 71.73 | −2.65 | CN17T200 | 153.74 | 157.50 | 2.44 |
| CN6T600 | 47.53 | 45.96 | −3.30 | CN17T300 | 152.92 | 157.50 | 2.99 |
| CN7T20 | 119.09 | 120.90 | 1.52 | CN17T400 | 139.98 | 143.95 | 2.84 |
| CN7T100 | 118.85 | 120.90 | 1.73 | CN17T500 | 109.51 | 111.35 | 1.68 |
| CN7T200 | 118.42 | 120.90 | 2.09 | CN17T600 | 70.62 | 71.35 | 1.03 |
| CN7T300 | 117.73 | 120.90 | 2.69 | CN18T20 | 147.44 | 151.03 | 2.44 |
| CN7T400 | 107.75 | 110.50 | 2.56 | CN18T100 | 147.15 | 151.03 | 2.64 |
| CN7T500 | 87.09 | 85.47 | −1.86 | CN18T200 | 146.66 | 151.03 | 2.98 |
| CN7T600 | 54.27 | 54.77 | 0.91 | CN18T300 | 145.86 | 151.03 | 3.54 |
| CN8T20 | 165.74 | 163.72 | −1.22 | CN18T400 | 133.50 | 138.04 | 3.40 |
| CN8T100 | 165.43 | 163.72 | −1.03 | CN18T500 | 104.44 | 106.78 | 2.24 |
| CN8T200 | 164.90 | 163.72 | −0.71 | CN18T600 | 67.35 | 68.42 | 1.58 |
| CN8T300 | 164.00 | 163.72 | −0.17 | CN19T20 | 160.17 | 160.27 | 0.06 |
| CN8T400 | 150.07 | 149.64 | −0.28 | CN19T100 | 159.90 | 160.27 | 0.23 |
| CN8T500 | 117.35 | 115.75 | −1.36 | CN19T200 | 159.43 | 160.27 | 0.53 |
| CN8T600 | 75.67 | 74.17 | −1.99 | CN19T300 | 158.65 | 160.27 | 1.02 |
| CN9T20 | 187.22 | 187.12 | −0.05 | CN19T400 | 145.19 | 146.49 | 0.89 |
| CN9T100 | 186.86 | 187.12 | 0.14 | CN19T500 | 113.44 | 113.31 | −0.11 |
| CN9T200 | 186.26 | 187.12 | 0.47 | CN19T600 | 73.11 | 72.60 | −0.69 |
| CN9T300 | 185.24 | 187.12 | 1.02 | CN20T20 | 169.49 | 169.38 | −0.07 |
| CN9T400 | 169.51 | 171.03 | 0.90 | CN20T100 | 169.20 | 169.38 | 0.10 |
| CN9T500 | 132.57 | 132.30 | −0.20 | CN20T200 | 168.71 | 169.38 | 0.40 |
| CN9T600 | 85.50 | 84.77 | −0.85 | CN20T300 | 167.90 | 169.38 | 0.88 |
| CN10T20 | 159.90 | 158.98 | −0.58 | CN20T400 | 153.65 | 154.81 | 0.76 |
| CN10T100 | 159.64 | 158.98 | −0.41 | CN20T500 | 120.03 | 119.75 | −0.24 |
| CN10T200 | 159.13 | 158.98 | −0.10 | CN20T600 | 77.35 | 76.73 | −0.81 |
| CN10T300 | 158.21 | 158.98 | 0.48 | CN21T20 | 179.27 | 178.36 | −0.51 |
| CN10T400 | 144.83 | 145.30 | 0.33 | CN21T100 | 178.97 | 178.36 | −0.34 |
| CN10T500 | 113.41 | 112.40 | −0.90 | CN21T200 | 178.45 | 178.36 | −0.05 |
| CN10T600 | 73.21 | 72.02 | −1.64 | CN21T300 | 177.59 | 178.36 | 0.44 |
| CN11T20 | 152.81 | 153.95 | 0.75 | CN21T400 | 162.51 | 163.02 | 0.32 |
| CN11T100 | 152.60 | 153.95 | 0.89 | CN21T500 | 126.95 | 126.10 | −0.67 |
| CN11T200 | 152.10 | 153.95 | 1.22 | CN21T600 | 81.81 | 80.80 | −1.23 |
| CN11T300 | 151.32 | 153.95 | 1.74 | | | | |

### 3.4.2　公式精度验证

通过147个节点模型的受压极限承载力有限元计算值和公式计算值的对比可知，二者之间的误差均在10%以内，平均误差仅为0.18%。如图20所示，以公式计算值为横坐标，有限元计算值为纵坐标，可以直观发现147个点基本落在直线$y=x$附近，这说明公式的拟合精度较高。

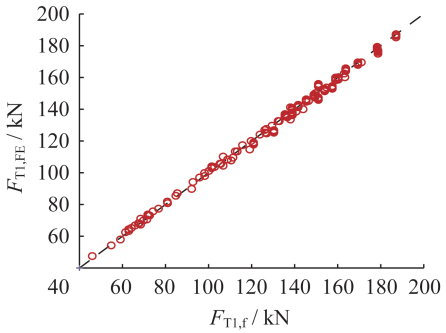


**图20　$F_{T1,FE}$与$F_{T1,f}$的对比**

**Fig. 20　Comparison of $F_{T1,FE}$ and $F_{T1,f}$**

### 3.4.3　公式适用范围验证

为了进一步验证该公式在适用范围内的可靠性，本小节建立了3个上述公式拟合样本外的模型，其具体参数如表5所示。由表6计算结果可知，螺栓球柱节点的高温受压承载力公式计算值与有限元计算值的误差均在10%以内。可见，该公式同样适用于拟合样本外的节点，具有较高的可靠度。

## 4　结论

本文通过对螺栓球柱节点开展高温受压性能研究，可以得出以下主要结论：

（1）螺栓球柱节点的破坏模式与加载板的约束条件有关。由于加载板对节点杆端的强约束作用会限制杆件偏转，导致其不会发生失稳破坏，承载性能优于实际情况下的承载性能。因此，去除加载板约束更符合实际情况，对螺栓球柱节点受压性能的评估也更加保守和安全。

（2）空心圆柱体作为节点主要的承力组件，受压时因先后在加载矩形管两端与非加载矩形管两端形成塑性铰而破坏。此外，随着温度的升高，节点的破坏模式没有发生改变。

（3）基于参数分析结果可知，增大空心圆柱体厚度、矩形管宽度和矩形管高度均可以提高螺栓球柱节点的高温受压承载性能；而增大空心圆柱体外径和高度时，螺栓球柱节点的高温受压承载性能下降。

（4）高温下钢材屈服强度的折减系数可以较为准确地预测节点高温受压承载力的变化。经验证，本文提出的螺栓球柱节点高温受压承载力公式能较为准确地预测螺栓球柱节点的高温受压极限承载力。

**表5　验证模型参数**

**Tab. 5　Parameters of models for validation**　单位：mm

| 模型编号 | $D$ | $t$ | $H$ | $b_1$ | $H_0$ |
|---|---|---|---|---|---|
| YZ1 | 130 | 8 | 120 | 60 | 120 |
| YZ2 | 170 | 12 | 120 | 60 | 120 |
| YZ3 | 170 | 12 | 150 | 60 | 120 |

**表6　验证结果分析**

**Tab. 6　Analysis of validation results**

| 模型编号 | 极限承载力 | | 误差/% | 模型编号 | 极限承载力 | | 误差/% |
|---|---|---|---|---|---|---|---|
| | $F_{T1,FE}$/kN | $F_{T1,f}$/kN | | | $F_{T1,FE}$/kN | $F_{T1,f}$/kN | |
| YZ1T20 | 128.03 | 120.18 | −6.13 | YZ2T400 | 196.15 | 186.94 | −4.70 |
| YZ1T100 | 127.80 | 120.18 | −5.96 | YZ2T500 | 153.68 | 144.60 | −5.90 |
| YZ1T200 | 127.39 | 120.18 | −5.66 | YZ2T600 | 99.21 | 92.65 | −6.61 |
| YZ1T300 | 126.69 | 120.18 | −5.14 | YZ3T20 | 195.91 | 187.03 | −4.53 |
| YZ1T400 | 115.92 | 109.84 | −5.24 | YZ3T100 | 195.52 | 187.03 | −4.34 |
| YZ1T500 | 90.64 | 84.97 | −6.25 | YZ3T200 | 194.86 | 187.03 | −4.02 |
| YZ1T600 | 58.47 | 54.44 | −6.89 | YZ3T300 | 193.77 | 187.03 | −3.48 |
| YZ2T20 | 216.86 | 204.53 | −5.69 | YZ3T400 | 177.35 | 170.95 | −3.61 |
| YZ2T100 | 216.39 | 204.53 | −5.48 | YZ3T500 | 138.77 | 132.23 | −4.71 |
| YZ2T200 | 215.58 | 204.53 | −5.13 | YZ3T600 | 89.51 | 84.72 | −5.34 |
| YZ2T300 | 214.27 | 204.53 | −4.55 | | | | |

## 参考文献：


[1] 郭小农，朱劭骏，王丽，等.铝合金板式节点平面内抗弯刚度研究[J].建筑结构，2018，48(14)：34-39.DOI：10.19701/j.jzjg.2018.14.007.
GUO Xiaonong，ZHU Shaojun，WANG Li，et al.Study on in-plane bending stiffness of aluminum alloy gusset joint[J].Building Structure，2018，48(14)：34-39.DOI：10.19701/j.jzjg.2018.14.007.(in Chinese)

[2] WANG X D，WENG K，LIU H B，et al.Experimental study on the mechanical property of visual bolt-ball Joint system[J].Advances in Structural Engineering，2013，16(10)：1749-1762.DOI：10.1260/1369-4332.16.10.1749.

[3] 郭小农，黄泽鞶，杨商飞，等.新型螺栓球柱节点静力承载性能试验研究[J].同济大学学报(自然科学版)，2015，43(11)：1626-1633.DOI：10.11908/ j.issn.0253-374x.2015.11.003.
GUO Xiaonong，HUANG Zewei，YANG Shangfei，et al.Experimental Study of static bearing behavior of bolted ball-cylinder joint[J].Journal of Tongji University (Natural Science Edition)，2015，43(11)：1626-1633.DOI：10.11908/j.issn.0253-374x.2015.11.003.(in Chinese)

[4] 陈志华，孙国军，王小盾，等.一种无檩螺栓球 节点网架结构：2010105121343[P].2010-10-20.
CHEN Zhihua，SUN Guojun，WANG Xiaodun，et al.Non-purlin gird structure of bolted-ball joint：2010105121343[P].2010-10-20.(in Chinese)

[5] GUO X N，ZENG Q，ZHU S J，et al.Bearing capacity of bolted ball-cylinder joint under uniaxial tensile force[J].Structures，2020，28：562-576.DOI：10.1016/j.istruc.2020.09.001.

[6] ZENG Q，GUO X N，HUANG Z W，et al.Uniaxial compression bearing capacity of bolted ball-cylinder joint[J].Engineering Structures，2019，183：976-986.DOI：10.1016/j.engstruct.2019.01.064.

[7] GUO X N，ZHU S J，LIU X，et al.Study on out-of-plane flexural behavior of aluminum alloy gusset joints at elevated temperatures[J].Thin-Walled Structures，2018，123：452-466.DOI：10.1016/j.tws.2017.11.045.

[8] FENG R，YOUNG B.Design of cold-formed stainless steel tubular joints at elevated temperatures [J].Engineering Structures，2012，35：188-202.DOI：10.1016/j.engstruct.2011.10.029.

[9] QIANG X H，WU N D，JIANG X，et al.Experimental and numerical analysis on full high strength steel extended endplate connections in fire[J].International Journal of Steel Structures，2018，18(4)：1350-1362.DOI：10.1007/s13296-018-0130-y.

[10] 史健勇，孙旋，刘文利，等.基于整体的大空间钢结构性能化防火设计方法研究[J].土木工程学报，2011，44(5)：69-78.DOI：10.15951/j.tmgcxb.2011.05.017.
SHI Jianyong，SUN Xuan，LIU Wenli，et al.Study of performance-based fire resistance design methodology for large space structures[J].China Civil Engineering Journal，2011，44(5)：69-78.DOI：10.15951/j.tmgcxb.2011.05.017.(in Chinese)

[11] QIANG X H，BIJLAARD F S K，KOLSTEIN H，et al.Behaviour of beam-to-column high strength steel endplate connections under fire conditions-part 1：experimental study[J].Engineering Structures，2014，64：23-38.DOI：10.1016/j.engstruct.2014.01.028.

[12] 程园园，李春祥，曹黎媛.高温下钢材力学性能研究进展[J].结构工程师，2017，33(1)：189-197.DOI：10.15935/j.cnki.jggcs.2017.01.027.
CHENG Yuanyuan，LI Chunxiang，CAO Liyuan.Research progress on mechanical properties of steel material at high temperature[J].Structural Engineers，2017，33(1)：189-197.DOI：10.15935/j.cnki.jggcs.2017.01.027.(in Chinese)

[13] 赵金城.高温下钢材力学性能的试验研究[J].建筑结构，2000，30(4)：26-28.DOI：10.19701/j.jzjg.2000.04.007.
ZHAO Jincheng.Experimental study on mechanical properties of steel at elevated temperature[J].Building Structure，2000，30(4)：26-28.DOI：10.19701/j.jzjg.2000.04.007.(in Chinese)

[14] 中华人民共和国国家质量监督检验检疫总局，中国国家标准化管理委员会.紧固件机械性能 螺栓、螺钉和螺柱：GB/T 3098.1—2010[S].北京：中国标准出版社，2010.
General Administration of Quality Supervision，Inspection and Quarantine of the People′s Republic of China，Standardization Administration of the People′s Republic of China.Mechanical Properties of Fasteners—Bolts，Screws and Studs：GB/T 3098.1—2010[S].Beijing：China Standards Press，2010.(in Chinese)

[15] 中华人民共和国住房和城乡建设部，中华人民共和国国家质量监督检验检疫总局.建筑钢结构防火技术规范：GB 51249—2017[S].北京：中国计划出版社，2017.
Ministry of Housing and Urban-Rural Development of the People′s Republic of China，General Administration of Quality Supervision，Inspection and Quarantine of the People′s Republic of China.Code for Fire Safety of Steel Structures in Buildings：GB 51249—2017[S].Beijing：China Planning Press，2017.(in Chinese)

[16] 李国强，李明菲，殷颖智，等.高温下高强度螺栓20MnTiB钢的材料性能试验研究[J].土木工程学报，2001，34(5)：100-104.
LI Guoqiang，LI Mingfei，YIN Yingzhi，et al.Experimental study on material properties of high strength bolt 20MnTiB steel at elevated temperature [J].China Civil Engineering Journal，2001，34(5)：100-104.(in Chinese)

# 基于改进鸽群层级的无人机集群视觉巡检模型

陈麒[1]，崔昊杨[2]
(1. 汕头职业技术学院，广东 汕头 515000；2. 上海电力大学，上海 200090)

**摘要：**为解决无人机在执行输电线路巡检工作过程中易受环境干扰，以及传统单人单机工作模式巡检效率低下等问题，提出基于改进鸽群层级算法的无人机集群视觉巡检模型。根据载机车辆与待检塔位的GPS坐标计算出启航无人机的初始地标点，并规划运动轨迹；根据当前在巡无人机结束巡检点的位置更新待起飞无人机初始地标，实现启航与在巡无人机巡检地标的动态衔接，完成对地图指南针算子的改进；利用改进的自适应模板匹配算法优化在巡无人机的Adaboost视觉识别系统，通过自适应比对线路间距实现无人机与输电线路间相对位置的自主调整，在动态调节姿态的基础上提高检测质量。实验结果表明：相比于传统鸽群方法，该模型在巡检效率方面的在空巡检时间提高了12%、巡检距离提高了27.5%，风吹、地形变化的情况下巡线质量相比于常规识别模型分别提高了21%和15%。

**关键词：**无人机输电线路巡检；改进鸽群层级算法；改进Adaboost；视觉识别
中图分类号：TP391.9 文献标志码：A 文章编号：1004-731X(2022)06-1275-11
DOI: 10.16182/j.issn1004731x.joss.21-1121

## Visual inspection model of UAV cluster based on improved pigeon flock hierarchy

*Chen Qi*[1], *Cui Haoyang*[2]
(1. Shantou Vocational and Technical College, Shantou 515000, China; 2. Shanghai Electric Power University, Shanghai 200090, China)

**Abstract:** Aim at UAV being vulnerable to the environmental interference and the low efficiency of the traditional single-person-UAV model in the transmission line inspection, *a visual inspection model for the power line by UAV is proposed based on the improved pigeon flock hierarchy. The initial landmark point of the UAV is generated based on GPS coordinates of the aircraft-carrying vehicle and the tower to be inspected, and the movement trajectory is planned. The return point of the UAV is used to update the initial landmark of onward UAV, which realizes the dynamic handover between the work-exchanging UAV, and the landmark point is optimized. An advanced adaptive template matching algorithm is adopted to improve the adaboost visual recognition of the patrol UAV, which can autonomously adjust the relative position between UAV and the line by adaptively comparing the line spacing*. Experimental results show that the proposed model improves the inspection time in the air by 12% and the distance by 27.5% in terms of inspection efficiency, and the quality of the inspection under the conditions of wind blows and terrain changes increase by 21% and 15% respectively.

**Keywords:** UAV transmission line inspection; improved pigeon hierarchy algorithm; improved Adaboost; visual recognition

收稿日期：2021-11-03 修回日期：2021-12-27
基金项目：上海市地方院校能力建设(15110500900)
第一作者：陈麒(1980-)，男，硕士，副教授，研究方向为自动化与嵌入式。E-mail：2532080998@qq.com
通讯作者：崔昊杨(1978-)，男，博士，教授，研究方向为图像处理、设备状态分析。E-mail：CuiLab_shiep@163.com

# 引言

利用无人机开展输电线路空中巡检，克服了传统人工线路巡检受地理环境限制导致巡线工作任务重、效率低的不足。同时，巡检人员可借助机载镜头开展超近视距检查塔、线、串，大大提高了巡检效率与工作质量[1-2]。但是，当前线路巡检所用的大疆御2 Zoom、大疆精灵等系列无人机均需操控员手动远程操控，这一单人单机巡线方式不仅效率低下，还会因人员操作技术水平差异导致巡线质量参差不齐。因此，自主式巡检的无人机集群控制，成为了输电线路运维工作的研究方向之一[3]。

以鸽群算法(pigeon-inspired optimization, PIO)[4-5]为代表的群体智能优化算法通过地图、指南针算子、地标算子实现多目标集群控制，相比以Voronoi图法[6]为代表的启发式算法、以混合整数线性规划法[7]为代表的精确方法、以及以蚁群[8]和粒子群优化[9]为代表的传统智能算法，具有非固定起始点和多目标并行控制的优势，且路径规划精度可保持较高水平。但是，PIO算法仅对多路线进行规划，未考虑时空协同，受控对象在完成各自任务时可能出现任务区域叠加，从而导致任务重复执行，造成计算机资源浪费。另一方面，因南方地区输电线路大量分布于山岭间，无人机巡线过程中易遭受强风及面临地形起伏等情况，机身则对应出现因风荷载影响稳定或随地形而起落等现象，这将导致已建立的输电线目标跟踪模型出现误差，进而偏离航线，甚至丢失目标。自适应增强boosting算法[10]相比于归一化互相关模板匹配[11](normalized cross correlation, NCC)、快速鲁棒特征匹配[12](speeded up robust feature, SURF)等基于特征的目标跟踪方法在水平跟踪时具有较高的准确率，同时较基于卷积神经网络的物体检测算法[13]、基于深度卷积网络的目标跟踪算法[14]具备更快的识别速度，但在处理无人机机身不稳定问题时的自适应能力仍然存在不足，跟踪效果有待提高。

本文提出基于改进PIO算法的无人机集群输电线路视觉巡检模型。该模型将线路巡检分为系统层次的集群控制和个体层次的单机巡线2部分。根据载机车辆GPS位置坐标与待检输电线路的塔位坐标计算出车辆与输电线路之间的相对坐标与运动轨迹，并导入2个GPS点之间的地形信息(如海拔)构建地图；通过释放的控制信号中心(由无人机承担此工作，该无人机称为总机)计算出移动中的车辆与下一巡检点之间的最优距离，将在巡无人机、启航无人机与返程无人机的最佳坐标作为变量，对鸽群算法的地图指南针算子进行进化计算；利用改进的自适应模板大小比对算法对在巡无人机的Adaboost视觉识别进行优化，通过自适应对比线路间距实现无人机自主调整机身与输电线路之间的相对位置。

## 1 基于改进鸽群层级的输电线路无人机集群视觉巡检模型

南方的电力线路大量分布于山岭间，实时图传耗电量大，且信号容易中断，故本文无人机采取巡线视频录制，返回后再导入巡检数据中心的工作模式。该模式可保证即使人–机交互中断，无人机仍可自主巡检。但该方法对启航无人机与返航无人机工作衔接、复杂背景下实现目标实时准确跟踪有极高的要求。在这一巡检模式下，无人机集群在巡检过程中，需要根据实时位置与巡检地形的不同进行编队姿态动态重构。此时，需要动态地对无人机活动区域进行预描述，以提高巡检效率；同时，为提高巡检拍摄视频与图像的质量，需要无人机自适应地调节自身拍摄位置与姿态。

为实现上述功能，本文组装了如图1所示的无人机，并提出一种基于改进鸽群层级算法的无人机集群控制模型。该模型主要由集群控制和视觉巡检2部分构成。其中，集群控制以地形实况、无人机与载机车辆相对位置为变量进行无人机群动态控制；视觉巡检通过自适应判断无人机与输电线路间的相对位置完成姿态调节。如图1所示，总机无人机起到信号中继作用，巡检无人机则在总机无人机中继信号的控制下，持续开展巡检作业。

(a) 总机无人机

(b) 输电线路巡检无人机

图1 本文组装的四旋翼无人机
Fig. 1 Schematic diagram of UAV assembled

## 1.1 鸽群层级集群动态控制

标准鸽群算法[15]的控制逻辑如图2~3所示。头鸽对跟随鸽进行层级控制，该方法信息传递高效，但由于参考位置相对固定，导致其难以适应机载平台发生位移后实时对无人机进行集群控制。

图4演示了标准鸽群算法的地图指南针算子通过磁感和太阳进行地图绘制和方向调整的逻辑。此时，第$i$只鸽子在$t$时刻的速度信息$v_i$和位置信息$x_i$可表示为[4-5,15]

$$v_i(t) = e^{-Rt} v_i(t-1) + \text{rand}\,[x_{gb}(t) - x_i(t)] \quad (1)$$

$$x_i(t+1) = x_i(t) + v_i(t+1) \quad (2)$$

式中：$R$为罗盘算子(取值0~1)；$x_{gb}$为历史最佳位置。

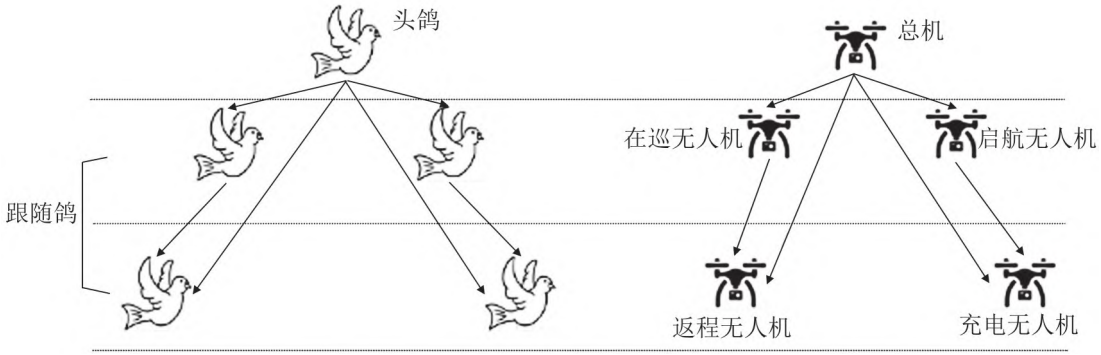


图2 鸽群控制逻辑示意图
Fig. 2 Logic diagram of common PIO algorithm

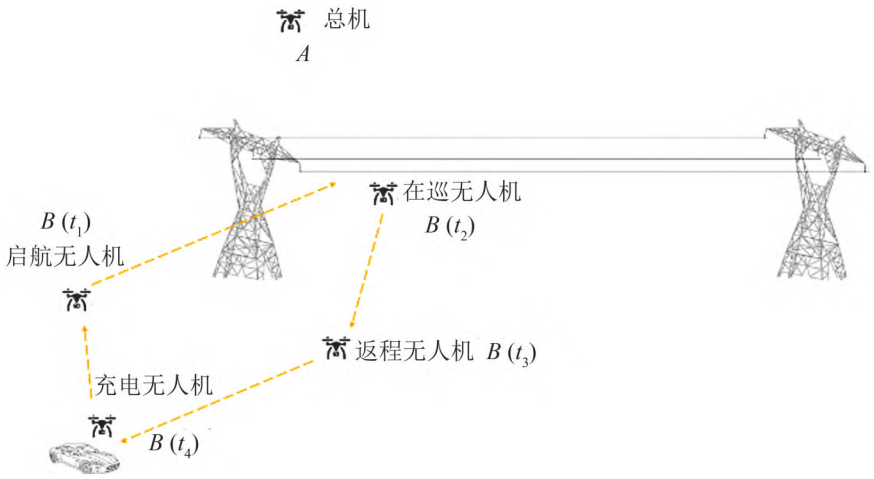


图3 传统鸽群控制的无人机线路巡检系统
Fig. 3 Inspection model by multi-UAV by normal PIO algorithm

## 1.2 基于相对位置调整的改进鸽群层级集群动态控制

以载机汽车、巡检无人机及待检电力线路之间的动态GPS坐标变化为变量对鸽群算法的地图指南针算子(环境信息图)进行改进，实现总机对其余无人机运动路径的动态规划。

本文构建的无人机群如图5~6所示，以4架无人机为1组进行说明。

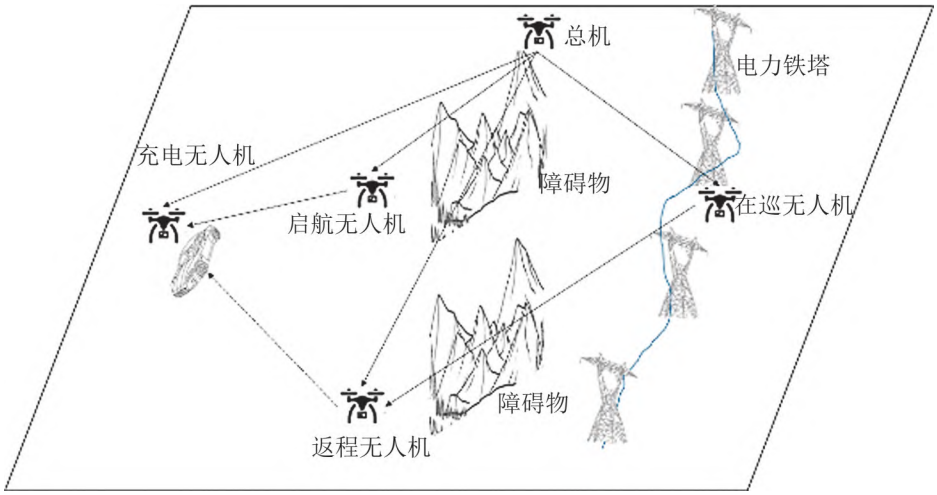


图4　基于传统鸽群控制的无人机巡检系统

Fig. 4　Process of inspection by multi-UAV with common PIO algorithm

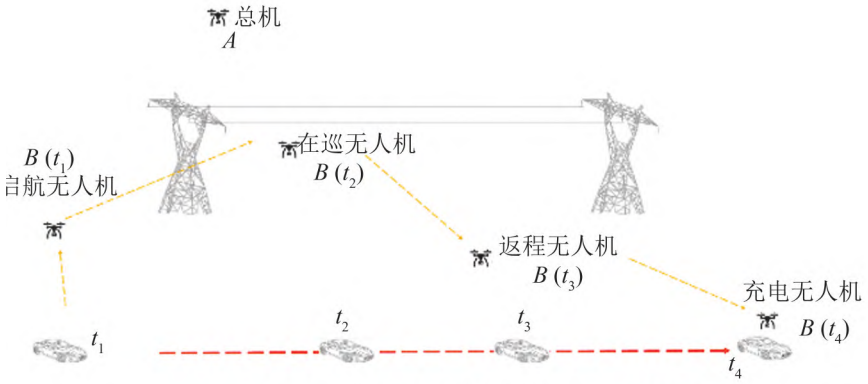


(a) 基于相对位置优化PIO算法的无人机巡线系统

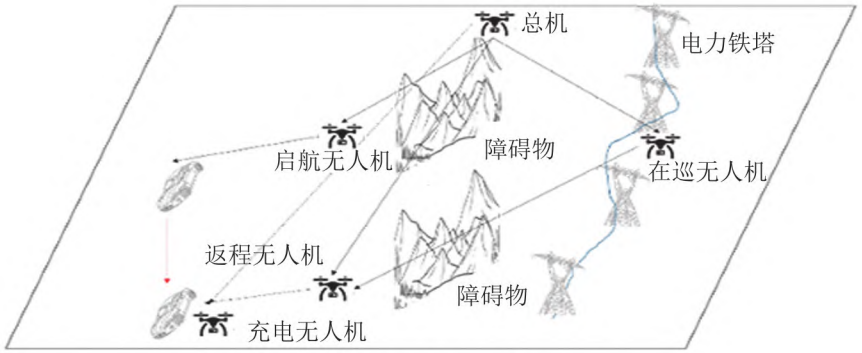


(b) 优化PIO算法的多无人机巡检

图5　改进鸽群控制的无人机巡检系统

Fig. 5　Patralling system by multi-UAV with proposed PIO algorithm

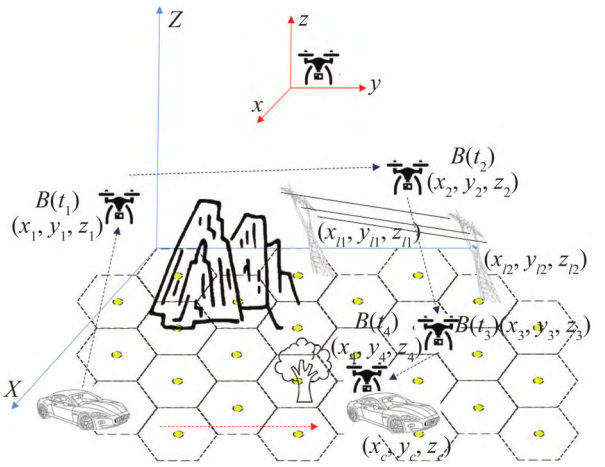


图6　改进鸽群层级算法控制下的各设备相对坐标系

Fig. 6　Relative location for UAVs and vehicle by optimized PIO

将无人机简化为点模型，其GPS经纬度相对坐标(含高程)集合为$A=[a_1, a_2, a_3, a_4]=[(x_{a_1}, y_{a_1}, z_{a_1})$、$(x_{a_2}, y_{a_2}, z_{a_2})$、$(x_{a_3}, y_{a_3}, z_{a_3})$、$(x_{a_4}, y_{a_4}, z_{a_4})]$、输电线路的各塔位GPS经纬度相对坐标为$(x_l, y_l, z_l)$、车辆经纬度相对坐标为$(x_c, y_c, z_c)$。同时，为避免电池过放，需设定路径约束条件，即无人机主动进行电量管理，保证从当前位置返回至载机平台时电量不少于10%，同时下一辆无人机起飞接替巡检(为节省电量和规避障碍，无人机将垂直上升至450 m后进行返航)，约束公式为

$$\begin{cases} z = [W' - (\sqrt{(f)^2 + (mg)^2} \cdot \\ \quad \sqrt{(x_{a_3} - x_c)^2 + (y_{a_3} - y_c)^2} \cdot \\ \quad \cos\theta + m \cdot g \cdot h(z_3 - z_2)]/W > 10\% \\ f = \dfrac{1}{2}\rho v_{air}^2 C_D A \end{cases} \tag{3}$$

式中：$f$、$\rho$、$v_{air}$、$C_D$、$A$、$m$和$g$分别为无人机返航阻力、空气密度、当前风速、阻力系数、受力面积、无人机质量和重力加速度；$\theta$为重力与空气阻力的合力与水平路线的夹角；$W$、$W'$分别为无人机启航与返航时电量。接替巡检任务的无人机将以上一架无人机停止巡检位置为地标，则第$i$架巡检无人机的中心位置为(在巡无人机停止巡检准备返航、启航无人机准备接替巡检的目的地坐标)

$$x_{ci}(t-1) = \frac{\sum_{i=1}^{I(t-1)} x_i(t-1)F(x_i(t-1))}{I(t-1)\sum_{i=1}^{I(t-1)} F(x_i(t-1))} \tag{4}$$

$$I(t) = I(t-1)/2 \tag{5}$$

$$F(x_i(t-1)) = \begin{cases} \dfrac{1}{\text{fitness}(x_i(t-1)) + \varsigma}, \text{最小优化} \\ \text{fitness}(x_i(t-1)), \text{最大优化} \end{cases} \tag{6}$$

式中：$F$为适应度值；$I$为$t$时刻空中无人机数量。

加入路径约束$g$和中心位置$x_{ci}$，更新后的地图指南针算子由式(1)修改为

$$v_i(t) = e^{-Rt}v_i(t-1)r(t) + u(t)\,\text{rand}[x_{ci}(t) - x_i(t)] \tag{7}$$

$$r(t) = r_e + (r_s - r_e)e^{-z(t/t_{max})^2} \tag{8}$$

$$u(t) = u_s + (u_e - u_s)(1 - \arccos(-2t/t_{max} + 1)/\pi) \tag{9}$$

式中：$r_e$、$r_s$、$t_{max}$、$u_s$和$u_e$分别为地图指南针算子初始值、指南针算子终值、最大迭代次数、认知因子初值和认知因子终值。

## 1.3 基于改进Adaboost算法的姿态自适应控制

由于该模型采取离线识别的方式巡检输电线路，故需平衡取舍巡检影像质量、飞机电量与应对干扰的鲁棒性等因素。目前，常用的目标识别方法以VGG16 (visual geometry group network)、SSD(single shot multibox detector)和YOLO(you only look once)等基于深度卷积网络的算法为主。VGG16计算资源占用多，电量消耗大；SSD随着设定网络加深，高层特征图中小目标信息容易丢失，导致其在处理复杂环境背景干扰下的输电线路等小目标时存在检测效果差的问题；YOLO虽然可对视频完成端到端的全局目标检测，但是无法开展区域采样工作。Adaboost算法集成多个弱分类器为单个强分类器，属于目标检测中的集成分类范畴，兼具弱学习算法计算复杂度低和强学习算法准确率高的优点[16]。同时，其准确率可随训练次数的增加明显提高，且不存在过拟合的问题。该算法可以从理论上满足高质量离线巡检输电线路

的要求。标准Adaboost算法开展样本进行训练时，弱回归器$P_m(X)$的最大误差$e_m$与权重$w_m$计算如下[16]：

$$e_m = \sum_{n=1}^{N} w_m(n)\ \overset{A}{E}_{m,n},\ n = 1, 2, \cdots, N \tag{10}$$

$$w_{m+1}(n) = \frac{w_{m+1}(n)}{\sum_{n=1}^{N} w_{m+1}(n)} = w_m(n)\left(e_m/(1-e_m)\right)^{1-\overset{A}{E}_{m,n}} \tag{11}$$

式中：$\overset{A}{E}_{m,n}$为每个样本的相对误差。进而可得到强回归器：

$$P(X) = \sum_{m=1}^{K} \ln\frac{1-e_m}{e_m} \cdot P_m(X) \tag{12}$$

因强风与地形起伏导致的无人机机身姿态偏移，会使无人机巡检所得影像出现目标错位或是模糊等情况。为此，本文利用模板匹配算法对Adaboost算法进行改进，以实现巡检过程中的无人机姿态动态调整。设预留在无人机的模板图像为VI$(x, y)$，检测视频中的目标图像为VI′$(x, y)$，如图7所示。

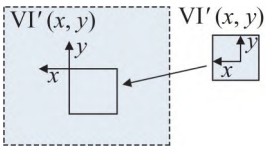


图7 模板匹配示意图

Fig. 7 Diagram of template matching

NCC[17]算法方法利用VI$(x, y)$从目标图像VI′$(x, y)$左上角以一个像素点$(x', y')$为单位进行移动，每到达一个位置点，计算模板和当前位置图像块的相似程度，即相关系数$R(x', y')$。最后，通过计算相关系数$R(x', y')$[17]的最大值定位设备，即：

$$R(x', y') = \left[\sum_{x', y'} \mathrm{VI}(x, y) \cdot \mathrm{VI}'(x'+x, y'+y) - \frac{1}{wh}\sum_{x', y'} \mathrm{VI}(x, y) \sum_{x', y'} \mathrm{VI}'(x'+x, y'+y)\right] \Bigg/ \left[\sqrt{\sum_{x', y'} \mathrm{VI}(x, y)^2 - \frac{1}{wh}\left[\sum_{x', y'} \mathrm{VI}(x, y)\right]^2} \cdot \sqrt{\sum_{x', y'} \mathrm{VI}'(x'+x, y'+y)^2 - \frac{1}{wh}\left[\sum_{x', y'} \mathrm{VI}'(x+x', y+y')\right]^2}\right] \tag{13}$$

式中：$w$、$h$分别为图像的长、高。

如图8~9所示，当无人机受风和因地形变化出现受迫姿态变化时，得到检测图像中的输电线路同回路各相导线间的间隔存在较大差别。为此，本文根据相似三角形理论[18]，以无人机视觉中三相电力线间距为依据，将偏移分解为水平偏移和垂直偏移，以此为基础进行姿态动态调整和Adaboost训练集权重更新[19-20]。此时，水平调整距离为$\Delta H$、垂直调整距离为$\Delta S$：

$$\begin{cases} \Delta H = H(d_{1,j}/d) - H \\ \Delta S = (d_{1,j}d - d_1 d)/d_1 \end{cases} \tag{14}$$

式中：$H$、$d$分别为正常情况下无人机离输电线的距离(本文取4 m)、初始偏移位移$d_{1,j}=[d_{1,1}, d_{1,2}, d_{1,3}, d_{1,4}]$为第$j$位置的线路间隔。将$\Delta H$和$\Delta S$作为训练集权重的改进量，强化偏移量对识别的影响，更新后的强训练器和权重为

$$P'(X) = \sum_{m=1}^{K} \alpha'_m \cdot P_m(X) \tag{15}$$

$$\alpha'_m = \frac{\alpha_m}{\sum_{m=1}^{K} \alpha_m} \sqrt{\left[(1+\Delta S/(d_1+d_2))^2 + (1+\Delta H/H)^2\right]/2} \tag{16}$$

## 2 实验与分析

为验证本文模型的性能，随机选取某段10 kV电力线路进行验证。实验分为2部分：①无人机集群动态控制，采用无人机巡检在空时间与巡检距离作为本文模型与经典PIO模型评判指标；②线路自适应巡检，采用环境有风与无风、地形上升与下降情况进行对比，采用60 s内输电线路完整呈现在视频中的时间作为识别准确率，并将其作为自适应巡检的评价指标，定义识别准确率为

$$Q = t_{\mathrm{in}}/60 \times 100\% \tag{17}$$

式中：$t_{\mathrm{in}}$为3根输电线均出现于视频中的时长。此处需说明，虽然深度学习网络常用的识别率评价指标为$AP$或$mAP$[14]，但本文只需输电线路完全出现在视频中则算正确，故采用完整呈现时间作为评价指标。

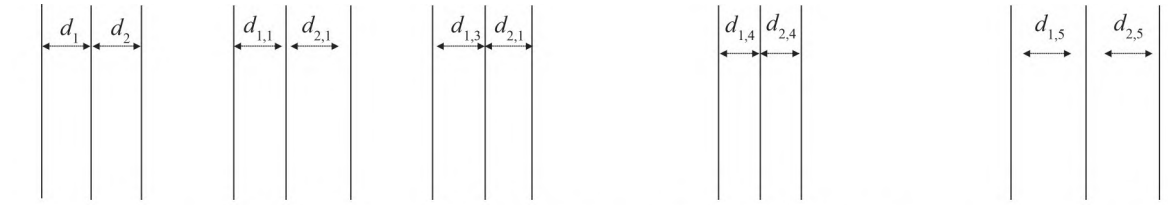


(a) 正常位置的俯视图　(b) 无人机向左偏离正常位置的俯视图　(c) 无人机向右偏离正常位置的俯视图　(d) 无人机与正常位置垂直远离的俯视图(模拟地形上升)　(e) 无人机与正常位置垂直拉进的俯视图(模拟地形下降)

图8　无人机与待检线路不同相对位置下的偏差示意图

Fig. 8　Deviation of UAV and line to be inspected in different relative location

(a) 无人机位置正常情况下拍摄的输电线路图

(b) 无人机与输电线路相对位置上移的输电线路图

(c) 无人机与输电线路相对位置上移且右移的输电线路图

图9　无人机与待检线路不同相对位置下的 输电线路巡检结果示例图

Fig. 9　Diagram of transmission line inspection results under different relative positions between drone and theline to be inspected

## 2.1 改进鸽群层级集群无人机动态控制

本文改进PIO无人机集群控制方式生成的无人机规划路径随车辆位置变化动态控制的结果如图10~11所示。与此同时，为了验证本文模型的有效性，又将本文实验分为2部分，分别为车辆位置变化时的标准PIO无人机集群控制和改进PIO无人机集群控制，并采用相同电量情况下的实验巡检时间、巡检距离作为评判标准，对比结果如图12所示。

(a) 启航无人机　(b) 在巡无人机　(c) 返航无人机　(d) 充电无人机

图10　无人机完整的实验线路轨迹图

Fig. 10　Trajectory by UAVs on mission

从图11~12的对比可见，由于启航无人机启航时会以当前在巡无人机位置A为地标，但是从车辆到地标存在一定的距离，而此阶段的在巡无人机会继续向前巡检一段距离，故用式(7)更新地图指南针算子后得到新的地标A′，启航无人机将前往最新地标位置继续巡检。

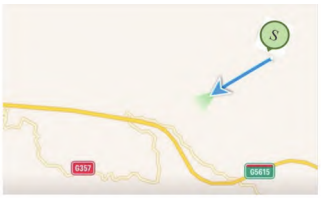


(a) 起飞时的地标

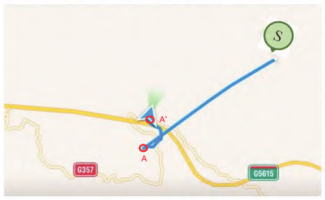


(b) 更新后的地标

图 11　改进地图指南针算子后的更新地标

Fig. 11　Updating landmarks by improving map compass operator

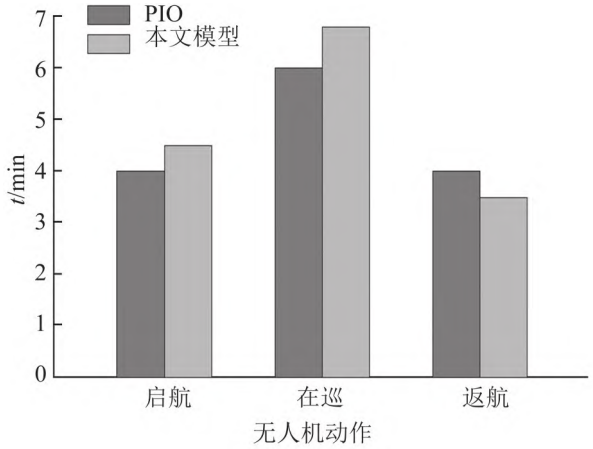


(a) 巡航时间对比

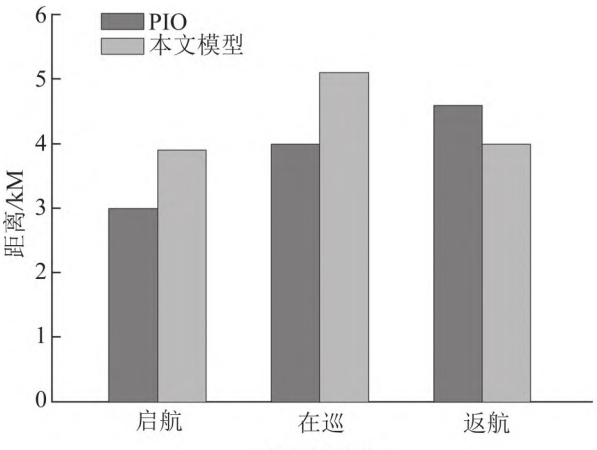


(b) 巡航效率对比

图 12　本文改进 PIO 模型与标准 PIO 算法性能对比

Fig. 12　Performance comparison of improved PIO model and standard PIO algorithm

此外，从图 12 可见，虽然地标更新后导致启航时间有所增加，但是车辆的移动缩短了返航距离，故在空巡检时间得到增加。本文模型可实现 6.8 min 在空巡检时间，相比标准 PIO 算法的 6 min 平均提高了 12%；巡检距离达到 5.1 km，相比标准 PIO 的 4 km 提高了 27.5%。此外，由于车辆位置变化造成返航点动态更新，返航时间也由标准 PIO 算法的 4 min 缩短到 3.5 min，返航距离由 4.6 km 缩减至 4 km，降幅分别为 12.5% 和 13%，提高了返航的安全性和经济性。由此可见，改进后的无人机集群控制不仅实现了启航无人机地标随在巡无人机位置变化而主动调整的动态控制，还可以完成返航无人机随车辆运动而自行修正路线。

## 2.2 改进 Adaboost 无人机视觉的自适应巡线

本文无人机巡检得到的视频效果截图如图 13 所示，改进算法的性能提升如图 14 与表 1 所示。由图 13~14 可以看出，即使在受风导致机身飘移、地形变化导致目标大小变化、以及树丛等同色背景干扰的情况下，本文模型仍能准确识别输电线路，通过机身与镜头调整可基本固定目标线路于视频中央区域，视频质量提升显著。在风速为 6 m/s 的环境情况下，本文模型平均识别准确率 $Q$ 为 96%，比标准 Adaboost 算法的 72.4% 提高了 23.6%；下陡坡情况下，本文模型识别准确率与 Adaboost 均为 100%；上陡坡情况下，本文模型识别准确率 $Q$ 依旧能保持 100%，比 Adaboost 的 83.5% 提高了 16.5%。本文方法在无人机受风时的识别率不能达到 100% 的原因主要在于，当遭遇较大横风时，因电池容量有限，电机难以将无人机带回原轨迹，导致识别率下降。

此外，为了验证本文模型综合性能，在改进鸽群算法的基础上通过无人机运行不同算法对同一段线路进行巡检对比，即采取改进 Adaboost、Adaboost、SVM、SURF 和 VGG16 算法对同一段线路进行巡检，选取同等电量情况下的巡检距离和识别率作为评判指标，结果如表 1 所示。从表 1

可知，SURF 通过特征识别的方法对比本文方法虽然大幅降低了 CUP 电量损耗，无人机巡检距离最长，但是易受背景环境干扰，目标识别率最低；Adaboost 对比本文算法少了模板匹配改进模块，程序运行用电量稍有降低，巡检距离更远，但受风情况下，目标识别率低于本文方法；SVM 算法耗电量低于本文算法，巡检距离增加，但识别率较低；VGG16 在有风和无风情况下识别率最高，但每 1% 的识别率提高需减少 20% 的巡检距离，需在两指标中进行取舍。综上所述，本文模型在环境影响、地形变化、电池容量有限等限制条件和目标识别与定位准确率之间达到了较好的平衡。此处需说明，搭载 5 种算法进行的 5 次实验所面对的风速存在部分差异(当时风速最大差异值在 1 m/s)，实验结果存在可接受的误差波动。

(a) 背景干扰　(b) 地势降低

(c) 机身受右向风　(d) 地势下降且机身受右向风

图 13　本文模型自适应跟踪效果
Fig. 13　Adaptive tracking effect of model proposed

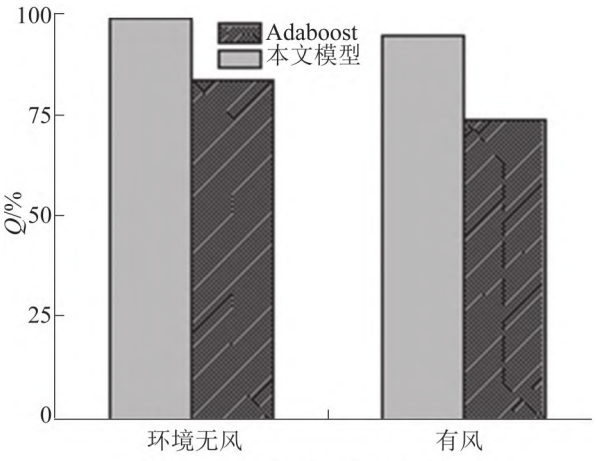


(a) 环境有风和无风情况下识别率对比

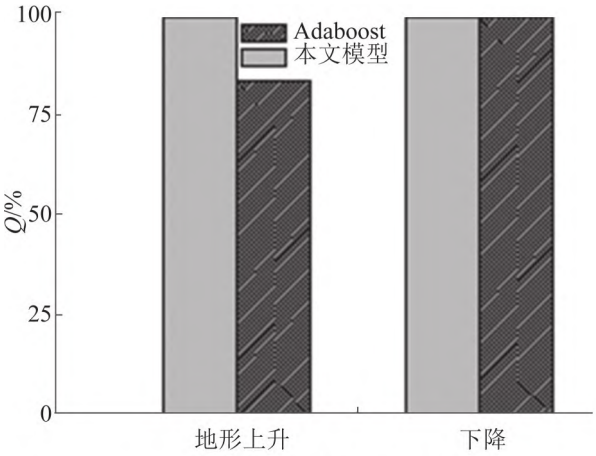


(b) 环境有风和无风情况下识别率对比

图 14　本文模型与 Adaboost 在目标跟踪下的性能对比
Fig. 14　Performance comparison on target tracking between the proposed algorithm and Adaboost algorithm

表 1　同等电量下本文模型与其他算法的效率对比
Table 1　Comparison of efficiency of this model with other algorithms under the same power

| 算法 | 无风/有风 | |
|---|---|---|
| | 线路巡检距离/km | 线路识别率/% |
| 本文 | 5.6/4.7 | 100/96 |
| A | 5.9/4.8 | 85/72.4 |
| SURF | 6.6/5.4 | 79/55 |
| SVM | 6.2/5.1 | 96/80 |
| V | 4.9/3.9 | 100/97 |

## 3　结论

针对目前无人机单人单机手动操作巡线模式效率低下和巡检影像成果质量参差不齐的情况，提出了一种无人机集群视觉巡检模型。该模型通过路径约束和地标更新对鸽群算法进行改进，实现了无人机集群动态控制。实验证明，基于本文算法控制的无人机在空巡检时间提高 12%、巡检距离提高 27.5%。此外，为保证强风和地形变化环境下的巡检图像质量，本文通过模板匹配算法改进 Adaboost 算法的方法进行优化，结果显示，在 6 m/s 风速环境下的输电线路识别准确率能达到 96%，在地形高差为±10 m 的环境下输电线路识别准确率依旧达到 100%，证明通过无人机集群式控制与基于视觉的姿态调整，可有效提高线路运维工作的效率。

## 参考文献：

[1] 顾超越, 李喆, 史晋涛, 等. 基于改进Faster-RCNN的无人机巡检架空线路销钉缺陷检测[J]. 高电压技术, 2020, 46(9): 3089-3096.
Gu Chaoyue, Li Zhe, Shi Jintao, et al. Detection for Pin Defects of Overhead Lines by UAV Patrol Image Based on Improved Faster-RCNN[J]. High Voltage Engineering, 2020, 46(9): 3089-3096.

[2] 梁文勇, 吴大伟, 谷山强, 等. 输电线路多旋翼无人机精细化自主巡检航迹优化方法[J]. 高电压技术, 2020, 46(9): 3054-3061.
Liang Wenyong, Wu Dawei, Gu Shanqiang, et al. Optimization Method for Fine Autonomous Inspection Route of Transmission Lines by Multi-rotor Unmanned Aerial Vehicle[J]. High Voltage Engineering, 2020, 46(9): 3054-3061.

[3] Duan H B, Qiao P X. Pigeon-Inspired Optimization: A New Swarm Intelligence Optimizer for Air Robot Path Planning[J]. International Journal of Intelligent Computing and Cybernetics(S1756-378X), 2014, 7(1): 24-37.

[4] Zhang B, Duan H B. Three-Dimensional Path Planning for Uninhabited Combat Aerial Vehicle Based on Predator-Prey Pigeon-Inspired Optimization in Dynamic Environment[J]. IEEE/ACM Transactions on Computational Biology and Bioinformatics(S1545-5963), 2017, 14(1): 97-107.

[5] 戴佳佳, 范丽鹏, 庞明勇. 特征驱动的三维网格模型自适应重采样算法[J]. 系统仿真学报, 2019, 31(5): 853-860.
Dai Jiajia, Fan Lipeng, Pang Mingyong. Adaptively Resampling 3D Mesh Models Based on Editable Features [J]. Journal of System Simulation, 2019, 31(5): 853-860.

[6] 张衡, 程浩忠, 柳璐, 等. 基于点估计法随机潮流的输电网多阶段规划研究[J]. 电网技术, 2018, 42(10): 3204-3211.
Zhang Heng, Cheng Haozhong, Liu Lu, et al. Research on Multistage Transmission Network Expansion Planning Using Point Estimation Method Based on Stochastic Power Flow[J]. Power System Technology, 2018, 42(10): 3204-3211.

[7] Qi S, Qing L Z, Shu X W, et al. Dynamic Path Planning for Unmanned Vehicles Based on Fuzzy Logic and Improved Ant Colony Optimization[J]. IEEE Access(S2169-3536), 2020, 8: 62107-62115.

[8] Meera Dash, Trilochan Panigrahi, Renu Sharma. Distributed Parameter Estimation of IIR System Using Diffusion Particle Swarm Optimization Algorithm[J]. Journal of King Saud University Engineering Sciences (S1018-3639), 2019, 31(4): 345-354.

[9] 杨虹, 张雅声, 徐灿. 基于trace特征的ISAR像空间目标识别[J]. 电子学报, 2020, 48(3): 431-441.
Yang Hong, Zhang Yasheng, Xu Can. Space Target Recognition Based on Trace Feature of ISAR Image[J]. Acta Electronica Sinica, 2020, 48(3): 431-441.

[10] Lan R S, Yong J, Ding L G, et al. Automated Flare Prediction Using the AdaBoost Algorithm[J]. Research in Astronomy and Astrophysics(S1674-4527), 2012, 12(9): 1191-1196.

[11] Dinh V Q, Pham C C, Jeon J W. Robust Adaptive Normalized Cross-Correlation for Stereo Matching Cost Computation[J]. IEEE Transactions on Circuits and Systems for Video Technology(S1051-8215), 2017, 27(7): 1421-1434.

[12] Feng Y. Mobile Terminal Video Image Fuzzy Feature Extraction Simulation Based on SURF Virtual Reality Technology[J]. IEEE Access(S2169-3536), 2020, 8: 156740-156751.

[13] 毛远宏, 贺占庄, 马钟. 重构迁移学习的红外目标分类[J]. 电子科技大学学报, 2020, 49(4): 609-614.
Mao Yuanhong, He Zhanzhuang, Ma Zhong. Infrared Target Classification with Reconstruction Transfer Learning[J]. Journal of University of Electronic Science and Technology of China, 2020, 49(4): 609-614.

[14] Chen Z, Bai Z J. Classification of Color Images Based on Vgg16 Network Model and Lib-SVM[J]. International Journal of Compu-tational and Engineering(S2414-1895), 2019, 4(2): 32-34.

[15] Xing H H, Zi L W, Qiang F, Mobile Robot ADRC With an Automatic Parameter Tuning Mechanism Via Modified Pigeon-Inspired Optimization[J]. IEEE/ASME Transactions on Mechatronics(S1083-4435), 2019, 24(6): 2616-2626.

[16] Zhang F, Wang Y, Ni J, et al. SAR Target Small Sample Recognition Based on CNN Cascaded Features and AdaBoost Rotation Forest[J]. IEEE Geoscience and Remote Sensing Letter(S1545-598X), 2020, 17(6): 1008-1012.

[17] 吴鹏, 徐洪玲, 宋文龙. 结合小波金字塔的快速NCC图像匹配算法[J]. 哈尔滨工程大学学报, 2017, 38(5): 791-796.
Wu Peng, Xu Hongling, Song Wenlong. A Fast NCC Image Matching Algorithm Based on Wavelet Pyramid Search Strategy[J]. Journal of Harbin Engineering University, 2017, 38(5): 791-796.

[18] 宿德志, 王玉良, 吴世永, 等. 基于相似三角形的星图识别[J]. 光学精密工程, 2019, 27(11): 2467-2473.

Su Dezhi, Wang Yuliang, Wu Shiyong, et al. Star Identification Algorithm Based on Similar Triangle Principle[J]. Optics and Precision Engineering, 2019, 27 (11): 2467-2473.

[19] 潘志庚, 刘荣飞, 张明敏. 基于模糊综合评价的疲劳驾驶检测算法研究[J]. 软件学报, 2019, 30(10): 2954-2963.
Pan Zhigeng, Liu Rongfei, Zhang Mingmin. Research on Fatigue Driving Detection Algorithm Based on Fuzzy Comprehensive Evaluation[J]. Journal of Software, 2019, 30(10): 2954-2963.

[20] Shahzad M, Maurer M, Fraundorfer F, et al. Buildings Detection in VHR SAR Images Using Fully Convolution Neural Networks[J]. IEEE Transactions on Geoscience and Remote Sensing(S0196-2892), 2019, 57(2): 1100-1116.

机床与液压
MACHINE TOOL&HYDRAULICS

编辑部 电话：020—32385312 邮箱：jcy@gmeri.com
广告部 电话：020—32385311 邮箱：webmaster@gmeri.com
传真：020—32389600 邮编：510530
地址：广州市萝岗区新瑞路2号

# 录用通知

尊敬的作者： 魏协奔

您好！我社于 2021-12-17 收到您寄来的稿件一篇，稿件登记编号：JY20213015，文章标题：《轧机齿轮箱多通道振动监测系统设计与研究》，稿件经初审，处理意见如下：录用。

该文拟定于在本刊 2022 年 11 月第 21 期发表(根据排版情况，文章可能提前或推迟一月发表)。

特此通知。

《机床与液压》编辑部

2022-03-15

**本刊郑重声明：(作者如不同意以下声明，请与我刊联系退稿)**

**1. 作者投稿，请严格遵守《中华人民共和国著作权法》的有关规定，文责自负；**

**2. 投稿文章如有剽窃、不正当使用或引用他人作品，投稿者将承担由此所引起的一切法律责任；**

**3. 凡经本刊采用的文章，请勿一稿多投，本刊对违约者保留追究法律责任的权利。**

**4. 作者稿件在本刊发表，即视同作者同意本刊可以在本刊网站转载和被其他有关数据库收录其文章的权利。**

谢谢您的支持和合作！